Three-dimensional Thermal and Airflow (3D-TAF) Model of a Dome-covered House in Canada

Yaolin Lin

A Thesis

in

The Department

of

Building, Civil, and Environmental Engineering

Presented in Partial Fulfillment of the Requirements
for the Degree of Doctor of Philosophy at
Concordia University
Montreal, Quebec, Canada

April, 2007

Canada

ABSTRACT

Three-dimensional Thermal and Airflow (3D-TAF) Model of a Dome-covered House in Canada

Yaolin Lin, Ph.D.
Concordia University, 2007

A dome-covered house is an example of designing sustainable buildings by learning from the optimized biological forms from the nature. This dissertation presents a three-dimensional thermal and air flow (3D-TAF) model that estimates the energy needs of a dome-covered house.

The mathematical model is composed of two components, that is, the thermal model and the air flow model, which are solved iteratively at every time step until the convergence is reached. The thermal model calculates the temperature of some nodes of interest of the simulation domain. The heat balance equations are written for: (a) the dome glazing; (b) the exterior envelope and the floor of the house; (c) the air inside the house; and (d) the earth surfaces inside the dome. The airflow model calculates the air velocities inside the dome, which are required by the thermal model to estimate the convective heat flow rate at the interface solid-air (e.g., between the dome cover and the dome air). It calculates also the vertical and horizontal temperature gradient of the air inside the dome.

Numerical method for solving the mathematical model is presented, which includes the discretization schemes, formation of the system of equations, initial values of the unknowns, solution algorithm and calculation procedure.

The validity of the mathematical model is demonstrated by comparison with a simplified computer model under MATLAB environment, with results from a 2D CFD model under the COMSOL Multiphysics environment, and with measured data and simulation results from similar structures, published by other researchers. The results have verified that the model gives good prediction on the temperature of the dome glazing, the air temperature and the air movement inside the dome.

A transparent dome, built above one house located in Montreal is selected as a case study. The simulation results predict a reduction of 62.6% of the annual heating load of a house when a dome is used, compared with the case of an unprotected house. Sensitivity analysis of the impact of optical properties of the dome glazing, natural infiltration/exfiltration through the dome/house, shape of the dome, and ground thermal properties on the heating load of the house is presented.

Acknowledgements

I would like to thank my supervisor, Dr. Radu Zmeureanu, for giving me full support on all aspects of this research work throughout these years. His precise vision, valuable advices are the key factors to the success of this research.

I would also like to thank my supervising committee, Dr. F. Haghighat, Dr. M. Zaheeruddin and Dr. A.K.W. Ahmed for their comments and suggestions on this work.

I am grateful to Dr. K. Qiu for discussions about CFD model and Ms. P. Karava for discussions about the zonal model. And it is enjoyable to talk with Weimin, Sami, Xuyu, Larry and David on everyday life. I am indebted to Mr. Sylvain Bélanger for solving some computer problems.

I could never forget all my friends and colleagues, who have enriched my life at Concordia University in the past three years.

I thank my parents for their unconditional love and support that have helped me survived during the difficult time in my life.

Table of Contents

List of Figures

List of Tables

NOMENCLATURE

A,B,C: coefficients of the clear sky model, given in ASHRAE (1992)

ACH: air change rate per hour, h^{-1}

A_{dome}: surface area of the dome, m^2

$A_{f,ij}$: air-solid interface area, m^2

A_g : ground area inside the dome, excluding the floor area of the house, m^2

A_{ij} : area of cell (i,j) of the dome surface, m^2

A_l : area of the wall/roof surfaces, m^2

A_L : equivalent area, cm^2/m^2

A_s : amplitude of surface temperature, °C

A_n: coefficient presented in a Table in Montes and Fernandez (2001)

$A_{z,ij}$: boundary area, m^2

C_d: discharge coefficient

C_N: clearness number

c_p : specific heat, J/kg·°C

C_p : pressure coefficient

d: thickness of glazing, m

dx: thickness of layer, m

E_j: blackbody emissivity power, W/m^2

En_i : energy in zone i, J

$\dot{En}_{ij}$:   rate of heat transfer from zone i to zone j, W

$\dot{En}_{sink}$: rate of energy removed from zone, W

$\dot{En}_{source}$: rate of energy supplied by the source in zone, W

ET: equation of time, min.

F_{ij}:   view factor between surface i and surface j

$F_{ij,g}$:   view factor between cell (i,j) and the ground surface inside the dome

$F_{ij,g,out}$: view factor between the cell (i,j) and the ground outside the dome

$IF_{p,k}$:   total interchange view factor between surface p and surface k

$F_{rad,k}$:   radiative fraction for the kth internal heat gain element

F_s :   special allowance factor (ballast factor in the case of fluorescent and metal halide

fixtures)

F_u :   use factor, ratio of wattage in use to total installed wattage

h_a :   convective coefficient over the inside wall surface, $W/m^2 \cdot °C$

h_{c_glass} : outside convective coefficient for glass, $W/m^2 \cdot °C$

$h_{in,ij}$:   convective coefficient over the inside surface of cell (i,j), $W/m^2 \cdot °C$

$h_{in,g}$:   convective coefficient over the ground surface inside the dome, $W/m^2 \cdot °C$

$h_{in,l,out}$: convective coefficient over the exterior wall/roof surfaces of the house inside

the dome, $W/m^2 \cdot °C$

h_n :   natural component of the convective coefficient, $W/m^2 \cdot °C$

$h_{o,ij}$:   convective coefficient at the outside surface of cell (i,j), $W/m^2 \cdot °C$

$h_{r,p,k}$: radiation coefficient between surface p and surface k, $W/m^{2\circ}C$

$h_{r,ij,g,out}$:radiation coefficient between cell (i,j) and the ground outside the dome, $W/m^2 \cdot {}^\circ C$

$h_{r,ij,sky}$: radiation coefficient between cell (i,j) and sky, $W/m^2 \cdot {}^\circ C$

$h_{win,in}$: convective coefficient over the inside surface of the window, $W/m^2 \cdot {}^\circ C$

$h_{win,o}$: convective coefficient over the outside surface of the window, $W/m^2 \cdot {}^\circ C$

H: height of the dome, m

H*: dimensionless lenghth

H_i: height of the ith layer, m

I_{DN} : direct normal solar radiation, W/m^2

I_d: diffuse solar radiation, W/m^2

I_{df} : transmitted diffuse incident solar radiation, W/m^2

I_d': transmitted beam solar radiation reaching the ground surface inside the dome directly, W/m^2

I_d'': transmitted beam solar radiation that is reflected by the inside cell surfaces and reaches the ground surface inside the dome, W/m^2

$I_{ds,ij}$: diffuse incident solar radiation from the sky that reaches cell (i,j), W/m^2

$I_{dg,ij}$: incident solar radiation reflected from the ground outside the dome that reaches cell (i,j) of the dome surface , W/m^2

J: radiosity of each surface, W/m^2

k : thermal conductivity of the layer, $W/m \cdot {}^\circ C$

l: length of the common border between two cells, m

L: site latitude, deg.

LST: local standard time, min.

LON_{st}: standard longitude, deg.

LON_{loc} : local longitude, deg.

$\dot{m}_a$:   natural infiltration rate, kg/s

m_{ij} :   mass of one cell (i,j) of the dome surface, kg

$\dot{m}_{ij}$:   mass flow rate between zone (i) and zone (j), kg/s

m_{in} :   mass of air inside the dome, kg

$\dot{m}_{i1,j1-i2,j2}$: mass flow rate from zone (i1, j1) to zone (i2, j2), kg/s

$\dot{m}_{M+1,2-M+1,1}$: mass flow rate from the central zone of the 2nd layer to the central zone of the 1st layer, kg/s

$\dot{m}_{sink}$: rate of mass removed from zone, kg/s

$\dot{m}_{source}$: rate of mass supplied by the source in zone, kg/s

n: pressure exponent

n_d: Julian date, days

n_{lag} : phase lag of soil surface temperature, days

N_c: coefficient

p: pressure, Pa

q: heat flux, W/m^2

q_{conv} : convective heat transfer, W/m^2

$q_{conv,ij}$: convective heat flux over the inside or outside cell surface (i,j), W/m^2

$q_{conv,in,ij}$: convective heat gain/loss from the air inside the dome, W/m^2

$q_{conv,l,in}$: convective heat transfer over the inside wall surface, W/m^2

$q_{conv,l,out}$: convective heat transfer over the outside wall surface, W/m^2

$q_{conv,out,ij}$: convective heat gain/loss from the outside air, W/m^2

$q_{LWR,ij}$: long-wave radiation between cell (i,j) and the outdoor environment (ground and sky), W/m^2

$q_{rad,ihg,l}$: radiation heat flux due to internal heat gain, W/m^2

q_{sol} : absorbed solar radiation, W/m^2

$q_{sol,ij}$: absorbed incident solar radiation (including direct, diffuse and ground reflected solar radiation) on cell (i,j), W/m^2

$q_{sol,l,int}$: absorbed solar radiation at the inside wall surface, W/m^2

$q_{sol,l,out}$: absorbed solar radiation at the outside wall surface, W/m^2

q_{surf} : net surface-to-surface radiation, W/m^2

$q_{surf,ij}$: net long-wave surface-to-surface radiation between the cell (i,j) and other surfaces inside the dome, W/m^2

$q_{surf,l,in}$: net surface-to-surface radiation leaving the inside wall surface, W/m^2

$q_{surf,l,out,t}$: net surface-to-surface radiation leaving the outside wall surface, W/m^2

q_{win} : heat loss through the window, W/m^2

$Q_{conv,in}$: convective heat flux over the surface of the boundary for the air inside the dome,

W

Q_{exf} : exfiltration heat gain/loss from the air inside the house, W

$Q_{exf,s}$: sensible heat gain/loss from exfiltration, W

Q_f: airflow rate, m^3/s

Q_{HVAC} : heat addition rate by the heating system, W

Q_{inf} : infiltration heat gain/loss from the air outside the dome, W

$Q_{inf,s}$: sensible heat gain/loss from infiltration, W

$Q_{internal,conv}$: convective part of internal heat gain, from people and lighting, W

Q_k : heat gain for the kth internal heat gain element, W

R: dome radius, m

R_w: thermal resistance of the glazing, $m^2 \cdot {}^\circ C/W$

SHGC: solar heat gain coefficient

t: time, s

th: thickness of the wall, m

T : temperature, $^\circ C$

T^*: dimensionless temperature

T_0 : reference temperature at which ρ_0 is calculated, 293K

T_a : temperature of the air inside the house, $^\circ C$

$T_{d,i,j}$: temperature of the perimeter zone adjacent to cell(i,j), $^\circ C$

$T_{f,1}$: temperature of the floor surface, $^\circ C$

$T_{g,out}$: surface temperature for the ground outside the dome, $^\circ C$

$T_{g,z}$:   soil temperature at depth z, °C

T_{ms} :   mean annual surface temperature, °C

$T_{i,j}$:   temperature of cell (i,j) of the dome, °C

T_{is} :   inner layer temperature of the window, °C

$T_{j,in}$:   temperature of inside surface j, °C

$T_{l,in}$:   temperature of inside wall surface l, °C

T_o :   outdoor air temperature, °C

T_{os} :   outer layer temperature of the window, °C

T_{sky} :   sky temperature for a horizontal surface, °C

$T_{sky,\Sigma}$:   sky temperature for a tilted surface, °C

U_w :   U-value of the window, W/m^2·°C

V^* :   dimensionless velocity

V_{az} :   wind speed at the height of z, m/s

V_{in} :   volume of the dome, excluding the house, m^3

V_{exf} :   natural exfiltration airflow rate, m^3/s

V_H :   wind speed at dome height, m/s

V_{House} : volume of the house, m^3

V_{inf} :   natural infiltration airflow rate, m^3/s

V_o :   wind speed at the height of z_0, m/s

V_w :   wind speed over the surface, m/s

W :   total installed light wattage, W

x: thickness of the layer, m

z: depth, m

z_o :   height at which standard wind speed measurements are taken, 10 m

Greek Symbols

$\alpha_s, \alpha_h, \alpha_f, \alpha_a$:   temperature diffusion coefficient of soil, wall layer, floor layer, and air, respectively, m^2/s

α, γ, τ: absorptance, reflectance and transmittance of a flat glazing, respectively

α_{kl} :   absorptance of the reflected cell surface

τ_w: equivalent transmittance of the dome

ε_{ij} :   surface long-wave length emissivity

$\varepsilon_{f,ij}$: ± 1; gives the sign of flow direction

Ψ: azimuth angle, deg.

θ: incident angle, deg.

θ_{kl} :   incident angle of the cell (k,l), deg.

θ_{pq} :   incident angle of the cell (p,q), deg.

ρ: density, kg/m3

ρ_0:   density of air at 293K, 1.205 kg/m^3

σ_0:   dome truncation angle, deg.

σ_c :   Stephan-Boltzmann constant, $5.67 \cdot 10^{-8} W/m^2 \cdot K^4$

ω: hour angle, deg.

β: solar altitude, deg.

β_a: volume expansion coefficient, K^{-1}

ν: kinematic viscosity, m^2/s^2

Σ: tilted angle, deg.

ΔT: temperature difference, °C

Δp: pressure difference, Pa

Δp_r :   reference pressure difference, Pa

Subscripts

b: beam radiation

conv: convection

d: diffuse radiation

dome: dome surface

DN :   direct normal

eq: dome-equivalent planar surface

exf: exfiltration

f: flow

f: full

f: interface

G: ground

g: ground

h: horizontal surface

i: indoor

inf: infiltration

m: model

o: outdoor

sol: solar radiation

surf: surface-to-surface radiation

w :   wall

z :   zone

Chapter 1 Introduction

1.1 Nature and Sustainable Buildings

The concept of sustainable buildings originates from the sustainable development. The sustainable development was defined by the WCED (World Commission on Environment and Development), as the development that meets the needs of the present of humanity without compromising the ability of our future generations to meet their own needs (WCED, 1987).

The term "sustainable buildings" is introduced in the contexts of sustainability. As there are many different viewpoints about sustainability, there are also various kinds of definitions for sustainable buildings (Yashiro, 2000; Keeken, 2001; Resource Venture, 2003; Landman, 2003; DCLU, 2003; and Abusada, 2003).

Sustainable buildings are regarded as buildings that fit the sustainable development, by satisfying the needs of the present without compromising the ability of future generations to meet their own needs (Keeken, 2001), to keep resources in balance with nature (Resource Venture, 2003), to use resources efficiently and to keep the environment healthy (Yashiro, 2000; Landman, 2003), to consider environmental, economic and social impact as an integrated whole (DCLU, 2003), to achieve compromise in conserving the buildings regarding the diversity in different needs of generation in a programmed lifetime (Abusada, 2003), and to improve the quality of life and harmonize with the ecosystem throughout the buildings lifecycle (Yashiro, 2000). It is also recognized as the

whole process including site planning, design, material, renewable energy, etc. (Royal Netherlands Embassy, 2003; Norton 2003), to minimize the negative impact on the present and future environment and natural resources including urban structure and land use (ASHRAE, 2003; Kremers, 2003), to prolong the availability of natural resources (Kremers, 2003), to support the existence of humanity without destroying the environmental and cultural context (Yasser, 1997).

Energy consumption plays a significant role in analyzing the performance of the sustainable buildings. According to a U.S. statistical report (DOE, 2004), the buildings in the U.S. account for 36% of the total primary energy consumption, of which residential buildings alone account for 21%. The buildings consume 71% of the electricity, of which residential buildings alone account for 36%. The energy consumption of buildings already exceeds that of industries. With respect to electricity consumption, the share of buildings is 2.45 times as much as the sum of the electricity used for industrial and transportation.

A large proportion of GHG (green house gases) emissions, air pollutants, and solid wastes are produced by the building sector due to the large amount of energy consumption. In the U.S., the amount of CO_2 emission produced by the buildings accounts for 38% in the year 2002 (DOE, 2004).

Similar situation exists in Canada, where the energy use by the building sector accounts for 30.8% (Natural Resources Canada, 2004). The energy demand for residential buildings alone has been increased from 1, 289 petajoules (PJ) to 1, 399 PJ since 1990. At the same time, there is an increase of GHG Emissions from 70 megatonnes (MT) of

CO_2 equivalent to 75 MT of CO_2 equivalent due to residential building energy consumption.

It can be concluded from above that building energy consumption accounts for a large proportion of primary energy use and GHG emissions. Thus it has great impact on our environment and affects the sustainability of our future life.

In 1982, The United Nation's World Charter for Nature adopted the principle that every form of life is unique and should be respected irrespective of its value to humankind (UN, 1982). It calls for an understanding of our dependence on natural resources and the need to control our exploitation of them and also recognized that mankind is a part of nature and life depends on the uninterrupted functioning of natural systems. In order to design sustainable buildings, nature should not be disregarded.

While designers are striving to use material and energy more efficiently, it is expected that much of the conventional, modern architectures are not sustainable over the long term due to the limited consideration of the interaction between buildings and environment. On the other hand, nature itself has evolved for billions of years and there should be lessons that can be learned from, especially the habitats that have been built harmonily with the environment by creatures (Tsui, 1999). Nature has provided us many solutions on various aspects of sustainability, including building materials properties, building envelope, environmental considerations, sensors and monitoring, team integration and functionality (John et al., 2005). Therefore, it is possible to design sustainable buildings by learning from nature. Designing buildings by learning from the optimum forms existing in nature is a possible way to fulfill this endeavor since these

forms have undergone billions of years of evolution and still exist in nature.

Dome structure is based on self-generating forms in nature, bubble clusters being typical examples. It is based on the natural form-optimizing process in biological structures and can be translated into the architectural world in the form of pneumatic structure (Arslan and Sorguc 2004; Srach, 2004). The dome configuration applies nature's principles of forming a highly efficient system.

The advantages of a transparent dome built above a group of houses in Canada are the following (Croome, 1985): it can provide a shelter to withstand high winds and extreme temperature, and it can help for storing solar radiation in the external walls of the house and in the ground. Thus it reduces the heating load of the house in the winter. If the dome is transparent or translucent, it can provide pleasant view without sense of enclosure.

1.2 Research Objectives

The aim of this research is to analyze the energy performance of a dome-covered house, as an example of designing sustainable buildings by learning from the optimum biological forms from the nature, since energy consumption is an important indicator on the sustainability of buildings. In detail, the research intends to:

- Develop a mathematical model to simulate the energy performance of a dome-covered house. The model will take into account the thermal interactions between the outdoor environment and the ensemble dome and house.

- Compare the energy performance of this dome-covered house with the same house unprotected by a dome.

- Explore the impact of optical/thermal properties of dome glazing, natural infiltration/exfiltration of the dome/house, shape of the dome, and ground thermal properties, on the performance of the dome-covered house.

- Explore the impact of weather conditions, including the wind speed, wind direction and solar radiation on the thermal performance of the dome-covered house.

- Evaluate the air flow and temperature distribution inside the dome.

1.3 Organization of the Dissertation

The dissertation is organized as follows:

- Chapter 2 presents a literature review about the thermal performance of dome-like structures. A survey on the existing mathematical models is made, and some limitations of the models are identified.

- Chapter 3 gives a description on physical phenomena inside the dome, the geometric information of the dome, and a comparison between the proposed model and other mathematical models.

- Chapter 4 presents the thermal model of a dome-covered house. The heat balance equations are written at the dome surface, for the air inside the dome, at the outside surfaces of the house, at the inside surfaces of the house, at the ground surfaces, and for the air inside the house. Comparisons between the simulation results from different versions of the single-node model, where the air inside the

dome is assumed well-mixed, are presented.

- Chapter 5 introduces the air flow model that evaluates the air flow and temperature distribution inside the dome.

- Chapter 6 presents the numerical solution of the mathematical model, including the discretization schemes, formation of the system of equations, initial values of the unknowns, solution algorithm and calculation procedure.

- Chapter 7 presents the verification and validation of the mathematical model. The mathematical model is verified with a simplified model under MATLAB environment, CFD simulations under the COMSOL Multiphysics environment, experimental measurements and simulation results from similar structures published by other researchers.

- Chapter 8 presents a case study with a transparent dome built above one house located in Montreal. Sensitivity analysis of the impact of optical/thermal properties of dome glazing, natural infiltration/exfiltration through the dome/house, shape of the dome, and ground thermal properties on the performance of the dome-covered house is presented.

- Chapter 9 ends the dissertation with the summary of major contributions and suggestions for future work.

Chapter 2 Literature Review

This chapter first presents a survey of thermal performance of domes, then some thermal models and optical models of dome-like structure are reviewed, and conclusions from the literature review are outlined in the final section.

2.1 Thermal Performance of Domes

More attention has been given to the structural configuration than to the thermal performance of dome-like transparent buildings. According to the Buckminster Fuller Institute web site (BFI, 2005), the largest geodesic-dome structures are presented in Table 2-1, in descending order of diameters:

Table 2-1 Largest geodesic-dome structures

No.	Name	Location	Diameter [m]
1	Fantasy Entertainment Complex	Kyosho Isle, Japan	216
2	Multi-Purpose Arena	Nagoya, Japan	187
3	Tacoma Dome	Tacoma, WA, USA	161
4	Superior Dome	Northern Michigan Univ Marquette, MI, USA	160
5	Walkup Skydome	Northern Arizona Univ. Flagstaff, AZ, USA	153
6	Round Valley High School Stadium	Springerville, AZ USA	134
7	Former Spruce Goose Hangar	Long Beach, CA, USA	126
8	Formosa Plastics Storage Facility	Mai Liao, Taiwan	122
9	Union Tank Car Maintenance Facility	Baton Rouge, LA USA	117
10	Lehigh Portland Cement Storage Facility	Union Bridge, MD USA	114

The Multi-Purpose Arena is the world's second largest dome with a single-layered lattice structure. It has an interior roof frame structure acting as a shading system that allows the adjustment of natural light (Takenaka Corporation, 2000). This arena has the total floor space of 119,707 m^2, six floors above ground, a maximum height of 66.9 m, and a span of 187.2 m. It can accommodate 40,500 spectators. The structure is made of steel-framed

single-layered lattices, and it was completed in 1997. The dome has hexagonal windows located at the top to provide the arena with natural lighting. It has 144 triangular translucent screens, each around 10 m per side and can be adjusted for daylighting.

According to Monolithic Dome Institute (2006), a monolithic dome of about 340 m^2 of living space, having walls and ceiling with the thermal resistances of 10.5 m^2·°C/W, and low emissive windows has reduced the energy cost by over \$2, 000 per year compared with a conventional masonry house of the same size.

Croome (1985) presented his concept of building a covered township in the northern part of Canada, using a double layer membrane. By computer simulation he predicted the reduction of about 16% of the annual heating energy needs for houses built under that cover, compared with houses without cover. Figure 2-1 presents the simulated mean temperature in the covered township for various months of the year at specified mean monthly outside temperature by simulation.
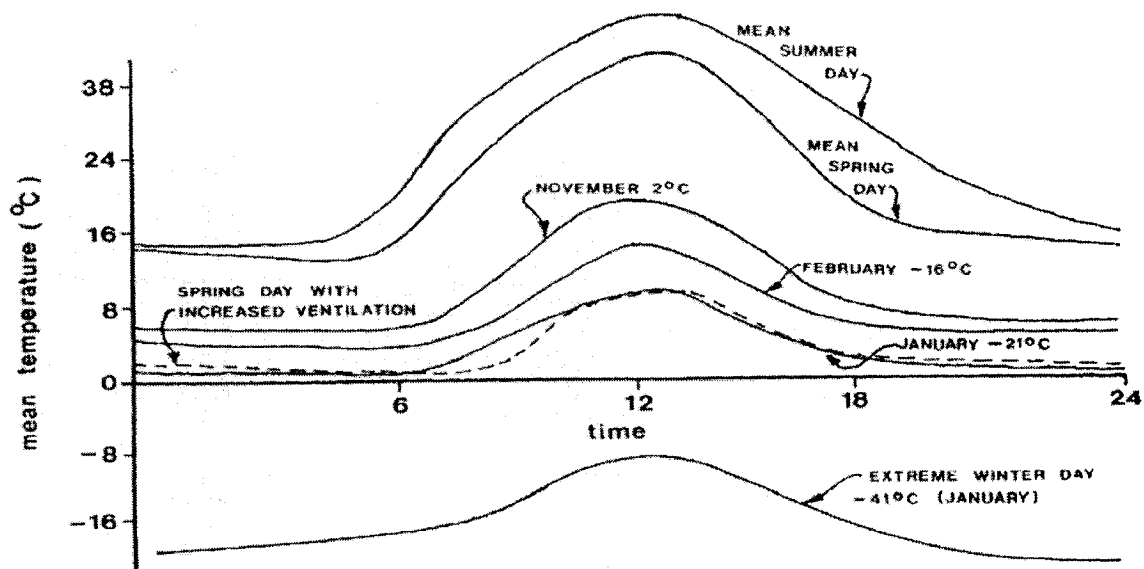
Figure 2-1 Mean temperature in the covered township for various months of the year at specified mean monthly outside temperature (Croome, 1985)

It can be concluded that, if properly designed, a dome-covered house can have a reduced heating load, and may even achieve the reduction of the annual energy consumption.

2.2 Models for the Prediction of Air Temperature

Only a few thermal models have been presented so far for domes, mostly based on the heat balance approach. Croome and Moseley (1984a) developed a quasi-steady state model with one node for the cover and one node for the inside air to predict the air temperature inside the dome, and observed that the solution obtained through the finite difference method tends to overestimate the air temperature throughout the day because of the model used for coupling the indoor air and ground temperatures inside the dome. Luttmann-Valencia (1990) developed a single node model that predicts the air temperature inside Biosphere II, located in Arizona (U.S.). Sharma et al. (1999) presented a four-zone model that predicts the air temperature inside a greenhouse, by assuming that there is no air movement between zones. In those models, the air infiltration and airflow rate are either given as the airflow rate (Luttmann-Valencia, 1990) or air change rate per hour (Sharma et al., 1999). Singh et al. (2006) presented a single node model that predicts the air temperature inside a greenhouse located in Ludhiana (India), by assuming that there is no air movement inside the greenhouse. Jain (2007) modeled the thermal performance of a greenhouse, based on the following assumptions: a) the inside air has no heat capacity; b) optical property of the glazing does not change with the incident angle of solar radiation; c) there is no long-wave radiation between surfaces; d) the glazing has no heat capacity; e) solar radiation reaching the inside surface is proportional to the view factor between the greenhouse external surface and the inside surface, that is, the incident angle is not considered.

Those models (Croome and Moseley 1984a, 1984b; Luttmann-Valencia, 1990; Sharma et al., 1999; Singh et al., 2006; Jain, 2007) did not solve for the temperature distribution over the cover, and the convective heat transfer coefficient is used as a constant value, regardless of the temperature difference, tilted angle, flow direction and variation of air velocity at different locations. Moreover, the temperature variation and air movement inside the dome are neglected, and the distribution of solar radiation that is transmitted through the glazing is estimated in a simple way.

A few researchers have used the system identification methods to predict air temperature inside greenhouse: fuzzy modeling method (Salgado and Cunha, 2005) and neural networks model (Seginer et al., 1994; Frausto and Pieters, 2004). These techniques do not require the evaluation of heat transfer coefficients; however, they need measurements in existing domes, from which the inverse models are generated. Therefore, these techniques cannot be used for design purposes.

Nara (1979) presented a 2D CFD model for calculating the air velocity and temperature distribution due to thermal convection inside a reduced-model of a farm building under adiabatic boundary condition. The Boussinesq approximation is combined with the Navier-Stokes equation to describe the natural convection. Boulard et al. (1997) used a reduced-scale model of a greenhouse with a high temperature of the floor to simulate the impact of solar radiation on the greenhouse. The k-ε model was added to simulate the turbulent flow. Grashof number was used in these two papers to ensure the similarity between the full scale model and reduced scale experimental model. The numerical models (Nara, 1979; Boulard et al., 1997) showed good agreements with experimental

results for the closed greenhouse. Shklyar and Arbel (2004) examined the wind-driven isothermal flow patterns and mass fluxes in a full-scale, pitched-roof, single span glasshouse using standard and high-Reynolds-number k-ε models.

The CFD models presented above (Nara, 1979; Boulard et al., 1997; Shklyar and Arbel, 2004) are based on steady state models, and therefore are quite different from the actual transient climatic conditions. Moreover, the temperature variation and air flow exist inside the dome due to the large volume and continuous change of the direction of the incoming solar radiation. Although the CFD model can be used to evaluate the air temperature distribution, the calculations using a CFD model for such large scale structure requires to subdivide the volume of the dome into a large number of nodes and will suffers from a significant user effort for problem definition as well as requiring substantial computation effort.

2.3 Mathematical Models of Optical Properties of Dome Glazing

So far transparent and translucent domes have been used as skylights for daylighting and energy saving purposes. Some models (e.g., Wilkinson, 1992; Laouadi and Atif, 1998; Laouadi and Atif, 1999; IESNA, 2000), have been developed to predict the optical and thermal properties of dome skylights. Those models replace the single-glazed hemispherical skylight by an optically and thermally equivalent single-glazed planar skylight. For example, Wilkinson (1992) predicted the daylight factor inside a translucent dome. Laouadi and Atif (1998, 1999) developed an optical model to predict the optical (transmittance, absorptance and reflectance) and thermal properties of transparent skylights. ASHRAE procedure for calculation of the U-value of the structure assumes the

dome skylight as a tilted glazing (ASHRAE 2001b).

Wilkinson (1992) developed theoretical relations for the calculation of daylight factor based on horizontal illuminance formulation inside and outside a dome. Three types of radiation were considered: diffuse radiation from isotropic and CIE (Commission Internationale de l'Eclairage) overcast skies, and beam radiation. The dome surface was assumed to be a diffuse transmitter and reflector (translucent). Direct beam solar radiation passing through the dome was treated as diffuse radiation. In this model, the ground-reflected radiation is not taken into account.

Laouadi and Atif (1998) developed an optical model to predict the equivalent transmittance, absorptance and reflectance of a transparent, hemispherical, dome skylight, based on the following assumptions: (1) the light transmittance, absorptance and reflectance at any point on the dome surface are equal to those of a planar surface at the same incident angle; and (2) the amount of light reflection from the interior space under the dome back to the dome interior surface is not accounted for. Laouadi and Atif (1999) presented a model to calculate the equivalent solar heat gain factor (SHGC) and U-value of a transparent dome.

IESNA (Illuminating Engineering Society of North America) (2000) suggested the following mathematical formula to calculate the equivalent visible transmittance of single and double glazed dome skylights:

$$\tau_w = 1.25 \cdot \tau \cdot (1.18 - 0.416 \cdot \tau) \tag{2-1}$$

where:

τ_w=dome transmittance;

τ=flat-sheet transmittance.

This approach does not take into account for the dome shape, and it has not been validated with measurements.

ASHRAE (2001b) used the procedure for windows to calculate the solar and total heat gain for dome skylight. For instance, for a clear glass dome, with the normal transmittance of 0.86, the SHGC is 0.7 if the skylight has the height of 45 cm, and the width-to-height ratio is 2.5.

Those models (IESNA, 2000; Wilkinson, 1992; Laouadi and Atif, 1998; Laouadi and Atif, 1999) simplify the calculation of the solar radiation through the dome skylights, and then apply the dome skylight in the building performance simulation tools. However, at different locations of the dome skylight, the absorption of solar radiation is different, and therefore the temperature varies over the dome skylight. The variation of the glazing temperature over the dome skylight has an impact on the thermal performance of the building and should be regarded. The solution to this problem is to treat the dome skylight as composed of a number of inclined surfaces, or control volumes.

2.4 Experiments

Sase et al. (1984) carried out a wind tunnel test on the air flow and temperature distribution of a naturally ventilated greenhouse. They used the Archimedes number for the similarity of the ventilation phenomena. Croome and Moseley (1984b) presented measurements of the air temperature inside an airhouse located in London (U.K.), along

with the outside air temperature and solar radiation. Asfia and Dhir (1996) conducted an experimental study of the natural convective heat transfer in internally heated hemispherical pool with external cooling. Boulard et al. (1997) studied the air infiltration for six greenhouses, and they presented the infiltration rate as a function of vent opening area of the greenhouse, incoming wind speed and the average height of the greenhouse.

Boulard et al. (1998) conducted an experimental study of the airflow and temperature distribution induced by natural convection using floor heating to simulate the absorption of solar radiation at the floor surface. Temperature was measured by thermocouples and airflow was measured by hot wire anemometry. A modified Grashof number was used for similarity analysis of the flow pattern. The authors noticed a strong temperature drop just above the heated soil surface that represent about 70% of the total temperature difference between the soil surface and the outdoor air.

Montero et al. (2001) studied the effect of wind flow past a crop protection greenhouse. Reynolds number was used for similarity analysis. Lamrani et al. (2001) conducted an experimental study of the air flow and temperature distribution in a confined greenhouse using a reduced scale, mono-span chamber with floor heating. The chamber was kept airtight and with insulated walls. The temperature was measured with thermal couple and the air velocities were measured by laser anemometry. A modified Rayleigh number was used for similarity analysis.

Zhao et al. (2001) carried out an experiment in a full scale greenhouse and studied the vertical temperature gradient in a naturally ventilated greenhouse. He presented a linearized relationship between the normalized temperature T^* and height H^* inside the

greenhouse, with R-square greater than 0.82:

$$T^* = \frac{T}{T_{3.15}}$$
(2-2)

$$H^* = \frac{H}{3.6}$$
(2-3)

where:

T=measured air temperature, °C;

$T_{3.15}$=air temperature measured at 3.15m, °C;

H=height at measured point, m.

Bartzanas et al. (2005) studied the influence of heating system on microclimate inside a greenhouse and found that, without air heater, the air velocity above the crop is less than 0.035m/s, and when the air heater is turned on, the air velocity can reach 0.2m/s.

The experiments based on such models neglect the real impact of solar radiation, and are confined to 2D box-type room or room with pitched roof. Due to the complicate physical phenomena inside such structures, it is difficult to determine the similarity conditions between the full scale model and the reduced scale experimental model.

2.6 Other Related Studies

Smith (1999) developed a mathematical model to predict the impact of thermal exchange within pyranometers, simulated as a small glass dome exposed to natural convection. Porta-Gándara and Gómez-Muñoz (2005) modeled a Buckminster Fuller-type geodesic-dome to estimate the solar energy that passes through the dome, when it is covered with

electrochromic glazing, compared with the case of a common glass. Electrochromic glazing may be used to prevent the overheating inside such structure in the summer.

Roy et al. (2002) wrote a review of studies that considered the greenhouse indoor climate as uniform and Boulard et al. (2002) wrote a review of those studies on the greenhouse indoor climate using computational fluid dynamics (CFD) software. Those models, however, consider only the convective heat transfer in greenhouse and are steady state models.

Tang et al. (2003) developed a model of the heat transfer through dome roof, and predicted that the daily heat flow through a hemispherical roof under hot dry climatic conditions is greater by about 40% than in the case of flat roof. Wittkopf et al. (2006) proposed a model that divided a virtual sky dome (VSD) into 145 surfaces to simulate day lighting.

2.7 Conclusions

The optical models tried to simplify the dome skylight as a planar window to be used in simulation programs for calculation of solar radiation. However, a planar equivalence can not show the distribution of the solar radiation through the dome and can result in large errors when calculating the thermal performance of a dome-like structure. A model that can simulate the distribution of solar radiation is needed for the simulation of thermal performance of domes. The model should be able to evaluate the impact of the dome shape on the thermal behavior of the air inside the dome, and on the house. The new model should also take into account the solar radiation that reaches the inside surface of the dome glazing, because it will also increase the cell temperature.

The thermal models did not calculate the temperature distribution over the cover, and a constant value was used for the convective heat transfer coefficient, regardless of the temperature difference, tilted angle, flow direction and variation of air velocity at different locations. Moreover, the temperature variation and air movement inside the dome were neglected, and the distribution of solar radiation inside the dome after the first transmission was simplified.

The existing models also did not take into account the interaction between ground and dome/house. Therefore, a model that takes into account the thermal interactions between the ground/dome and dome/house is needed. The new model will also address the interaction between the solar radiation and the dome/air/ground/house and the surface-to-surface radiation. Moreover, an air flow model will be applied to evaluate the air flow inside the dome.

Chapter 3 Physical Phenomena and Geometric Information

The physical phenomena occurring inside the dome, and between the dome and the outside environment are presented in this chapter. First, the physical phenomena are addressed. Second, the geometric description of the dome and the coordinate system are described. In the end, a qualitative comparison between the proposed model and other mathematical models is presented.

3.1 Physical Phenomena

The dome is exposed to the outside environment, and the house is surrounded by the air inside the dome. Therefore, the model will focus on thermal interactions between the outdoor environment and the ensemble dome and house.

The heat flows involved in this model are (Figure 3-1):

1) Heat gain through dome glazing, including direct solar beam radiation (Q_{sol}), diffuse solar radiation from sky ($Q_{d,sky}$) and ground reflected solar radiation ($Q_{d,g}$)

2) Long-wave radiation between dome surface and ground ($Q_{surf,g}$)

3) Long-wave radiation between dome surface and sky ($Q_{surf,sky}$)

4) Convection over inside dome surface ($Q_{cv,in}$)

5) Convection over outside dome surface($Q_{cv,out}$)

6) Infiltration/exfiltration through the dome (Q_{inf})

7) Infiltration/exfiltration through the house (Q_{exf})

8) Heat loss through the ground (Q_{ground})

9) Heat loss through the floor of the house (Q_{floor})

10) Heat losses/gains from the external wall/roof surfaces of the house (Q_{wall})

11) Absorption and reflection of the solar radiation by the external wall/roof surfaces of the house and ground (Q_{abs} and Q_{ref})

12) Surface-to-surface radiation between the dome surface and the outside wall/roof surfaces of the house and the ground surface inside the dome ($Q_{surf,d}$)

13) Surface-to-surface radiation between the inside wall/roof surfaces of the house ($Q_{surf,h}$)

14) Convection over the inside house surfaces ($Q_{cv,h}$)
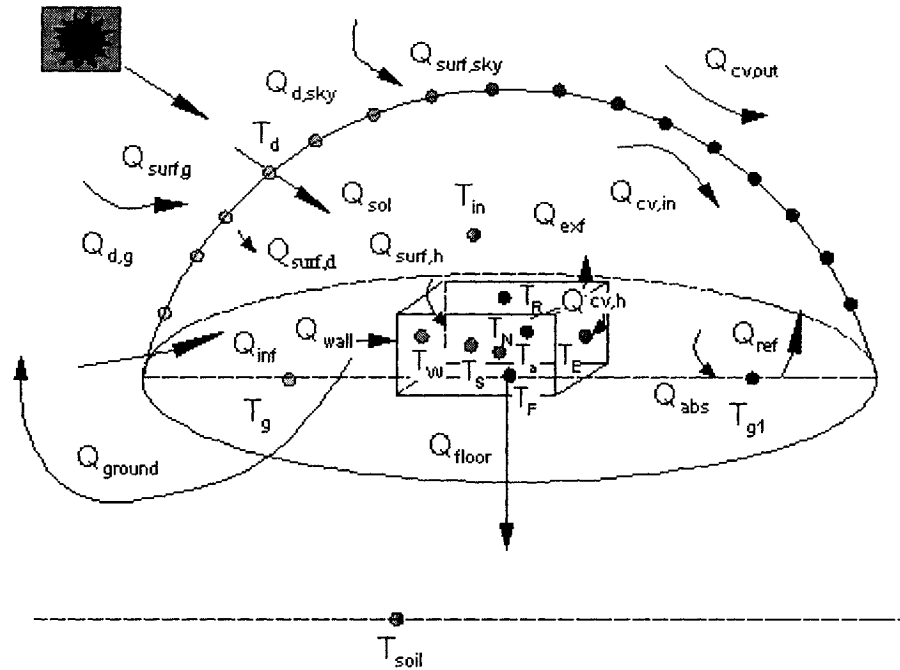
Figure 3-1 Heat flows of the proposed model

The floor is composed of 100 mm concrete slab and 50 mm insulation. The soil temperature at the depth of 1.0 m is assigned as the boundary condition for the ground inside the dome, while the temperature of the soil surface inside the dome is calculated from the heat balance equation. The temperature of the soil under the floor is assumed to be equal to the temperature of the ground inside the dome at the same depth. The heat transfer through windows is considered as quasi-steady state. The house has three double-glazed windows, mounted on the south wall, east wall and west wall, respectively.

The heat transfer phenomena of the exterior envelope of the dome-covered house are similar to the one without cover. In addition, there is long-wave radiation between dome surface, the ground and the external wall/roof surfaces of the house inside the dome, and the inside dome air temperature is unknown.

It is assumed that the radiation transmitted through the glazing that reaches the inside wall/roof/ground surfaces will be absorbed by these surfaces. The radiation absorbed by each surface will result in a temperature increase over that surface. The reflected solar radiation from the ground and diffuse radiation from the sky reaching the dome surface are assumed to be proportional to the view factor between the dome surface and ground/sky. The transmitted radiation (from the ground and the sky) reaching each surface inside the dome is assumed to be proportional to the view factors between the dome surface and the destination surfaces.

A dome is defined by its truncation angle σ_0 and radius R (Figure 3-2). When the truncation angle approaches zero, it becomes a hemisphere.
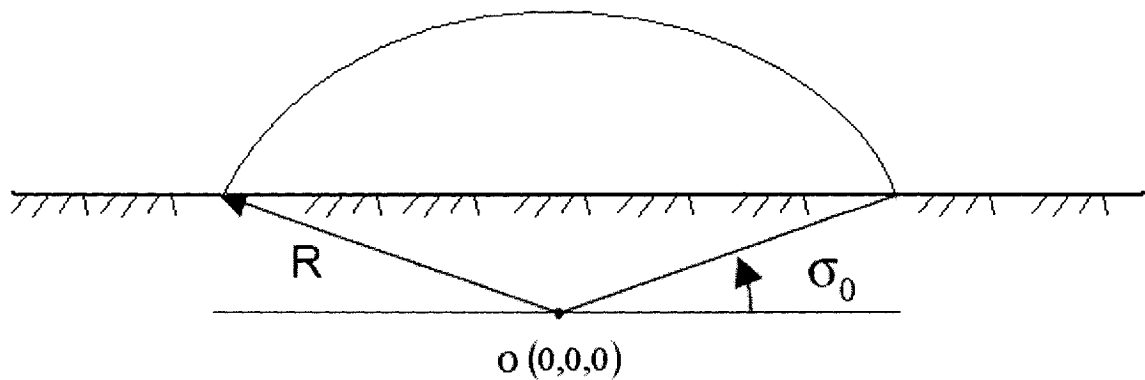
Figure 3-2 A hemispherical truncated dome

The dome (radius=R, truncation angle=σ_0) isolates the house (height=H, width=W and length=L, house azimuth=Ψ_0) from the outside and forms a micro climate, which means that the protected house will experience less weather oscillations than the one that is exposed to the outside climate directly.

The mathematical model is composed of a thermal model and an air flow model. The proposed model that is based on the heat balance method, includes the following five parts: (1) the heat balance of the dome glazing, (2) the heat balance of the air inside the dome, (3) the heat transfer through the exterior envelope and the floor of the house, (4) the heat transfer through the ground inside the dome, (5) the heat balance of the room air. Two air flow models are presented: the single-node model and the zonal model. In the single-node model, the most fundamental assumption is that the air in the thermal zone can be modeled as well mixed, meaning it has a uniform temperature throughout the zone. ASHRAE Research Project 664 established that this assumption is valid over a wide range of conditions (Fisher and Pedersen, 1997). However, for large spaces, such as waiting halls of railway stations, a maximum variation of 3°C has been measured for a space with dimensions of 34m·19m (Chow et al., 2002). In the zonal model, the air inside the dome is divided into a number of zones, and the air movement and temperature distribution are evaluated.

The next major assumption is that each surface of the house (walls, roof, windows, and floor) can be treated as having: uniform surface temperature, uniform long-wave (LW) and short-wave (SW) irradiation, diffuse radiating surface, and the heat transfer is calculated as one dimensional.

The following issues may be of interest for modeling this dome:

(1) There may be trees and plants inside the dome that shade the ground/wall/roof surfaces. The water evaporation process from plants increases the humidity ratio inside the dome, which can result in condensation on the dome.

(2) The outside convective coefficient and inside convective coefficient are normally changing with time due to temperature difference between the surface and the air, air velocity and direction. They also may vary with the inclination of surface. The convective coefficient over the exterior wall surface of the house inside the dome is lower than in the case of a house without dome cover. Hence, the convective heat transfer rate at the house envelope is reduced.

(3) The temperature of the air inside the dome is generally higher than the outdoor air temperature in winter, since the solar radiation is absorbed by the ground inside the dome and external surfaces of the house. Natural ventilation can be adopted to prevent over-heating in summer.

(4) Ventilation supplied by underground tunnel might be of interest because the temperature of the air brought from underground will be higher than the outside air in winter and lower in summer. Thus, supplying the air from underground tunnel to the dome will help to reduce the heating/cooling load of the house.

The structural design and analysis of the dome are not included in this study.

3.2 Coordinate System

A Cartesian coordinate system is used, with Y axis towards east, X axis towards south and Z axis perpendicular to the plan of X and Y (Figure 3-3). In addition, a spherical coordinate system is used to define the location of each cell of the dome, and to calculate the incident angle of solar radiation for each cell. In Figure 3-3, φ is the tilt of cell (i,j) that is defined as the angle between the outside normal of the cell and the horizontal

plane, and ψ is the azimuth angle of each cell (i,j) that is measured from the east. For

instance, ψ=0 for a cell facing east, and ψ=90 for a cell facing south. The origin O (0,0,0)

is presented in Figure 3-2.
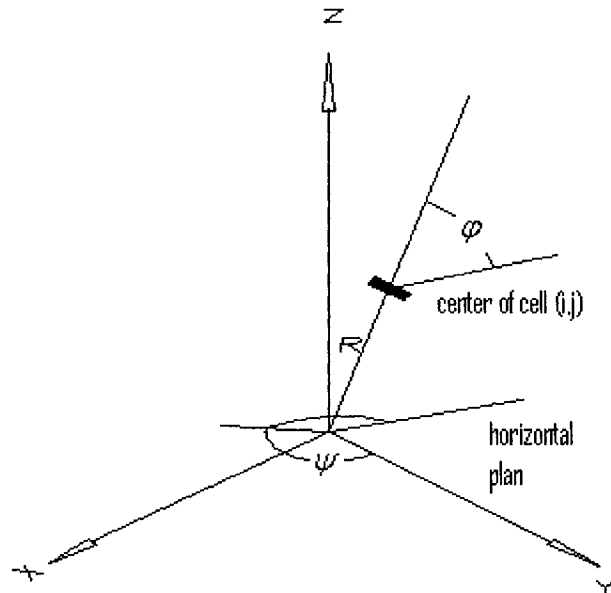
Figure 3-3 Coordinate system

For a given radius R, the relationship between the coordinates of a cell in the Cartesian

and the spherical systems is as follows:

$$x = R \cdot \cos\varphi \cdot \sin\psi$$
$$y = R \cdot \cos\varphi \cdot \cos\psi \qquad\qquad (3\text{-}1)$$
$$z = R \cdot \sin\varphi$$

3.3 Division of the Dome Surface

The dome surface is divided into M (horizontal) and N (vertical) inclined surfaces (Figure 3-4).
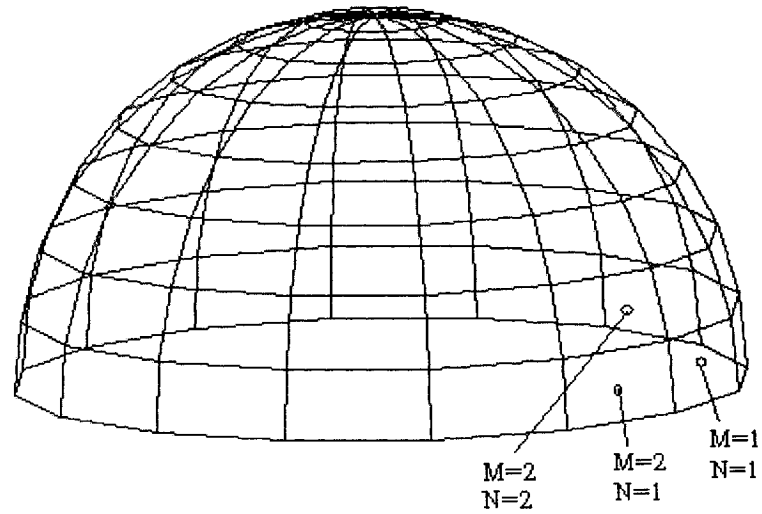
Figure 3-4 Divisions of the dome surface

The plan view of the dome divisions is shown in Figure 3-5.
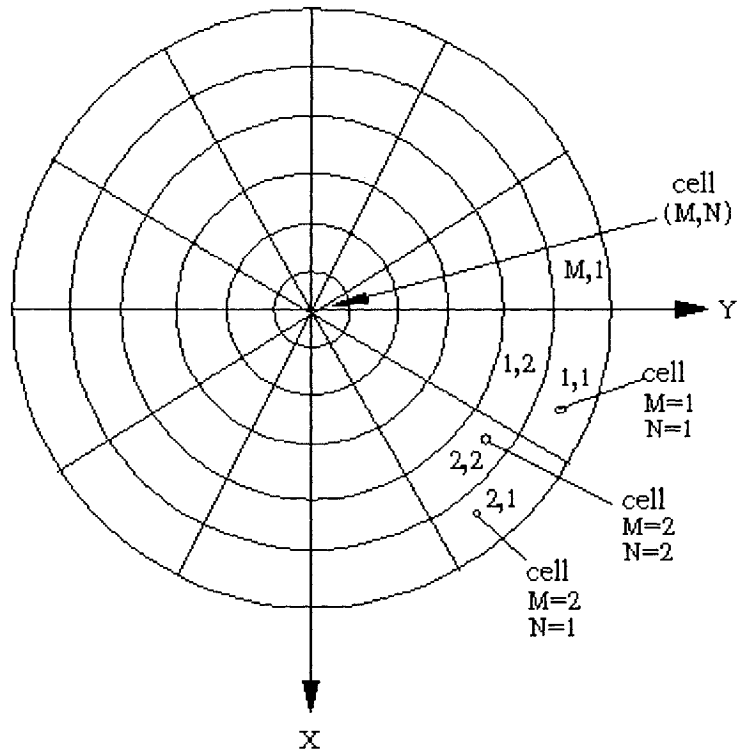
Figure 3-5 Plan view of the dome divisions

The center point for each cell (i,j), where i=1 to M, and j=1 to N, is defined as follows (Figure 3-3):

$$x_{i,j} = R \cdot \cos\varphi_j \cdot \sin\psi_i$$
$$y_{i,j} = R \cdot \cos\varphi_j \cdot \cos\psi_i \qquad (3-2)$$
$$z_{i,j} = R \cdot \sin\varphi_j$$

and the equation for the dome is given as:

$$x^2 + y^2 + z^2 = R^2 \qquad (3-3)$$

where:

$$\psi_i = \frac{360(i - 0.5)}{M} \quad \text{in deg., or} \quad \psi_i = \frac{2\pi(i - 0.5)}{M} \quad \text{in rad.} \tag{3-4}$$

and

$$\varphi_j = \frac{(90 - \sigma_0)(j - 0.5)}{N} + \sigma_0 \quad \text{in deg., or} \quad \varphi_j = \frac{(\pi/2 - \sigma_0)(j - 0.5)}{N} + \sigma_0 \quad \text{in rad.} \tag{3-5}$$

The tilted angle of each cell (i,j) is obtained by (Figure 3-6):

$$\Sigma_j = 90 - \varphi_j \quad \text{in deg., or} \quad \Sigma_j = \pi/2 - \varphi_j \quad \text{in rad.} \tag{3-6}$$
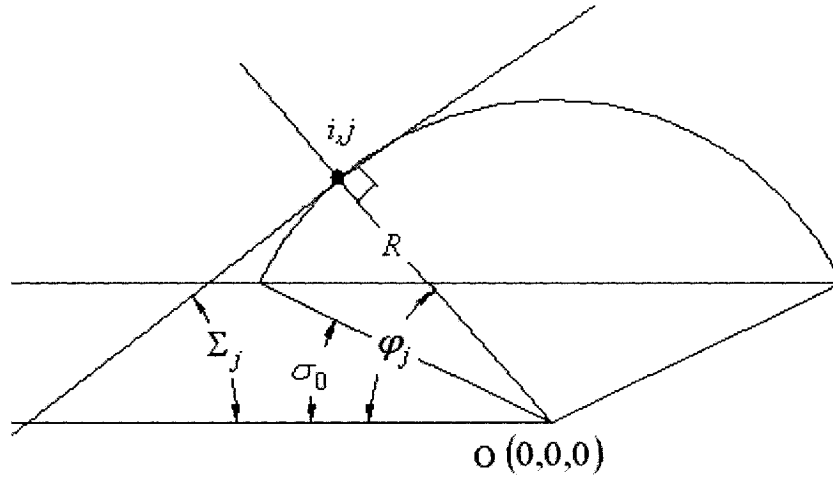
Figure 3-6 Tilted angle

The surface of the dome can be seen as composed of small elements with the surface area calculated by:

$$dA = R \cdot d\varphi \cdot R \cdot \cos\varphi \cdot d\psi = R^2 \cdot \cos\varphi \cdot d\varphi \cdot d\psi \tag{3-7}$$

The surface area of cell (i,j) is calculated as:

$$A_{i,j} = R^2 \cdot \int_{\varphi_1}^{\varphi_2} \cos\varphi \cdot d\varphi \cdot \int_{\psi_1}^{\psi_2} d\psi$$

$$= R^2 \left\{ \sin\left[\frac{\pi/2 - \sigma_0}{N} j + \sigma_0 \right] - \sin\left[\frac{\pi/2 - \sigma_0}{N}(j-1) + \sigma_0 \right] \right\} \left[\frac{2\pi}{M}(i) - \frac{2\pi}{M}(i-1) \right] \quad (3-8)$$

$$= \frac{2\pi\pi}{M}^2 \left\{ \sin\left[\frac{\pi/2 - \sigma_0}{N} j + \sigma_0 \right] - \sin\left[\frac{\pi/2 - \sigma_0}{N}(j-1) + \sigma_0 \right] \right\}$$

where

$$\varphi_1 = \left(\frac{\pi}{2} - \sigma_0 \right) \cdot \frac{(j-1)}{N} + \sigma_0 \qquad (3-9)$$

$$\varphi_2 = \left(\frac{\pi}{2} - \sigma_0 \right) \cdot \frac{j}{N} + \sigma_0 \qquad (3-10)$$

$$\psi_1 = \frac{2\pi \cdot (i-1)}{M} \qquad (3-11)$$

$$\psi_2 = \frac{2\pi \cdot i}{M} \qquad (3-12)$$

For example, if R=20 m, M=16, N=12, i=4, j=3 and $\sigma_0 = \frac{\pi}{6}$, then

$$\varphi_1 = \frac{(\pi/2 - \pi/6) \cdot (3-1)}{12} + \frac{\pi}{6} = \frac{2\pi}{9} \qquad (3-13)$$

$$\varphi_2 = \frac{(\pi/2 - \pi/6) \cdot 3}{12} + \frac{\pi}{6} = \frac{\pi}{4} \qquad (3-14)$$

$$\psi_1 = \frac{2\pi \cdot (4-1)}{16} = \frac{3\pi}{8} \qquad (3-15)$$

$$\psi_2 = \frac{2\pi \cdot 4}{16} = \frac{\pi}{2} \qquad\qquad (3\text{-}16)$$

$$A_{4,3} = 20^2 \int_{\frac{2\pi}{9}}^{\frac{\pi}{4}} \cos\varphi \cdot d\varphi \int_{\frac{3\pi}{8}}^{\frac{\pi}{2}} d\psi = 20^2 \left(\sin\left(\frac{\pi}{4}\right) - \sin\left(\frac{2\pi}{9}\right) \right) \cdot \left(\frac{\pi}{2} - \frac{3\pi}{8} \right) = 10.103\,\mathrm{m}^2 \qquad (3\text{-}17)$$

A finite difference approach is adopted in this research by considering each cell as a small control volume. Heat balance equations are written for each control volume. As compared to the finite element method, the finite difference method is straight forward and easy to apply (Chapra and Canale 2002).

3.4 Comparison between the 3D-TAF Model and other Mathematical Models

The three-dimensional transient thermal and air flow (3D-TAF) model is developed in Chapter 4 and Chapter 5. Table 3-1 presents the comparison between the 3D-TAF model and other mathematical models. The 3D-TAF model differs from other models in the following aspects:

- The 3D-TAF model takes into account the direct normal solar radiation, diffuse solar radiation from sky, reflected solar radiation by ground, transmission of solar radiation through the cover, absorption of solar radiation by the cover, second transmission of solar radiation through the cover and second reflection of transmitted solar radiation by the cover.

- The 3D-TAF model considers the variation of transmittance, reflectance and absorptance of the glazing with incident angle while other models do not calculate

all those components.

- The 3D-TAF model considers the convective coefficient as a function of wind speed, wind direction, tilted angle, surface location, and the temperature difference between surface and outdoor/indoor air, while other models consider the convective coefficient as a constant.

- The 3D-TAF model uses the total interchange view factor to calculate the long-wave radiation between the inside surface of the dome, the external surfaces of the house, and long-wave radiation between the inside surfaces of the house, and also calculate the long-wave radiation from the ground and the sky while other models treat long-wave radiation in a simple way.

- The 3D-TAF model is the only model that adopts the zonal model approach, and simulates the thermal stratification and air movement inside the dome. The 3D-TAF model takes into account natural air infiltration through the dome cover, and the air exfiltration through the house walls.

- The 3D-TAF model considers the heat balance over the external house surfaces, heat conduction through the wall/roof/floor and heat balance over the inside surfaces of the house, and the heat balance of the air inside the house.

Table 3-1 Comparison of different mathematical models

		Lin (2007)	Luttmann-Valencia (1990)	Sharma et al. (1999)	Tang et al. (2003)	Porta-Gándara and Gómez-Muñoz (2005)	Singh et al. (2006)	Wittkopf et al. (2006)
Cover								
Discretization		13 rings and 42 cells per ring	No	No	Δφ=2° (Rings) ΔΨ=2° (Cells) plus one cell at the top*	Triangles	No	8 rings with different number of cells per ring
Number of cells		546	1	1	5941 for $\sigma_0=20°$**	160	1	145
$h_{cv,out}$	Wind speed	Yes	Yes	No	No	No	Yes	No
	Wind direction	Yes	No	No	No	No	No	No
	Tilted angle	Yes	No	No	No	No	No	No
	T_{air}-T_{cell}	Yes	No	No	No	No	No	No
	Location of cell	Yes	No	No	No	No	No	No
$h_{cv,in}$	Tilted angle	Yes	No	No	No	No	No	No
	T_{air}-T_{cell}	Yes	No	No	No	No	No	No
Solar radiation	Direct normal	Yes	Yes	Yes	Yes	Yes	Yes	No
	Diffuse radiation from sky	Yes	Yes	Yes	Yes	Yes	Yes	No
	Reflected radiation by ground	Yes	No	No	Yes	No	No	No
	Transmission through cover	Yes	Yes	Yes	No	Yes	Yes	No
	Absorption by cover	Yes	Yes	No	Yes	No	Yes	No

Category	Parameter						
Solar radiation (cont.)	Second transmission and reflection	Yes	No	No	No	No	No
	Variation of τ, ρ, α with incident angle	Yes	No	No	Yes	Yes	No
Long-wave radiation	Total interchange view factor	View factor	View factor	No	View factor	No	No
	From sky	Yes	Yes	No	Yes	No	Yes
	From ground	Yes	Yes	No	No	No	No
	From other cells	Yes	No	No	No	No	Yes (self)
	From ground inside the dome	Yes	Yes	No	No	No	Yes
	From outside surfaces of the house	Yes	No	No	No	No	No
	Conduction through cover	3D	1D	No	3D (1D at the top)	No	1D
	Heat balance equations	Transient	Steady state	No	Transient	No	Steady state
Indoor air	Discretization	13 layers with 43 zones per layer	No	Yes	No	No	No
	Number of zones	559	1	4	No	No	1
	Approach	Zonal model	Well mixed	$q=hA(T_i\text{-}T_j)$	No	No	Well mixed
	Infiltration	Yes	No	Constant	No	No	No
	Ventilation	No	Constant	No	No	No	No
	Exfiltration from house	Yes	No	No	No	No	No
	Thermal stratification	Yes	No	No	No	No	No
	Heat balance equation for indoor air	Transient	Steady state	Transient	No	No	Steady state

Ground

	10	3	0			1	
Number of layers	10	3	0	No	No	1	No
Absorption of solar radiation transmitted through the glazing	Yes	Yes	Yes	No	No	No	No
Absorption of solar radiation reflected from the inside surface of the cover	Yes	No	No	No	No	No	No
Long-wave radiation from the cover	Yes	Yes	No	No	No	Yes	No
Long-wave radiation from the outside surface of the house	Yes	No	No	No	No	No	No
$h_{cv,soil}$ $T_{in}-T_{soil}$	Yes	No	No	No	No	No	No
$h_{cv,soil}$ Air flow direction	Yes	No	No	No	No	No	No
Heat balance equation	Transient	Transient	Steady state	No	No	Steady state	No
House							
Absorption of solar radiation transmitted through the glazing	Yes	No	No	No	No	No	No
Heat conduction through the walls/floor/roof	1-D	No	No	No	No	No	No
Long-wave radiation between the cover/ground/house	Yes	No	No	No	No	No	No
$h_{cv,out,house}$ T_a-T_{wall}	Yes	No	No	No	No	No	No
$h_{cv,out,house}$ Air flow direction	Yes	No	No	No	No	No	No
$h_{cv,in,house}$ T_a-T_{wall}	Yes	No	No	No	No	No	No
$h_{cv,in,house}$ Air flow direction	Yes	No	No	No	No	No	No
Heat balance equations for the wall/roof/floor surfaces	Transient	No	No	No	No	No	No

Heat balance equations for windows	Steady state	No	No	No	No	No	No
Heat balance equation for the room air	Transient	No	No	No	No	No	No
Long-wave radiation between inside walls	Yes	No	No	No	No	No	No
Solution of system of heat balance equations Type	Non-linear	Linear	Linear	Non-linear	No	Non-linear	No
Coupling heat and mass transfer	Yes	Yes	No	No	No	No	No
Method	Gauss-Seidal+ Broyden	Gauss elimination	Newton-Raphson + Runge-Kutta	Analytical solution	No	Gauss-Seidal	No

*φ is the polar angle from zenith (deg.), Ψ is the azimuth angle (deg.)

**σ_0 is the truncation angle of the dome

Chapter 4 Thermal Model

The chapter presents the thermal model for estimating the energy needs of the ensemble dome-house. The house has four walls, a flat roof, a floor, and three double-glazed windows. The heat balance equations are written at the dome surface, at the exterior envelope of the house, at the ground surface inside the dome, and for the air inside the house. This chapter presents also a preliminary version of the model, which used the heat balance of the air inside the dome that was considered to be well-mixed. This simplified model is presented in section 4.2. The final version of the 3D-TAF model contains, however, the air flow model (Chapter 5) that simulates the air movement and temperature distribution inside the dome. Comparisons between the simulation results from different versions of the computer model are presented at the end of this chapter.

4.1 Heat Balance at the Dome Surface

The dome surface is divided into a number of cells. The heat balance equation at the center of each cell (i,j) is written as (Figure 4-1):
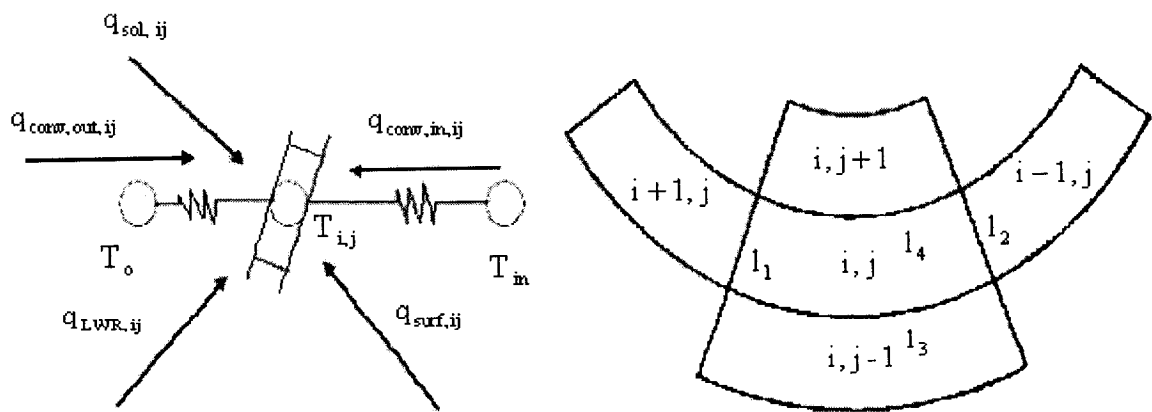
Figure 4-1 Heat balance of the cell (i,j) at the dome surface

$$k \cdot d \cdot l_1 \cdot \left(T_{i+1,j} - T_{i,j}\right) + k \cdot d \cdot l_2 \cdot \left(T_{i-1,j} - T_{i,j}\right)$$
$$+ k \cdot d \cdot l_3 \cdot \left(T_{i,j-1} - T_{i,j}\right) + k \cdot d \cdot l_4 \cdot \left(T_{i,j+1} - T_{i,j}\right) \tag{4-1}$$
$$+ \left(q_{sol,ij} + q_{conv,ij} + q_{LWR,ij} + q_{surf,ij}\right) \cdot A_{ij} = m_{ij} \cdot c_p \cdot \frac{dT_{i,j}}{dt}$$

where:

$q_{sol,ij}$ =absorbed incident solar radiation (including direct, diffuse and ground reflected solar radiation) by the cell (i,j), W/m^2;

$q_{conv,ij}$ =convective heat flux over the inside and outside surface of the cell (i,j), W/m^2;

$q_{LWR,ij}$ =long-wave radiation between the outdoor environment (ground and sky) and the cell (i,j), W/m^2;

$q_{surf,ij}$ =net long-wave surface-to-surface radiation between surfaces inside the dome and the cell (i,j), W/m^2;

m_{ij} =mass of the cell (i,j), kg;

c_p =specific heat of the dome cover (e.g., glazing), J/kg·°C;

T=temperature, °C;

t=time, s;

k=conductivity of dome cover (e.g., glazing), W/m·°C;

A$_{ij}$=surface area, m^2;

d=thickness of dome cover (e.g., glazing), m;

l=length of the common border between two cells, m.

4.1.1 Solar Radiation through Glazing

The solar radiation that is absorbed by the cell surface is composed of (1) the direct solar radiation (Figure 4-2), and (2) the diffuse solar radiation. The coordinates of the point where the direct solar radiation, transmitted through each cell, and reaches inside surfaces, are calculated by solving for the intersection between the solar beam trajectory and the dome surface. The diffuse radiation, after being transmitted through the glazing, is assumed to reach all the inside surfaces proportionally to the view factor between each cell and inside surfaces. For the transmitted direct beam solar radiation, the model calculates for each cell (p,q) the incident angle θ_{pq} between the exterior solar radiation and the outside normal to the cell, and then the incident angle θ_{kl} between the transmitted solar radiation and the inside normal to the cell (k,l), where the beam is absorbed by cell (k,l), reflected to the ground, or transmitted out to the environment.
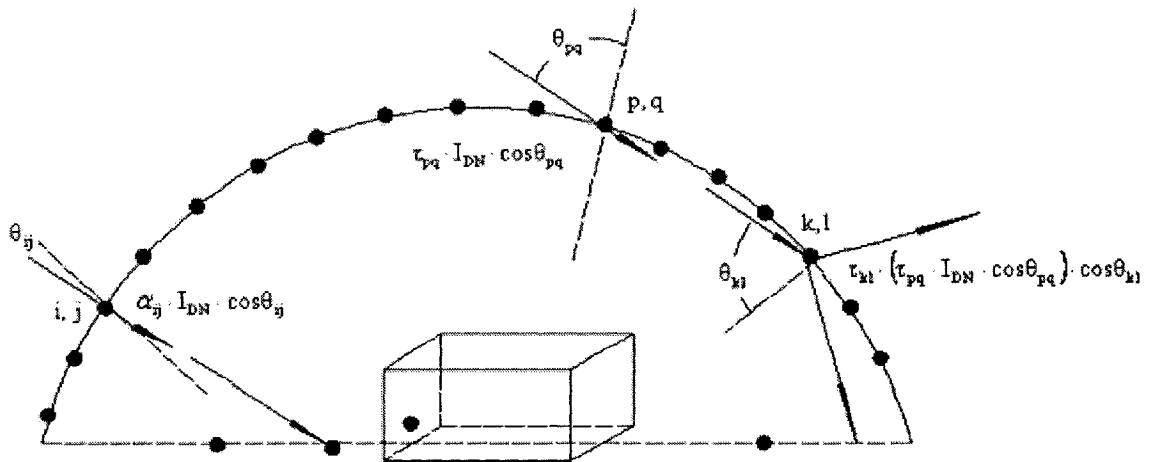
Figure 4-2 Direct solar beam over the dome surface

The solar radiation absorbed by a cell (i,j) is calculated as follows:

$$q_{sol,ij} = I' + I''$$ (4-2)

where:

I'=absorbed direct solar radiation by the cell (i,j), W/m^2;

I''=absorbed diffuse solar radiation by the cell (i,j).

In the case of cell (i,j) (Figure 4-2) that receives the direct solar radiation:

$$I' = \alpha_{ij} \cdot I_{DN} \cdot \cos\theta_{ij}$$ (4-3)

where:

α_{ij}=absorptance of the glazing surface at incident angle θ_{ij};

I_{DN}=direct normal incident solar radiation, W/m^2;

θ_{ij}=incident angle for the cell (i,j), deg..

The direct normal solar radiation can be calculated as:

$$I_{DN} = C_N \frac{A}{\exp(B/\sin\beta)}$$ (4-4)

where:

C_N=clearness number (McQuiston et al., 2000);

A and B=solar coefficients (ASHRAE, 1992).

In the case of cell (k,l) that receives the transmitted solar radiation from the cell (p,q):

$$I' = \alpha_{kl} \cdot \left(\tau_{pq} \cdot I_{DN} \cdot \cos\theta_{pq} \right) \cdot \cos\theta_{kl} \qquad (4\text{-}5)$$

where:

τ_{pq} =transmittance of the glazing at incident angle θ_{pq}.

Since the vector $R\left(x_{ij}, y_{ij}, z_{ij}\right)$ is also the normal of the tangent surface of the cell (i,j), the incident angle for the cell (i,j) can be calculated by:

$$\cos\theta_{ij} = \frac{\left| -x_{ij} \cdot \cos\beta \cdot \cos\psi_s + y_{ij} \cdot \cos\beta \cdot \sin\psi_s - z_{ij} \cdot \sin\beta \right|}{R} \qquad (4\text{-}6)$$

where:

β =solar altitude, deg.;

Ψ_s=solar azimuth, deg..

Solar altitude β (the angle between sun rays and the horizontal plan) and the solar azimuth Ψ_s (the angle between the shadow of solar beam on the horizontal surface and due south) can be found from:

$$\sin\beta = \sin L \cdot \sin\delta + \cos L \cdot \cos\delta \cdot \cos\omega \qquad (4\text{-}7)$$

and

$$\sin\psi_s = (\cos\delta \cdot \sin\omega)/\cos\beta \qquad (4\text{-}8)$$

where:

L=latitude, deg.;

ω=hour angle, deg.;

δ=solar declination (the angle between sun rays and the equator plane), deg..

The hour angle can be calculated as follows:

$$\omega = \pm\frac{1}{4}(\text{number of minutes from local solar noon}) \qquad (4\text{-}9)$$

The apparent solar time can be calculated by:

$$AST = LST + ET + 4(LON_{st} - LON_{loc}) \qquad (4\text{-}10)$$

where:

LST=local standard time, min.;

ET=equation of time, min.;

LON_{st}=standard longitude, 75 for Montreal, deg.;

LON_{loc}=local longitude, deg..

Montreal has the following coordinates: 45° 28' **N** and 73° 45' **W**

The equation of time can be calculated by (Spencer, 1971):

$$ET = 229.2 \begin{pmatrix} 0.000075 + 0.001868\cos N_c - 0.032077\sin N_c \\ -0.014615\cos 2N_c - 0.04089\sin 2N_c \end{pmatrix} \tag{4-11}$$

where:

$$N_c = (n_d - 1)360/365 \tag{4-12}$$

n_d=day of the year.

The solar declination can be given by (Spencer, 1971):

$$\delta = 0.3963723 - 22.9132745\cos N_c + 4.0254304\sin N_c - 0.3872050\cos 2N_c$$
$$+ 0.05196728\sin 2N_c - 0.1545267\cos 3N_c + 0.08479777\sin 3N_c \tag{4-13}$$

For example, if R=20 m, M=16, N=12, i=4, j=3 and $\sigma_0 = 30°$, the incident angle on July

21st, at local solar noon, in Montreal, can be calculated using the following procedure:

$$n_d = 31 + 28 + 31 + 30 + 31 + 30 + 21 = 202 \tag{4-14}$$

$$N_c = (202 - 1)360/365 = 198.25 \tag{4-15}$$

$$\delta = 0.3963723 - 22.9132745 \cdot \cos 198.25 + 4.0254304 \cdot \sin 198.25 - 0.3872050 \cdot \cos(2 \cdot 198.25)$$
$$+ 0.05196728 \cdot \sin(2 \cdot 198.25) - 0.1545267 \cdot \cos(3 \cdot 198.25) + 0.08479777 \cdot \sin(3 \cdot 198.25)$$
$$= 20.6°$$

$$\tag{4-16}$$

$$ET = 229.2 \cdot \begin{pmatrix} 0.000075 + 0.001868 \cdot \cos 198.25 - 0.032077 \cdot \sin 198.25 \\ -0.014615 \cdot \cos(2 \cdot 198.25) - 0.04089 \cdot \sin(2 \cdot 198.25) \end{pmatrix} = -6.2\text{min} \tag{4-17}$$

$$\sin\beta = \sin45.47\sin20.6 + \cos45.47\cos20.6\cos0 = 0.251 + 0.656 = 0.907 \tag{4-18}$$

$$\cos\beta = \sqrt{1 - 0.907^2} = 0.420 \tag{4-19}$$

$$\psi_4 = \frac{360(4 - 0.5)}{16} = 78.75 \tag{4-20}$$

$$\varphi_3 = \frac{(90 - 30)(3 - 0.5)}{12} + 30 = 42.5 \tag{4-21}$$

$$
\begin{aligned}
x_{i,j} &= 20\cos42.5\sin78.75 = 14.46 \\
y_{i,j} &= 20\cos42.5\cos78.75 = 2.88 \\
z_{i,j} &= 20\sin42.5 = 13.51
\end{aligned}
\tag{4-22}
$$

$$\cos\theta_{ij} = \frac{\left| -14.46 \cdot 0.420 \cdot \cos0 + 2.88 \cdot 0.420 \cdot \sin0 - 13.51 \cdot 0.907 \right|}{20} = 0.916 \tag{4-23}$$

$$\theta_{ij} = \cos^{-1}0.916 = 23.6° \tag{4-24}$$

The absorbed diffuse solar radiation by the cell (i,j) is composed of (1) the absorbed diffuse solar radiation over the outside glazing surface, and (2) the absorbed diffuse solar radiation over the inside glazing surface.

The absorbed diffuse solar radiation over the outside glazing surface can be calculated as:

$$I''_1 = \alpha_{ij} \cdot \left(I_{ds,ij} + I_{dg,ij} \right) \tag{4-25}$$

where:

$I_{ds,ij}$ =diffuse incident solar radiation on the cell (i,j) from the sky, W/m^2;

$$I_{ds,ij} = C \cdot I_{DN} \cdot F_{ij,sky}$$ (4-26)

where:

C =coefficient (ASHRAE, 1992);

I_{DN} =direct normal radiation, W/m^2;

$F_{ij,sky}$ =view factor between the cell (i,j) and the sky.

$$F_{ij,sky} = \frac{1 + \cos\Sigma_{ij}}{2}$$ (4-27)

Σ_{ij} =tilted angle for the cell (i,j), deg..

$I_{dg,ij}$ =incident solar radiation reflected from the ground outside the dome to the cell (i,j), W/m^2;

$$I_{dg,ij} = I_H \gamma_g F_{ij,g}$$ (4-28)

$$I_H = I_{DN}(C + \sin\beta)$$ (4-29)

γ_g =ground reflectance;

$F_{ij,g,out}$ =view factor between the cell (i,j) and the ground outside the dome;

$$F_{ij,g,out} = \frac{1 - \cos\Sigma_{ij}}{2}$$ (4-30)

The value of ground reflectance is assumed to be 0.2 for a typical ground surface (ASHRAE 2001b). In winter, if the ground is covered by snow, the reflectance for the ground will be much higher, and can be assumed to be equal to 0.7.

The absorbed diffuse solar radiation over the inside glazing surface can be written as:

$$I''_2 = \alpha_{ij} \cdot \sum_{\substack{k=1,M \\ l=1,N}} F_{kl,ij} \cdot \tau_{kl} \cdot \left(I_{ds,kl} + I_{dg,kl} \right) \tag{4-31}$$

where:

$F_{kl,ij}$ =view factor between cells (k,l) and (i,j).

The total absorbed diffuse solar radiation is:

$$I'' = I''_1 + I''_2 \tag{4-32}$$

4.1.2 Convective Heat Flux

The convective heat flux over the cell (i,j) surface can be calculated as follows:

$$q_{conv,ij} = q_{conv,out,ij} + q_{conv,in,ij} \tag{4-33}$$

where:

$q_{conv,out,ij}$ =convective heat flux over the outside cell surface, W/m^2;

$q_{conv,in,ij}$ =convective heat flux over the inside cell surface, W/m^2.

The convective heat flux over the outside cell surface can be calculated as follows:

$$q_{conv,out,ij} = h_{o,ij}(T_o - T_{i,j})$$ (4-34)

where:

$h_{o,ij}$ =convective coefficient at the outside surface of cell (i,j) of the dome, $W/m^2 \cdot °C$;

T_o =outdoor air temperature, $°C$;

$T_{i,j}$ =temperature of cell (i,j) of the dome, $°C$.

The outside convective heat transfer coefficient for very smooth surfaces (e.g., glass) is calculated as (Yazdanian and Klems, 1994):

$$h_{c\_glass} = \sqrt{h_n^2 + [aV_w^b]^2}$$ (4-35)

where:

h_{c_glass} =outside convective coefficient for glass, $W/m^2 \cdot °C$;

h_n =natural component of the convective coefficient, $W/m^2 \cdot °C$;

a,b=constants (Table 4-1);

V_w =wind speed over the surface, m/s.

Table 4-1 Coefficients (Yazdanian and Klems, 1994)

Wind direction	a $[W/m^2 \cdot °C(m/s)^b]$	b -
Windward	2.38	0.89
Leedward	2.86	0.617

The natural convection component h_n is calculated as (ASHRAE, 1993):

$$h_n = 9.482 \cdot \frac{\sqrt[3]{|\Delta T|}}{7.238 - |cos\Sigma|} \text{ (for upward heat flow)} \tag{4-36}$$

or

$$h_n = 1.810 \cdot \frac{\sqrt[3]{|\Delta T|}}{1.382 + |cos\Sigma|} \text{ (for downward flow)} \tag{4-37}$$

where:

ΔT =Temperature difference between the surface and air, °C;

Σ =tilted angle of the surface, deg..

The wind velocity V_w over the dome surface, at the center of each cell, can be calculated by using the C_p coefficient:

$$V_w = \sqrt{|C_p|} V_H \tag{4-38}$$

where:

$$C_p = \frac{p - p_0}{\frac{1}{2}\rho V_H^2} \tag{4-39a}$$

$$p \approx p_0 + \frac{1}{2}\rho V_w^2 \tag{4-39b}$$

p=pressure on the cell surface, Pa;

p_0= barometric pressure, Pa;

V_H=wind speed at dome height, m/s.

The wind speed at dome height can be calculated using TARP's detailed convection model. The wind speed is calculated as follows (Walton, 1983):

$$V_H = V_o \cdot \beta_t \cdot \left(\frac{H}{z_o} \right)^{\alpha_t} \qquad (4\text{-}40)$$

where:

V_H =wind speed at dome height, m/s;

V_o =wind speed at the height of z_0 (standard condition), m/s;

H=dome height, m;

z_o =height at which standard wind speed measurements are taken, z_0=10 m;

α_t and β_t are terrain-dependent coefficients, α_t=0.15 and β_t=1.00 (Table 4-2).

Table 4-2 Terrain roughness coefficients (Walton, 1983)

Class	Description	α_t	β_t
1	ocean or other body of water with at least 5 km of unrestricted expanse	0.10	1.30
2	flat terrain with some isolated obstacles (buildings or trees well separated from each other	0.15	1.00
3	rural areas with low buildings, trees, etc.	0.20	0.85
4	urban, industrial, or forest area	0.25	0.67
5	center of large city	0.35	0.47

Taniguchi et al. (1982) performed experimental measurements of the C_p coefficient for a hemisphere (Fuller dome) immersed in a turbulent boundary layer. Montes and Fernandez (2001) proposed a 13-term Fourier series formulation to calculate the pressure coefficient for a hemispherical dome. Yeung (2006) presented a dimensionless

expression for the distribution of the pressure coefficient over a cylinder.

There are only a few experimental results from wind tunnel (Newman and Goland, 1982; Newman et al., 1984; Savory and Toy, 1986; Taylor 1992) for the ordinary dome ($\sigma_0 \geq 0$). Newman and Goland (1982) developed a model to simulate the two-dimensional inflated building in a thick boundary layer under an onshore wind or flow over sparsely wooded country. The model predicts the tension in the membrane quite well, but for the external pressure based on C_p coefficient, the prediction is generally too low. Newman et al. (1984) presented the experimental results for the pressure distribution on three domes with different height-to-base diameter ratio (h/c=0.5, 0.37 and 0.25). Savory and Toy (1986) presented an experimental investigation of the flow over hemispheres and hemisphere-cylinders immersed in three different boundary layers. Savory and Toy's experimental results showed that for a smooth dome, when the Reynolds number exceeds $1.2 \cdot 10^5$, the pressure distribution becomes independent of the Reynolds number. Taylor (1992) studied the pressure distribution on hemispherical domes with height-to-base diameter ratio of 1, 0.5 and 0.33 and Reynolds number between $1.1 \cdot 10^5$ and $3.1 \cdot 10^5$, in two different turbulent intensity profiles. Taylor's experimental results also showed that for flows of high turbulent intensity (>15%), increasing the Reynolds number above $1.7 \cdot 10^5$ does not significantly affect the mean of fluctuating pressure coefficient. Taylor's experimental results also agreed well with results from Newman et al. (1984).

For a typical dome with diameter of 40 m, exposed in the wind speed of 10 m/s, the Reynolds number can be as high as $2.8 \cdot 10^7$. Since the Reynolds number in Newman et al. (1984) is about $1.6 \cdot 10^5$, which is greater than $1.2 \cdot 10^5$, and pressure distribution is

expected to be independent of the Reynolds number (Taylor, 1992), the experimental results of Newman et al. (1984) can be used to simulate the pressure coefficient over the dome surface. Based on those experimental data, a regression-based model is developed, which estimates the C_p coefficient in terms of the angle φ between the outside normal of the surface and the zenith (windward as negative and leeward as positive) and Ψ between the shadow of the normal of the surface over the horizontal surface and wind direction.

The correlation-based model is written as:

$$C_{p,\psi,\varphi} = a_0 + a_1\varphi + a_2\varphi^2 + a_3\varphi^3 + a_4\varphi^4 + a_5\varphi^5 + a_6\varphi^6 \qquad (4\text{-}41)$$

The coefficients a_0 to a_6 are presented in Table 4-3. Each coefficient has 15 effective digits, however, due to space limit, only the first six effective digits of each coefficient are presented.

Table 4-3 Coefficients of the correlation-based model of C_p coefficient over dome surface

h/c	Ψ	$a_0[10^{-1}]$	$a_1[10^{-3}]$	$a_2[10^{-4}]$	$a_3[10^{-6}]$	$a_4[10^{-7}]$	$a_5[10^{-10}]$	$a_6[10^{-11}]$	R^2
0.25	180	-5.06590	5.45527	5.96264	-4.99366	-1.69527	5.60957	1.32509	0.9952
	170	-5.09100	5.69151	6.24630	-5.35280	-2.05800	8.25368	2.09757	0.9952
	160	-5.21213	5.46336	6.05903	-4.51950	-1.83241	5.87777	1.35837	0.9945
	150	-5.19364	5.16509	5.66884	-3.10883	-1.72176	1.88613	1.26262	0.9927
	140	-.516555	4.99092	4.33974	-2.08810	-0.912685	-0.972642	0.0629160	0.9961
	130	-.514331	3.37692	4.46402	-2.99180	-1.78669	7.25219	3.514806	0.9974
	120	-.512639	3.54730	3.21681	-1.93708	-0.721927	1.22390	0.275958	0.9961
	110	-5.11976	1.74575	1.83021	-1.55672	-0.0598124	3.19561	-0.759972	0.9972
	100	-5.16232	0.280471	0.964618	-0.112987	0.317487	-0.198371	-1.24297	0.9949
	90	-5.17320	$-8.74 \cdot 10^{-9}$	0.636196	$2.85 \cdot 10^{-9}$	0.464181	$-4.12 \cdot 10^{-10}$	-1.36210	0.9987
0.37	180	-5.46875	3.17248	5.13812	-2.68387	-1.31252	3.40393	1.11434	0.994
	170	5.34631	3.33558	4.94097	-2.64077	-1.24851	3.34680	1.03841	0.9923
	160	-5.52627	3.32778	5.18439	-2.27525	-1.42329	2.76048	1.29147	0.994
	150	-5.37900	3.05404	4.67608	-2.19070	-1.19626	3.07651	0.971138	0.9924
	140	-5.35899	2.37448	3.97551	-1.05161	-0.984007	1.13094	0.810756	0.9943
	130	-5.47489	2.33008	3.12483	-0.436507	-0.0663210	-0.0813025	0.515478	0.9947
	120	-5.54132	1.79715	2.79493	-0.34079	-0.554350	0.397088	0.375893	0.9985
	110	-5.43114	0.0904305	1.52993	-0.196396	-0.247570	0.482435	0.1643533	0.9951
	100	-5.46825	-0.139456	1.08098	-0.351980	-0.140884	0.723657	0.0658798	0.9976
	90	-5.53632	$-5.13 \cdot 10^{-9}$	0.793118	$1.93 \cdot 10^{-10}$	0.01736420	$-5.70 \cdot 10^{-10}$	-0.144618	0.9995
0.50	180	-6.59966	4.66474	4.38700	-3.06028	- 0.779096	3.01291	0.4532916	0.9963
	170	-6.51267	2.69493	4.50790	-2.16831	-0.870719	2.16247	0.5468827	0.9942
	160	-6.31701	3.64682	4.17292	-2.31240	-0.789660	2.23106	0.487071	0.9929
	150	-6.62797	2.32291	4.26215	-1.49092	-0.834760	1.41667	0.528829	0.9944
	140	-6.88900	3.26435	3.85574	-1.30205	-0.740410	1.12466	0.462759	0.9958
	130	-6.79791	2.13588	2.97486	- 0.499195	-0.495808	0.340727	0.272786	0.9979
	120	-6.81963	0.937160	2.10131	-0.0952453	-0.272050	0.122456	0.118917	0.9976
	110	-6.81252	0.806841	1.19346	-0.254888	-0.107132	0.438138	0.0326324	0.9967
	100	-6.78701	0.774443	0.679560	-0.0692872	-0.0208903	-0.0604355	-0.0259936	0.9972
	90	-6.83992	$7.65 \cdot 10^{-9}$	0.563472	$8.28 \cdot 10^{-12}$	$-3.07 \cdot 10^{-3}$	$-4.21 \cdot 10^{-12}$	-0.0374126	0.9984

The correlation results show good agreement with experimental data, with R-square values over 0.99 (Figures 4-3, 4-4, 4-5 and Table 4-3). In those figures, markers indicate experimental data for several angle Ψ and continuous curves indicate the correlation-based model.
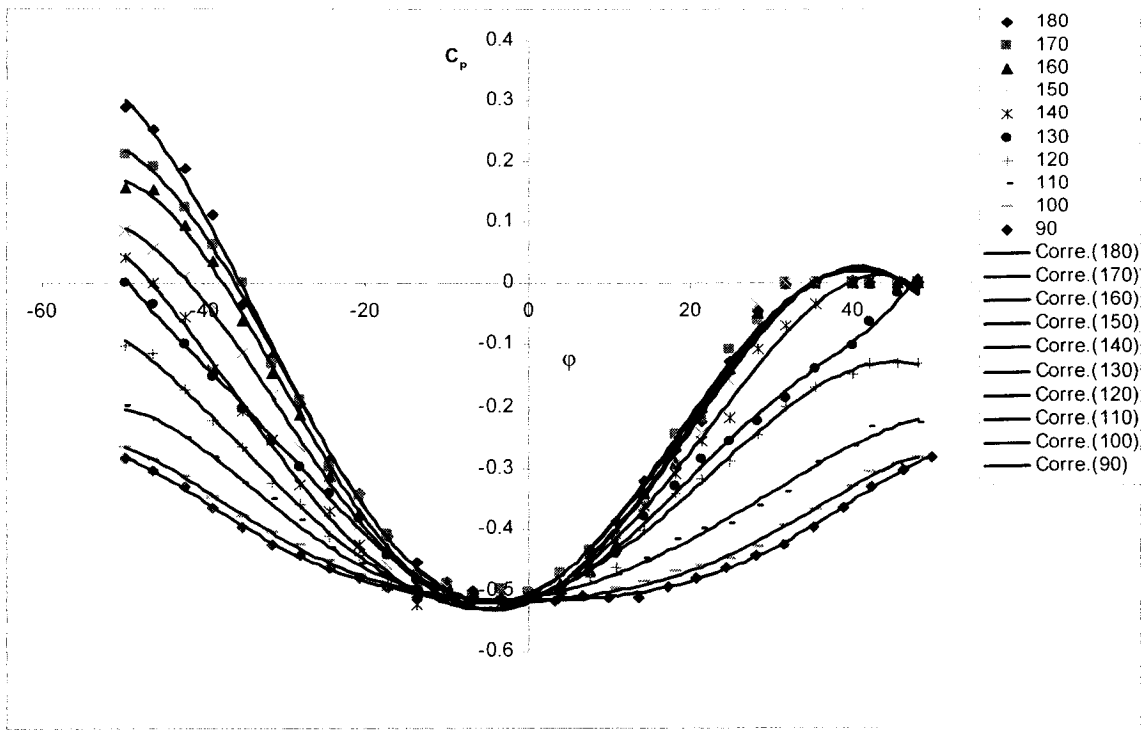
Figure 4-3 Pressure coefficients over dome surface (h/c=0.25)
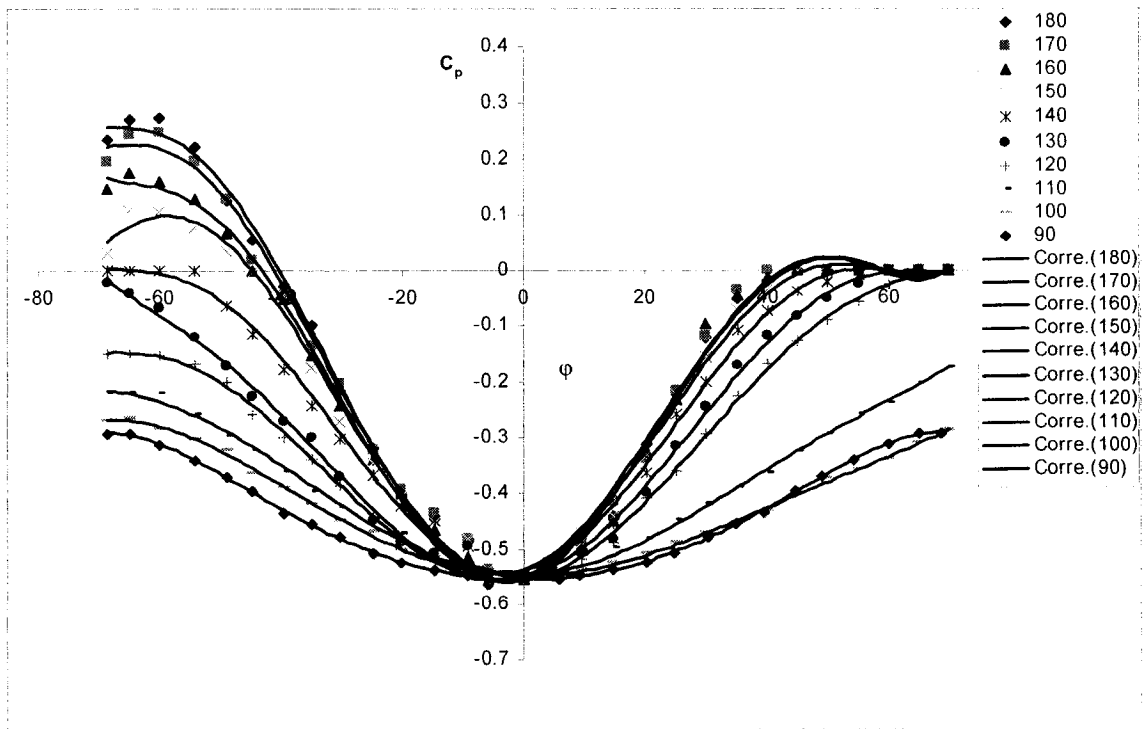
Figure 4-4 Pressure coefficients over dome surface (h/c=0.37)
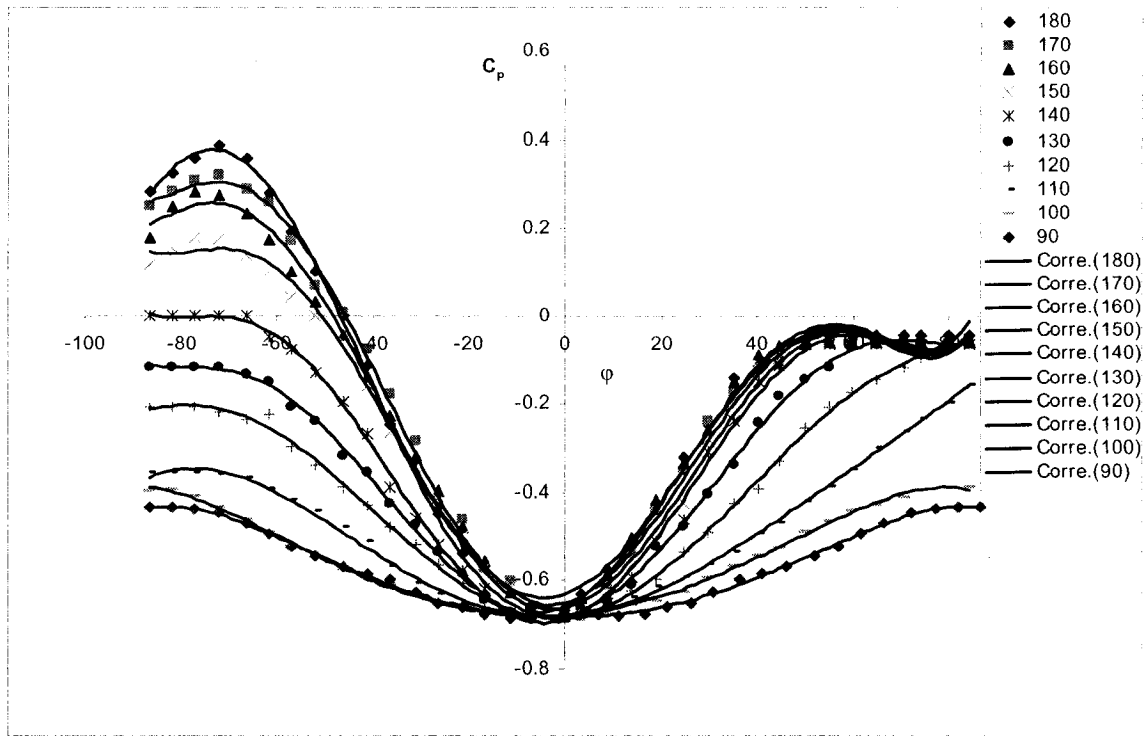
Figure 4-5 Pressure coefficients over dome surface (h/c=0.50)

For less smooth surfaces, the convective coefficient is modified according to (Walton, 1981):

$$h_c = h_n + R_f \left(h_{c,glass} - h_n\right) \tag{4-42}$$

where R_f is the roughness multiplier (Table 4-4).

Table 4-4 Surface roughness multiplier (Walton, 1981)

Roughness index	R_f	Example material
1	2.17	Stucco
2	1.67	Brick
3	1.52	Concrete
4	1.13	Clear pine
5	1.11	Smooth plaster
6	1.00	Glass

The convective heat flux over the inside surface of the cell (i,j) is calculated as follows:

$$q_{conv,in,ij} = h_{in,ij}\left(T_{in} - T_{i,j}\right)$$

(4-43)

where:

$h_{in,ij}$=convective coefficient at the inside dome surface, $W/m^2 \cdot {}^{\circ}C$;

T_{in}=temperature of the air inside the dome, $^{\circ}C$.

The value of $h_{in,ij}$ varies with the temperature difference between the dome surface and the surrounding air inside the dome, the air flow direction, and the tilted angle. Since the natural convection is the dominant factor:

$$h_{in,ij} = h_n$$

(4-44)

h_n is calculated by equations (4-36) and (4-37).

4.1.3 Long-wave Radiative Heat Flux

The long-wave radiation heat flux is calculated as follows:

$$q_{LWR,ij} = F_{ij,sky} \cdot \varepsilon_{ij} \cdot \sigma_c \cdot \left(T_{sky}^{\ 4} - T_{i,j}^{\ 4}\right) + F_{ij,g,out} \cdot \varepsilon_{ij} \cdot \sigma_c \cdot \left(T_{g,out}^{\ 4} - T_{i,j}^{\ 4}\right)$$

(4-45)

where:

ε_{ij}=surface long-wavelength emissivity;

σ_c=Stephan-Boltzmann constant, $5.67 \cdot 10^{-8} W/m^2 \cdot K^4$;

T_{sky}=sky temperature, K;

53

$T_{g,out}$ =surface temperature of the ground outside the dome, K.

The above equation can be simplified using the radiation coefficient:

$$q_{LWR,ij} = h_{r,ij,sky} \cdot \left(T_{sky} - T_{i,j}\right) + h_{r,ij,g,out} \cdot \left(T_{g,out} - T_{i,j}\right)$$ (4-46)

where:

$h_{r,ij,sky}$ =radiation coefficient between cell (i,j) and sky, $W/m^2 \cdot {}^{\circ}C$;

$h_{r,ij,g,out}$ =radiation coefficient between cell (i,j) and the ground outside the dome, $W/m^2 \cdot {}^{\circ}C$.

The radiation coefficient between cell (i,j) and the sky is calculated as follows:

$$h_{r,ij,sky} = \varepsilon_{ij} \cdot F_{ij,sky} \cdot \sigma_c \cdot \left(T_{sky}{}^2 + T_{i,j}{}^2\right) \cdot \left(T_{sky} + T_{i,j}\right)$$ (4-47)

The radiation coefficient between cell (i,j) and the ground outside the dome is calculated as follows:

$$h_{r,ij,g,out} = \varepsilon_{ij} \cdot F_{ij,g,out} \cdot \sigma_c \cdot \left(T_{g,out}{}^2 + T_{i,j}{}^2\right) \cdot \left(T_{g,out} + T_{i,j}\right)$$ (4-48)

The ground temperature is calculated from (ASHRAE, 2001a):

$$T_{g,z} = T_{ms} + A_s e^{-z\sqrt{\pi/\alpha_s\tau_0}} \sin\left[\frac{2\pi\left(n_d - n_{lag}\right)}{\tau_0} - z\sqrt{\frac{\pi}{\alpha_s\tau_0}}\right]$$ (4-49)

where:

$T_{g,z}$ =soil temperature at depth z, °C;

T_{ms} =mean annual surface temperature, °C;

A_s =surface temperature amplitude, °C;

z =depth, m;

α_s =thermal diffusivity of the soil, m^2/day;

τ_0 =annual period, 365 days;

n_d=Julian date, days;

n_{lag} =phase lag of soil surface temperature, days.

In the above equation, the depth will be assumed to be equal to zero in order to obtain the ground surface temperature outside the dome.

Nearest location to Montreal is the Champlain Valley (N.Y.) where T_{ms}=6.3°C, A_s=14.4°C and n_{lag}=111.6 days (CRREL, 1999).

The sky temperature for horizontal surface is calculated by using the model from BLAST program (McQuiston et al., 2000):

$$T_{sky} = T_o - 6 \tag{4-50}$$

where:

T_{sky} =sky temperature for a horizontal surface, °C;

T_o =outdoor air temperature, °C.

For surfaces that are not horizontal, the sky temperature is affected by the path length through the atmosphere (Walton, 1983):

$$T_{sky, \Sigma} = \left[\cos \frac{\Sigma}{2} \right] T_{sky} + \left[1 - \cos \frac{\Sigma}{2} \right] T_o \qquad (4\text{-}51)$$

where:

$T_{sky,\Sigma}$ = sky temperature for a tilted surface, °C.

The long-wave radiation heat flux between the inside surface of cells and the external surfaces of the walls/roof of the house is calculated differently from the case of the long-wave radiation heat flux between only two surfaces. The concept of total interchange view factor is employed to calculate the net surface-to-surface radiation heat gain among the cells.

Each cell surface of the dome is numbered as p=1,..., M·N+9, where node p= (i-1)·N+j represents cell (i,j), and nodes p=M·N+1,...,M·N+9 represent the ground surface inside the dome and external wall/window/roof surfaces of the house. The net radiant flux at the inside surface of cell (i,j) is determined by:

$$q_{surf,p} = \sum_{k=1}^{MN+9} IF_{p,k} \sigma_c \left(T_k^4 - T_p^4 \right) \qquad (4\text{-}52)$$

where:

$IF_{p,k}$=total interchange view factor between surface p and surface k;

T_k=Temperature of surface k, °C.

$$p = (i-1) \cdot N + j \tag{4-53}$$

Using the radiation coefficient, the above equation is written as:

$$q_{surf,p} = \sum_{k=1}^{MN+9} h_{r,p,k} (T_k - T_p) \tag{4-54}$$

where:

$h_{r,p,k}$ =radiation coefficient between surface p and surface k, $W/m^2 \cdot °C$.

The radiation coefficient between surface p and surface k is calculated as follows:

$$h_{r,p,k} = IF_{p,k} \cdot \sigma_c \cdot \left(T_k^2 + T_p^2\right) \cdot \left(T_k + T_p\right) \tag{4-55}$$

Calculation of the total interchange view factor

The net radiation exchange of a surface is equal to the difference between the surface radiosity and irradiation. The total long-wave incident radiation on surface A_j is:

$$A_j \frac{J_j - \varepsilon_j E_j}{\gamma_j} = \sum_{i=1}^{Ns} J_i F_{ij} A_i \tag{4-56}$$

where:

57

ε =emissivity of each surface;

J=radiosity of each surface, W/m^2;

E_j=blackbody emissivity power, W/m^2;

F_{ij}=view factor between two surfaces i and j (Appendix B);

Ns=number of surfaces, equal to M·N+9.

The system of equations is written in matrix form:

$$
\begin{bmatrix}
F_{11} - \dfrac{1}{\gamma_1} & F_{12} & F_{13} & \cdots & F_{1Ns} \\[2mm]
F_{21} & F_{22} - \dfrac{1}{\gamma_2} & F_{23} & \cdots & F_{2Ns} \\[2mm]
F_{31} & F_{32} & F_{33} - \dfrac{1}{\gamma_3} & \cdots & F_{3Ns} \\[2mm]
\vdots & \vdots & \vdots & \ddots & \vdots \\[2mm]
F_{Ns1} & F_{Ns2} & F_{Ns3} & \cdots & F_{NsNs} - \dfrac{1}{\gamma_{Ns}}
\end{bmatrix}
\cdot
\begin{bmatrix}
J_1 \\ J_2 \\ J_3 \\ \vdots \\ J_{Ns}
\end{bmatrix}
=
\begin{bmatrix}
-\dfrac{\varepsilon_1}{\gamma_1} E_1 \\[2mm]
-\dfrac{\varepsilon_2}{\gamma_2} E_2 \\[2mm]
-\dfrac{\varepsilon_3}{\gamma_3} E_3 \\[2mm]
\vdots \\[2mm]
-\dfrac{\varepsilon_{Ns}}{\gamma_{Ns}} E_{Ns}
\end{bmatrix}
\qquad (4\text{-}57)
$$

The blackbody emissivity power of surface i is calculated as follows:

$$E_i = \sigma_c T_i^4 \qquad (4\text{-}58)$$

where:

T_i =temperature of surface A_i, K

After solving the system of equations for the radiosity, the net radiant flux at surface i is determined by:

$$q_{surf,i} = \frac{\varepsilon_i}{\gamma_i}(E_i - J_i)$$

<div align="right">(4-59)</div>

Hottel and Sarofim (1967) developed a method to simplify the radiantion exchange calculation by precalculating all the geometry and material surface properties by specifying a total gray interchange area, S_{ij}. By applying this concept, the net radiation exchange at a surface becomes a simple summation of all the incident radiations from other surfaces to the destination surface.

With this method, the network equations can be solved once and used throughout the rest of the simulation period. In this research, a new view factor based on the total interchange area is defined and used to calculate the long-wave radiation between each inside surface.

The procedure is used for determining the new view factor by a series of subsidiary problems where the emissive powers of all surfaces but one are set to zero. This results in "Ns" radiosity problems. The radiosities resulting from each of those problems are designated as follows:

$_1J_1 \cdots _1J_{Ns}$	Solution	with	$E_1 \neq 0$
$_2J_1 \cdots _2J_{Ns}$	Solution	with	$E_2 \neq 0$
. .			
. .			
. .			
$_{Ns}J_1 \cdots _{Ns}J_{Ns}$	Solution	with	$E_{Ns} \neq 0$

<div align="right">(4-60)</div>

The pre-subscript indicates which surface was not assigned a zero emissive power. The solution begins by considering surface j as the surface with the nonzero emissive power,

then considering the flux at surface A_j to find the net radiation:

$$q_{j \to i} = \frac{\varepsilon_i}{\gamma_i}\left({}_j J_i - 0 \right) \qquad (4\text{-}61)$$

Consider the special case when i=j, $q_{i,net}$ is the emission rate $E_i \varepsilon_i$ minus the sel-absorption $q_{i \to i}$:

$$q_{i \to i} = \frac{\varepsilon_i}{\gamma_i}\left({}_i J_i - \varepsilon_i E_i \right) \qquad (4\text{-}62)$$

The Kronecker delta is used to express both equations in a single compact form:

$$q_{j \to i} = \frac{\varepsilon_i}{\gamma_i} \cdot \left(\frac{{}_j J_i}{E_j} - \delta_{ij}\varepsilon_j \right) \cdot E_j \qquad (4\text{-}63)$$

where:

$$\delta_{ij} = \begin{cases} 1 & \text{if} & i=j \\ 0 & \text{f} & i \neq j \end{cases}$$

Therefore the above equation represents the net heat flux to surface i due to the existence of surface j, as the sole net emitter. The net flux between i and j due to both surfaces being at finite temperature can be expressed as:

$$q_{j \to i} = \frac{\varepsilon_i}{\gamma_i} \cdot \left(\frac{{}_j J_i}{E_j} - \delta_{ij}\varepsilon_j \right) \cdot \left(E_j - E_i \right) = \frac{\varepsilon_j}{\gamma_j} \cdot \left(\frac{{}_i J_j}{E_i} - \delta_{ij}\varepsilon_i \right) \cdot \left(E_j - E_i \right) \qquad (4\text{-}64)$$

${}_j J_i$ is proportional to E_j, so that the term ${}_j J_i / E_j$ is independent of system temperature.

The term multiplying $\left(E_j - E_i\right)$ has all the effects of the geometry and of the emisivities of the parts on the net radiative flux between A_i and A_j. This leads to the definition of the interchange view factor:

$$IF_{ij} = \frac{\varepsilon_i}{\gamma_i}\left(\frac{{}_jJ_i}{E_j} - \delta_{ij}\varepsilon_j\right) = \frac{\varepsilon_j}{\gamma_j}\left(\frac{{}_iJ_j}{E_i} - \delta_{ij}\varepsilon_i\right) \tag{4-65}$$

IF_{ij}'s are produced using the radiosity equations with N_s different excitation vectors to produce the ${}_jJ_i$ matrix. When the first excitation vector is used, the result is ${}_1J_j$, which can be used to calculate IF_{1j}. The repeated process is needed for all the excitation vectors to determine the total interchange view factor.

$$\begin{bmatrix} F_{11}-\dfrac{1}{\gamma_1} & F_{12} & F_{13} & \cdots & F_{1Ns} \\ F_{21} & F_{22}-\dfrac{1}{\gamma_2} & F_{23} & \cdots & F_{2Ns} \\ F_{31} & F_{32} & F_{33}-\dfrac{1}{\gamma_3} & \cdots & F_{3Ns} \\ \cdot & \cdot & \cdot & \cdot & \cdot \\ \cdot & \cdot & \cdot & \cdot & \cdot \\ F_{Ns1} & F_{Ns2} & F_{Ns3} & \cdots & F_{NsNs}-\dfrac{1}{\gamma_{Ns}} \end{bmatrix} \cdot \begin{bmatrix} J_1 \\ J_2 \\ J_3 \\ \vdots \\ J_{Ns} \end{bmatrix} = \begin{bmatrix} -\dfrac{\varepsilon_1}{\gamma_1}E_1 \\ 0 \\ 0 \\ \vdots \\ 0 \end{bmatrix} \cdots \begin{bmatrix} 0 \\ 0 \\ -\dfrac{\varepsilon_3}{\gamma_3}E_3 \\ \vdots \\ 0 \end{bmatrix} \cdots \begin{bmatrix} 0 \\ 0 \\ 0 \\ \vdots \\ -\dfrac{\varepsilon_{Ns}}{\gamma_{Ns}}E_{Ns} \end{bmatrix} \tag{4-66}$$

Substituting equation (4-2), (4-34), (4-43), (4-46) and equation (4-54) into equation (4-1), and rearrange the unknown variables to the left-hand side, the following equation is developed (Figure 4-1):

$$q_{sol,ij} - \left(\begin{array}{c} h_{o,ij} + h_{in,ij} + h_{r,ij,sky} + h_{r,ij,g,out} + \sum_{l=1,M\cdot N+9} h_{r,ij,l} \\ + \dfrac{k \cdot d \cdot l_1}{A_{ij}} + \dfrac{k \cdot d \cdot l_2}{A_{ij}} + \dfrac{k \cdot d \cdot l_3}{A_{ij}} + \dfrac{k \cdot d \cdot l_4}{A_{ij}} \end{array} \right) \cdot T_{i,j}$$

$$+ \left(\begin{array}{c} h_{o,ij} \cdot T_o + h_{in,ij} \cdot T_{in} + h_{r,ij,sky} \cdot T_{sky} + h_{r,ij,g,out} \cdot T_{g,out} + \sum_{l=1,M\cdot N+9} h_{r,ij,l} \cdot T_l \\ + \dfrac{k \cdot d \cdot l_1}{A_{ij}} \cdot T_{i+1,j} + \dfrac{k \cdot d \cdot l_2}{A_{ij}} \cdot T_{i-1,j} + \dfrac{k \cdot d \cdot l_3}{A_{ij}} \cdot T_{i,j+1} + \dfrac{k \cdot d \cdot l_4}{A_{ij}} \cdot T_{i,j-1} \end{array} \right) \tag{4-67}$$

$$= \frac{m_{ij} \cdot c_p \cdot dT_{i,j}}{A_{ij} \cdot dt}$$

4.2 Heat Balance of the Air inside the Dome

In this section, a single-node model is presented. The air inside the dome is assumed well-mixed and is presented by one node. A zonal model that takes into account the air temperature distribution and air movement inside the dome is presented in Chapter 5. The following heat transfer processes are considered (Figure 4-6): the convective heat transfer over the boundary surface of the air inside the dome, infiltration heat gain/loss from the air outside the dome, and exfiltration heat gain/loss from the air inside the house.
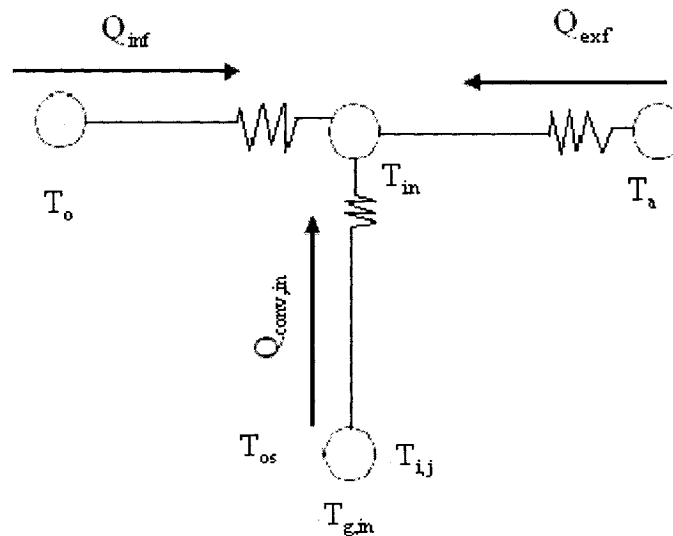
Figure 4-6 Heat balance of the air inside the dome

The heat balance equation for the air inside the dome is written as:

$$Q_{conv,in} + Q_{inf} + Q_{exf} = m_{in} c_p \frac{dT_{in}}{dt}$$ (4-68)

where:

$Q_{conv,in}$ =convective heat flow over the boundary surface for the air inside the dome, W;

Q_{inf} =infiltration heat gain/loss from the air outside the dome, W;

Q_{exf} =exfiltration heat gain/loss from the air inside the house, W;

m_{in} =mass of air inside the dome, kg;

c_p =specific heat of the air inside the dome, J/kg·°C.

The mass of the air inside the dome is calculated as:

$$m_{in} = \rho \cdot V_{in}$$ (4-69)

where:

ρ =density of the air, kg/m^3;

V_{in} =volume of air inside the dome, excluding the house, m^3.

The density of the air is calculated as:

$$\rho = \frac{\rho_0 T_0}{(T + 273.15)} \tag{4-70}$$

where:

ρ_0=density of air at 293K, 1.205 kg/m^3;

T_0=reference temperature at which ρ_0 is calculated, 293K;

T=temperature of the air, °C.

The convective heat flow is calculated as follows:

$$Q_{conv,in} = \sum_{\substack{i=1,M \\ j=1,N}} h_{in,ij} A_{ij}(T_{i,j} - T_{in}) + h_{in,g} A_g(T_{g,in,l} - T_{in}) + \sum_{l=1,8} h_{in,l,out} A_l(T_{l,out} - T_{in}) \tag{4-71}$$

where:

$h_{in,ij}$=convective coefficient over the inside surface of cell (i,j) of the dome, W/m^2·°C;

$h_{in,g}$=convective coefficient over the ground surface inside the dome, W/m^2·°C;

$h_{in,l,out}$=convective coefficient over the exterior wall/roof/window surfaces of the house

inside the dome, W/m^2·°C;

A_{ij}=area of cell (i,j) of the dome surface, m^2;

A_g=area of the ground inside the dome, excluding the floor area of the house, m^2;

A_1 =area of the wall/roof surfaces, m^2;

$T_{g,in,1}$ =ground surface temperature inside the dome, °C.

The infiltration heat flow is calculated as follows:

$$Q_{inf} = Q_{inf,s} \qquad (4\text{-}72)$$

where:

$Q_{inf,s}$ =sensible heat gain/loss from infiltration, W.

$$Q_{inf,s} = \rho \cdot V_{inf} \cdot c_p \cdot (T_o - T_{in}) \qquad (4\text{-}73)$$

where:

ρ =density of the air outside the dome, kg/m^3;

V_{inf} = airflow rate of natural infiltration, m^3/s;

c_p =specific heat of the air outside the dome, J/kg·°C.

The outdoor infiltration airflow rate is calculated as follows:

$$V_{inf} = \frac{ACH_d}{3600} \cdot V_{in} \qquad (4\text{-}74)$$

where:

ACH_d =air infiltration through the dome, expressed in air change rate per hour, h^{-1}.

The sensible heat gain/loss due to air exfiltration from the house is calculated as follows:

$$Q_{exf,s} = \rho \cdot V_{exf} \cdot c_p \cdot (T_a - T_{in})$$ (4-75)

where:

ρ =density of the air in the house, kg/m^3;

V_{exf} = exfiltration airflow rate, m^3/s;

c_p =specific heat of the air inside the house, $J/kg \cdot °C$;

T_a =temperature of the air inside the house, $°C$.

The exfiltration airflow rate from the house is calculated as follows:

$$V_{exf} = \frac{ACH_h}{3600} \cdot V_{House}$$ (4-76)

where:

ACH_h =air exfiltration from the house, expressed in air change rate per hour, h^{-1};

V_{House} =volume of the house, m^3.

Substituting equation (4-71), (4-73), (4-75) into equation (4-68), the following equation is developed:

$$-\left(\sum_{\substack{i=1,M \\ j=1,N}} h_{in,ij} A_{ij} + h_{in,g} A_g + \rho V_{inf} c_p + \rho V_{exf} c_p + \sum_{l=1,8} h_{in,l,out} A_{l,out} \right) T_{in} + \left(\sum_{\substack{i=1,M \\ j=1,N}} h_{in,ij} A_{ij} T_{i,j} + h_{in,g} A_g T_{g,in,l} \right)$$

$$+ \left(\sum_{l=1,8} h_{in,l,out} A_l T_{l,out} + + \rho V_{inf} c_p T_o + \rho V_{exf} c_p T_a \right) = \frac{m_{in} c_p dT_{in}}{dt}$$

(4-77)

4.3 Heat Transfer through the Wall/Roof of the House

4.3.1 Governing Equation

The wall is assumed to have four layers, and there are two boundary nodes and one internal node for each layer, thus there are nine nodes for each wall/roof.

The governing equation for the transient heat transfer process is:

$$\frac{\partial T}{\partial t} = \alpha_h \frac{\partial T^2}{\partial x^2}$$

(4-78)

where:

α_h = temperature diffusion coefficient for each layer of the wall, m^2/s;

x = thickness of the layer, m.

4.3.2 Heat Balance over the External Wall Surface

The following heat transfer processes are considered: the conduction heat flux through the outside wall surface, the convective heat transfer over the outside wall surface, the net surface-to-surface incident radiation over the outside wall surface, and the absorption of solar radiation at the outside wall surface.

The heat balance over the external wall surface is written as follows:

$$-k_1 \frac{\partial T}{\partial x}\Big|_{x=0} + q_{sol,l,out} + q_{conv,l,out} + q_{surf,l,out} = \rho_1 \cdot \frac{1}{4} dx_1 \cdot c_{pl} \cdot \frac{dT}{dt} \qquad (4\text{-}79)$$

where:

k_1 =thermal conductivity of the first layer of the wall/roof, W/m·°C;

$q_{sol,l,out}$ =absorbed solar radiation at the outside wall surface, W/m^2;

$q_{conv,l,out}$ =convective heat transfer over the outside wall surface, W/m^2;

$q_{surf,l,out,t}$ =net surface-to-surface radiation leaving the outside wall surface, W/m^2;

ρ_1 =density of the first layer of the wall, kg/m^3;

dx_1 =thickness of the first layer of the wall, m;

c_{pl} =specific heat of the first layer of the wall, J/kg·°C.

The direct radiation transmitted through each dome cell, which reaches the exterior wall surface, is assumed to be absorbed by that wall surface (Figure 4-7).
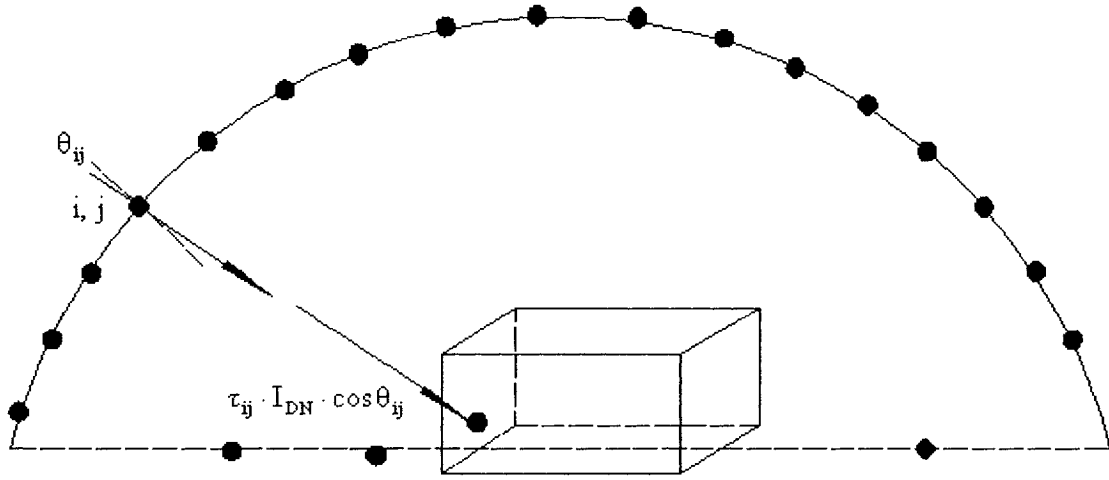
Figure 4-7 Transmitted incident solar radiation over the wall surface

The absorption of solar radiation at the outside wall surface is written as:

$$q_{sol,out} = \frac{\sum_{\substack{i=1,M \\ j=1,N}} \tau_{ij} \cdot A_{ij} \cdot \{I_{DN} \cdot \cos\theta_{ij} + F_{ij,1} \cdot (I_{ds,ij} + I_{dg,ij})\}}{A_1}$$
(4-80)

where:

τ_{ij}=transmittance of the cell (i,j);

θ_{ij}=incident angle for cell (i,j) of the dome surface, deg.;

$F_{ij,1}$=view factor between the cell (i,j) of the dome surface and the outside wall surface;

A_1=area of the outside wall surface, m^2.

The summation is performed over all cells that transmit solar radiation on the selected wall.

The net surface-to-surface incident radiation over the outside wall surface is written as:

$$q_{surf,l,out} = \sum_{\substack{j=1 \\ j\neq l}}^{M\cdot N+9} IF_{lj}\sigma_c\left(T_j^4 - T_{l,out}^4\right)$$

(4-81)

The radiation coefficient between surface l and surface j is calculated as follows:

$$h_{r,ij,out} = IF_{l,j}\cdot\sigma_c\cdot\left(T_{l,out}^2 + T_j^2\right)\cdot\left(T_{l,out} + T_j\right)$$

(4-82)

Thus, equation (4-81) is written as:

$$q_{surf,l,out} = \sum_{\substack{j=1 \\ j\neq l}}^{M\cdot N+9} h_{r,lj,out}\left(T_j - T_{l,out}\right)$$

(4-83)

The convective heat flux over the wall surface is calculated as follows:

$$q_{conv,l,out} = h_{in,l,out}\left(T_{in} - T_{l,out}\right)$$

(4-84)

where:

$h_{in,l,out}$ =convective coefficient over the outside wall surface, $W/m^2 \cdot °C$.

The inside convective coefficient is considered to be equal to the natural convective coefficient.

Substituting equation (4-83) and equation (4-84) into equation (4-79), the following heat balance equation is developed for the exterior surface of each wall/roof:

$$q_{sol,l,out} - \left(h_{in,l,out} + \sum_{\substack{j=1 \\ j \neq 1}}^{M \cdot N+9} h_{r,lj,out} \right) \cdot T_{l,out} + h_{in,l,out} \cdot T_{in} + \sum_{\substack{j=1 \\ j \neq 1}}^{M \cdot N+9} h_{r,lj,out} \cdot T_j \tag{4-85}$$

$$= \rho_1 \cdot \frac{1}{4} dx_1 \cdot c_{p1} \cdot \frac{dT}{dt} + k_1 \cdot \frac{\partial T}{\partial x} \Big|_{x=0}$$

4.3.3 Internal Nodes between Two Surfaces

For internal nodes between two different layers, the following equation is written, as an example for the surface between layers no.1 and no.2:

$$\frac{1}{4} \cdot \left(\rho_1 \cdot c_{p1} \cdot dx_1 + \rho_2 \cdot c_{p2} \cdot dx_2 \right) \cdot \frac{dT}{dt} = -k_1 \cdot \frac{dT}{dx} \Big|_{x=\frac{3}{4}dx_1} + k_2 \cdot \frac{dT}{dx} \Big|_{x=dx_1+\frac{1}{4}dx_2} \tag{4-86}$$

where:

$-k \cdot \dfrac{dT}{dx}$ =conduction heat flux at the interface of two layers, W/m^2;

k_1 =thermal conductivity of layer no.1 of the wall, $W/m \cdot °C$;

ρ_1 =density of layer no.1 of the wall, kg/m^3;

dx_1 =thickness of layer no.1 of the wall, m;

c_{p1} =specific heat of layer no.1 of the wall, $J/kg \cdot °C$.

4.3.4 Heat Balance over the inside Wall Surface

The following heat transfer processes are considered: the conduction heat flux through the inside wall surface, the convective heat transfer over the inside wall surface, the net

surface-to-surface incident radiation over the inside wall surface, and the absorption of solar radiation at the inside wall surface.

The heat balance over the inside wall surface is written as follows:

$$-k_4 \cdot \frac{\partial T}{\partial x}\Big|_{x=th} + q_{sol,l,in} + q_{conv,l,in} + q_{surf,l,in} + q_{rad,ihg} = \rho_4 \cdot \frac{1}{4} \cdot dx_4 \cdot c_{p4} \cdot \frac{dT}{dt} \qquad (4\text{-}87)$$

where:

k_4 =thermal conductivity of layer no.4, W/m·°C;

$q_{sol,l,int}$ =absorbed solar radiation at the inside wall surface, considered to be zero, W/m^2;

$q_{conv,l,in}$ =convective heat transfer over the inside wall surface, W/m^2;

$q_{surf,l,in}$ =net surface-to-surface radiation leaving the inside wall surface, W/m^2;

$q_{rad,ihg,l}$ =radiation heat flux due to internal heat gain, W/m^2;

th=thickness of the wall, m.

The convective heat flux over the wall surface is calculated as follows:

$$q_{conv,l,in} = h_a \left(T_a - T_{l,in} \right) \qquad (4\text{-}88)$$

where:

h_a =convective coefficient over the inside wall surface, W/m·°C;

$T_{1,in}$ =temperature of the inside wall surface, °C;

T_a =temperature of the room air, °C.

The net long-wave radiant flux at the inside surface is determined by:

$$q_{surf,1,in} = \sum_{\substack{k=1,9 \\ k\neq 1}} \frac{\varepsilon_1}{\gamma_1}\left(E_{1,in} - J_{k,in}\right) \qquad (4\text{-}89)$$

The equation of the total long-wave incident radiation for the system that is composed of the inside wall surfaces, windows, floor surface and inside roof surface is:

$$A_j \frac{J_j - \varepsilon_j E_j}{\gamma_j} = \sum_{i=1}^{9} J_i F_{ij} A_i \qquad (4\text{-}90)$$

The system of equations is written in a matrix form as follows:

$$\begin{bmatrix} F_{11}-\dfrac{1}{\gamma_1} & F_{12} & F_{13} & \cdots & F_{19} \\ F_{21} & F_{22}-\dfrac{1}{\gamma_2} & F_{23} & \cdots & F_{29} \\ F_{31} & F_{32} & F_{33}-\dfrac{1}{\gamma_3} & \cdots & F_{39} \\ \vdots & \vdots & \vdots & \vdots & \vdots \\ F_{91} & F_{92} & F_{93} & \cdots & F_{99}-\dfrac{1}{\gamma_9} \end{bmatrix} \bullet \begin{bmatrix} J_1 \\ J_2 \\ J_3 \\ \vdots \\ J_9 \end{bmatrix} = \begin{bmatrix} -\dfrac{\varepsilon_1}{\gamma_1}E_1 \\ -\dfrac{\varepsilon_2}{\gamma_2}E_2 \\ -\dfrac{\varepsilon_3}{\gamma_3}E_3 \\ \vdots \\ -\dfrac{\varepsilon_9}{\gamma_9}E_9 \end{bmatrix} \qquad (4\text{-}91)$$

where:

ε =emissivity of the inside surface; and

J=radiosity of the inside surface.

Equation (4-65) is applied to calculate the total interchange view factors between the inside surfaces of the house. For example, for a house of 10m ·10 m, with a height of 5 m, and without windows, the view factors and total interchange view factors are show in Table 4-5 and Table 4-6 (with emissivity of the wall=0.93 and reflectance of the wall=0.07). The indexes 1, 2, 3, 4, 5, and 6 represent west wall, south wall, east wall, north wall, roof and floor, respectively.

Table 4-5 View factors of inside surfaces of the house

View factor	1	2	3	4	5	6
1	0	0.29	0.12	0.29	0.15	0.15
2	0.145	0	0.145	0.42	0.145	0.145
3	0.12	0.29	0	0.29	0.15	0.15
4	0.145	0.42	0.145	0	0.145	0.145
5	0.15	0.29	0.15	0.29	0	0.12
6	0.15	0.29	0.15	0.29	0.12	0

Table 4-6 Total interchange view factors of inside surfaces of the house

Total interchange view factor	1	2	3	4	5	6
1	0	0.258	0.109	0.258	0.133	0.133
2	0.129	0	0.129	0.358	0.129	0.129
3	0.109	0.258	0	0.258	0.133	0.133
4	0.129	0.358	0.129	0	0.129	0.129
5	0.133	0.258	0.133	0.258	0	0.109
6	0.133	0.258	0.133	0.258	0.109	0

After solving for the total interchange view factor, the net surface-to-surface incident radiation over the inside wall surface is calculated by:

$$q_{surf,l,in} = \sum_{\substack{j=1 \\ j \neq l}}^{9} IF_{lj}\sigma_c \left(T_{j,in}^4 - T_{l,in}^4 \right) \tag{4-92}$$

The radiation coefficient between surface l and surface j is calculated as follows:

$$h_{r,ij,in} = IF_{l,j} \cdot \sigma_c \cdot \left(T_{l,in}^2 + T_{j,in}^2 \right) \cdot \left(T_{l,in} + T_{j,in} \right) \tag{4-93}$$

Thus, equation (4-92) is written as:

$$q_{surf,l,in} = \sum_{\substack{j=1 \\ j \neq l}}^{9} h_{r,lj,in} \left(T_{j,in} - T_{l,in} \right)$$

(4-94)

The radiation heat flux due to internal heat gain is calculated as follows:

$$q_{rad,ihg,l} = \frac{\sum_{k=1}^{2} Q_k F_{rad,k}}{\sum_{j=1}^{9} A_j}$$

(4-95)

where:

Q_k =heat gain for the kth internal heat gain element, W; and

$F_{rad,k}$ =radiative fraction for the kth internal heat gain element.

The internal heat gains considered in this model are generated by occupants and lighting. The instantaneously rate of heat gain from electric lighting is calculated from (McQuiston et al., 2000):

$$Q_{light} = WF_u F_s$$

(4-96)

where:

W =total installed light wattage, W;

F_u =use factor, ratio of wattage in use to total installed wattage;

F_s=special allowance factor (ballast factor in the case of fluorescent and metal halide fixtures).

F_u is assumed to be equal to 1.0 for each hour. For incandescent lamps, F_s is equal to 1.0. The heat gain to the space from incandescent fixtures is assumed to be 80% radiative and 20% convective (McQuiston et al., 2000).

The heat gain from people has two components: sensible (73W/person) and latent (59 W/person) for standing, light work and walking (McQuiston et al., 2000). The latent heat gain is assumed to become cooling/heating load instantly, whereas the sensible heat gain is partially delayed. The sensible heat gain for people generally is assumed to be 30% convective (instant cooling load) and 70% radiative (the delayed portion).

Substituting equation (4-88) and equation (4-94) into equation (4-87), the following equation is developed:

$$q_{sol,l,in} + q_{rad,ihg} - \left(h_a + \sum_{\substack{j=1 \\ j \neq l}}^{9} h_{r,lj,in} \right) \cdot T_{l,in} + h_a \cdot T_a + \sum_{\substack{j=1 \\ j \neq l}}^{9} h_{r,lj,in} \cdot T_{j,in}$$

$$= \rho_4 \cdot \frac{1}{4} \cdot dx_4 \cdot c_{p4} \cdot \frac{dT}{dt} + k_4 \cdot \frac{\partial T}{\partial x}\Big|_{x=th}$$

(4-97)

4.4 Heat Transfer through the Window

The heat transfer process through the window is considered as quasi-steady state:

$$q_{win} = U_w \left(T_{in} - T_a \right)$$

(4-98)

where:

$$U_w = \cfrac{1}{\cfrac{1}{h_{win,o}} + R_w + \cfrac{1}{h_{win,in}}}$$
(4-99)

$$T_{os} = T_{in} - \frac{q_{win}}{h_{win,o}}$$
(4-100)

$$T_{is} = T_a + \frac{q_{win}}{h_{win,in}}$$
(4-101)

where:

q_{win}=heat transfer through the window, W/m^2;

$h_{win,o}$=convective coefficient over the outside surface of the window, W/m$^2\cdot$°C;

$h_{win,in}$=convective coefficient over the inside surface of the window, W/m$^2\cdot$°C;

U_w=U-value of the window, W/m$^2\cdot$°C;

R_w=thermal resistance of the glazing, m$^2\cdot$°C/W;

T_{os}=outer layer temperature of the window, °C;

T_{is}=inner layer temperature of the window, °C;

T_{in}=air temperature inside the dome, °C;

T_a=room air temperature, °C.

Three double-glazed windows are considered, mounted on the south wall, east wall and

west wall, respectively.

4.5 Heat Balance of the Room Air

The following heat transfer processes are considered (Figure 4-8): the convective heat transfer over the wall surfaces, the exfiltration heat loss to the house, heat gain from lighting, people and heating system.
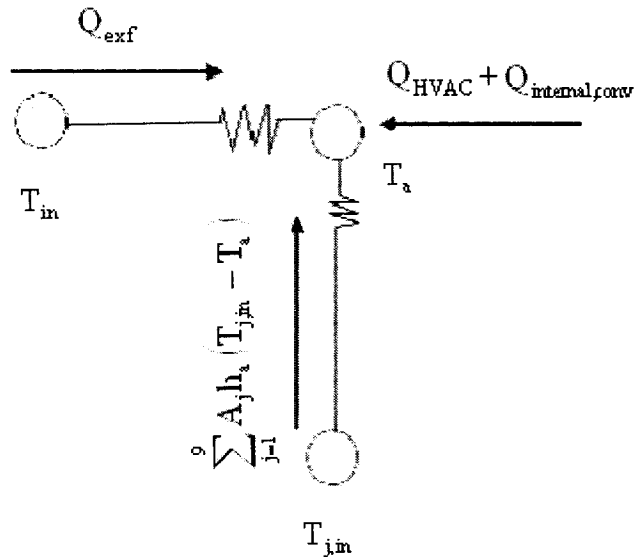
Figure 4-8 Heat balance of the room air

The indoor air of the house is assumed well mixed and therefore it is represented by one node. The indoor air temperature T_a is held at the thermostat set-point value by a heating system. The heat balance for the indoor air is written as:

$$Q_{HVAC} + \sum_{j=1}^{9} A_j h_a \left(T_{j,in} - T_a\right) + Q_{exf} + Q_{internal,conv} = 0 \qquad (4-102)$$

where:

$T_{j,in}$=temperature of inside surface j, °C;

Q_{HVAC} =heat addition rate by the heating system, W;

$Q_{internal,conv}$ =convective part of internal heat gain, from people and lighting, W;

T_a =room air temperature, equal to 21°C;

The convective part of the internal heat gain is written as follows:

$$Q_{internal,conv} = \sum_{k=1}^{M} Q_k \left(1 - F_{rad,k}\right)$$ (4-103)

The heat gain/loss due to exfiltration can be calculated as follows:

$$Q_{exf} = Q_{exf,s}$$ (4-104)

where:

$Q_{exf,s}$ =sensible heat gain/loss from exfiltration, W.

$$Q_{exf,s} = \rho V_{exf} c_p \left(T_{in} - T_a\right)$$ (4-105)

where:
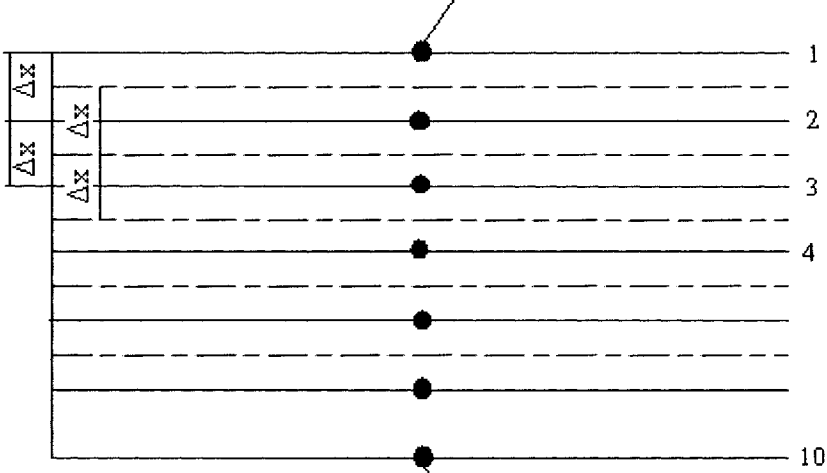
ρ =density of the air inside the house, kg/m^3;

V_{exf} =exfiltration airflow rate, m^3/s;

c_p =specific heat of the air inside the house, J/kg·°C.

4.6 Heat Transfer through the Ground inside the Dome

The ground surface is divided into ten layers (Figure 4-9), where nodes 2-9 are internal

nodes, node 1 and node 10 are boundary nodes.

$$-k \cdot \frac{\partial T}{\partial x}\bigg|_{x=0} + q_{sol} + q_{conv} + q_{surf} = \rho \cdot \frac{1}{2} \cdot dx \cdot c_p \cdot \frac{dT}{dt}$$

$$T_{g,in,10} = T_{ms} + A_s \cdot e^{-1.0 \cdot \sqrt{\pi/\alpha_s \cdot \tau_0}} \cdot \sin\left[\frac{2\pi \cdot (n_d - n_{lag})}{\tau_0} - 1.0 \cdot \sqrt{\frac{\pi}{\alpha_s \cdot \tau_0}} \right]$$

Figure 4-9 Heat transfer through the ground inside the dome

4.6.1 Governing Equation

The equation for the heat transfer process for the ground is written as:

$$\frac{\partial T}{\partial t} = \alpha_s \frac{\partial T^2}{\partial x^2}$$
(4-106)

where:

α_s =temperature diffusion coefficient of the soil, m²/s; and

x =depth in the soil, m.

4.6.2 Heat Balance over the Ground Surface inside the Dome

The following heat transfer processes are considered at the ground surface inside the dome: the absorption of solar radiation over the ground surface, the convective heat transfer over the ground surface, the conduction heat transfer at the outside ground surface, the surface-to-surface incident radiation over the ground surface, and the conduction heat transfer through the ground.

The heat balance over the ground surface inside the dome is written as:

$$-k \cdot \frac{\partial T}{\partial x}\bigg|_{x=0} + q_{sol} + q_{conv} + q_{surf} = \rho \cdot \frac{1}{2} \cdot dx \cdot c_p \cdot \frac{dT}{dt} \tag{4-107}$$

where:

k =thermal conductivity of the soil, W/m·°C;

c_p =specific heat of soil, J/kg·°C;

q_{sol} =absorbed solar radiation by the ground surface, W/m^2;

q_{conv} =convective heat transfer at the ground surface, W/m^2;

q_{surf} =net surface-to-surface radiation at the ground surface, W/m^2.

The total solar radiation transmitted through each cell, which reaches the ground surface, is composed of (1) transmitted diffuse solar radiation, (2) transmitted direct solar

radiation, and (3) transmitted solar radiation that is reflected by the inside cell surfaces of the dome. All those components are assumed to be totally absorbed by the ground surface. Therefore, the incident solar radiation on the ground surface is calculated as follows:

$$q_{sol} = I_{df} + I_d' + I_d''$$ (4-108)

where:

I_{df} =transmitted diffuse solar radiation on the ground surface, W/m^2;

I_d' =transmitted direct solar radiation reaching directly the ground surface, W/m^2;

I_d'' =transmitted direct solar radiation that is reflected by the inside cell surfaces of the dome and reaches the ground surface, W/m^2.

The transmitted diffuse solar radiation on the ground surface is calculated as follows:

$$I_{df} = \frac{\sum_{\substack{i=1,M \\ j=1,N}} \tau_{ij} \cdot A_{ij} \cdot F_{ij,g} \cdot \left(I_{ds,ij} + I_{dg,ij}\right)}{A_g}$$ (4-109)

where:

A_g =area of the ground surface inside the dome, excluding the house, m^2;

$F_{ij,g}$ =view factor between the cell (i,j) and the ground surface inside the dome;

$I_{ds,ij}$ =diffuse incident solar radiation from the sky that reaches cell (i,j), W/m^2;

$I_{dg,ij}$ =diffuse incident solar radiation from the ground that reaches cell (i,j), W/m^2.

The direct solar radiation that is transmitted through the dome glazing, which reaches the ground surface, is divided into two components: (1)one component is transmitted through the dome, and reaches directly the ground surface, and (2) another component is reflected by the inside dome surface and then reaches the ground surface (Figure 4-10). The first radiation component is calculated as:

$$I_d' = \frac{\sum\limits_{\substack{i=1,M \\ j=1,N}} A_{ij} \cdot \tau_{ij} \cdot I_{DN} \cdot \cos\theta_{ij}}{A_g} \qquad (4\text{-}110)$$
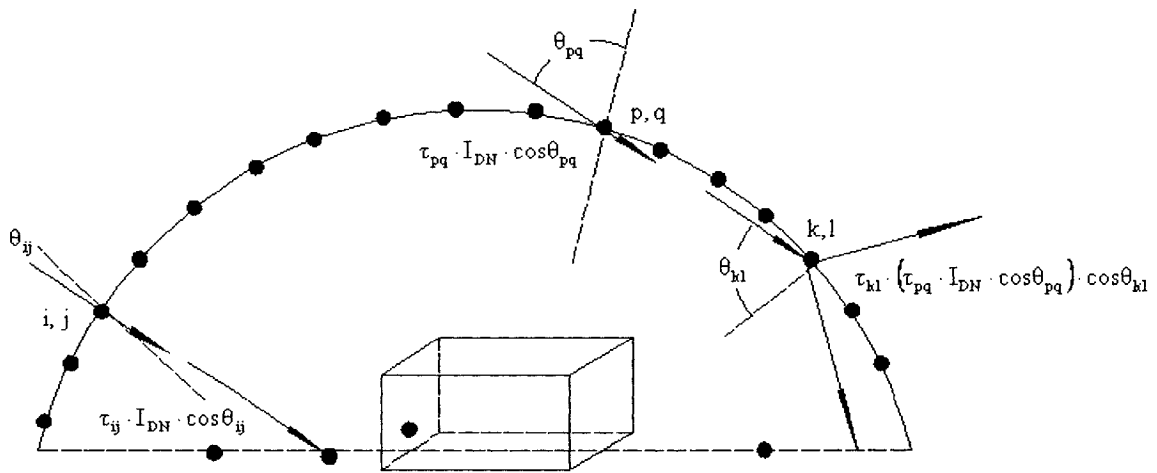
Figure 4-10 Beam radiation transmitted through the dome surface that reaches the ground surface

The second radiation component is calculated as:

$$I_d'' = \frac{\sum\limits_{\substack{i=1,M \\ j=1,N}} A_{pq} \cdot \tau_{pq} \cdot I_{DN} \cdot \cos\theta_{pq} \cdot \left(1 - \cos\theta_{kl} \cdot \left(\alpha_{kl} + \tau_{kl}\right)\right)}{A_g} \qquad (4\text{-}111)$$

where:

θ_{kl} =incident angle of the cell (k,l) that reflects the transmitted solar radiation, deg.;

θ_{pq} =incident angle of the cell (p,q), deg.;

α_{kl} =absorbance of the cell (k,l).

Cell (p,q) is the surface where the solar beam first reaches the dome, and cell (k,l) is the surface where it reflects solar radiation to the ground.

The convective heat flux over the ground surface is calculated as follows:

$$q_{conv} = h_{in,g}\left(T_{in} - T_{g,in,1}\right)$$
(4-112)

The surface-to-surface incident radiation over the ground surface is calculated using the total interchange view factor:

$$q_{surf} = \sum_{\substack{i=1 \\ i \neq g}}^{N \cdot M+9} IF_{ig} \cdot \sigma_c \cdot \left(T_i^4 - T_{g,in,1}^4\right)$$
(4-113)

The radiation coefficient between surface l and surface j is calculated as follows:

$$h_{r,ig} = IF_{ig} \cdot \sigma_c \cdot \left(T_i^2 + T_{g,in,1}^2\right) \cdot \left(T_i + T_{g,in,1}\right)$$
(4-114)

Thus, equation (4-113) is written as:

$$q_{surf} = \sum_{\substack{i=1 \\ i \neq g}}^{M \cdot N+9} h_{r,ig} \cdot \left(T_i - T_{g,in,1}\right)$$

(4-115)

Substituting equation (4-112) and equation (4-115) into equation (4-107), the following equation is developed:

$$q_{sol} - \left(h_{in,g} + \sum_{\substack{i=1 \\ i \neq g}}^{M \cdot N+9} h_{r,ig}\right) \cdot T_{g,in,1} + h_{in,g} \cdot T_{in} + \sum_{\substack{i=1 \\ i \neq g}}^{M \cdot N+9} h_{r,ig} \cdot T_i = \rho \cdot \frac{1}{2} dx \cdot c_p \cdot \frac{dT}{dt} + k \cdot \frac{\partial T}{\partial x}\bigg|_{x=0}$$

(4-116)

4.6.3 Inside Boundary Condition

The ground temperature at the depth of 1.0 m is considered to be equal to the soil temperature obtained from ASHRAE (2001a). So that the inside boundary condition can be written based on equation (4-49), as:

$$T_{g,in,10} = T_{ms} + A_s \cdot e^{-1.0 \cdot \sqrt{\pi/\alpha_s \cdot \tau_0}} \cdot \sin\left[\frac{2\pi \cdot \left(n_d - n_{lag}\right)}{\tau_0} - 1.0 \cdot \sqrt{\frac{\pi}{\alpha_s \cdot \tau_0}}\right]$$

(4-117)

4.7 Heat Transfer through the Floor of the House

The floor is assumed to have two layers, two boundary nodes, one internal node for each layer, and one node at the interface between the two layers. Thus there are five nodes for the floor.

4.7.1 Governing Equation

The governing equation for the transient heat transfer process is written as follows:

$$\frac{\partial T}{\partial t} = \alpha_f \frac{\partial T^2}{\partial x^2}$$

(4-118)

4.7.2 Heat Balance over the Floor Surface

The following heat transfer processes are considered at the outside surface of the floor: the conduction heat flux through the floor surface, the convective heat transfer over the floor surface, the net surface-to-surface incident radiation over the floor surface, and the absorption of solar radiation at the floor surface.

The heat balance over the floor surface is written as follows:

$$-k_1 \cdot \frac{\partial T}{\partial x}\bigg|_{x=th} + q_{sol,1,in} + q_{conv,f} + q_{surf,f} + q_{rad,ihg} = \rho_1 \cdot \frac{1}{4} dx_1 \cdot c_{p1} \cdot \frac{dT}{dt}$$

(4-119)

where:

k_1 =thermal conductivity of the first layer, W/m·°C;

$q_{sol,1,in}$ =absorbed solar radiation at the floor surface, W/m^2;

$q_{conv,f}$ =convective heat transfer over the floor surface, W/m^2;

$q_{surf,f}$ =net surface-to-surface radiation leaving the floor surface, W/m^2;

$q_{rad,ihg,1}$ =radiation heat flux due to internal heat gains, W/m^2;

th=thickness of the first floor layer, m.

The convective heat flux over the floor surface is calculated as follows:

86

$$q_{conv,l,in} = h_a \left(T_a - T_{f,l} \right) \tag{4-120}$$

where:

h_a =convective coefficient over the floor surface, W/m·°C; and

$T_{f,l}$ =temperature of the floor surface, °C.

The surface-to-surface incident radiation over the floor surface is calculated using the total interchange view factor:

$$q_{surf} = \sum_{\substack{j=1 \\ j \neq f}}^{9} IF_{jf} \sigma_c \left(T_{j,in}^4 - T_{f,l}^4 \right) \tag{4-121}$$

The radiation coefficient between the floor surface and inside surface j is calculated as follows:

$$h_{r,jf} = IF_{jf} \cdot \sigma_c \cdot \left(T_{j,in}^2 + T_{f,l}^2 \right) \cdot \left(T_{j,in} + T_{f,l} \right) \tag{4-122}$$

Thus, equation (4-121) is written as:

$$q_{surf,l,in} = \sum_{\substack{j=1 \\ j \neq f}}^{9} h_{r,jf} \left(T_{j,in} - T_{f,l} \right) \tag{4-123}$$

Substituting equation (4-120) and equation (4-121) into equation (4-119), the following equation is developed:

87

$$q_{sol,l,in} + q_{rad,ihg} - \left(h_a + \sum_{\substack{j=1 \\ j \neq f}}^{9} h_{r,jf} \right) \cdot T_{f,l} + h_a \cdot T_a + \sum_{\substack{j=1 \\ j \neq f}}^{9} h_{r,jf} \cdot T_{j,in}$$

$$= \rho_1 \cdot \frac{1}{4} \cdot dx_1 \cdot c_{pl} \cdot \frac{dT}{dt} + k_1 \cdot \frac{\partial T}{\partial x} \bigg|_{x=th}$$

(4-124)

4.7.3 Internal Node at the Interface of Two Layers

The equation is written as follows:

$$\frac{1}{4} \cdot \left(\rho_1 \cdot c_{pl} \cdot dx_1 + \rho_2 \cdot c_{p2} \cdot dx_2 \right) \cdot \frac{dT}{dt} = -k_1 \cdot \frac{dT}{dx} \bigg|_{x=\frac{3}{4}dx_1} + k_2 \cdot \frac{dT}{dx} \bigg|_{x=dx_1+\frac{1}{4}dx_2}$$

(4-125)

where:

$-k_i \cdot \dfrac{dT}{dx}$ =conduction heat flux at an interface, W/m^2;

k_1 =thermal conductivity of layer no.1 of the floor, W/m·°C;

ρ_1 =density of layer no.1 of the floor, kg/m^3;

dx_1 =thickness of layer no.1 of the floor, m;

c_{pl} =specific heat of layer no.1 of the floor, J/kg·°C.

4.7.4 Inside Boundary Condition

The temperature at the bottom of the second layer is assumed to be equal to the soil temperature at the same depth inside the dome, based on equation (4-106).

4.8 Comparison between Different Versions of the Program

4.8.1 Descriptions of Different Versions of the Computer Program

Several versions of the computer program were developed during this study. This section presents the influence of different approaches and assumptions. For this purpose, a simple case study is evaluated, for a dome-covered house. The house has no windows and has a well-insulated floor, with a dome with radius R=40 m that is divided into 2184 cells. In each version, hourly weather data are used, that is, the outdoor air temperature, the wind speed and wind direction vary over 24 hours. Table 4-7 gives the description on each version of the computer program. The variables for each version are listed as follows:

h_n=natural convective coefficient, $W/m^2 \cdot {}^\circ C$;

V_{az}=incoming wind velocity at the height of z, m/s; and

V_w=wind velocity over the cell surface, m/s.

Subscript o is for outside surface, i refers to inside surface, and z is the height of the cell where the convective coefficient is estimated.

Table 4-7 Version of the computer model with one-node for air inside the dome

Version	h_o [W/m^2·°C]	h_{in} [W/m^2·°C]	Conduction in glazing	Computing time	Computer specification
0	17.0	3.0	1D	8h59min	Pentium IV 3.06G
1	$\sqrt{h_n^2 + [aV_{az}^b]^2}$	3.0	1D	9h08min	Pentium IV 3.06G
2	$\sqrt{h_n^2 + [aV_{az}^b]^2}$	3.0	3D	9h17min	Pentium IV 3.06G
3	$\sqrt{h_n^2 + [aV_{az}^b]^2}$	h_{n*1}	1D	10h05min	Pentium IV 3.06G
4	$\sqrt{h_n^2 + [aV_w^b]^2}$	3.0	1D	9h35min	Pentium IV 3.06G
5	$\sqrt{h_n^2 + [aV_w^b]^2}$	h_{n*1}	3D	10h38min	Pentium IV 3.06G
6	$\sqrt{h_n^2 + [aV_{az}^b]^2}$	h_{n*2}	1D	22h55min	Pentium IV 3.06G
7	$\sqrt{h_n^2 + [aV_w^b]^2}$	h_{n*2}	3D	22h32min	Pentium IV 3.06G
8	$\sqrt{h_n^2 + [aV_{az}^b]^2}$	h_{n*3}	1D	44h44min	Pentium IV 3.06G
9	$\sqrt{h_n^2 + [aV_w^b]^2}$	h_{n*3}	3D	35h36min	Pentium IV 3.06G

Notes

1 The value of the natural convective coefficient is obtained by using the temperature at the previous time step.

2 When the difference between the hourly temperature of all cells of two adjacent identical days is greater than 0.05°C, the value of the natural convective coefficient is obtained by using the temperature at the previous time step. When the difference between two identical days is less than 0.05°C, the value of the natural convective coefficient is obtained by using the hourly temperature of the last identical day.

3 The natural convective coefficient is obtained by using an iterative process in which both cell temperature and convective coefficient are calculated. The iterative process ends when the difference between the absolute values of the last two computing results is less than 0.001°C.

4.8.2 Hourly Outdoor Air Temperature and Wind Direction

Figures 4-11 to 4-13 present the variation with time of outdoor air temperature, wind direction, and C_p value for some selected cells (Table 4-8), respectively. The C_p values vary with the wind direction and the location of the cell at the dome surface. The high-west/high-east cells have lower C_p values than the low-east/low-west cells, respectively.

Table 4-8 Position of the selected cells

	Low-east	High-east	Low-west	High-west
Azimuth from due north [deg.]	94.3	94.3	265.7	265.7
Tilted angle [deg.]	67.3	18.8	67.3	18.8
Height of the center from horizontal plan [m]	0.88	12.1	0.88	12.1
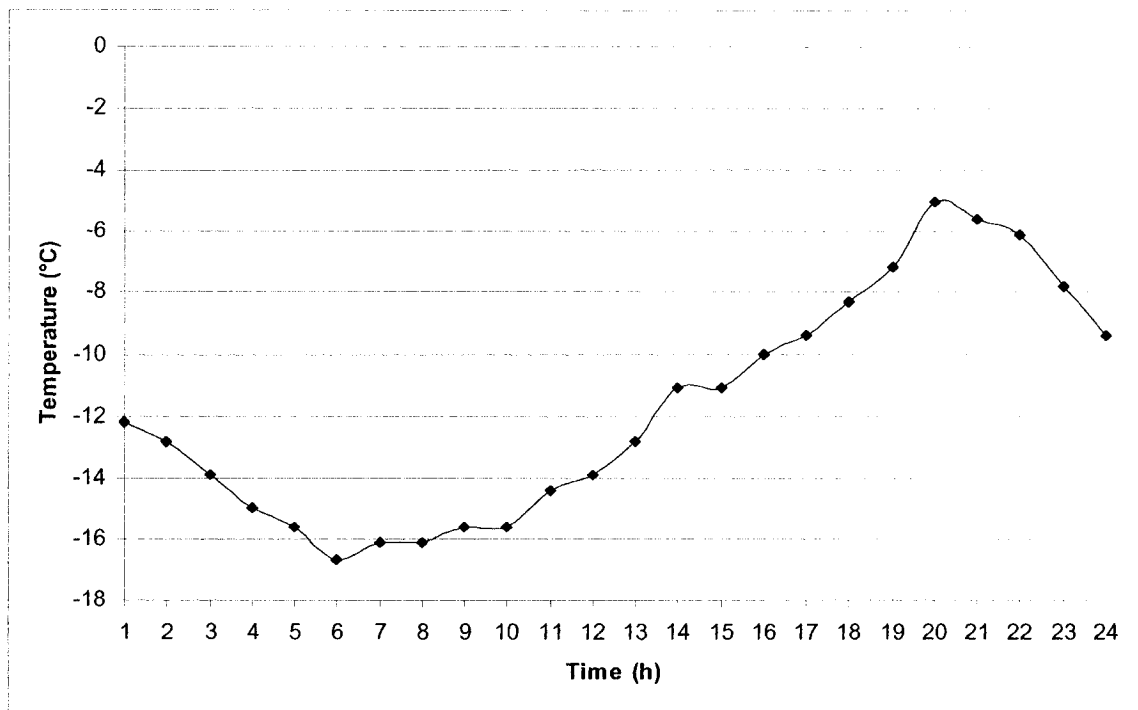
Figure 4-11 Outdoor air temperature
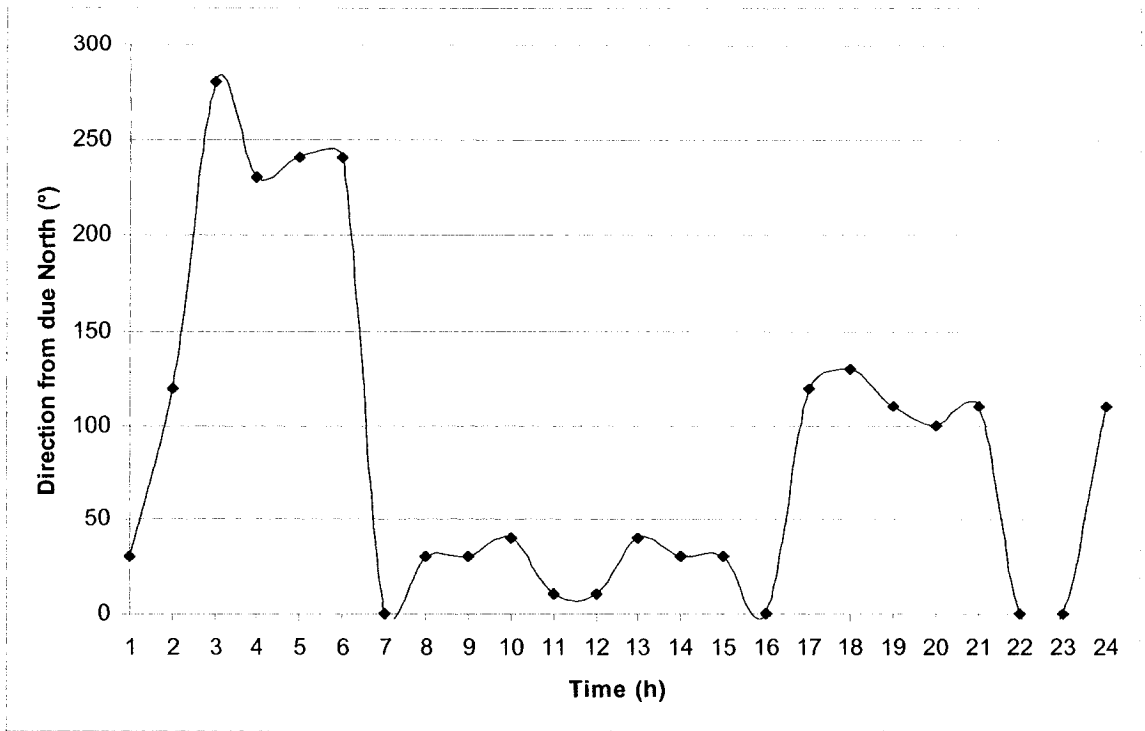
Figure 4-12 Wind direction
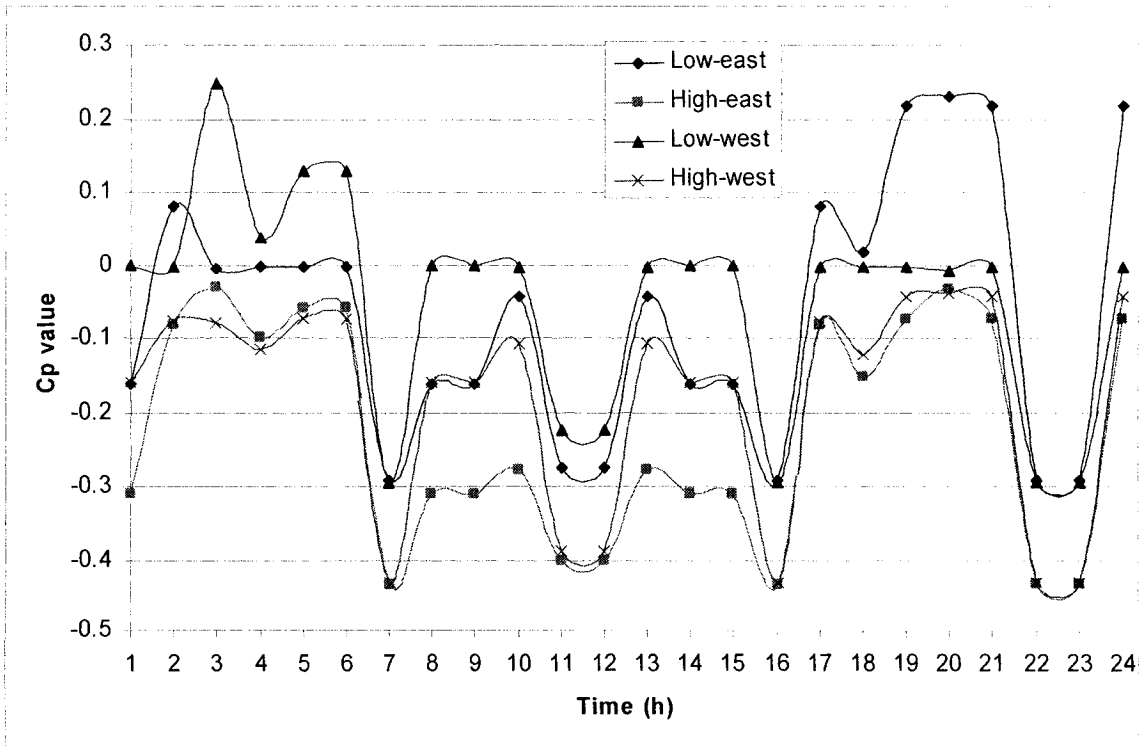
Figure 4-13 C_p values for selected cells

4.8.3 Heating Load of the House

Figures 4-14 and 4-15 show the comparison between the heating loads of the house that is located inside the dome on January 21st, when different versions of the computer model are used. Models that use the variable outside convective coefficient in terms of C_p value, and the variable inside convective coefficient (versions no.5, 7 and 9), predict the lowest heating load, while model that uses constant values for both outside convective coefficient and inside convective coefficient (version no.0) predicts the highest heating load. Models that calculate the variable outside convective coefficient with C_p value (versions no. 4, 5, 7 and 9), predict slightly lower heating load than other model that uses constant outside convective coefficient (versions no. 0) or that calculate the outside convective coefficient with incoming wind velocity (versions no. 1, 2, and 4). The simulation of 3D conduction through glazing has little impact on the heating load of the house compared with 1D model, and the values of the inside convective coefficients have great impact on the heating load. Calculation of the convective coefficient by using an iterative process has very small impact on the heating load of the house compared with a straight forward method that directly calculates the convective coefficient from the computed values of temperature.
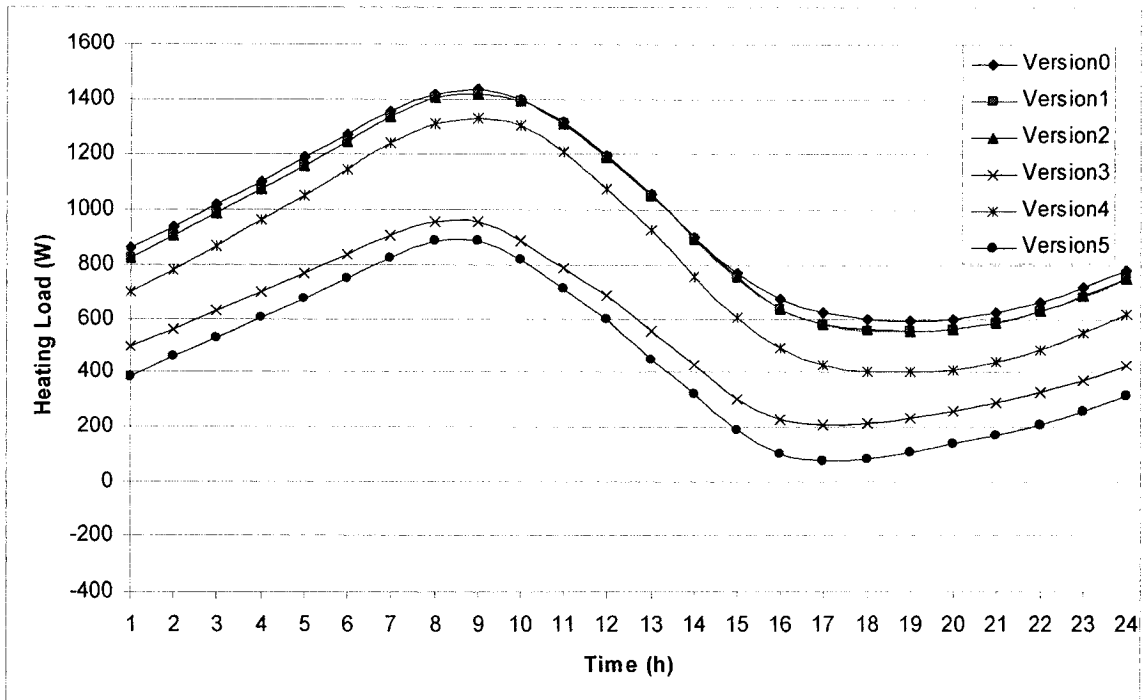
Figure 4-14 Comparison on the heating load on January 21st
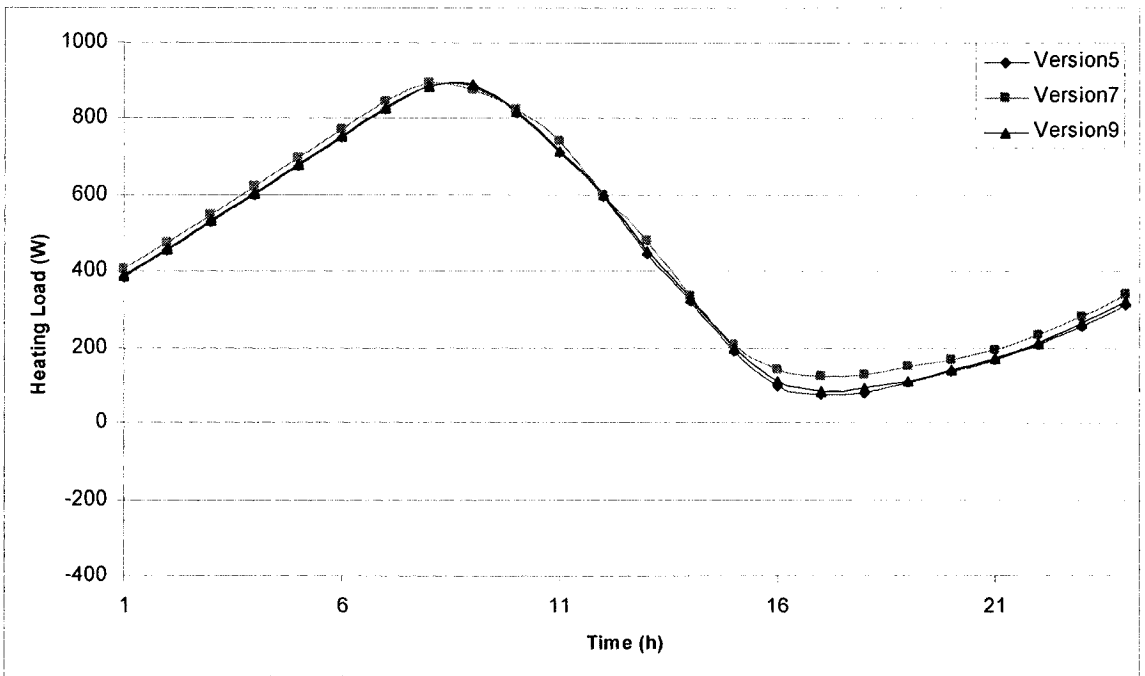
Figure 4-15 Comparison on the heating load on January 21st by different iteration processes

4.8.4 Air Temperature inside the Dome

Figures 4-16 and 4-17 show the comparison between the air temperature inside the dome as predicted by different versions of the computer model. It is observed that the models that calculate the inside natural convective coefficient (versions no.3, 5, 7, and 9) predict higher air temperature than the models that use constant inside convective coefficient (versions no.0 to 2, 4). The models that use the surface air velocity to calculate the outside convective coefficient (versions 4, 5, 7, and 9) predict higher temperature than the models that use the incoming air velocity to calculate the outside convective coefficient (versions no.1 to 3). Calculation of the convective coefficient by an iterative process, by using information from the previous time step, has very small impact on the computed air temperature inside the dome.
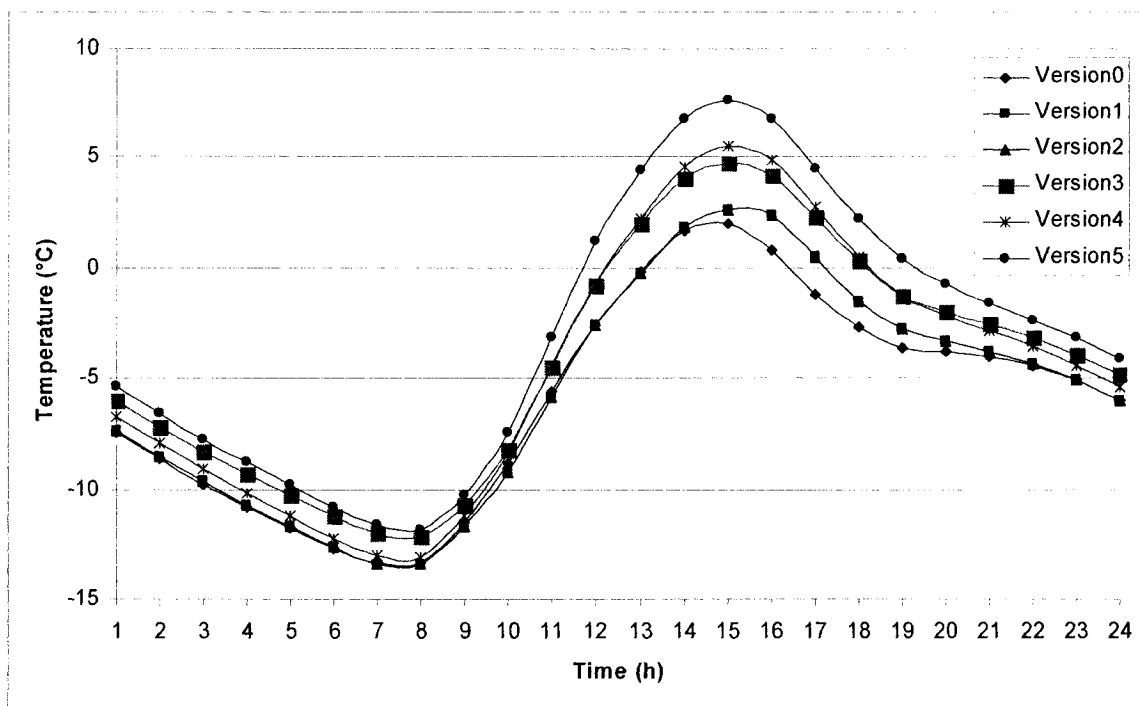
Figure 4-16 Comparison between the air temperature inside the dome on January 21st
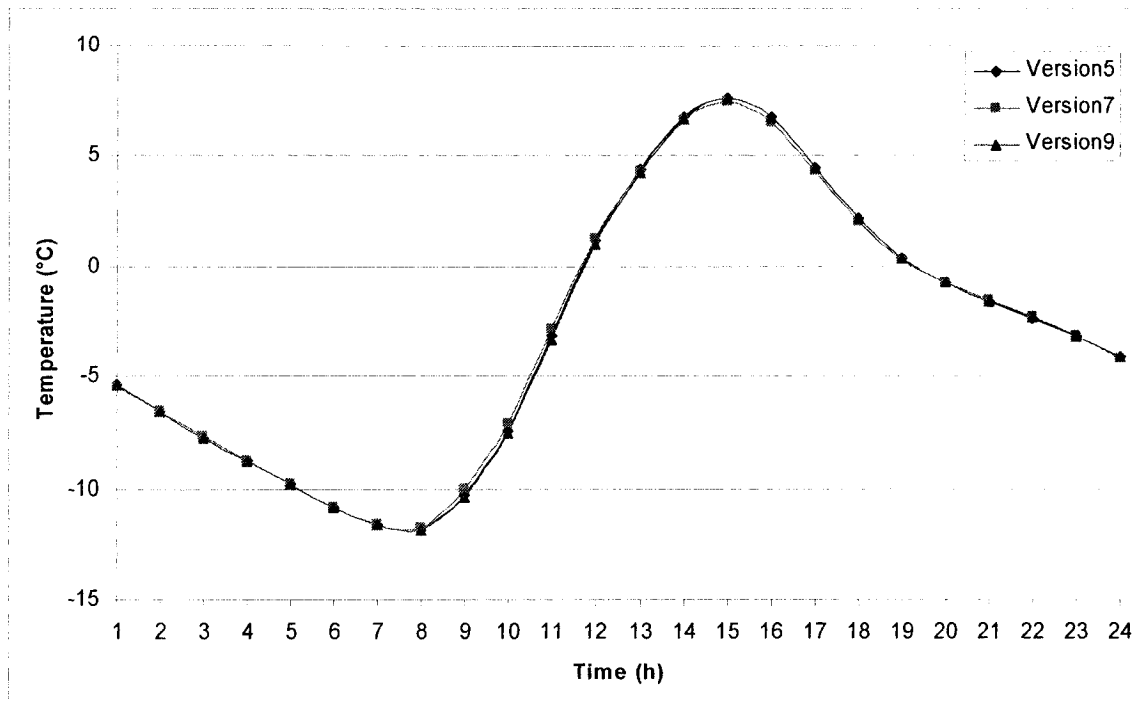
Figure 4-17 Comparison between the air temperature inside the dome on January 21st by different iteration processes

4.8.5 Ground Surface inside the Dome

Figures 4-18 and 4-19 show the difference between the ground surface temperature inside the dome as predicted by each version of the computer model. The impact of the different models on the ground surface temperature inside the dome is similar to the impact on the air temperature inside the dome.
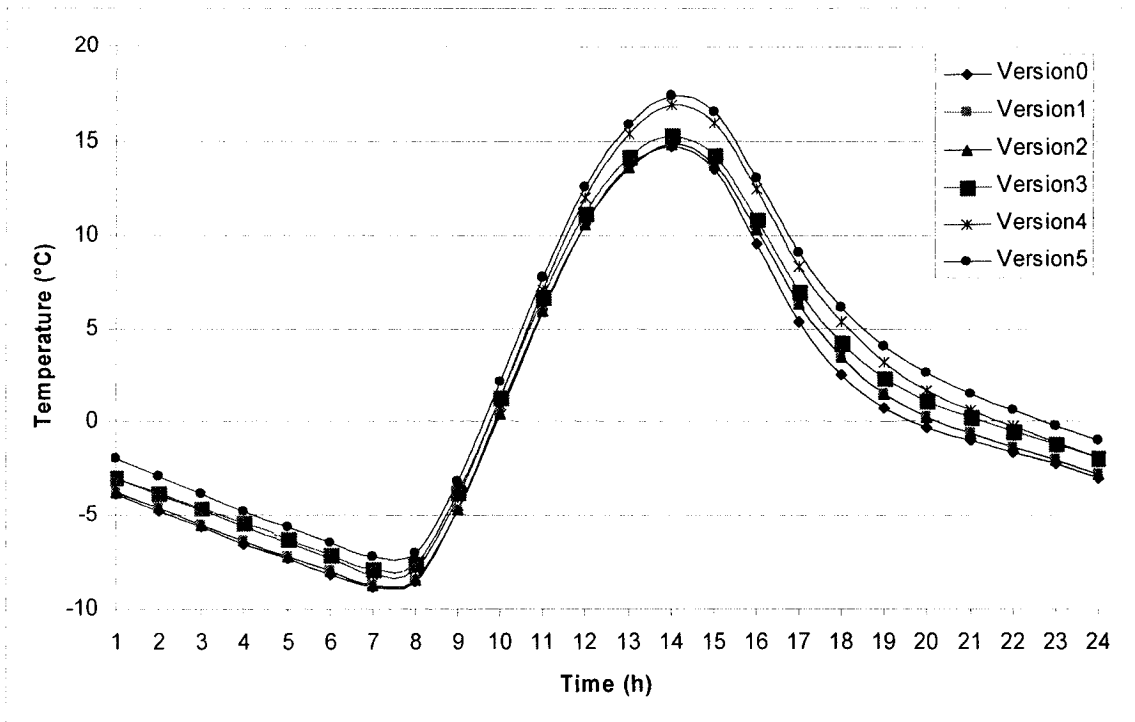
Figure 4-18 Comparison between the ground surface temperature inside the dome on January 21st
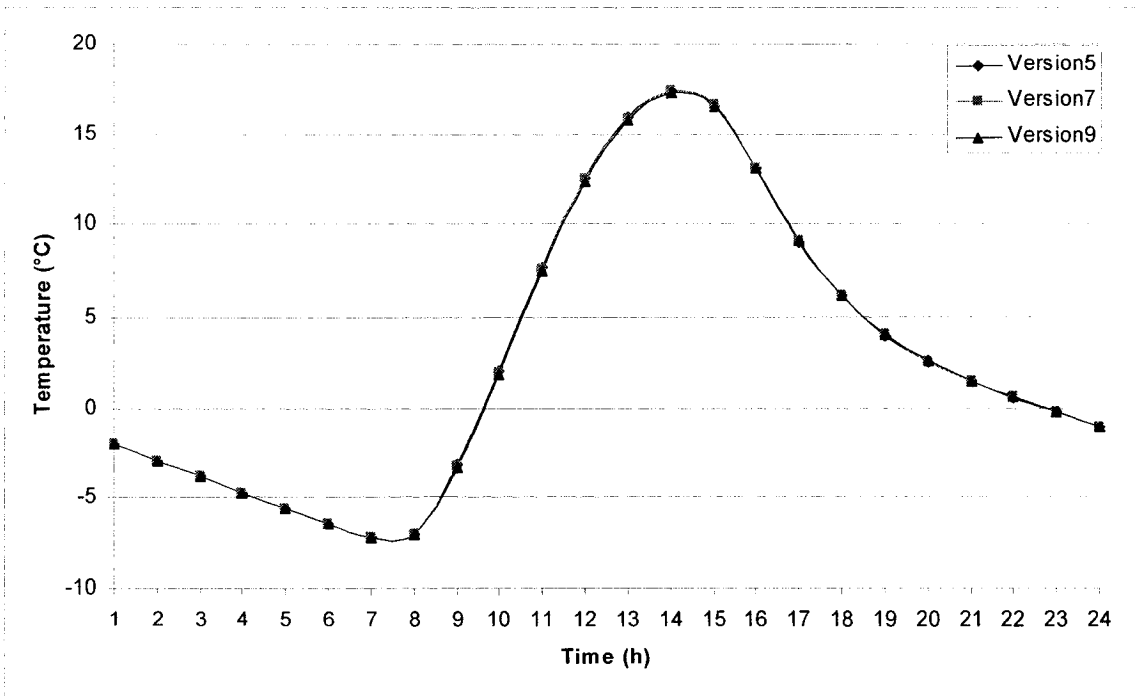
Figure 4-19 Comparison between the ground surface temperature inside the dome on January 21st by different iteration processes

4.8.6 Temperature of Selected Cells of the Dome Cover

Figure 4-20 shows the temperature of some selected cells of the dome surface. Model that uses the natural convection and surface air velocity to calculate the inside and outside convective coefficient (versions no.5) predicts higher temperature than others. The use of information from the previous time step to calculate the inside and outside convective coefficient, leads to minor differences between versions with respect to the calculation of cell temperatures (less than 0.5°C).
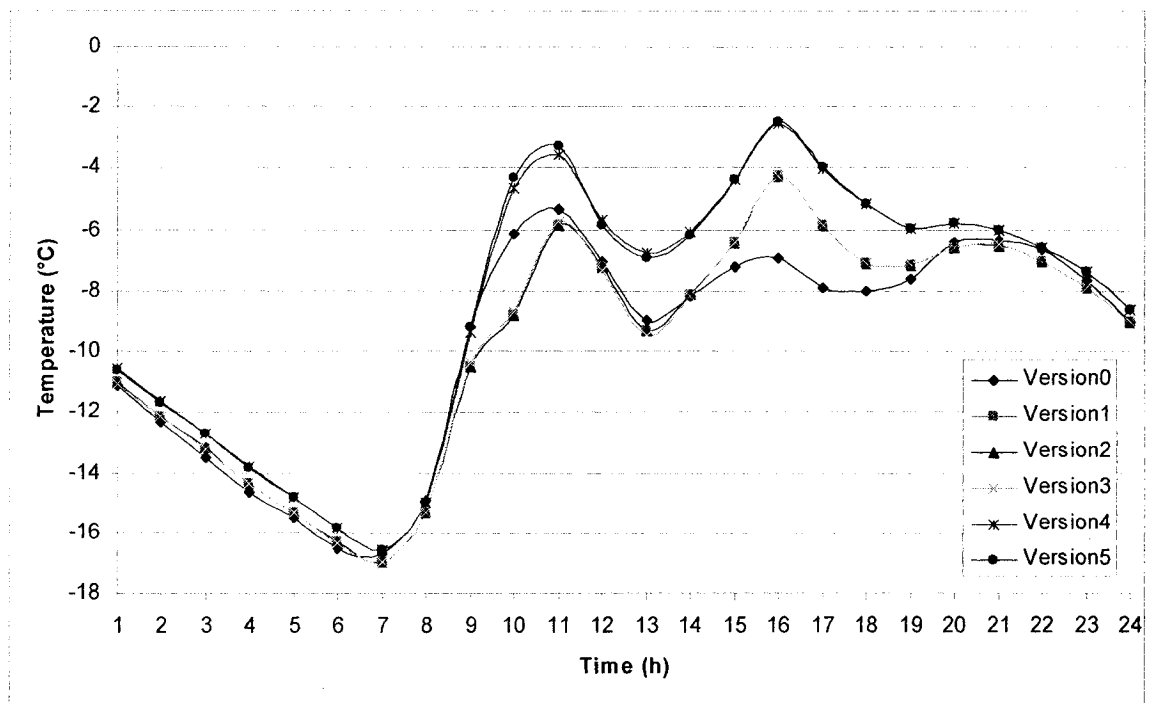
Figure 4-20 Comparison between the temperature of the low-east cell

4.8.7 Incoming Wind Speed and Surface Air Velocity

Figure 4-21 displays the variation with time of the incoming wind speed and the surface wind speed over the selected cells, which is calculated by using the C_p value.
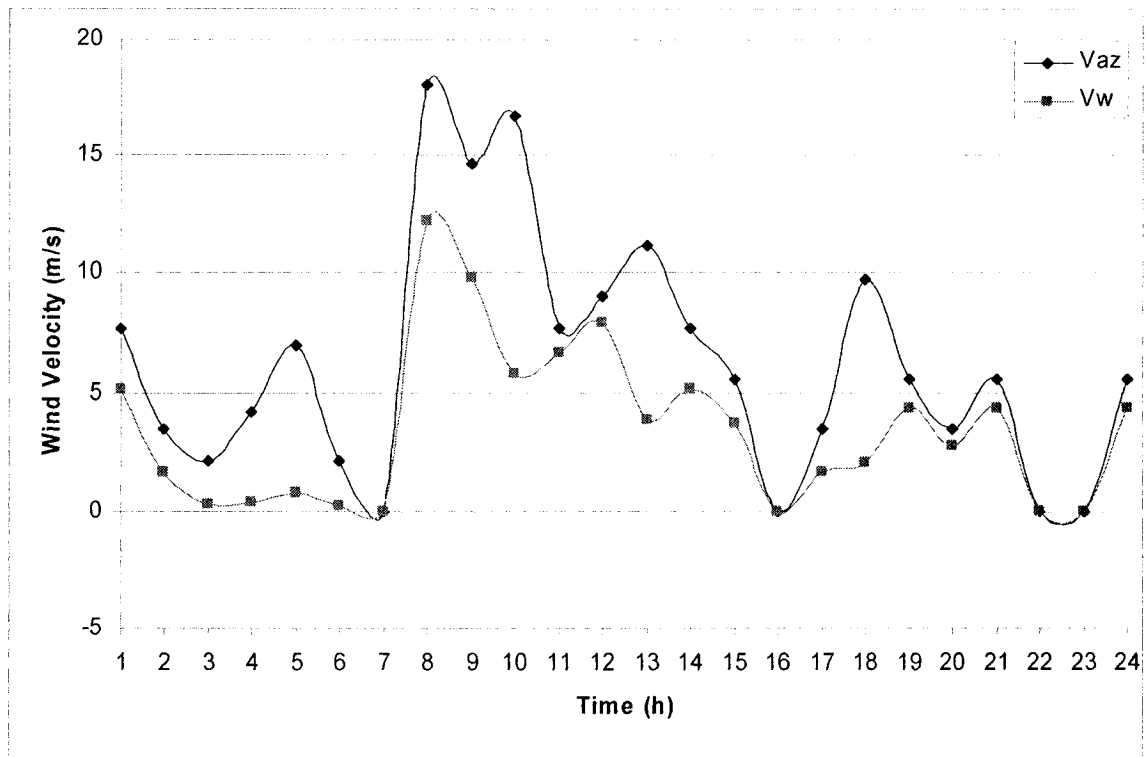
Figure 4-21 Comparison between the incoming wind speed and the wind at the low-east cell

4.8.8 Outside Convective Coefficient

Figure 4-22 presents the outside convective coefficient obtained from different versions of the computer model at the surface of a low-east cell. For instance, at 10:00AM, the outside convective coefficient varies from $12W/m^2 \cdot {}^\circ C$ (versions no.4, and 5) to $30W/m^2 \cdot {}^\circ C$ (versions no.1 to 3). The use of a constant value is not a good approximation of the outside convective coefficient. The outside convective coefficient obtained from the incoming wind velocity (versions no. 1 to 3) is always higher than the value obtained from the surface air velocity (versions no. 4 and 5), since the incoming wind velocity is always higher than the surface air velocity.
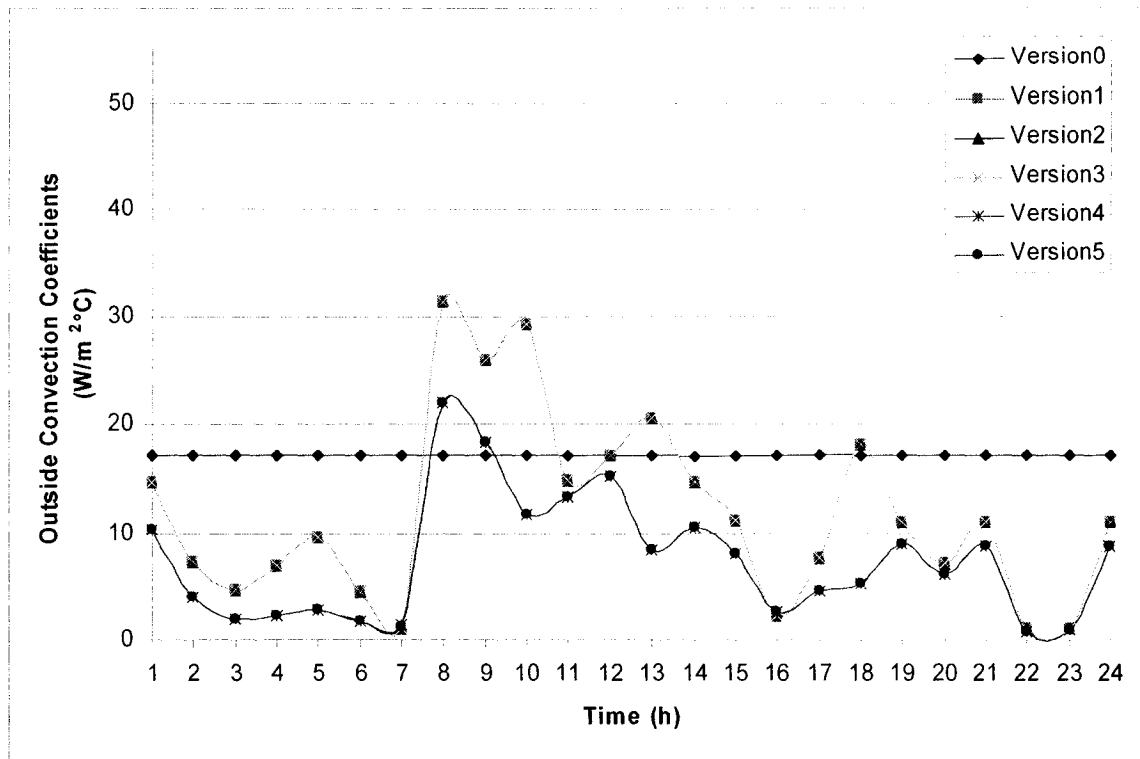
Figure 4-22 Comparison between the outside convective coefficient of the low-east cell

4.8.9 Inside Convective Coefficient

Figure 4-23 presents the comparison of the inside convective coefficient calculated by different versions of the computer model for the low-east cell. The calculated inside convective coefficient is lower than the constant value used in versions no. 0 to 2, and 4. When there is no solar radiation, that is between 20:00 and 6:00 hours, the different versions of the computer model predict similar values of the inside convective coefficient. There are some differences between the calculated inside convective coefficient during the day time.
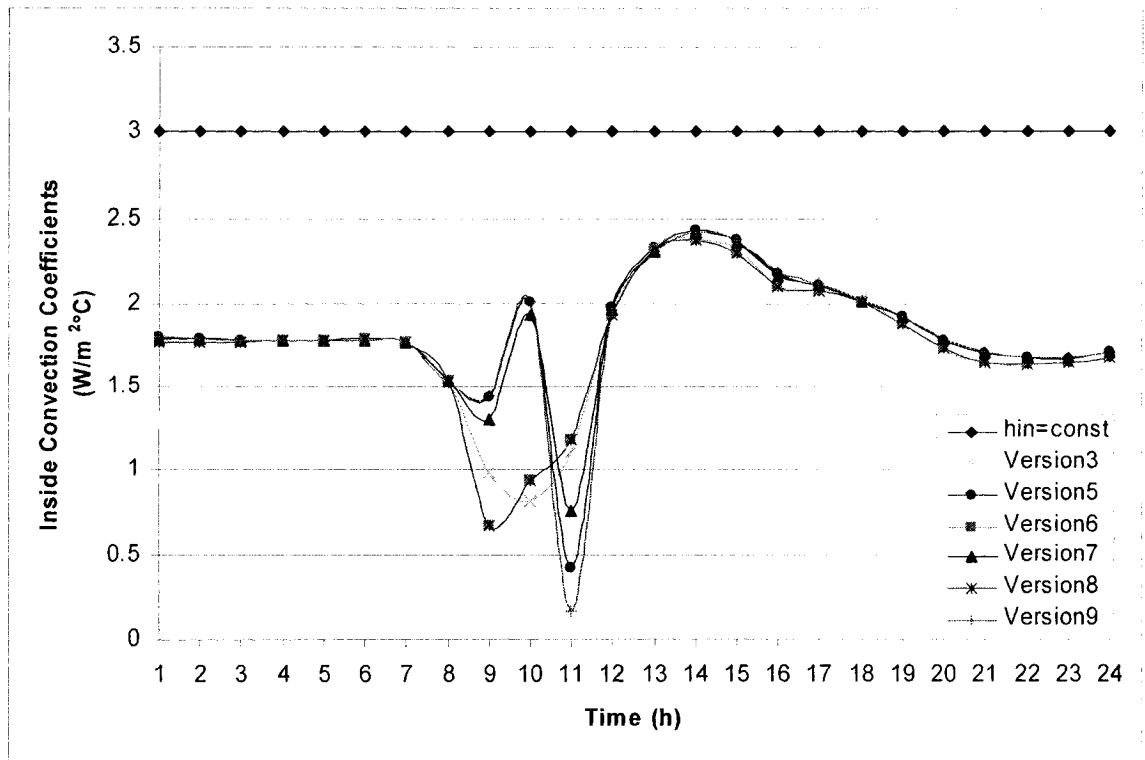
Figure 4-23 Comparison between the inside convective coefficient of the low-east cell

4.8.10 Summary of Findings from the Comparison of Different Versions

The following comments are made based on the results from different versions:

1) The use of 3D conduction of the glazing has little impact on the heating load, the cell temperature, the air temperature inside the dome, the ground surface temperature, and the computing time.

2) The use of a constant h_o leads to the highest heating load; the use of incoming air velocity to calculate h_o leads to slightly lower heating load; and the use of surface air velocity, calculated with the C_p value leads to the lowest heating load.

3) The inside convective coefficient has the greatest impact on the heating load of the house. The use of a constant h_{in} leads to much higher heating load than the

calculation of h_{in} as a function of the temperature difference between the air and the cell temperature, either by using the value at the previous time step or by the iterative process. The calculation of the inside convective coefficient results in an increase of the computing time by about one hour.

4) The calculation of the natural convective coefficient by an iterative process seems to have very small impact on the heating load of the house, air temperature inside the dome (less than 0.5°C), the ground surface temperature and the temperature of the selected cells. The computing time, however, increases by 3 times, compared with other versions.

5) In terms of accuracy and computing time, it is recommended to use a 1D heat conduction model, to calculate the natural convection by using the temperature at the previous time step, and calculate the wind velocity at the cell surface with C_p value.

However, in the computer model, the house has three double-glazed windows, and airflow pattern and air temperature distribution inside the dome are to be evaluated, and in this case, accuracy is the main issue, therefore, 3D conduction through dome cover is considered, and an iteration process is used to calculate the inside and outside convective coefficient.

Chapter 5 Air Flow Model

This chapter presents a 3D zonal model that evaluates the air flow and temperature distribution of the air inside the dome. First, the assumptions for the zonal model are given, and then the mass balance and heat balance equations are written for each zone.

5.1 Introduction

In order to avoid the use of CFD models for the evaluation of the vertical temperature stratification in large spaces, some researchers have used simplified zonal models (Togari et al., 1993; Arai et al., 1994). In such models, the space is vertically divided into a number of zones, where the interior surface temperature is either assumed to be known or calculated by a simplified network model. Acceptable accuracy was achieved between simulation results using the simplified zonal models and small-scale experimental data, which proves that it is possible to use a zonal model method to predict the air temperature for large space. Inard et al (1996) presented a zonal model of the airflow and temperature distribution in a room by modeling the room as a set of connected zones involving mass and thermal continuity equations between zones. He found good agreement with experimental data. Jiru (2006) also found that the zonal model predicts the airflow pattern reasonably well for natural convection. The zonal model has mostly been used for box-type rooms, and steady state processes only (Togari et al., 1993; Arai et al., 1994; Inard et al., 1996; Wurtz et al., 1999; Haghighat et al., 2001; Jiru 2006), and has not been applied to complicate shapes like a dome.

In this study, the zonal model is used to evaluate the air velocity and air temperature

distribution inside the dome. The following assumptions are made: (1) the air space is divided into 559 zones (546 perimeter zones and 13 central zones); the central zones are separated from the perimeter zones by a half of an ellipsoid surface (Figure 5-1); (2) the air temperature and density are uniform in each zone; (3) the boundaries between these zones are considered to be totally permeable to air; (4) the air flow between two adjacent zones are governed by the difference in pressure.

5.2 Description of Grid Used for the Zonal Model

The air inside the dome is divided into N layers, and each layer is composed of M perimeter zones and one central zone. Each perimeter zone has an air-to-solid interface area equal to the surface area of the adjacent dome cell corresponding to the same layer. For a dome cover with M·N cells, the dome air is divided into (M+1) ·N zones. Figure 5-1 and Figure 5-2 present the front view and plan view of the zone divisions.
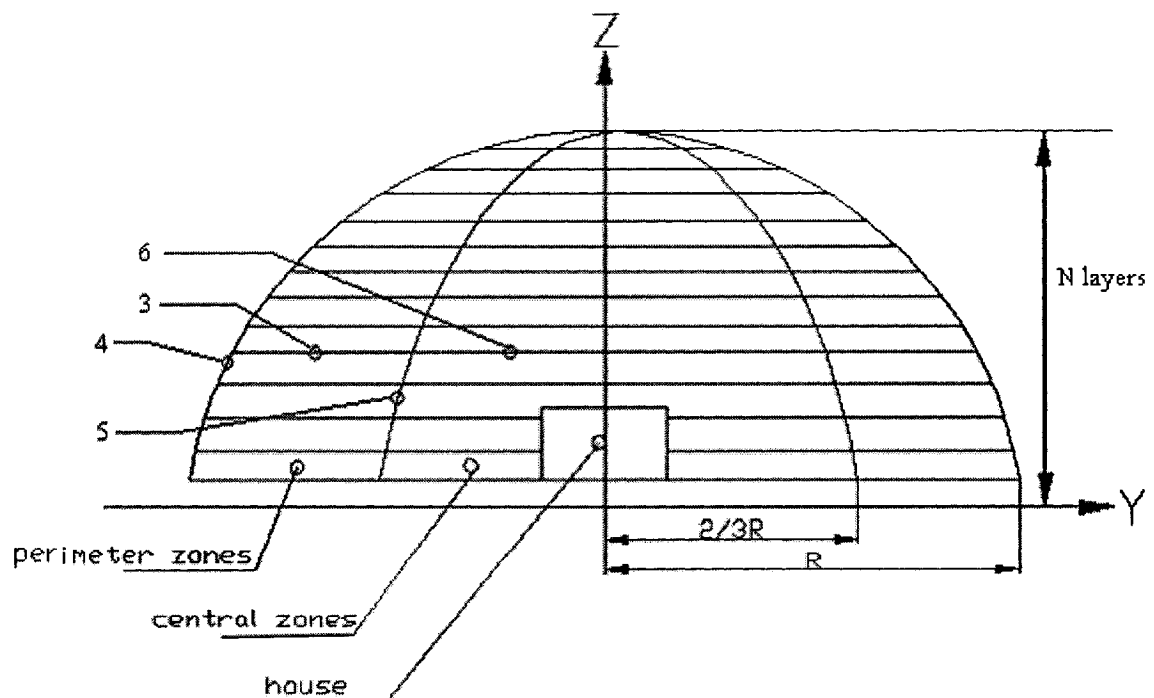
Figure 5-1 Front view of the zonal model
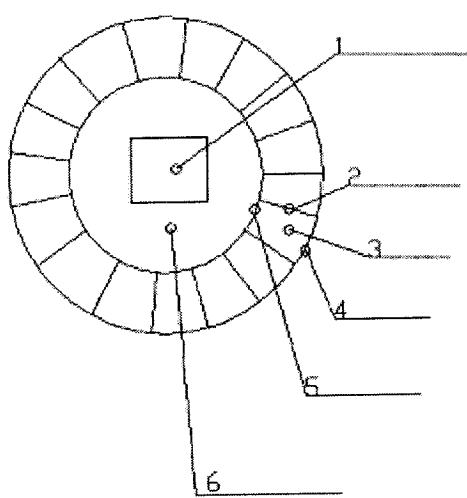
1:house
2:interface between two perimeter
  zones at the same layer
3:interface between two perimeter
  zones at two different layers
4:outer surface of the perimeter
  zone
5:interface between the perimeter
  zone and the central zone
6:interface between two central zones

Figure 5-2 Plan view of the zonal model

The equation for dome cover (Figure 5-1) is written as:

$$y^2 + z^2 = R^2 \quad (\varphi \geq \sigma_0)$$

(5-1)

The equation of the interface between perimeter and central zones (i.e., the ellipse in the front view, presented in Figure 5-1), is written as:

$$\left(\frac{3}{2}y\right)^2 + z^2 = R^2 \quad (\varphi \geq \sigma_0)$$

(5-2)

The surface area of the interface between the central zone, located between z_1 ($\varphi=\varphi_1$) and z_2 ($\varphi=\varphi_2$), and all perimeter zones, is calculated as:

$$A_{cj} = \int_{z_1}^{z_2} 2\pi\pi\sqrt{1 + y'^2}\, dz$$

(5-3)

where:

105

$$\varphi_1 = \sigma_0 + \left(\frac{90 - \sigma_0}{N}(j-1) \right) \qquad (5\text{-}4)$$

$$\varphi_2 = \sigma_0 + \left(\frac{90 - \sigma_0}{N} j \right) \qquad (5\text{-}5)$$

and

$$z_1 = R \cdot \sin\varphi_1 \qquad (5\text{-}6)$$

$$z_2 = R \cdot \sin\varphi_2 \qquad (5\text{-}7)$$

From equation (5-2):

$$y' = \frac{-\dfrac{4}{9}z}{y} \qquad (5\text{-}8)$$

Finally:

$$A_{cj} = \frac{4}{9}\pi R^2 \int_{\sigma_1}^{\sigma_2} \cos\varphi \sqrt{\frac{5}{9}\cos^2\varphi + \frac{4}{9}} \, d\varphi \qquad (5\text{-}9)$$

The surface area of the interface between one perimeter zone and the central zone is obtained as:

$$A_{lj} = \frac{A_{cj}}{M} \qquad (5\text{-}10)$$

The surface area of the interface between the two perimeter zones of the same layer is calculated as:

$$Apj = \int_{z_1}^{z_2} \left(\sqrt{R^2 - z^2} - \frac{2}{3}\sqrt{R^2 - z^2} \right) dz$$

$$= \frac{1}{3} \int_{z_1}^{z_2} \sqrt{R^2 - z^2} \, dz \qquad\qquad (5\text{-}11)$$

$$= \frac{1}{3} R^2 \left(\frac{\sigma}{2} + \frac{\sin 2\sigma}{4} \right) \Big|_{\sigma_1}^{\sigma_2}$$

The volume of the central zone of each layer is obtained as:

$$Vcj = \int_{z_1}^{z_2} \pi r^2 dz$$

$$= \frac{4}{9} \int_{z_1}^{z_2} \pi R^2 \cos^2 \sigma \, dz$$

$$= \frac{4}{9} \int_{z_1}^{z_2} \pi R^2 \cos^2 \sigma R \cos \sigma d\sigma \qquad\qquad (5\text{-}12)$$

$$= \frac{4}{27} \pi R^3 \left(\cos^2 \sigma \sin \sigma + 2\sin \sigma \right) \Big|_{\sigma_1}^{\sigma_2}$$

The whole volume of a layer that contains all zones of that layer is calculated as:

$$Vwj = \int_{z_1}^{z_2} \pi r^2 dz$$

$$= \int_{z_1}^{z_2} \pi R^2 \cos^2 \sigma \, dz$$

$$= \int_{z_1}^{z_2} \pi R^2 \cos^2 \sigma R \cos \sigma d\sigma \qquad\qquad (5\text{-}13)$$

$$= \frac{1}{3} \pi R^3 \left(\cos^2 \sigma \sin \sigma + 2\sin \sigma \right) \Big|_{\sigma_1}^{\sigma_2}$$

Therefore, the volume for one perimeter zone is calculated as:

$$Vpj = \frac{Vwj - Vcj}{M} = \frac{5}{27M} \pi R^3 \left(\cos^2 \sigma \sin \sigma + 2\sin \sigma \right) \Big|_{\sigma_1}^{\sigma_2} \qquad\qquad (5\text{-}14)$$

5.3 Air Flow between Two Adjacent Zones

The airflow between two adjacent zones can be classified into four types (Figure 5-3): (1)

the air flow between two perimeter zones of adjacent layers, (2) the air flow between two central zones of adjacent layers, (3) the air flow between a perimeter zone and a central zone of the same layer, and (4) the air flow between two perimeter zones of the same layer.
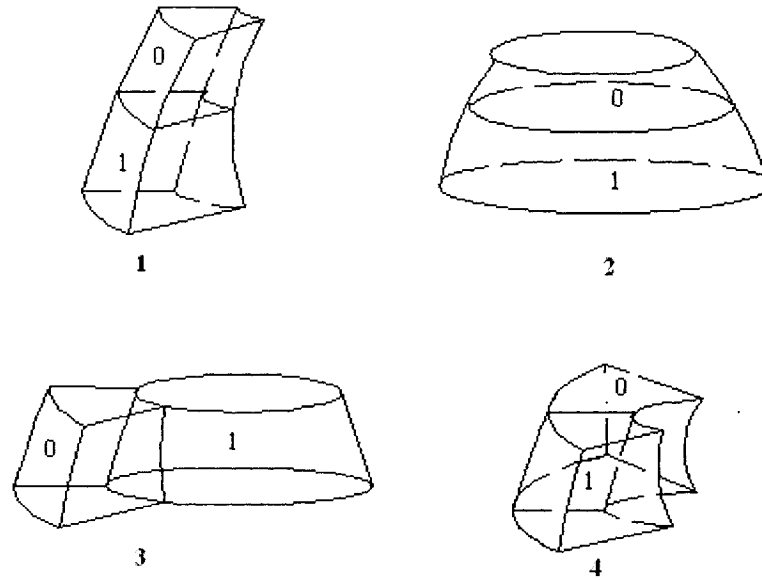
Figure 5-3 Types of adjacent zones

The mass flow rate crossing the boundary of two adjacent zones of the same layer is expressed as follows (Inard et al., 1996; Wurtz et al., 1999; Haghighat et al., 2001):

$$\dot{m}_{ij} = \varepsilon_{f,ij} C_d \rho_j A_{z,ij} \left| P_j - P_i \right|^n \qquad (5\text{-}15)$$

where:

$\dot{m}_{ij}$ =airflow rate between zones i and j, kg/s;

$\varepsilon_{f,ij}$ =±1 gives the sign of flow direction (e.g., $\varepsilon_{f,ij}$ =1 if P_j is greater than P_i, that is the

flow direction is from j to i);

C_d=discharge coefficient, taken as 0.83 (Wurtz et al., 1999; Haghighat et al., 2001);

n =coefficient for the flow type, n=1.0 by assuming a laminar flow;

ρ_j =density of the outflow air that is calculated in terms of air temperature of zone j, kg/m^3;

$A_{z,ij}$=boundary surface area.

The mass flow rate crossing the horizontal boundary of two adjacent zones i and j is expressed by (Inard et al., 1996; Wurtz et al., 1999; Haghighat et al., 2001):

$$\dot{m}_{ij} = \varepsilon_{f,ij} C_d \rho_j A_{z,ij} \left| P_j - P_i - \frac{1}{2}\left(\rho_i gH_i + \rho_j gH_j\right) \right|^n \qquad (5\text{-}16)$$

where:

H=height of the zone, m.

5.4 Infiltration/Exfiltration

The infiltration/exfiltration through the dome cover and the walls of the house is calculated by the power law (ASHRAE, 2001a):

$$Q_f = c(\Delta p)^n \qquad (5\text{-}17)$$

where:

Q_f=airflow rate, m^3/s;

c=flow coefficient, $m^3/(s \cdot Pa^n)$;

n =pressure exponent, dimensionless.

By using the effective leakage area, equation (5-17) can be written as follows (ASHRAE, 20001a):

$$\dot{m}_a = \rho \frac{C_d A_L}{10000} \sqrt{\frac{2}{\rho}} (\Delta p_r)^{0.5-n} |(\Delta p)|^n \qquad (5\text{-}18)$$

where:

$\dot{m}_a$ =mass flow rate, kg/s;

C_d=1.0;

A_L=effective leakage area, 1.0 cm^2/m^2 (ASHRAE, 20001a);

n=0.65;

Δp_r =reference pressure difference, 4 Pa;

Δp=difference between the wind pressure over the cell surface and the associated zone (in the case of air infiltration/exfiltration through the dome cover), or the pressure difference between zone and the air pressure inside the house, and the near zone inside the dome (in the case of air exfiltration through the house walls), Pa.

The infiltration/exfiltration through the first layer dome surface is written as:

$$m_{a,d}^{\cdot} = \rho \frac{C_d A_L}{10000} \sqrt{\frac{2}{\rho}} (\Delta p_r)^{0.5-n} |(p_w - p_i)|^n \qquad (5-19)$$

where:

p_i=zone air pressure, Pa

The infiltration/exfiltration through the top of the dome surface is written as:

$$m_{a,e}^{\cdot} = \rho \frac{C_d A_L}{10000} \sqrt{\frac{2}{\rho}} (\Delta p_r)^{0.5-n} |(p_w - p_i - \rho_0 gH + 0.5\rho_i gH_{13})|^n \qquad (5-20)$$

where:

H=height of the dome, m;

ρ_0=density of the outdoor air, kg/m^3;

H_{13}=height of the top layer (Figure 5-4), m.
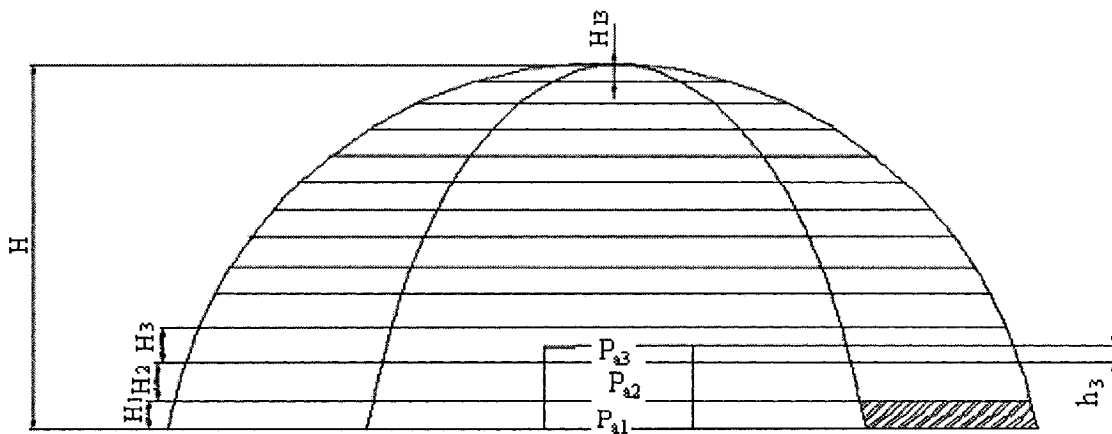
Figure 5-4 Geometry of each layer

The infiltration/exfiltration airflow rates are calculated only for the first layer and the top

of the dome, because the infiltration/exfiltration is supposed to be located at this level. The pressure difference between the air inside the dome and the wind pressure determine the air flow direction.

For the infiltration/exfiltration through the external surfaces of the house, the following formulas are applied, with

$$\dot{m}_{a,h} = \rho \frac{C_d A_L}{10000} \sqrt{\frac{2}{\rho}} (\Delta p_r)^{0.5-n} |p_i - p_{ai}|^n \text{ (for the first two layers inside the dome)} \quad (5\text{-}21)$$

where:

p_{ai}=room air pressure at the mid-height of the ith layer, Pa.

and

$$\dot{m}_{a,h} = \rho \frac{C_d A_L}{10000} \sqrt{\frac{2}{\rho}} (\Delta p_r)^{0.5-n} |p_i - p_{a3} + 0.5(\rho_{a3} + \rho_i)g(H_3 - h_3)|^n \text{ (for the third layer inside}$$

the dome)   (5-22)

where:

H_3=height of the third layer of the air (Figure 5-4), m;

h_3=height of the third layer inside the room (Figure 5-4), m.

5.5 Energy and Mass Balance Equation

5.5.1 General Informulation

The mass balance of zone i is written as:

$$\sum_{i=1}^{n} \dot{m}_{ij} + \dot{m}_{source} + \dot{m}_{sink} = 0 \qquad (5\text{-}23)$$

where:

$\dot{m}_{ij}$ =mass flow rate from zone i to zone j, kg/s;

$\dot{m}_{source}$ = mass flow rate supplied by the source in zone, kg/s;

$\dot{m}_{sink}$ =mass flow rate removed from zone, kg/s.

The energy balance of zone i is written as:

$$\frac{dEn_i}{dt} = \sum_{i=1}^{n} \dot{En}_{ij} + \dot{En}_{source} + \dot{En}_{sink} \qquad (5\text{-}24)$$

where:

En_i =energy in zone i, J;

$\dot{En}_{ij}$ =rate of energy transfer from zone i to zone j, W;

$\dot{En}_{source}$ =rate of energy supplied by the source in zone, W;

$\dot{En}_{sink}$ =rate of energy removed from zone, W;

t=time, s.

If the perimeter zone, which is adjacent to cell (i,j), is called zone (i,j), and the central zone of the same layer is called zone (M+1,j), the equation for energy transfer through the glazing that enters the zone (i,j) is:

$$\dot{En}_{source} = h_{i,j} A_{f,i,j} \left(T_{i,j} - T_{d,i,j} \right)$$ (5-25)

where:

$h_{i,j}$=convective coefficient over the air-to-solid interface, $W/m^2 \cdot °C$;

$T_{i,j}$=temperature of the cell(i,j), °C;

$A_{f,i,j}$=air-to-solid interface, equal to the area of the cell (i,j), m^2;

$T_{d,i,j}$=temperature of the perimeter zone adjacent to the cell (i,j), °C.

The equation for the heat transfer between the wall/roof surface and the central zone (i=M+1) is written as:

$$\dot{En}_{source} = \sum_{i=1}^{Number \ of \ wall \ surfaces} h_{in} A_{wi} \left(T_{wi} - T_{d,M+1,j} \right)$$ (5-26)

where:

A_{wi}=air-solid interface area, m^2;

$T_{d,M+1,j}$=temperature of the central zone of the jth layer, °C.

T_{wi}=temperature of a wall, °C.

5.5.2 Mass Balance Equation for Perimeter Zones of the 1st Layer

The mass balance equation for the perimeter zones (i,1) (Figure 5-5) of the first layer is written as:

$$\dot{m}_{a,d} + \dot{m}_{i+1,1-i,1} + \dot{m}_{i-1,1-i,1} + \dot{m}_{i,2-i,1} + \dot{m}_{M+1,1-i,1} = 0$$ (5-27)

where:

$\dot{m}_{i1,j1-i2,j2}$ =mass flow rate from zone (i1, j1) to zone (i2, j2), kg/s.
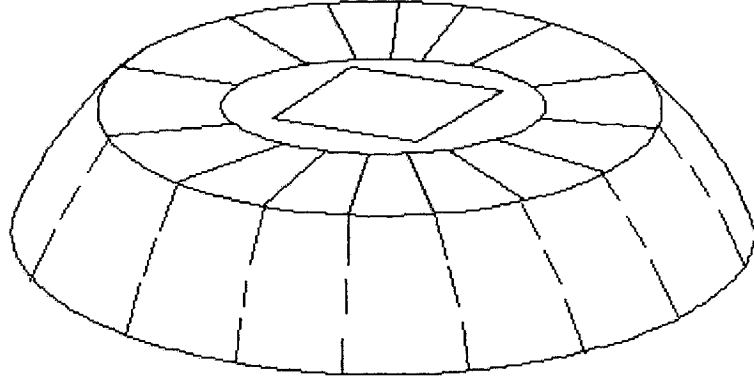
Figure 5-5 First layer of the zonal model

5.5.3 Energy Balance Equation for Perimeter Zones of the 1ˢᵗ Layer

The energy balance for the perimeter zones of the first layer (Figure 5-6) is written as:

$$
h_{i,1}A_{f,i,1}\left(T_{i,1} - T_{d,i,1}\right) + h_{i,g}A_{f,i,g}\left(T_{g,in,1} - T_{d,i,1}\right) + c_p \dot{m}_{i+1,1-i,1}\left(T_{d,i+1,1} - T_{d,i,1}\right)
$$

$$
+ c_p \dot{m}_{i-1,1-i,1}\left(T_{d,i-1,1} - T_{d,i,1}\right) + c_p \dot{m}_{a,d}\left(T_o - T_{d,i,1}\right) + c_p \dot{m}_{i,2-i,1}\left(T_{d,i,2} - T_{d,i,1}\right)
$$

$$
+ c_p \dot{m}_{M+1,1-i,1}\left(T_{d,M+1,1} - T_{d,i,1}\right) = \rho_{i,1}V_{i,1}c_p \frac{dT_{d,i,1}}{dt}
$$

(5-28)

where:

T$_g$=ground surface temperature inside the dome, °C;

A$_{f,i,1}$ and A$_{f,i,g}$=cell-air interface area and ground-air interface area, respectively, m²;

T$_o$=outdoor air temperature, °C;

T$_{i,1}$=temperature of the cell (i,1), °C;

115

$T_{d,i,1}$=zone air temperature; i=1 to M refers to perimeter zones, and i=M+1 refers to the center zones, °C;

$\dot{m}_{i+1,1-i,1}$=mass flow rate between zone (i+1,1) and zone (i,1), kg/s.

5.5.4 Mass Balance Equation for the Central Zone of the 1st Layer

The mass balance for the central zone (Figure 5-6) of the first layer is written as:

$$\sum_{i=1,M} \dot{m}_{i,1-M+1,1} + \dot{m}_{M+1,2-M+1,1} + \dot{m}_{a,h} = 0 \qquad (5-29)$$

where:

$\dot{m}_{M+1,2-M+1,1}$=mass flow rate from the central zone of the 2nd layer to the central zone of the 1st layer, kg/s
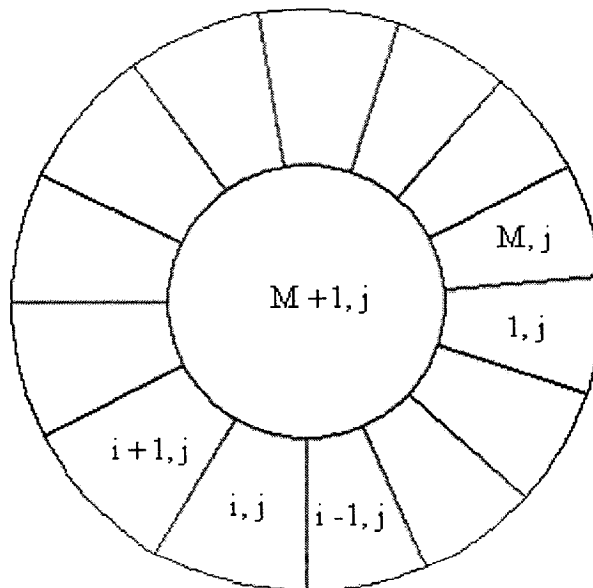
Figure 5-6 Middle layer of the zonal model

5.5.5 Energy Balance Equation for the Central Zone of the 1st Layer

The energy balance for the central zone of the first layer is written as:

$$\sum_{i=1,M} c_p \, \dot{m}_{i,1-M+1,1}\left(T_{d,i,1} - T_{d,M+1,1}\right) + c_p \, \dot{m}_{M+1,2-M+1,1}\left(T_{d,M+1,2} - T_{d,M+1,1}\right) + c_p \, \dot{m}_{a,h}\left(T_a - T_{d,M+1,1}\right)$$

$$+ \sum_{j=1,4} h_{M+1,w,j} A_{f,M+1,w,j}\left(T_{w,j} - T_{d,M+1,1}\right) + h_{M+1,g} A_{f,M+1,g}\left(T_{g,in,1} - T_{d,M+1,1}\right) = \rho_{M+1,1} V_{M+1,1} c_p \frac{dT_{d,M+1,1}}{dt}$$

$$(5-30)$$

where:

$A_{f,M+1,w,j}$ =surface area of the interface between walls/roof and the air inside the dome, m^2;

$T_{w,j}$=wall surface temperature, °C; and j=1,4 refers to the wall surfaces, °C.

5.5.6 Mass Balance Equation for Perimeter Zones of an Intermediate Layer

The mass balance for perimeter zones of an intermediate layer is written as:

$$\dot{m}_{i+1,j-i,j} + \dot{m}_{i-1,j-i,j} + \dot{m}_{i,j+1-i,j} + \dot{m}_{i,j-1-i,j} + \dot{m}_{M+1,j-i,j} = 0 \qquad (5-31)$$

5.5.7 Energy Balance Equation for Perimeter Zones of an Intermediate Layer

The energy balance for perimeter zones of an intermediate layer is written as:

$$h_{i,j} A_{f,i,j}\left(T_{i,j} - T_{d,i,j}\right) + c_p \, \dot{m}_{i+1,j-i,j}\left(T_{d,i+1,j} - T_{d,i,j}\right) + c_p \, \dot{m}_{i-1,j-i,j}\left(T_{d,i-1,j} - T_{d,i,j}\right)$$

$$+ c_p \, \dot{m}_{i,j+1-i,j}\left(T_{d,i,j+1} - T_{d,i,j}\right) + c_p \, \dot{m}_{i,j-1-i,j}\left(T_{d,i,j-1} - T_{d,i,j}\right) \qquad (5-32)$$

$$+ c_p \, \dot{m}_{M+1,j-i,j}\left(T_{d,M+1,j} - T_{d,i,j}\right) = c_p \rho_{i,j} V_{i,j} \frac{dT_{d,i,j}}{dt}$$

5.5.8 Mass Balance Equation for Central Zone of an Intermediate Layer

The mass balance for the central zones of an intermediate layer is written as:

$$\sum_{i=1,M} \dot{m}_{i,j-M+1,j} + \dot{m}_{M+1,j+1-M+1,j} + \dot{m}_{M+1,j-1-M+1,j} = 0 \tag{5-33}$$

5.5.9 Energy Balance Equation for Central Zone of an Intermediate Layer

The energy balance for central zone of an intermediate layer is written as:

$$\sum_{i=1,M} c_p \, \dot{m}_{i,j-M+1,j}\left(T_{d,i,j} - T_{d,M+1,j}\right) + c_p \, \dot{m}_{M+1,j+1-M+1,j}\left(T_{d,M+1,j+1} - T_{d,M+1,j}\right)$$

$$+ c_p \, \dot{m}_{M+1,j-1-M+1,j}\left(T_{d,M+1,j-1} - T_{d,M+1,j}\right) = c_p \rho_{M+1,j} V_{M+1,j} \frac{dT_{d,M+1,j}}{dt} \tag{5-34}$$

5.5.10 Mass Balance Equation for Perimeter Zones of the Nth Layer

The mass balance for perimeter zones of the Nth layer (Figure 5-7) is written as:

$$\dot{m}_{i+1,N-i,N} + \dot{m}_{i-1,N-i,N} + \dot{m}_{M+1,N,i,N} + \dot{m}_{i,N-1-i,N} = 0 \tag{5-35}$$
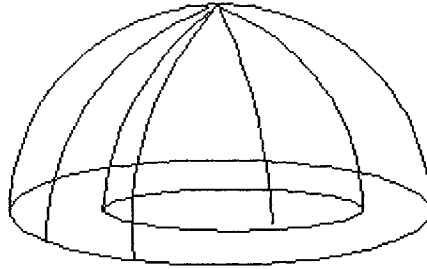
Figure 5-7 The Nth layer of zonal model

5.5.11 Energy Balance Equation for Perimeter Zones of the Nth Layer

The energy balance for perimeter zones of the Nth layer is written as:

$$h_{i,N}A_{f,i,N}\left(T_{i,N} - T_{d,i,N}\right) + c_p \dot{m}_{i+1,N-i,N}\left(T_{d,i+1,N} - T_{d,i,N}\right) + c_p \dot{m}_{i-1,N-i,N}\left(T_{d,i-1,N} - T_{d,i,N}\right)$$

$$+ c_p \dot{m}_{i,N-1-i,N}\left(T_{d,i,N-1} - T_{d,i,N}\right) + c_p \dot{m}_{M+1,N-i,N}\left(T_{d,M+1,N} - T_{d,i,N}\right) = \rho_{i,N}V_{i,N}c_p \frac{dT_{d,i,N}}{dt} \qquad (5\text{-}36)$$

5.5.12 Mass Balance Equation for Central Zone of the Nth Layer

The mass balance for central zone of the Nth layer is written as:

$$\dot{m}_{a,e} + \sum_{i=1,M}\dot{m}_{i,N-M+1,N} + \dot{m}_{M+1,N-1,M+1,N} = 0 \qquad (5\text{-}37)$$

5.5.13 Energy Balance Equation for Central Zone of the Nth Layer

The energy balance for central zone of the Nth layer is written as:

$$c_p \dot{m}_{a,e}\left(T_o - T_{d,M+1,N}\right) + \sum_{i=1,M}c_p \dot{m}_{i,N-M+1,N}\left(T_{d,i,N} - T_{d,M+1,N}\right)$$

$$+ c_p \dot{m}_{M+1,N-1-M+1,N}\left(T_{d,M+1,N-1} - T_{d,M+1,N}\right) = \rho_{M+1,N}V_{M+1,N}c_p \frac{dT_{d,M+1,N}}{dt} \qquad (5\text{-}38)$$

Chapter 6 Numerical Solution of the Mathematical Model

This chapter presents the numerical solution of the mathematical model, including the selection of derivative scheme, the formulation of the system of equations, the initial values of the unknown variables, and the solution algorithm.

6.1 Introduction

The mathematical model presented in Chapters 4 and 5 involves a system of linear and nonlinear equations. Nonlinear equations are generated due to the surface-to-surface long-wave radiation in the thermal model, and due to the coupling of air movement and heat transfer between zones. However, if the radiation coefficients are used to calculate the surface-to-surface radiation, then the whole system for temperatures as unknowns can be considered as quasi-linear. The radiation coefficients can be generated by using the total interchange view factor discussed in Chapter 4. The system of equations can then be broken into two sub-systems—one containing the unknown temperatures and one containing the unknown pressures, and the two sub-systems can be solved using the coupling method.

This chapter also presents the rearrangement of the equations for the calculation of unknown variables, the selection of guess values, solution algorithm and calculation procedure.

6.2 Selection of Derivative Scheme

The use of truncated Taylor series expansion leads to different approaches of derivatives. Care has to be taken in choosing a scheme for a specific simulation problem, since some schemes do have higher order of accuracy but cannot pass the condition of stability or can only be used with relative limited time and space steps. The explicit scheme is known to be convergent and stable only for a small time step. The convergence means that as δt approaches zero, the results approach the true solution, and the stability means that errors at any stage of the computation are not amplified but are attenuated as the computation progresses (Isaacson and Keller, 1996). The implicit scheme is unconditionally stable and therefore allows a longer time step to be used, but it has the limitations that the approximation is first-order accurate, and it always requires the solution of a set of equations. The Crank-Nicolson scheme is a semi-implicit scheme, which is second-order accurate but can allow for a longer time step than the explicit scheme. Since the program will use one hour as the time step, the implicit scheme is used for all equations.

6.3 Formulation of the System of Equations

The inside convective coefficients of the dome cover are calculated based on the updated air temperature difference, air flow direction and air velocity, tilted angle of the surface, and the radiation coefficients calculated using the total interchange view factor and the updated surface temperature difference.

The temperature of the dome cells, the temperature of the ground inside the dome, and the outside surfaces of the house (walls/roof) are presented as $T_{I,out}$ in some of the

following equation. Temperature of cell (i,j), and temperature of the cells adjacent to cell (i,j), are presented as: $T_{i,j}$, $T_{i-1,j}$, $T_{i+1,j}$, $T_{i,j-1}$ and $T_{i,j+1}$.

Under the implicit scheme and assuming the specific heat is constant, the heat balance equation at the surface of each cell (i,j) (equation 4-67) is written as follows:

$$
\left(\frac{m_{ij} \cdot c_p}{A_{ij} \cdot \Delta t} + h_o + h_{in} + h_{r,ij,sky} + h_{r,ij,g,out} + \sum_{l=1,N\cdot M+9} h_{r,ij,l,out} \atop \frac{k \cdot d \cdot l_1}{A_{ij}} + \frac{k \cdot d \cdot l_2}{A_{ij}} + \frac{k \cdot d \cdot l_3}{A_{ij}} + \frac{k \cdot d \cdot l_4}{A_{ij}} \right) \cdot T_{i,j,t+1} -
$$

$$
\left(h_{in} \cdot T_{in,t+1} + \sum_{l=1,N\cdot M+9} h_{r,ij,l,out} \cdot T_{l,out,t+1} + \frac{k \cdot d \cdot l_1}{A_{ij}} \cdot T_{i+1,j,t+1} + \frac{k \cdot d \cdot l_2}{A_{ij}} \cdot T_{i-1,j,t+1} + \frac{k \cdot d \cdot l_3}{A_{ij}} \cdot T_{i,j+1,t+1} + \frac{k \cdot d \cdot l_4}{A_{ij}} \cdot T_{i,j-1,t+1} \right) \tag{6-1}
$$

$$
= \frac{m_{ij} \cdot c_p}{A_{ij} \cdot \Delta t} \cdot T_{i,j,t} + q_{sol,ij,t} + h_o \cdot T_{o,t+1} + h_{r,ij,sky} \cdot T_{sky,t+1} + h_{r,ij,g,out} \cdot T_{g,out,t+1}
$$

When the thermal model uses results from the air flow model, $T_{in,t+1}$ is replaced by the corresponding $T_{d,i,j,t+1}$, which is the air temperature of the air zone adjacent to cell (i,j).

The heat balance equation of the air inside the dome (equation 4-77) is written as:

$$\left(\frac{m_{in} c_p}{\Delta t} + \sum_{\substack{i=1,M \\ j=1,N}} h_{in} A_{ij} + h_{in} A_g + \rho V_{inf} c_p + \rho V_{exf} c_p + \sum_{l=1,8} h_{in} A_l \right) T_{in,t+1}$$

$$- \left(\sum_{\substack{i=1,M \\ j=1,N}} h_{in} A_{ij} T_{i,j,t+1} + h_{in} A_g T_{g,in,1,t+1} + \sum_{l=1,8} h_{in} A_l T_{l,t+1} \right) \tag{6-2}$$

$$= \frac{m_{in} c_p}{\Delta t} T_{in,t} + \rho V_{inf} c_p T_{o,t+1} + \rho V_{exf} c_p T_a$$

This equation is applied only to the single-node model.

The heat balance equation at the outside surface of walls/roof (equation 4-85) is written as:

$$\left(h_{in,1,out} + \sum_{\substack{j=1 \\ j \neq l}}^{M \cdot N + 9} h_{r,lj,out} + \frac{k_l}{\frac{1}{2} \cdot dx_l} \right) \cdot T_{1,out,t+1} - \frac{k_l}{\frac{1}{2} \cdot dx_l} \cdot T_{1,2,t+1} - h_{in,1,out} \cdot T_{in,t+1}$$

$$- \sum_{\substack{j=1 \\ j \neq l}}^{M \cdot N + 9} h_{r,lj,out} \cdot T_{j,t+1} = \rho_1 \cdot \frac{1}{4} \cdot dx_1 \cdot c_{pl} \cdot \frac{T_{1,out,t}}{dt} + q_{sol,1,out,t+1} \tag{6-3}$$

The heat balance equation for the internal node of the 1st layer of the exterior walls/roof of the house (equation 4-78) is:

$$\left(1 + 2 \frac{\alpha_{h1} dt}{\left(\frac{1}{2} \cdot dx_1 \right)^2} \right) T_{1,2,t+1} - \frac{\alpha_{h1} dt}{\left(\frac{1}{2} \cdot dx_1 \right)^2} \left(T_{1,out,t+1} + T_{1,3,t+1} \right) = T_{1,2,t} \tag{6-4}$$

The equation for the interface of layers 1 and 2 of the walls/roof of the house (equation 4-86) is written as:

$$\frac{1}{4}\cdot\left(\rho_1\cdot c_{p1}\cdot dx_1 + \rho_2\cdot c_{p2}\cdot dx_2\right)\cdot\frac{T_{1,3,t+1}-T_{1,3,t}}{dt} = k_1\cdot\frac{T_{1,2,t+1}-T_{1,3,t+1}}{\frac{1}{2}\cdot dx_1} + k_2\cdot\frac{T_{1,4,t+1}-T_{1,3,t+1}}{\frac{1}{2}\cdot dx_2}$$

(6-5)

where:

dx_1=thickness of layer 1, m;

dx_2=thickness of layer 2, m.

The above equation is reorganized as:

$$\left(1+\frac{\frac{k_1}{dx_1}+\frac{k_2}{dx_2}}{\frac{\rho_1\cdot c_{p1}dx_1 + \rho_2\cdot c_{p2}dx_2}{2\cdot dt}}\right)\cdot T_{1,3,t+1} - \frac{\frac{k_1}{dx_1}}{\frac{\rho_1\cdot c_{p1}dx_1 + \rho_2\cdot c_{p2}dx_2}{2\cdot dt}}\cdot T_{1,2,t+1}$$

$$-\frac{\frac{k_2}{dx_2}}{\frac{\rho_1\cdot c_{p1}dx_1 + \rho_2\cdot c_{p2}dx_2}{2\cdot dt}}\cdot T_{1,4,t+1} = T_{1,3,t}$$

(6-6)

The equation for other nodes is written as the followings:

$$\left(1+2\frac{\alpha_{h2}dt}{\left(\frac{1}{2}\cdot dx_2\right)^2}\right)T_{1,4,t+1} - \frac{\alpha_{h2}dt}{\left(\frac{1}{2}\cdot dx_2\right)^2}\left(T_{1,3,t+1}+T_{1,5,t+1}\right) = T_{1,4,t}$$

(6-7)

124

$$\left(1+\frac{\dfrac{k_2}{dx_2}+\dfrac{k_3}{dx_3}}{\dfrac{\rho_2\cdot c_{p2}dx_2+\rho_3\cdot c_{p3}dx_3}{2\cdot dt}}\right)\cdot T_{1,5t+1}-\frac{\dfrac{k_2}{dx_2}}{\dfrac{\rho_2\cdot c_{p2}dx_2+\rho_3\cdot c_{p3}dx_3}{2\cdot dt}}\cdot T_{1,4t+1}$$

$$-\frac{\dfrac{k_3}{dx_3}}{\dfrac{\rho_2\cdot c_{p2}dx_2+\rho_3\cdot c_{p3}dx_3}{2\cdot dt}}\cdot T_{1,6t+1}=T_{1,5t} \qquad (6\text{-}8)$$

$$\left(1+2\frac{\alpha_{h3}dt}{\left(\dfrac{1}{2}\cdot dx_3\right)^2}\right)T_{1,6,t+1}-\frac{\alpha_{h3}dt}{\left(\dfrac{1}{2}\cdot dx_3\right)^2}\left(T_{1,5,t+1}+T_{1,7,t+1}\right)=T_{1,6,t} \qquad (6\text{-}9)$$

$$\left(1+\frac{\dfrac{k_3}{dx_3}+\dfrac{k_4}{dx_4}}{\dfrac{\rho_3\cdot c_{p3}\cdot dx_3+\rho_4\cdot c_{p4}\cdot dx_4}{2\cdot dt}}\right)\cdot T_{1,7t+1}-\frac{\dfrac{k_3}{dx_3}}{\dfrac{\rho_3\cdot c_{p3}\cdot dx_3+\rho_4\cdot c_{p4}\cdot dx_4}{2\cdot dt}}T_{1,6t+1}$$

$$-\frac{\dfrac{k_4}{dx_4}}{\dfrac{\rho_3\cdot c_{p3}\cdot dx_3+\rho_4\cdot c_{p4}\cdot dx_4}{2\cdot dt}}T_{1,8t+1}=T_{1,7t} \qquad (6\text{-}10)$$

$$\left(1+2\frac{\alpha_{h4}dt}{\left(\dfrac{1}{2}\cdot dx_4\right)^2}\right)T_{1,8,t+1}-\frac{\alpha_{h4}dt}{\left(\dfrac{1}{2}\cdot dx_4\right)^2}\left(T_{1,7,t+1}+T_{1,9,t+1}\right)=T_{1,8,t} \qquad (6\text{-}11)$$

The heat balance at the inside wall/roof surfaces (equation 4-97) is written as follows:

$$\left(h_a + \sum_{\substack{j=1 \\ j \neq 1}}^{6} h_{r,lj,in} + \rho_4 \cdot \frac{1}{4} \cdot \frac{dx_4}{dt} \cdot c_{p4} + \frac{k_4}{\left(\frac{1}{2} \cdot dx_4 \right)} \right) \cdot T_{l,in,t+1}$$

$$- \sum_{\substack{j=1 \\ j \neq 1}}^{9} h_{r,lj,in} \cdot T_{j,in,t+1} - \frac{k_4}{\left(\frac{1}{2} \cdot dx_4 \right)} \cdot T_{1,8,t+1} = \rho_4 \cdot \frac{1}{4} dx_4 \cdot c_{p4} \cdot \frac{T_{l,in,t}}{dt} + q_{sol,l,in} + q_{rad,ihg} + h_a \cdot T_a$$

(6-12)

Substituting equation (4-98) to equation (4-100), (4-101), and the heat balance equations for the inside and outside window surfaces are written as:

$$h_{win,o} T_{os,t+1} + \left(U_w - h_{win,o} \right) T_{in,t+1} = T_a \tag{6-13}$$

$$T_{in,t+1} - h_{win,in} T_{is,t+1} = \left(U_w - h_{win,in} \right) T_a \tag{6-14}$$

When combined with the air flow model, $T_{in,t+1}$ is the air temperature of the air zone adjacent to the window.

The heat balance equation at the ground surface inside the dome (equation 4-116), is written as follows:

$$\left(\rho \cdot c_p \cdot \frac{dx}{2 \cdot dt} + \frac{k}{dx} + h_{in,g} + \sum_{\substack{i=1 \\ i \neq g}}^{M \cdot N+9} h_{r,ig} \right) \cdot T_{g,in,1,t+1} -$$

(6-15)

$$\left(\frac{k}{dx} \cdot T_{g,in,2,t+1} + h_{in,g} \cdot T_{in,t+1} + \sum_{\substack{i=1 \\ i \neq g}}^{M \cdot N+9} h_{r,ig} \cdot T_{i,t+1} \right) = \rho \cdot c_p \cdot \frac{dx}{2dt} \cdot T_{g,in,1,t} + q_{sol,t+1}$$

When combined with the air flow model, $T_{in,t+1}$ is the air temperature of the air zone

adjacent to the ground surface inside the dome.

The following equations can be derided based on the discretion of equation (4-106), for each internal node of the ground inside the dome:

$$\left(1 + 2\alpha_s \frac{dt}{dx^2}\right)T_{g,in,2,t+1} - \alpha_s \frac{dt}{dx^2}\left(T_{g,in,1,t+1} + T_{g,in,3,t+1}\right) = T_{g,in,2,t} \qquad (6\text{-}16)$$

$$\left(1 + 2\alpha_s \frac{dt}{dx^2}\right)T_{g,in,3,t+1} - \alpha_s \frac{dt}{dx^2}\left(T_{g,in,2,t+1} + T_{g,in,4,t+1}\right) = T_{g,in,3,t} \qquad (6\text{-}17)$$

$$\left(1 + 2\alpha_s \frac{dt}{dx^2}\right)T_{g,in,4,t+1} - \alpha_s \frac{dt}{dx^2}\left(T_{g,in,3,t+1} + T_{g,in,5,t+1}\right) = T_{g,in,4,t} \qquad (6\text{-}18)$$

$$\left(1 + 2\alpha \frac{dt}{dx^2}\right)T_{g,in,5,t+1} - \alpha \frac{dt}{dx^2}\left(T_{g,in,4,t+1} + T_{g,in,6,t+1}\right) = T_{g,in,5,t} \qquad (6\text{-}19)$$

$$\left(1 + 2\alpha_s \frac{dt}{dx^2}\right)T_{g,in,6,t+1} - \alpha_s \frac{dt}{dx^2}\left(T_{g,in,5,t+1} + T_{g,in,7,t+1}\right) = T_{g,in,6,t} \qquad (6\text{-}20)$$

$$\left(1 + 2\alpha_s \frac{dt}{dx^2}\right)T_{g,in,7,t+1} - \alpha_s \frac{dt}{dx^2}\left(T_{g,in,6,t+1} + T_{g,in,8,t+1}\right) = T_{g,in,7,t} \qquad (6\text{-}21)$$

$$\left(1 + 2\alpha_s \frac{dt}{dx^2}\right)T_{g,in,8,t+1} - \alpha_s \frac{dt}{dx^2}\left(T_{g,in,7,t+1} + T_{g,in,9,t+1}\right) = T_{g,in,8,t} \qquad (6\text{-}22)$$

$$\left(1 + 2\alpha_s \frac{dt}{dx^2}\right)T_{g,in,9,t+1} - \alpha_s \frac{dt}{dx^2}\left(T_{g,in,8,t+1} + T_{g,in,10,t+1}\right) = T_{g,in,9,t} \qquad (6\text{-}23)$$

The ground temperature ($T_{g,in,10}$) at the depth of 1.0 m, can be calculated from equation

127

(4-117) or as follows:

$$T_{g,in,10} = T_{ms} + A_s \cdot e^{-10 \cdot dx \cdot \sqrt{\pi / \alpha_s \cdot \tau_0}} \sin\left[\frac{2\pi \cdot (n_d - n_{lag})}{\tau_0} - 10 \cdot dx \cdot \sqrt{\frac{\pi}{\alpha_s \cdot \tau_0}}\right] \tag{6-24}$$

The equations for the internal nodes used in the analysis of the floor of the house, based on equation (4-118) are similar to equation (6-4):

$$\left(1 + 2\frac{\alpha_{fl} dt}{\left(\frac{1}{2} \cdot dx_1\right)^2}\right) T_{f,2,t+1} - \frac{\alpha_{fl} dt}{\left(\frac{1}{2} \cdot dx_1\right)^2}\left(T_{f,1,t+1} + T_{f,3,t+1}\right) = T_{f,2,t} \tag{6-25}$$

$$\left(1 + 2\frac{\alpha_{fl} dt}{\left(\frac{1}{2} \cdot dx_1\right)^2}\right) T_{f,4,t+1} - \frac{\alpha_{fl} dt}{\left(\frac{1}{2} \cdot dx_1\right)^2}\left(T_{f,3,t+1} + T_{f,5,t+1}\right) = T_{f,4,t} \tag{6-26}$$

The heat balance equation at the floor surface (equation 4-124) is written as follows:

$$\left(h_a + \sum_{\substack{j=1 \\ j \neq f}}^{9} h_{r,jf} + \rho_1 \cdot \frac{1}{4} \cdot \frac{dx_1}{dt} \cdot c_{p1} + \frac{k_1}{\left(\frac{1}{2} \cdot dx_1\right)}\right) \cdot T_{f,1,t+1}$$

$$-\sum_{\substack{j=1 \\ j \neq f}}^{9} h_{r,jf} \cdot T_{j,in,t+1} - \frac{k_1}{\left(\frac{1}{2} \cdot dx_1\right)} T_{f,2,t+1} = \rho_1 \cdot \frac{1}{4} dx_1 \cdot c_{p1} \cdot \frac{T_{f,t}}{dt} + q_{sol,1,in} + q_{rad,ihg} + h_a T_a \tag{6-27}$$

The heat balance equation for the internal nodes between two layers of the floor (equation 4-125) is discretized and rewritten the same way as equation (6-6):

$$\left(1+\frac{\dfrac{k_1}{dx_1}+\dfrac{k_2}{dx_2}}{\dfrac{\rho_1\cdot c_{p1}\cdot dx_1+\rho_2\cdot c_{p2}\cdot dx_2}{2\cdot dt}}\right)\cdot T_{1,3,t+1}-\frac{\dfrac{k_1}{dx_1}}{\dfrac{\rho_1\cdot c_{p1}\cdot dx_1+\rho_2\cdot c_{p2}\cdot dx_2}{2\cdot dt}}\cdot T_{1,2,t+1}$$

$$-\frac{\dfrac{k_2}{dx_2}}{\dfrac{\rho_1\cdot c_{p1}\cdot dx_1+\rho_2\cdot c_{p2}\cdot dx_2}{2\cdot dt}}\cdot T_{1,4,t+1}=T_{1,3,t} \qquad (6\text{-}28)$$

The energy balance for the perimeter zones of the first layer (equation 5-28) is written as:

$$\left(\rho_{i,1}V_{i,1}c_p+h_{f,i,1}A_{f,i,1}+h_{i,g}A_{f,i,g}+c_p\,\dot m_{i+1,1-i,1}+c_p\,\dot m_{i-1,1-i,1}\atop +c_p\,\dot m_{a,d}+c_p\,\dot m_{i,2-i,1}+c_p\,\dot m_{M+1,1-i,1}\right)T_{d,i,1,t+1}$$

$$-\left(h_{i,1}A_{f,i,1}T_{i,1,t+1}+c_p\,\dot m_{i+1,1-i,1}\,T_{d,i+1,1,t+1}+c_p\,\dot m_{i-1,1-i,1}\,T_{d,i-1,1,t+1}\atop +c_p\,\dot m_{i,2-i,1}\,T_{d,i,2,t+1}+c_p\,\dot m_{M+1,1-i,1}\,T_{d,M+1,1,t+1}+h_{i,g}A_{f,i,g}T_{g,in,t+1}\right) \qquad (6\text{-}29)$$

$$=\rho_{i,1}V_{i,1}c_pT_{d,i,1,t}+c_p\,\dot m_{a,d}\,T_{o,t+1}$$

The energy balance for the central zone of the first layer (equation 5-30) is written as:

$$\left(\rho_{M+1,1}V_{M+1,1}c_p+\sum_{i=1,M}c_p\,\dot m_{i,1-M+1,1}+c_p\,\dot m_{M+1,2-M+1,1}\atop +h_{M+1,g}A_{f,M+1,g}+\sum_{j=1,4}h_{M+1,w,j}A_{f,M+1,w,j}+c_p\,\dot m_{a,h}\right)T_{d,M+1,1,t+1}$$

$$-\left(\sum_{i=1,M}c_p\,\dot m_{i,1-M+1,1}\,T_{d,i,1,t+1}+c_p\,\dot m_{M+1,2-M+1,1}\,T_{d,M+1,2,t+1}\atop +h_{M+1,g}A_{f,M+1,g}T_{g,in,t+1}+\sum_{j=1,4}h_{M+1,w,j}A_{f,M+1,w,j}T_{w,j,t+1}\right) \qquad (6\text{-}30)$$

$$=\rho_{M+1,1}V_{M+1,1}c_pT_{d,M+1,1,t}+c_p\,\dot m_{a,h}\,T_a$$

The energy balance for perimeter zones of an intermediate layer (equation 5-32) is

written as:

$$\left(\begin{array}{l} c_p \rho_{i,j} V_{i,j} + h_{i,j} A_{f,i,j} + c_p \dot{m}_{i+1,j-i,j} + c_p \dot{m}_{i-1,j-i,j} \\ + c_p \dot{m}_{i,j+1-i,j} + c_p \dot{m}_{i,j-1-i,j} + c_p \dot{m}_{M+1,j-i,j} \end{array} \right) T_{d,i,j,t+1}$$

$$- \left(\begin{array}{l} h_{i,j} A_{f,i,j} T_{i,j,t+1} + c_p \dot{m}_{i+1,j-i,j} T_{d,i+1,j,t+1} + c_p \dot{m}_{i-1,j-i,j} T_{d,i-1,j,t+1} \\ + c_p \dot{m}_{i,j+1-i,j} T_{d,i,j+1,t+1} + c_p \dot{m}_{i,j-1-i,j} T_{d,i,j-1,t+1} + c_p \dot{m}_{M+1,j-i,j} T_{d,M+1,j,t+1} \end{array} \right) = c_p \rho_{i,j} V_{i,j} T_{d,i,j,t}$$

(6-31)

The energy balance for central zone of an intermediate layer (equation 5-34) is written as:

$$\left(c_p \rho_{M+1,j} V_{M+1,j} + \sum_{i=1,M} c_p \dot{m}_{i,j-M+1,j} + c_p \dot{m}_{M+1,j+1-M+1,j} + c_p \dot{m}_{M+1,j-1-M+1,j} \right) T_{d,M+1,j,t+1} -$$

$$\left(\sum_{i=1,M} c_p \dot{m}_{i,j-M+1,j} T_{d,i,j,t+1} + c_p \dot{m}_{M+1,j+1-M+1,j} T_{d,M+1,j+1,t+1} + c_p \dot{m}_{M+1,j-1-M+1,j} T_{d,M+1,j-1,t+1} \right)$$

$$= c_p \rho_{M+1,j} V_{M+1,j} T_{d,M+1,j,t}$$

(6-32)

The energy balance for perimeter zones of the Nth layer (equation 5-36) is written as:

$$\left(\rho_{i,N} V_{i,N} c_p + h_{i,N} A_{f,i,N} + c_p \dot{m}_{i+1,N-i,N} + c_p \dot{m}_{i-1,N-i,N} + c_p \dot{m}_{i,N-1-i,N} + c_p \dot{m}_{M+1,N-i,N} \right) T_{d,i,N,t+1}$$

$$- \left(\begin{array}{l} h_{i,N} A_{i,N} T_{i,N,t+1} + c_p \dot{m}_{i+1,N-i,N} T_{d,i+1,N,t+1} + c_p \dot{m}_{i-1,N-i,N} T_{d,i-1,N,t+1} \\ + c_p \dot{m}_{i,N-1-i,N} T_{d,i,N-1,t+1} c_p \dot{m}_{M+1,N-i,N} T_{d,M+1,N,t+1} \end{array} \right) = \rho_{i,N} V_{i,N} c_p T_{d,i,N,t}$$

(6-33)

The energy balance for central zone of the Nth layer (equation 5-38) is written as:

$$\left(\rho_{M+1,N} V_{M+1,N} c_p + c_p \dot{m}_{a,e} + \sum_{i=1,M} c_p \dot{m}_{i,N-M+1,N} + c_p \dot{m}_{M+1,N-1-M+1,N} \right) T_{d,M+1,N,t+1}$$

$$- \left(\sum_{i=1,M} c_p \dot{m}_{i,N-M+1,N} T_{d,i,N,t+1} + c_p \dot{m}_{M+1,N-1-M+1,N} T_{d,M+1,N-1,t+1} \right) \qquad (6\text{-}34)$$

$$= \rho_{M+1,1} V_{M+1,1} c_p T_{d,M+1,N,t} + c_p \dot{m}_{a,e} T_{o,t+1}$$

Those equations must be solved together with equations (5-27, 5-29, 5-31, 5-33, 5-35 and 5-37) to obtain the values for the temperature and pressure.

The heating/cooling load of the house, based on equation (4-102), is written as follows:

$$Q_{HVAC,t} = -\sum_{j=1}^{9} A_j h_a \left(T_{j,in,t} - T_a \right) - Q_{exf,t} - Q_{internal,conv,t} \qquad (6\text{-}35)$$

6.4 Form of the Matrix

The system of equations coupling the thermal balance model and airflow model are written as the follows:

$$\begin{bmatrix} A & O \\ O & C \end{bmatrix} \begin{bmatrix} T \\ P \end{bmatrix} = \begin{bmatrix} B \\ D \end{bmatrix} \qquad (6\text{-}36)$$

where A is the matrix containing the thermal and optical properties of the system. C is the matrix containing the interface properties between zones. B and D are the driving forces for the temperature and pressure, respectively. The driving forces for the pressure are related to the zone air temperature and zone height.

Figure 6-1 presents the form of the pressure matrix where l_1 represents the first layer, l_n represents a middle layer and l_N represents the top layer. Figure 6-2 presents the form of

the temperature matrix. Due to space limit, only four cells are presented for the dome glazing, and only four nodes are presented for each wall/roof/ground. The windows and floor are not shown in the matrix, and only three layers are presented for the pressure matrix.

```
          l₁              lₙ              l_N
    ┌                                              ┐
    │ ⎡ X  X      X  X  X                          │
    │ │ X  X  X      X      X                       │
  l₁⎨ │ X  X  X  X         X                        │
    │ │ X     X  X  X            X                  │
    │ ⎣ X  X  X  X  X                  X             │
    │ ⎡ X            X  X      X  X                 │
    │ │    X         X  X  X      X  X              │
  lₙ⎨ │       X      X  X  X  X      X              │
    │ │          X   X  X  X  X            X        │
    │ ⎣          X  X  X  X  X  X                  X │
    │    ⎡          X         X  X      X  X        │
    │    │          X         X  X  X         X     │
  l_N⎨   │             X      X  X  X  X           │
    │    │                X   X      X  X  X        │
    │    ⎣                   X  X  X  X  X  X       │
    └                                              ┘
```
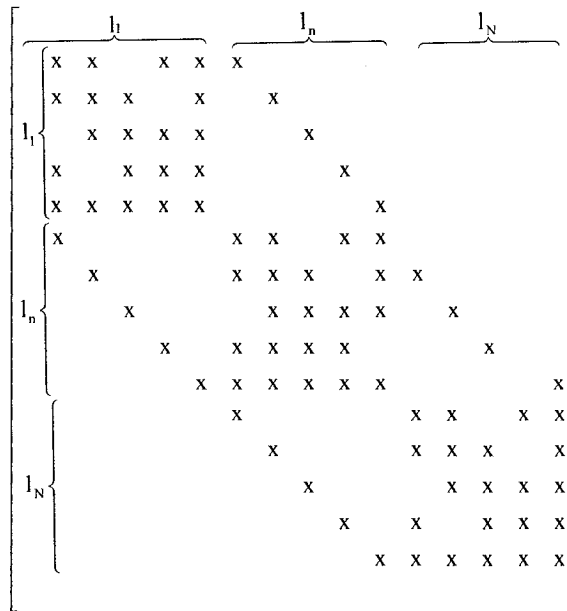
Figure 6-1 Form of matrix C

132
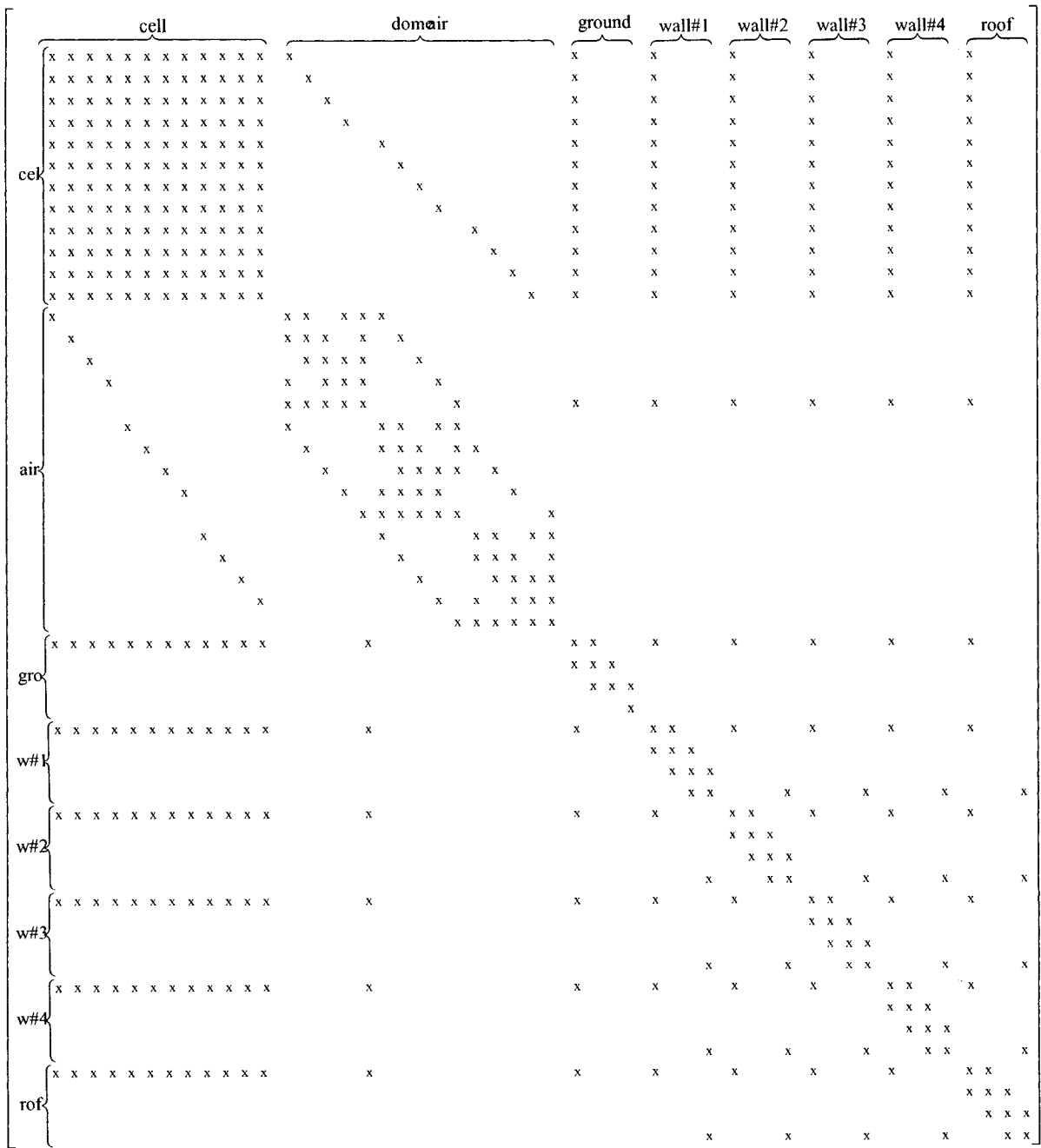
Figure 6-2 Form of matrix **A**

The variables of the system are listed as follows:

$T_1,...,T_{M\cdot N}$ =surface temperature of M·N cells of the dome glazing, previously expressed

as $T_{i,j}$, °C

$T_{M \cdot N+1}, \cdots, T_{M \cdot N+1+(M+1) \cdot N}$ =air temperature inside the dome, previously expressed as $T_{d,i,j}$, °C

$T_{M \cdot N+2+(M+1) \cdot N}, \ldots, T_{M \cdot N+11+(M+1) \cdot N}$ =ground temperature inside the dome, °C

$T_{M \cdot N+12+(M+1) \cdot N}, \ldots, T_{M \cdot N+56+(M+1) \cdot N}$ =wall/roof temperature, °C

$T_{M \cdot N+57+(M+1) \cdot N}, \ldots, T_{M \cdot N+62+(M+1) \cdot N}$ =window surface temperature, °C

$T_{M \cdot N+62+(M+1) \cdot N+1}, \ldots, T_{M \cdot N+62+(M+1) \cdot N+5}$ =floor temperature, °C

$P_1, \ldots, P_{(M+1) \cdot N+1}$ =relative pressure of the air for each zone, Pa

6.5 Solution Algorithm

6.5.1 Theoretical Coupling

To avoid solving for a sparse matrix, the systems of equations are not solved simultaneously for temperatures and pressures. The whole system of equations (6-36) is written separately by a linearized part that contains the temperatures only:

$$[A]\ [T] = [B] \tag{6-37}$$

and a non-linearized part that contains the pressures only:

$$[C]\ [P] = [D] \tag{6-38}$$

For a house with three double-glazed windows under a dome, the total number of unknown temperatures of system (6-37) is $M \cdot N + 67 + (M+1) \cdot N$: $M \cdot N$ unknown temperatures of cells, 67 unknown temperatures for layers of walls/roof/floor and ground,

and $(M+1) \cdot N$ unknown air temperatures inside the dome. There are $(M+1) \cdot N+1$ unknown air pressures. As the summation of the airflow rate in all zones is equal to zero, the number of mass balance equations is reduced by one, and there are only $(M+1) \cdot N$ equations for the pressures. Therefore, a relative reference pressure must be assigned to one perimeter zone, so that system (6-38) can be solved. The air pressure must be solved in order to find the airflow rate inside each zone.

6.5.2 Options

In the case of the dome surface that is divided into 546 cells (M=42 and N=13), there are 1172 unknown temperatures and 560 unknown air pressures. The linearized part of the system (equations for temperature) is solved by the Gauss-Seidel iteration technique, and the nonlinear part of the system (equations for pressure) is solved by the Newton-Raphson iteration technique or Broyden's method (Press et al., 1992). Two iteration schemes can be used to solve the two systems of equations: the decoupled approach ("ping-pong" approach) and the coupled approach ("onion" approach). In the decoupled approach, the thermal model and the flow model run in sequence, each model uses the results of the other model from the previous time step. In the coupled approach, the thermal and flow model iterate at each time step until satisfactory small error is achieved.

The limitation of the coupled method is that the computer program consumes more than two times computer resources (CPU and memory) when it is running. However, this method can produce more accurate results, as suggested by Hessen (1999).

6.5.3 Conclusion

There are two options to solve the system of equations, the coupled method and the de-

coupled method. The coupled method will consume more computer resources but may return more accurate results, and the de-coupled method will use less computer resources but have less accuracy on the results for long time step, as suggested by Hessen (1999), who applied the method to a multi-zone model to simulate the airflow in an atrium. Since this computer model uses a time step of one hour, and the accuracy is the main issue in the computation, the coupled approach is adopted in the program. Broyden's method is used instead of Newton-Raphson in this thesis because Broyden's method returns better results for the mass convergence in the case study.

6.6 Initial Values

The variables involved in this system are shown in equations (6-1) to (6-34), equations (5-27), (5-29), (5-31), (5-33), (5-35), and (5-37). The outdoor air temperature and room air temperature are known. The initial values of other variables are chosen based on the following criteria:

(1) The air temperature inside the dome is the average value of the outdoor air temperature and room air temperature at the previous time step:

$$T_{in,0} = \frac{1}{2}\left(T_{o,24} + T_a\right) \tag{6-39}$$

where:

$T_{o,24}$ =out door air temperature at hour 24.

(2) The surface temperature of the dome glazing is the average value of the outdoor air temperature, room air temperature and the air temperature inside the dome:

$$T_{ij,0} = \frac{1}{3}\left(T_{o,24} + T_a + T_{in,0}\right)$$

(6-40)

(3) The exterior wall/roof temperature is closer to the dome air temperature, and the interior wall/roof temperature is closer to the room air temperature than the air temperature inside the dome:

$$T_{l,i,0} = \frac{(10-i)}{10.0}T_{in,0} + \frac{i}{10.0}T_a$$

(6-41)

where:

i=ith node of the wall, from outside to inside.

(4) The ground temperature inside the dome is equal to the soil temperature based on equation (4-49):

$$T_{g,in,i,0} = T_{ms} + A_s e^{-i \cdot dx\sqrt{\pi/\alpha_s \cdot \tau_0}}\sin\left[\frac{2\pi \cdot \left(n_d - n_{lag}\right)}{\tau_0} - i \cdot dx\sqrt{\frac{\pi}{\alpha_s \cdot \tau_0}}\right]$$

(6-42)

(5) The initial value for the relative pressure of the first layer is given as:

$$P_{0,0} = \frac{1}{M}\sum_{i=1}^{M}P_{wi,0}$$

(6-43)

where P_{wi} is the wind pressure over the dome surface.

(6) The pressure of other layers decreases with height:

$$P_{i,0} = P_{0,0} - \rho g z_i$$

(6-44)

137

where z_i is the height of the middle of each zone.

6.7 Calculation Procedure

The program was written in Fortran 90 (Adams et. al., 1992), and the calculation procedure is presented below (Figure 6-3):

(1) Read the input data (weather data, geometric data and thermal properties) from the input file (with optical values obtained from Window 5.2)

(2) Calculate the time independent coefficients, including the view factors between each cell and the wall surface, roof surface and ground surface and other cells of the dome surface (these coefficients are used for long-wave radiation), and calculate the total interchange view factor between all surfaces based on equation (4-65) (Figure 6-4). The Gauss-Seidel iteration scheme is used to calculate the view factor, where the convergence criterion is:

$$|F * -F| \leq 1.0E - 06 \tag{6-45}$$

where:

F*=view factor obtained by the last iteration step

F=view factor obtained by the present iteration step

In order to improve the accuracy of the calculation on the view factor, all these variables are of double precision.

(3) Calculate the incident solar radiation over each surface and the internal heat gain of the house for every time step (Figure 6-5).

(4) Assign the initial temperature to each node, assign air pressure to each zone, compute for the airflow rate between adjacent zones, and establish the matrix A

and the vector **B**. The Broyden method is used to calculate the airflow rate, and the Gauss-Seidel iteration scheme is used for solving the system of equations for the temperature. The absolute error tolerance between temperatures at two iteration steps is equal to 1.0E-04 °C, and the absolute error tolerance between temperatures at two time step when the airflow rate is updated (ε) is equal to 1.0 °C. The absolute error tolerance between two identical days (ε_1) is equal to 1.0 °C.

(5) Applying a double iteration loop to calculate the temperature for each node and the cooling/heating load for each day, as shown in the following steps:

    For I=1, IMax (Maximum identical days, equal to 9)

        For j=1 to 24 (Hours in the day)

        Solving equation (6-38) using Broyden method

        Calculate the airflow rate between adjacent zones

        Iteration for the temperature of each node by solving equation (6-37)

        Next j

        If the result is convergent

        Evaluate cooling/heating load (equation 6-35), go to (6)

    Next I

(6) Present the result in a text file.
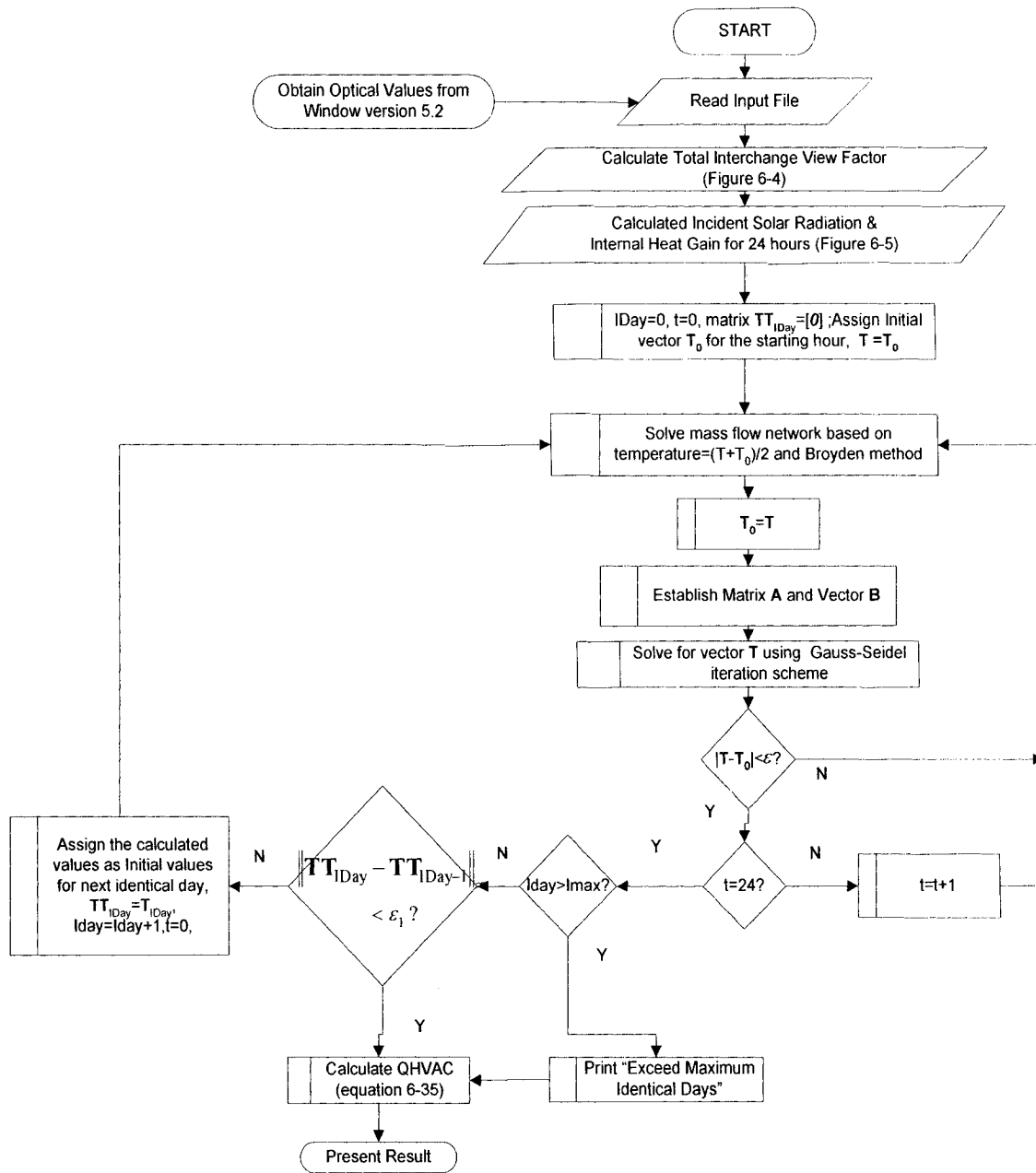
Figure 6-3 Flow chart for the overall calculation procedure
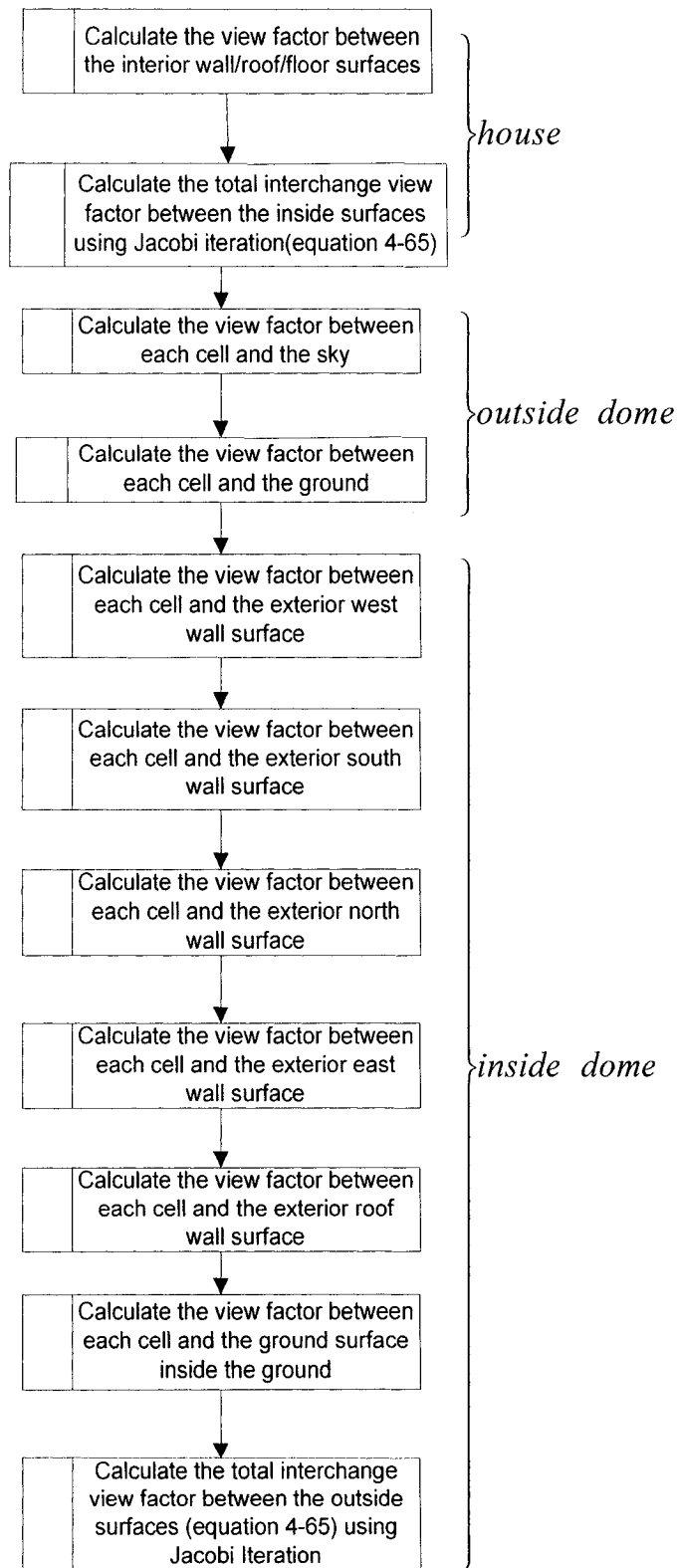
Figure 6-4 Flow chart for the calculation of interchange view factor
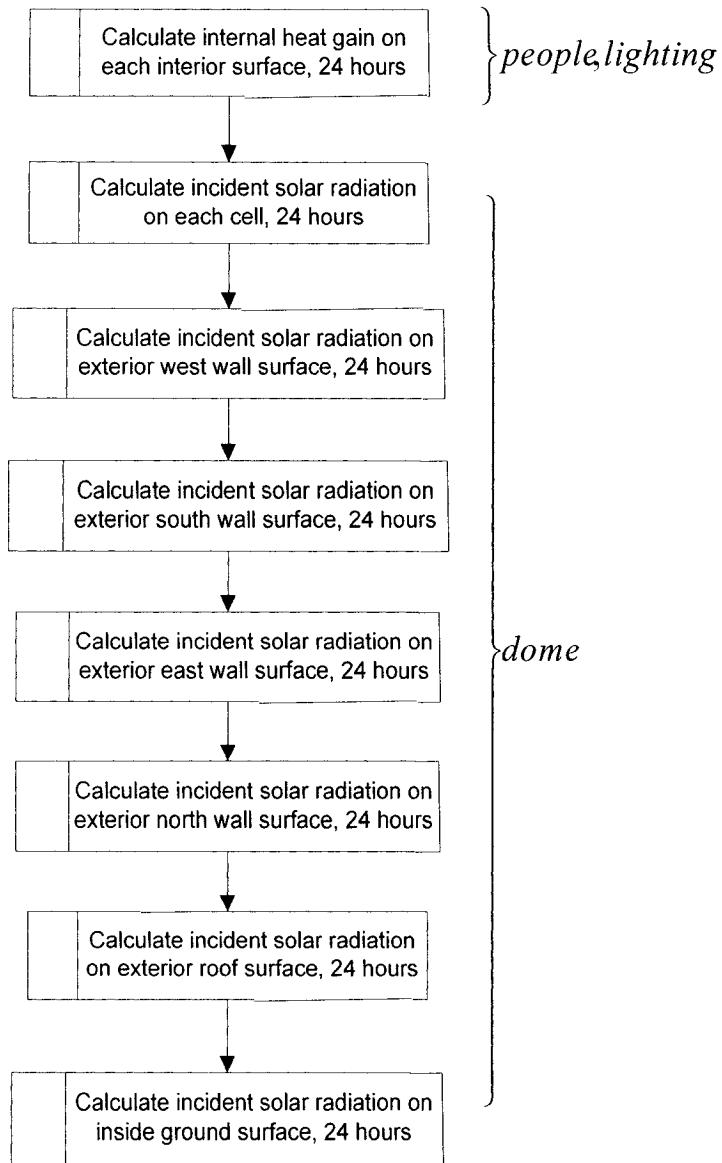
Figure 6-5 Flow chart for the calculation of incident solar radiation
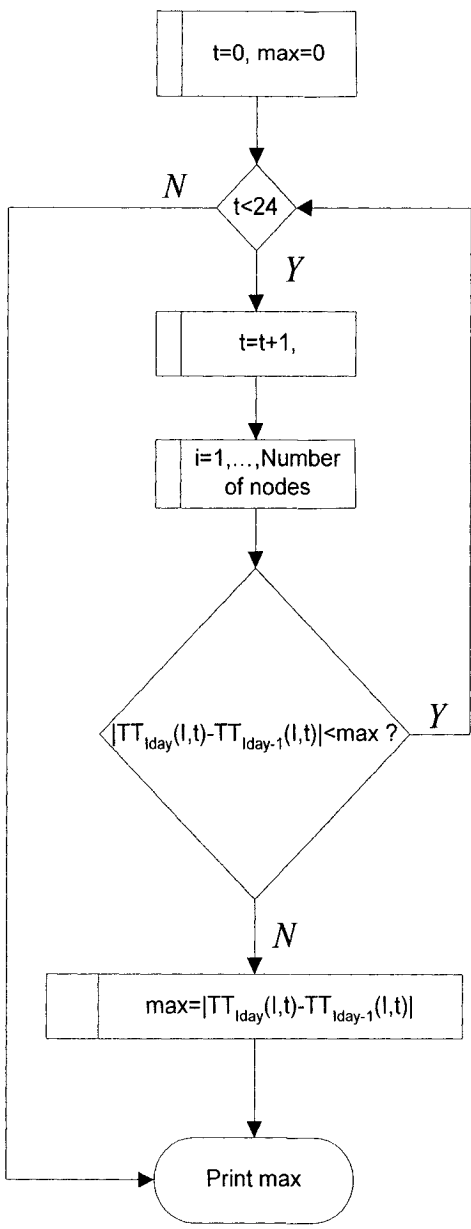
Figure 6-6 Flow chart for verifying the convergence

Chapter 7 Comparison

This chapter presents the verification and validation of the program for the following aspects: response to a step function input, glazing temperature, air temperature distribution and air flow pattern inside the dome.

The results of the model presented in this thesis are compared with results from a simplified model and a CFD model, which are implemented in commercial softwares, as well as experimental measurements with Singh et al. (2006) and simulation results from Luttman-Valencia (1990).

7.1 Thermal Response of the Dome to a Step-function Change of the Outdoor Air Temperature

Two cases are considered in this section: the first case uses a simplified thermal model, developed under MATLAB environment, while the second case uses experimental data.

7.1.1 Comparison with a Simplified Model under MATLAB Environment

A simplified case was used for the verification of the computer model. In this case, the ground is composed of one layer, and it is well insulated below this layer. The house is removed from the dome. There is no wind, sky radiation, long-wave radiation between the dome and outdoor ground, and solar radiation. Under these circumstances, a simplified mathematical model is developed, which is composed of three nodes: one for the air inside the dome (equation 7-1), one for the ground inside the dome (equation 7-2), and one for the glazing (equation 7-3):

$$h_{in} \cdot A_{dome} \cdot \left(T_s - T_{in}\right) + h_{in} \cdot A_g \cdot \left(T_g - T_{in}\right) = m_{in} \cdot c_{p,in} \cdot \frac{dT_{in}}{dt} \qquad (7\text{-}1)$$

$$h_r \cdot \left(T_s - T_g\right) + h_{in} \cdot \left(T_{in} - T_g\right) = \frac{1}{2} \cdot \rho_g \cdot dx \cdot c_{p,g} \cdot \frac{dT_g}{dt} \qquad (7\text{-}2)$$

$$h_{out} \cdot \left(T_o - T_s\right) + h_{in} \cdot \left(T_{in} - T_s\right) + h_r \cdot \left(T_g - T_s\right) = \rho_s \cdot d_s \cdot \frac{dT_s}{dt} \qquad (7\text{-}3)$$

where:

A_{dome}=area of the dome surface, m^2;

A_g=area of the ground inside the dome, m^2;

$c_{p,g}$=specific heat of soil, J/kg· °C;

$c_{p,in}$=specific heat of air, J/kg· °C;

d_s=thickness of the glazing, m;

dx=thickness of the 1st layer of the ground, m;

h_{in}=convective coefficient over inside surfaces, W/m^2·°C;

h_{out}=convective coefficient over the outside surface of the dome, J/m^2· °C;

h_r=radiation coefficient, J/m^2· °C;

T_g=temperature of the ground surface, °C;

T_{in}=air temperature inside the dome, °C;

T_s=glazing temperature, °C;

m_{in}=mass of the air inside the dome, kg;

ρ_g=density of soil, kg/ m^3;

ρ_s=density of the glazing, kg/ m^3.

The solution of equations (7-1)-(7-3) is obtained by using the MATLAB environment. Initially, the temperature of cells, of the ground inside the dome and of the air inside the dome is assumed to be equal to (-10°C). Then, the outdoor air temperature rises suddenly to 0°C. The variation of air temperature inside the dome under this step change of outdoor air temperature, as estimated by the detailed computer model (with one node for the air inside the dome) and by the simplified model, is presented in Figure 7-1.

The results presented in Figure 7-1 indicate a good agreement between the two models, as the maximum difference is less than 0.7°C. The three temperatures converge to the outdoor air temperature of 0°C after about 16.4 hours.
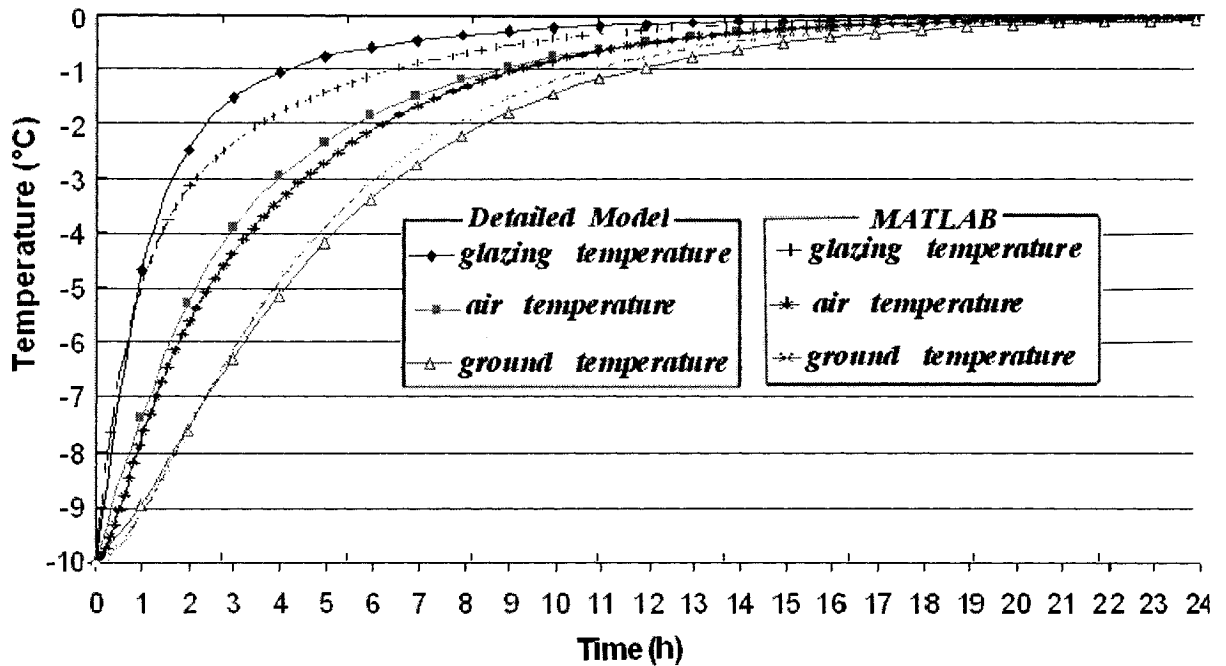
Figure 7-1 Variation of air temperature inside the dome following a step change of outdoor air temperature from (-10°C) to 0°C. Comparison between the detailed computer model and MATLAB solution to equations (7-1)-(7-3).

7.1.2 Comparison with Experimental Data

The simulation results from the single-node model are compared with the experimental data of two cases as presented by Smith (1999) for a dome-like pyranometer. The temperature of the glazing was measured by thermocouples at the mid-height of the pyranometer. In the first case, the temperatures of dome and air inside the dome are assumed to be equal to 0°C initially. Then, the outdoor air temperature rises suddenly to 19.25°C. In the second case, the initial temperature is (-4.65°C) and the final temperature is 22.85°C. The predictions of glazing temperature under these two conditions agree well with experimental data (Figures 7-2 and 7-3).
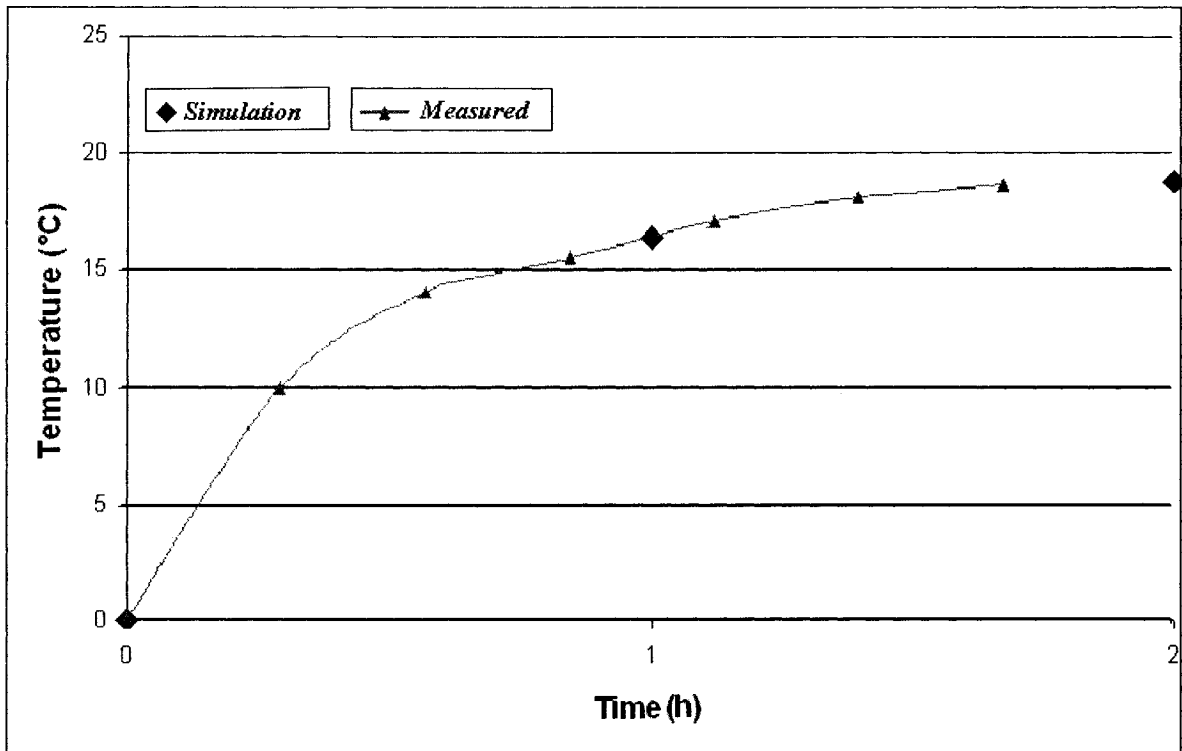
Figure 7-2 Variation of the glazing temperature following a step change of outdoor air temperature from 0°C to 19.25°C. Simulated vs. measured (Smith, 1999)
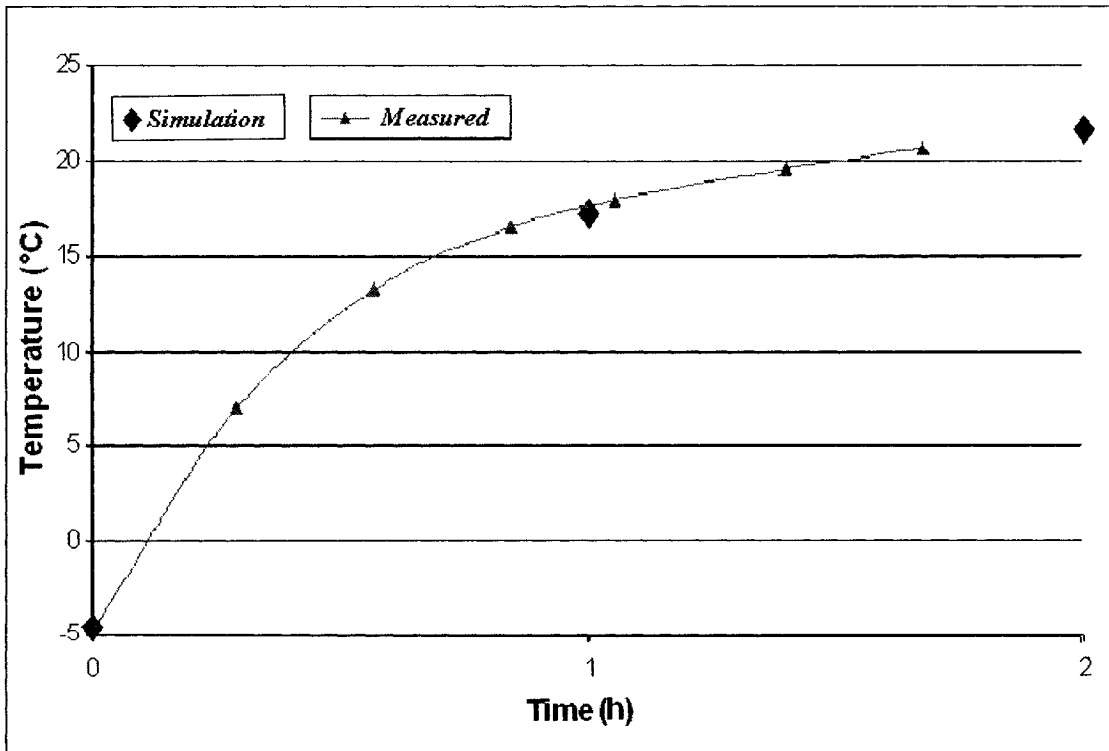
Figure 7-3 Variation of the glazing temperature following a step change of outdoor air temperature from (-4.65°C) to 22.85°C. Simulated vs. measured (Smith, 1999)

7.2 Comparison between the 3D-TAF Model and a CFD Model

A 2D dimensionless CFD model of a dome is developed in the COMSOL Multiphysics environment (COMSOL AB, 2005) using the dome diameter as the characteristic length. The boundary conditions for the COMSOL model are: the temperature of glazing (13 cells for the western part and 13 cells for the eastern part), and the temperature of the ground surface inside the dome. The air temperature distribution and air flow, as predicted by the 3D-TAF model, are compared with those predicted by the COMSOL program.

The incompressible Navier-Stokes equation is used as the governing equation for the air flow inside the dome (COMSOL AB, 2005):

$$\begin{cases} \rho \cdot \dfrac{\partial v}{\partial t} + \rho \cdot (v \cdot \nabla) \cdot v = -\nabla p + \mu \cdot \nabla^2 v + F \\ \nabla v = 0 \end{cases} \tag{7-4}$$

where:

F=volume force, N;

P=pressure, Pa;

v=velocity field, m/s;

ρ=fluid density, kg/m^3;

μ=dynamic viscosity, Pa·s.

The Boussinesq approximation is used to calculate the impact of temperature on the density:

$$\rho = \rho_0 \cdot \left(1 - \beta_a \cdot \Delta T\right) \tag{7-5}$$

where:

ρ_0 =reference density (in this model, the outdoor air density), kg/m^3;

β_a=volume expansion factor of air, K^{-1};

ΔT=temperature difference between the air and the reference temperature, K.

In this approximation, variations in temperature produce a buoyancy force that lifts the air. The buoyancy force in the Navier-Stokes equation is approximated as:

$$F = \begin{pmatrix} F_x \\ F_y \end{pmatrix} = \begin{pmatrix} 0 \\ \beta_a \cdot \rho \cdot g \cdot \Delta T \end{pmatrix} \tag{7-6}$$

where:

ΔT=temperature difference between the air and the reference temperature (in this model, the outdoor air temperature is used as the reference temperature), K;

g=gravitation of acceleration, m/s^2.

The change in energy is equal to the heat source minus the divergence of the diffusive heat flux:

$$\rho \cdot c_p \cdot \frac{\partial T}{\partial t} = Q - \nabla \left(-k \cdot \nabla T + \rho \cdot c_p \cdot T \cdot v \right) \qquad (7\text{-}7)$$

where:

c_p=specific heat of air, J/kg·K;

k=conductivity of air, W/m·K;

Q=heat source, there is no heat source in the control volumes, W;

T=air temperature, K.

The Navier-Stoke equation can be written in a dimensionless form by introducing the following scaled variables (Knopp, 2003):

$$t^* = \frac{t \cdot V}{D}, \qquad H^* = \frac{H}{D}, \qquad V^* = \frac{v}{V}, \qquad T^* = \frac{T - T_0}{T_{diff}} \qquad (7\text{-}8)$$

and the following dimensionless quantities:

$$P^* = \frac{p - \rho_0 \cdot g \cdot H}{\rho_0 \cdot V^2}, \qquad a^* = \frac{k}{c_p \cdot \rho_0 \cdot D \cdot V}, \qquad g^* = \frac{g \cdot D}{V^2}, \qquad c_p^* = \frac{k \cdot T_{diff}}{\rho_0 \cdot a_a \cdot V^2},$$

$$Q^* = \frac{Q \cdot D}{\rho_0 \cdot V^3}, \qquad \beta^* = \beta_{a,0} \cdot T_{diff}, \qquad Re^* = \frac{\rho_0 \cdot V \cdot D}{\mu}$$

$$(7\text{-}9)$$

where:

a*=dimensionless diffusion coefficient of the air;

c_p*=dimensionless specific heat of air;

D=characteristic length of the problem, m;

$$D = 2 \cdot R \qquad (7\text{-}10)$$

g*=dimensionless gravitation;

H*=dimensionless height;

p*=dimensionless air pressure;

Q*=dimensionless heat source, equal to zero in this model;

t*=dimensionless time;

T*=dimensionless temperature of air;

T_{diff}=characteristic temperature difference, K;

$$T_{diff} = T_{high} - T_{low} \qquad (7\text{-}11)$$

T_{high}= the highest temperature in the system, K;

T_{low}= the lowest temperature in the system, K;

V=characteristic velocity, m/s;

For the natural convection, the only driving forces are due to the buoyancy effects, and the characteristic velocity can be calculated as:

$$V = \left| \beta_{a,0} \cdot g \cdot T_{diff} \right|^{\frac{1}{2}}$$ (7-12)

V*=dimensionless velocity;

β*=dimensionless volume expansion rate of air;

$\beta_{a,0}$= volume expansion rate of outdoor air; K^{-1};

Re*=characteristic Reynolds number.

This yields the dimensionless system of equations for the CFD model:

$$\begin{cases} \dfrac{\partial V*}{\partial t*} + (V* \cdot \nabla) \cdot V = -\nabla p* + \dfrac{1}{Re*} \cdot \nabla^2 V + \beta* \cdot T* \cdot g* \\ \nabla V = 0 \end{cases}$$ (7-13)

$$\dfrac{\partial T*}{\partial t*} + \nabla(-a* \cdot \nabla T* + T* \cdot V*) = Q*$$ (7-14)

Figure 7-4 presents the dimensions of a full dome (H=R=20 m, σ_0=0°) selected for this comparision. Totally six cases are examined, using different boundary conditions. The six cases are divided into two groups:

a) Group no.1 contains four cases with a uniform ground surface temperature under the dome cover:

1) T_g=40°C, T_{top}=30°C

2) T_g=50°C, T_{top}=30°C

3) T_g=60°C, T_{top}=30°C

4) $T_g = 60°C$, $T_{top,west} = 30°C$, $T_{top,east} = 40°C$

b) Group no.2 contains two cases that consider variation of the ground surface temperature under the dome cover:

5) $T_{g,west} = 20°C$, $T_{g,east} = 40°C$, $T_{top,west} = 20°C$, $T_{top,east} = 30°C$

6) $T_{g,west} = 20°C$, $T_{g,east} = 50°C$, $T_{top,west} = 20°C$, $T_{top,east} = 30°C$

where T_{top} means the cover temperature above the height of 13.26 m, T_g means the ground temperature.

The dome-cover below the height of 13.26 m is well insulated. No solar radiation and wind have been considered in the above six cases. The dome air temperature extracted from the COMSOL program is the average air temperature of each central layer, calculated at the mid-height of the layer. Similarly, the vertical air velocity extracted from the COMSOL program is the average vertical air velocity of each central layer, calculated at the mid-height of the layer. There are totally 13 layers containing 559 zones for the 3D-TAF model and 400 elements containing 2,772 number of degrees of freedom for the 2D CFD model in the COMSOL program. The increase in the number of elements in the COMSOL program results in the instability of the solution and cannot provide better results for the air temperature and air velocity. A 3D CFD program was not used because of difficulties to draw a 3D mesh which contains 546 cells under the COMSOL Multiphysics environment.
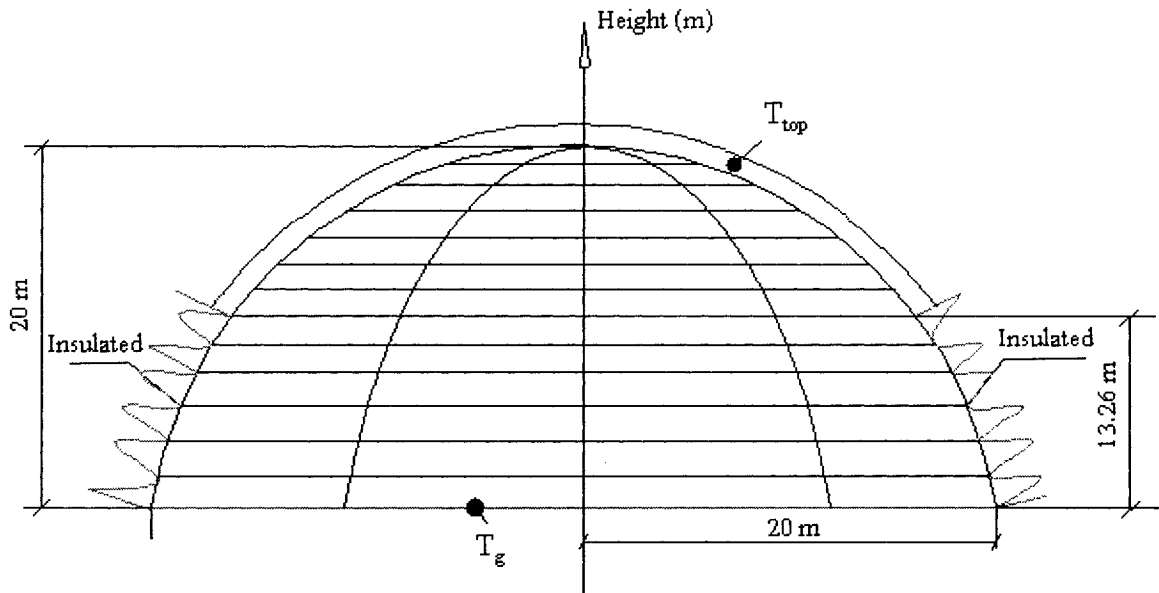
Figure 7-4 Dimension of the dome

According to equation (7-12), the characteristic air velocity for the six cases, are: 3.60 m/s, 7.09 m/s, 6.23 m/s, 6.23 m/s, 7.17 m/s, and 6.34 m/s, respectively.

COMSOL program does not converge to a solution within the default relative tolerance (10^{-6}) for the above six cases. The solution is obtained, however, with the relative errors and residuals estimated by COMSOL solver, as presented in Table 7-1:

Table 7-1 Relative errors and residuals predicted by COMSOL solver

	Case 1	Case 2	Case 3	Case 4	Case 5	Case 6
Relative error	0.007	0.0086	0.0059	0.0035	0.0063	0.0085
Relative residual	0.00019	0.0015	0.0023	0.00028	3.3e-005	0.0059

Figures 7-5 to 7-8 present the variation with height of the dome air temperature as predicted by the 3D-TAF model and the COMSOL program for case no.1 and no.2. The maximum difference between the air temperature predicted by the 3D-TAF model and the COMSOL program is found to be 1.72°C (Figure 7-5), and 3.45°C (Figure 7-7),

respectively. The 3D-TAF model predictions are quite close with the COMSOL program in these two cases.

The maximum difference between the air temperature of the first three layers predicted by the 3D-TAF model and the COMSOL program is found to be 0.75°C (Figure 7-5), and 2.74°C (Figure 7-7), respectively. The 3D-TAF model predictions are quite close with the COMSOL program. The results are of interest because in the case of a dome-covered house, the house is immersed in the first three layer of the air at the center of the dome. It is foreseeable that the 3D-TAF model can provide fairy good predictions of the cooling/heating load of the house inside the dome, compared with the COMSOL program, for $\Delta T = T_g - T_{top}$ between 10°C and 30°C. Other results are presented in Figures E-1 to E-6 (Appendix E).

Figure 7-5 Variation of the average dome air temperature with height. Comparison between the 3D-TAF model and the COMSOL program (Case 1)

Figure 7-6 Variation of the average dimensionless dome air temperature with the dimensionless height. Comparison between the 3D-TAF model and the COMSOL program (Case 1)
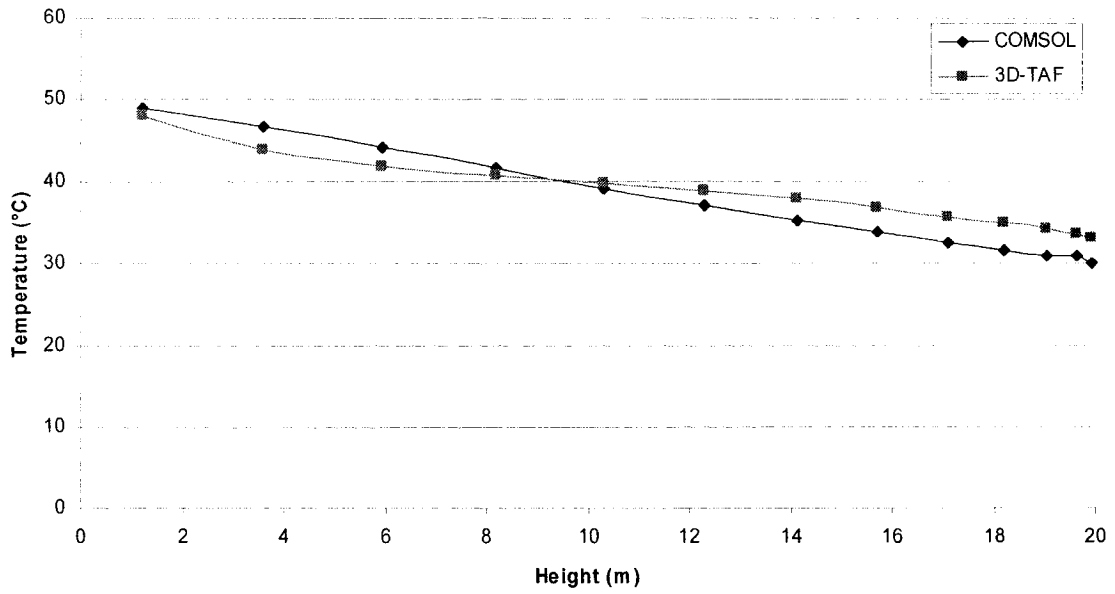
Figure 7-7 Variation of the average dome air temperature with height. Comparison between the 3D-TAF model and the COMSOL program (Case 2)
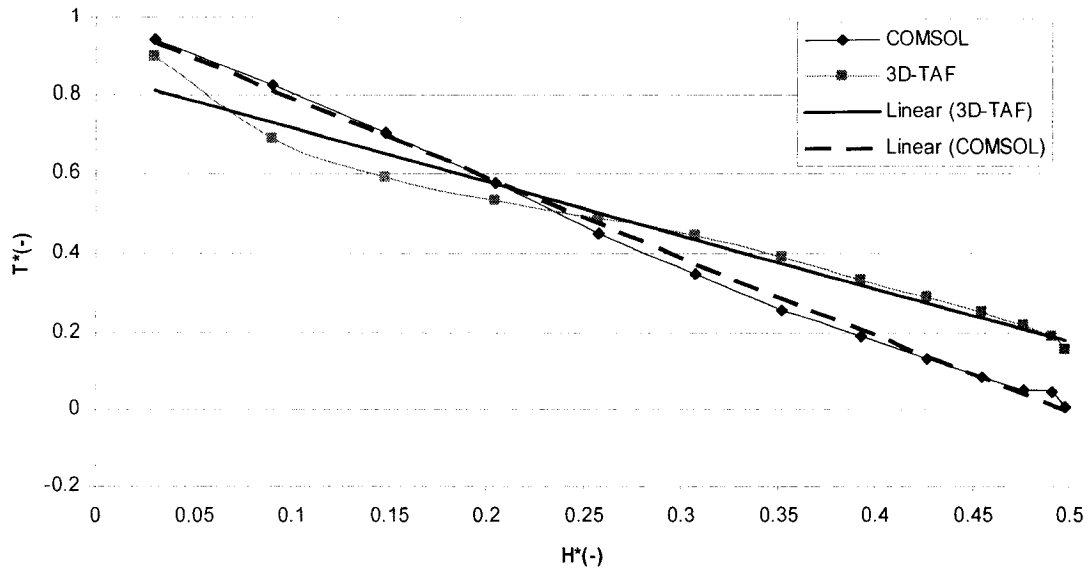
Figure 7-8 Variation of the average dimensionless dome air temperature with the dimensionless height. Comparison between the 3D-TAF model and the COMSOL program (Case 2)

It can be observed from Figures 7-5 to 7-8 and Figures E-1 to E-6 (Appendix E) that if the ground temperature does not have great variation in the horizontal direction (see cases no.5 and 6), the air temperature inside the dome has a linear relationship with the height inside the dome. The linear correlation model between the dimensionless air temperature and height can be expressed as:

$$T^* = a \cdot H^* + b \qquad (7\text{-}15)$$

where the coefficients a and b are obtained by the least-squares method, and are presented in Tables 7-2 and 7-3. Table 7-2 presents the coefficients for the first four cases and also the average coefficients of the first four cases. Table 7-3 presents the coefficients for the last two cases.

Table 7-2 Coefficients of the correlation-based model of the dimensionless temperature (cases (1-4)). 3D-TAF versus COMSOL

		a	b	R^2
Case 1	3D-TAF	-1.6497	0.9631	0.9754
	COMSOL	-1.9688	0.9759	0.9967
Case 2	3D-TAF	-1.3428	0.8486	0.9704
	COMSOL	-2.0031	0.9908	0.9967
Case 3	3D-TAF	-1.3997	0.9081	0.9734
	COMSOL	-1.9758	0.9674	0.9967
Case 4	3D-TAF	-1.2534	0.9429	0.9455
	COMSOL	-1.5133	0.9423	0.9724
Average	3D-TAF	-1.4114	0.9157	0.9866
	COMSOL	-1.8652	0.9691	0.9945

Table 7-3 Coefficient of the correlation-based model of the dimensionless temperature (cases (5-6)). 3D-TAF versus COMSOL

		a	b	R^2
Case 5	3D-TAF	-0.5606	0.6075	0.9434
	COMSOL	-0.3756	0.4711	0.669
Case 6	3D-TAF	-0.5919	0.6033	0.942
	COMSOL	-0.3148	0.4605	0.661

Figures 7-6, 7-8 to 7-11, and Figures E-1, E-3, E-5, and E-6 (Appendix E) present the linear relationship between the dimensionless air temperature and the dimensionless height inside the dome. R-square has values between 0.94 and 0.98 for the correlation developed from results of the 3D-TAF model, and between 0.66 and 0.997 when the data is generated by the COMSOL program. There is a good agreement between the results of two models, as the 3D-TAF model predicts an average dimensionless gradient of indoor air temperature of -1.41, while the CFD models predicts -1.87.
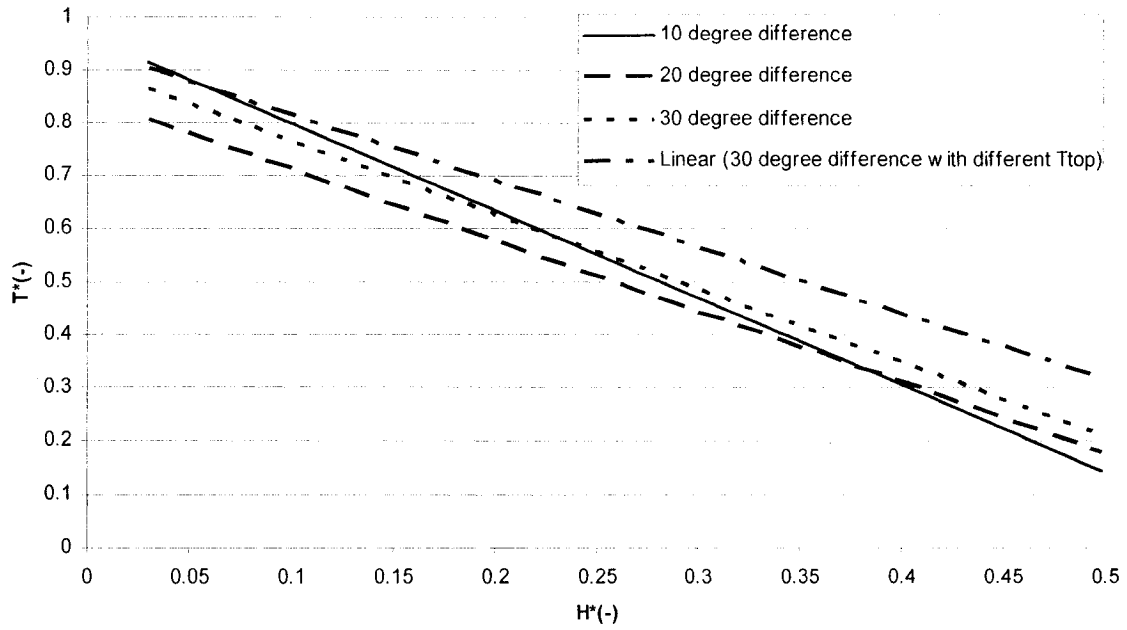
Figure 7-9 Linear correlation models between the average dimensionless dome air temperature and the dimensionless height, as extracted from the 3D-TAF model (Cases 1-4)
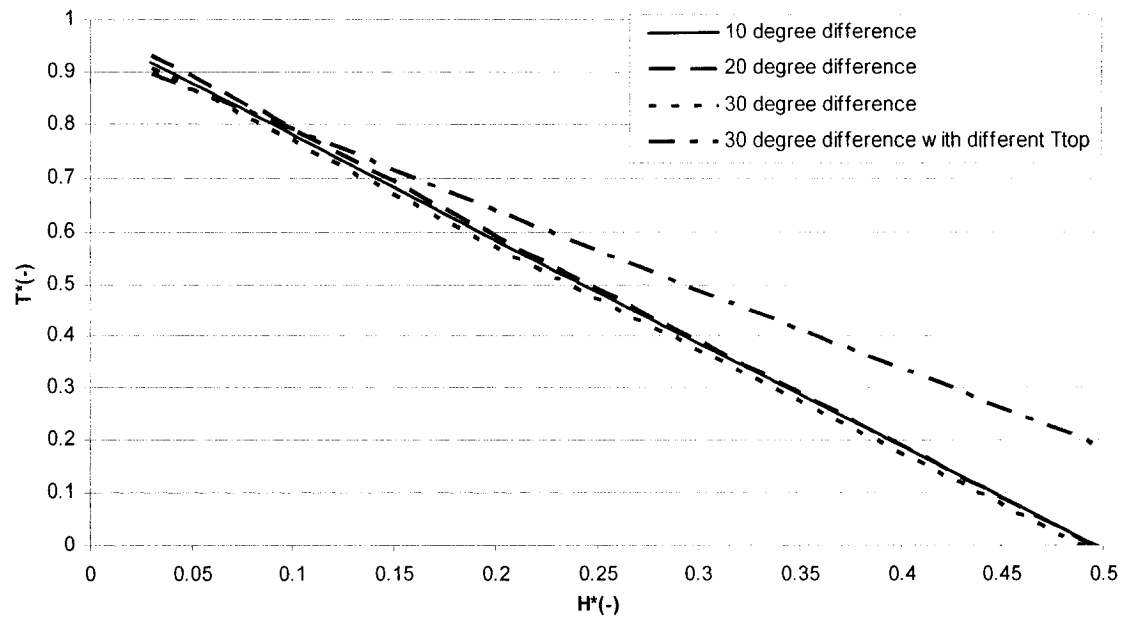
Figure 7-10 Linear correlation models of the average dimensionless dome air temperature with the dimensionless height, as extracted from the COMSOL program (Cases 1-4)

160

1
0.9
0.8
0.7
0.6
0.5
0.4
0.3
0.2
0.1
0

T* (-)

H* (-)

0   0.05   0.1   0.15   0.2   0.25   0.3   0.35   0.4   0.45   0.5

———— 3D-TAF

— — CFD

$y = -1.41H^* + 0.92$
$R^2 = 0.9866$

$y = -1.87H^* + 0.97$
$R^2 = 0.9945$
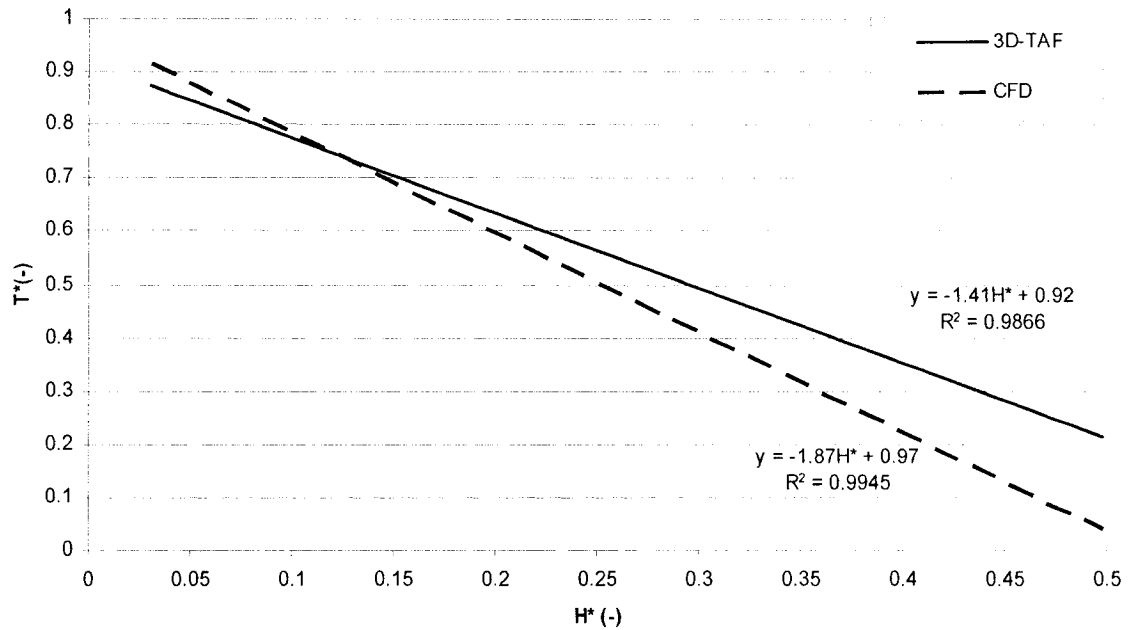
Figure 7-11 Average values on the variation of the dimensionless dome air temperature for the first four cases with the dimensionless height. Comparison between the 3D-TAF model and the COMSOL program

Figures 7-12 to 7-15 and Figures E-7 to E-10 (Appendix E) present the distribution of the dimensionless air temperature inside the dome, as predicted by the COMSOL program. There is a good agreement between the variation of dimensionless air temperature inside the dome, predicted by the 3D-TAF and CFD models, as presented in colors in Figures 7-12 to 7-15, for case no.1 and case no.2.
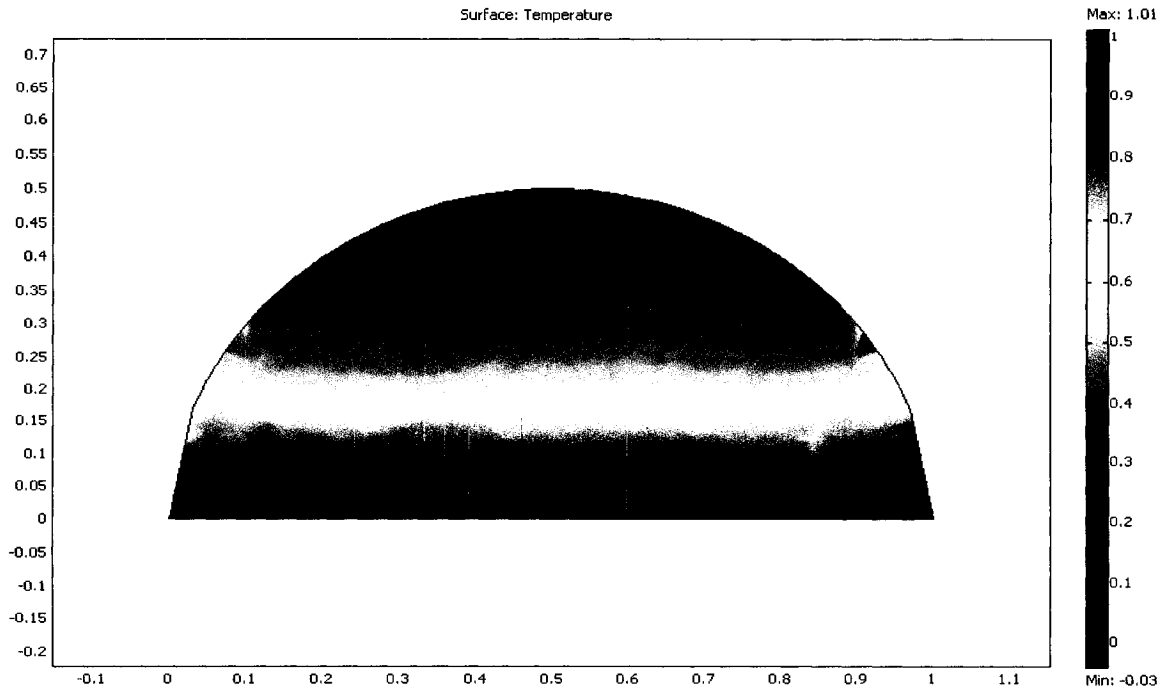
Figure 7-12 Temperature distribution predicted by the COMSOL program (Case 1)
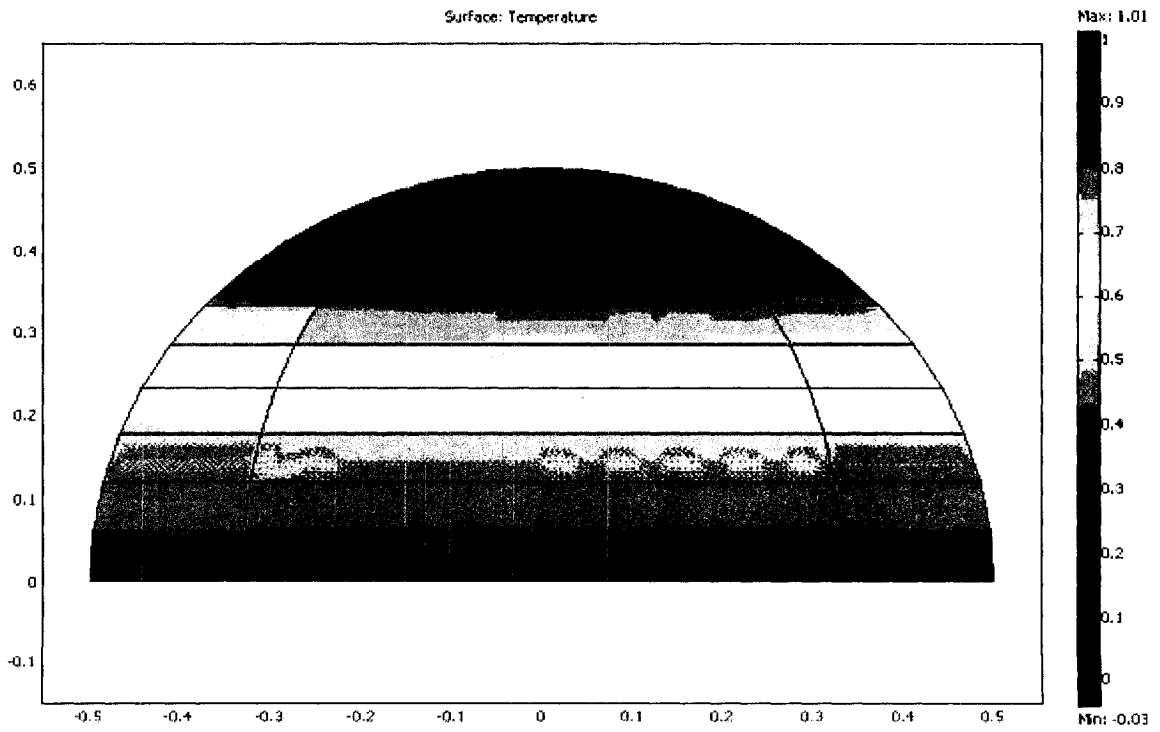
Figure 7-13 Temperature distribution predicted by the 3D-TAF model (Case 1)

162
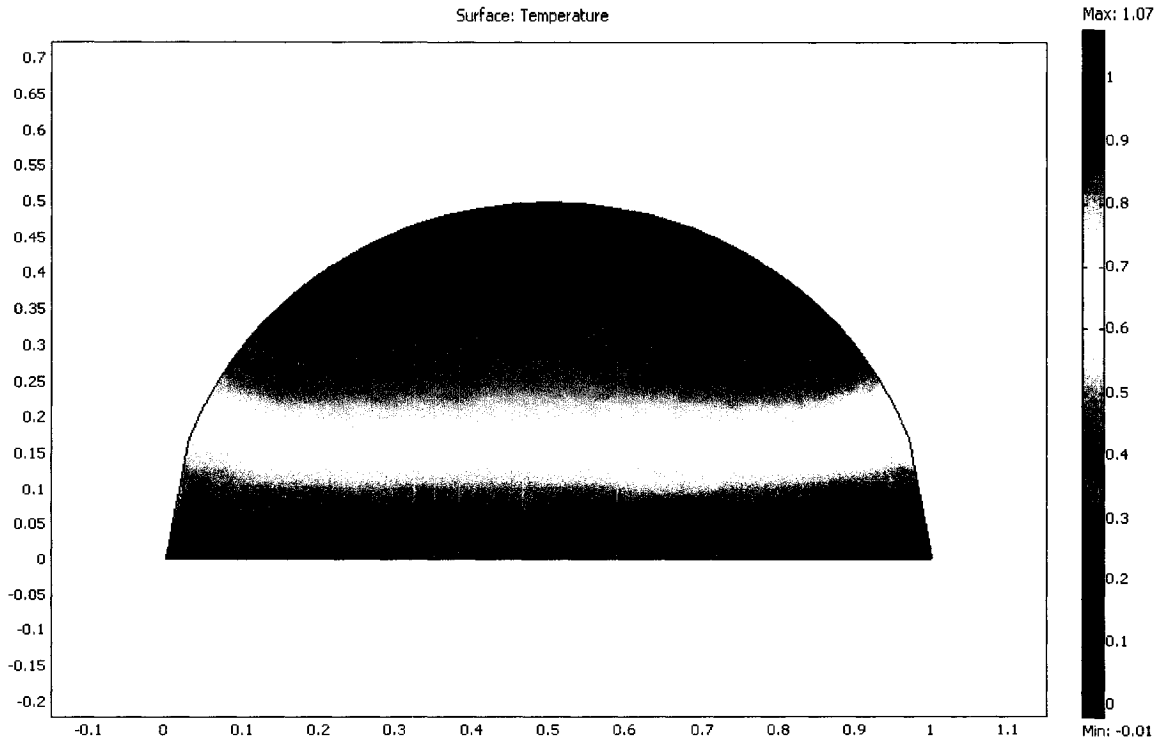
Figure 7-14 Temperature distribution predicted by the COMSOL program (Case 2)
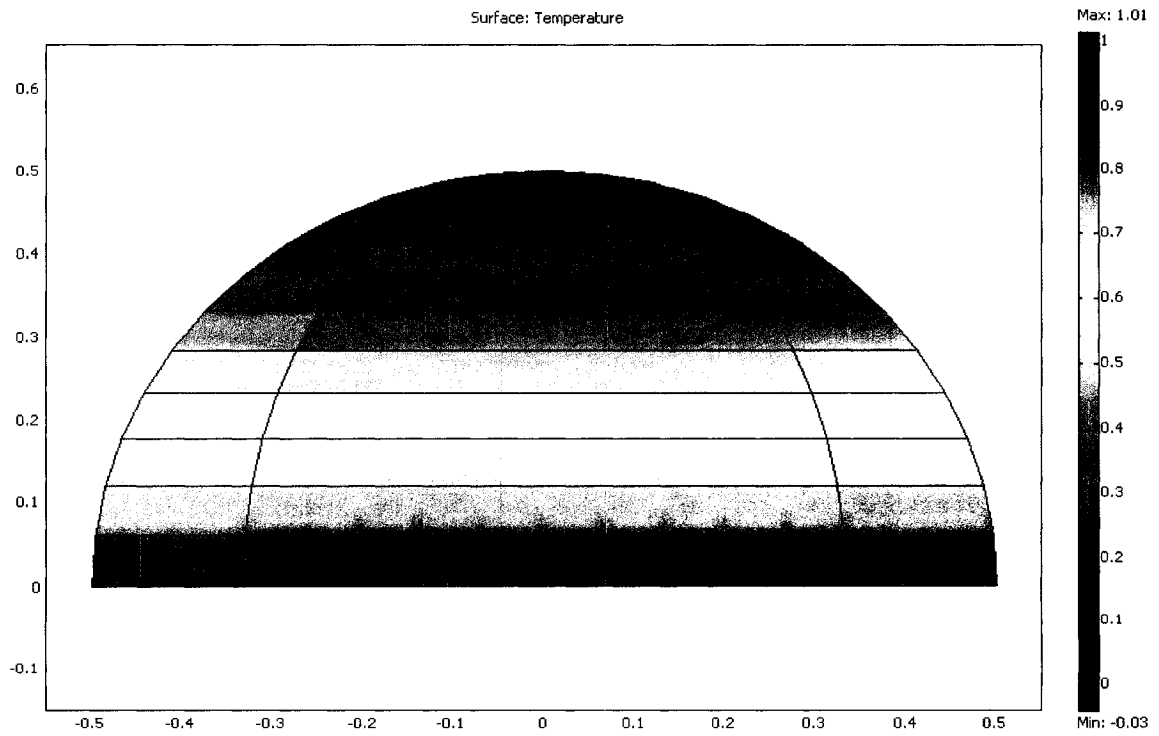
Figure 7-15 Temperature distribution predicted by the 3D-TAF model (Case 2)

163

Figures 7-16 to 7-23 and Figures E-11 to E-16 (Appendix E) compare the pattern of air movement and vertical air velocity on each central layer of the dome, as predicted by the 3D-TAF model with those predicted by the COMSOL program. Similar air velocity fields are found in those figures, e.g., both 3D-TAF and CFD models predict, for case no.1, that the airflow rises in the center of the dome and moves down near the cold surfaces of the dome (Figures 7-16 and 7-17). The maximum difference in vertical air velocity, for the six cases, are 0.044m/s, 0.068 m/s, 0.083 m/s, 0.1 m/s, 0.2 m/s and 0.24 m/s, respectively.
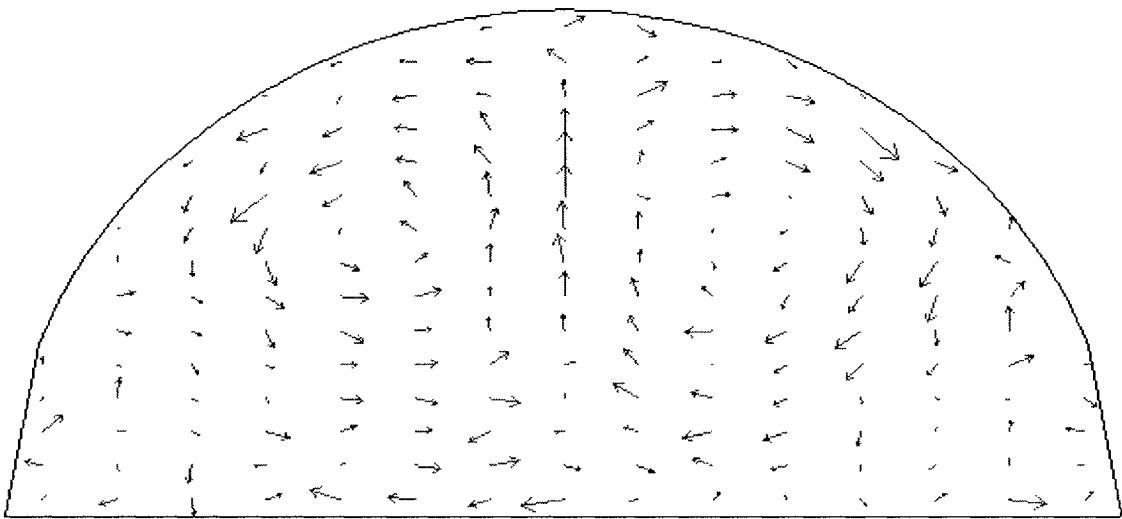
Figure 7-16 Velocity field predicted by the COMSOL program (Case 1)
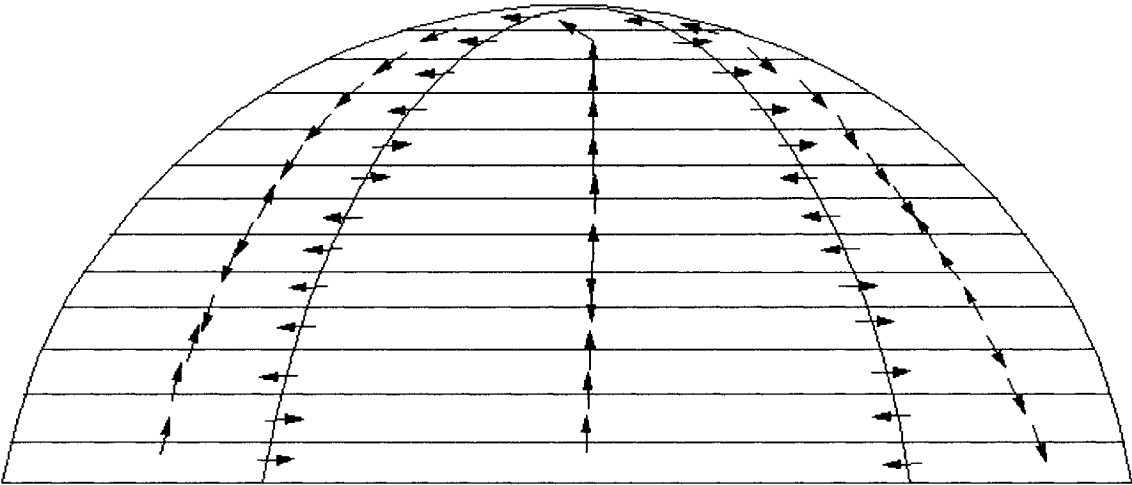
Figure 7-17 Velocity field predicted by the 3D-TAF model (Case 1)
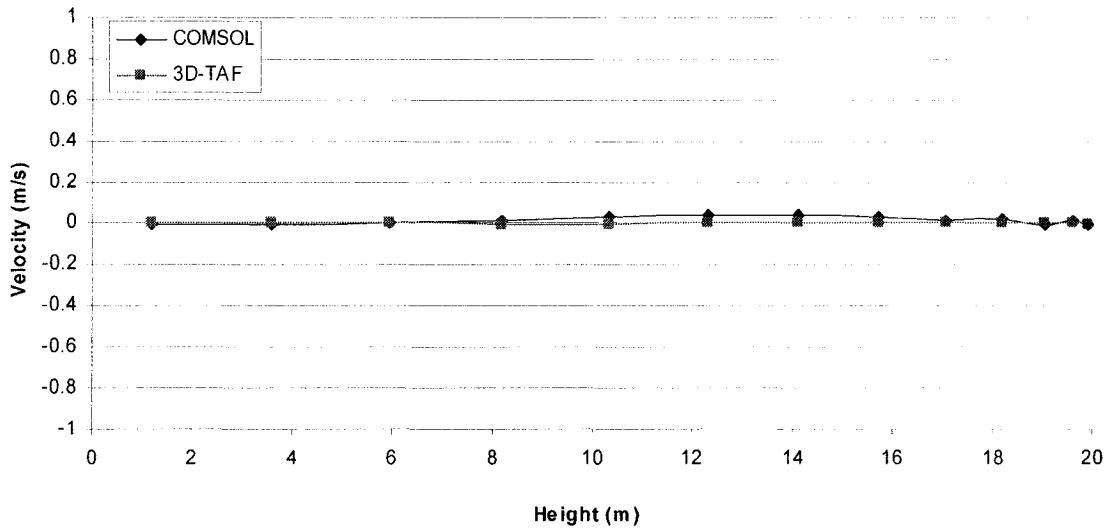
Figure 7-18 Variation of the air velocity with height. Comparison between the 3D-TAF model and the COMSOL program (Case 1)
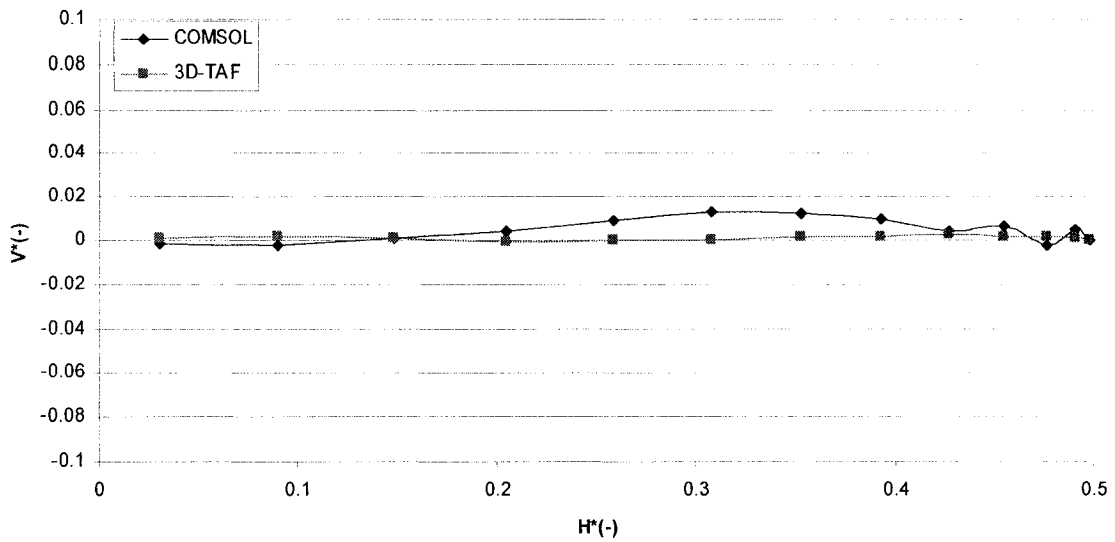
Figure 7-19 Variation of the dimensionless air velocity with the dimensionless height. Comparison between the 3D-TAF model and the COMSOL program (Case 1)
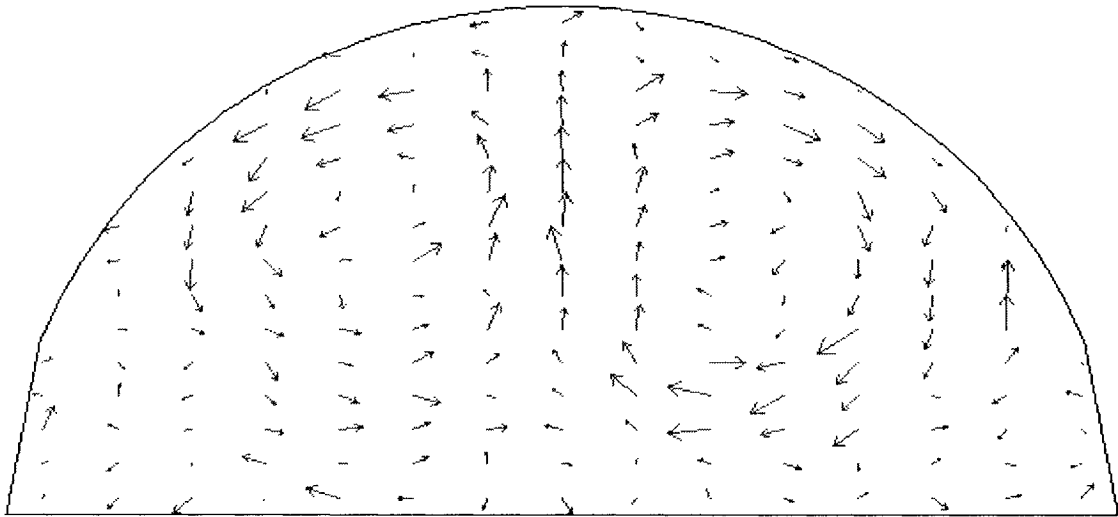
Figure 7-20 Velocity field predicted by the COMSOL program (Case 2)
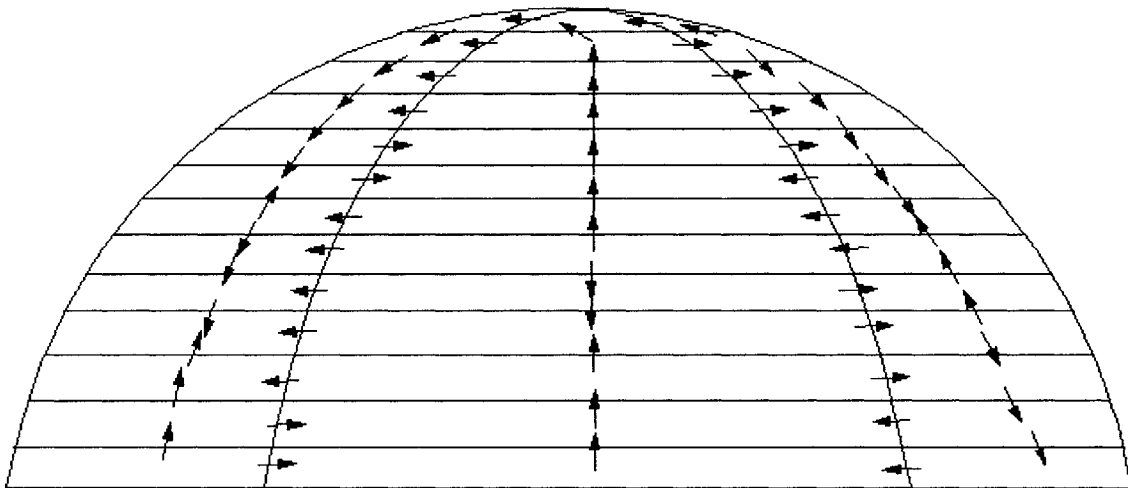
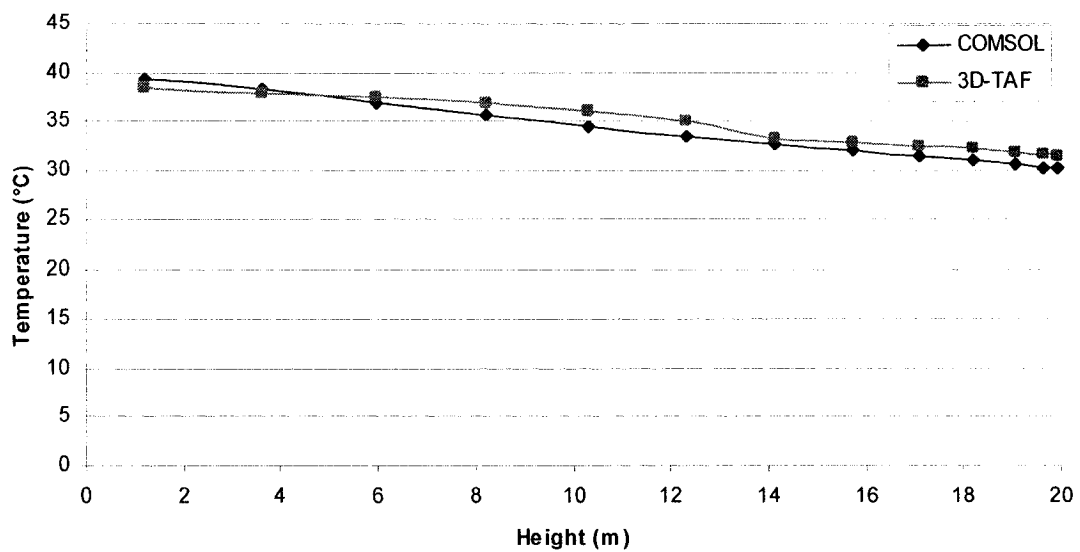Figure 7-21 Velocity field predicted by the 3D-TAF model (Case 2)

166

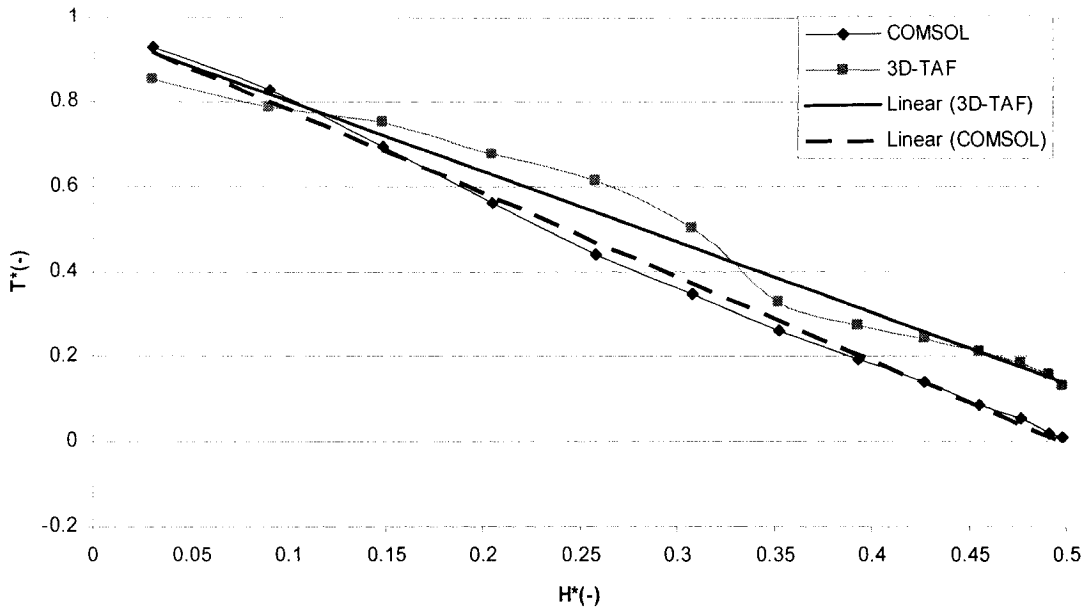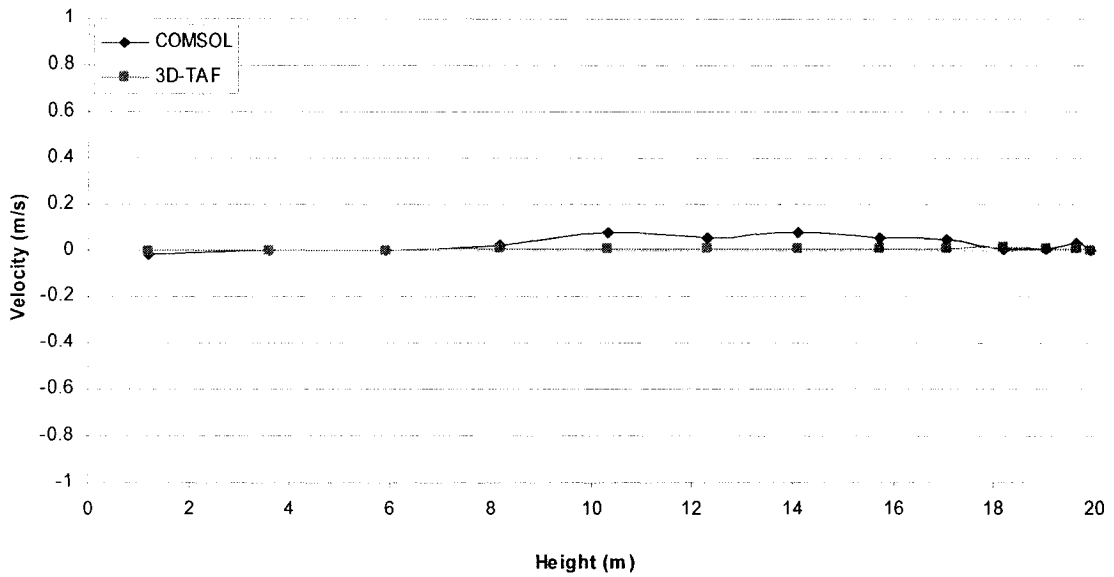Figure 7-22 Variation of the air velocity with height. Comparison between the 3D-TAF model and the COMSOL program (Case 2)
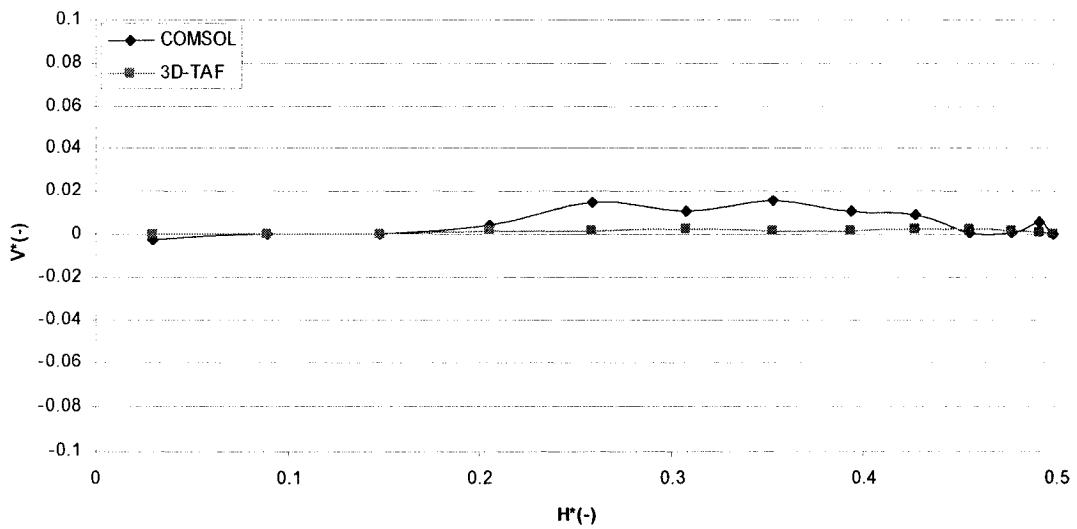
Figure 7-23 Variation of the dimensionless air velocity with the dimensionless height. Comparison between the 3D-TAF model and the COMSOL program (Case 2)

Figures 7-24 and 7-25 present the variations of the dimensionless vertical air velocity with the dimensionless height, as predicted by the 3D-TAF model and the COMSOL program. There is a very small difference between the air velocity predicted by the 3D-TAF model and the COMSOL program.
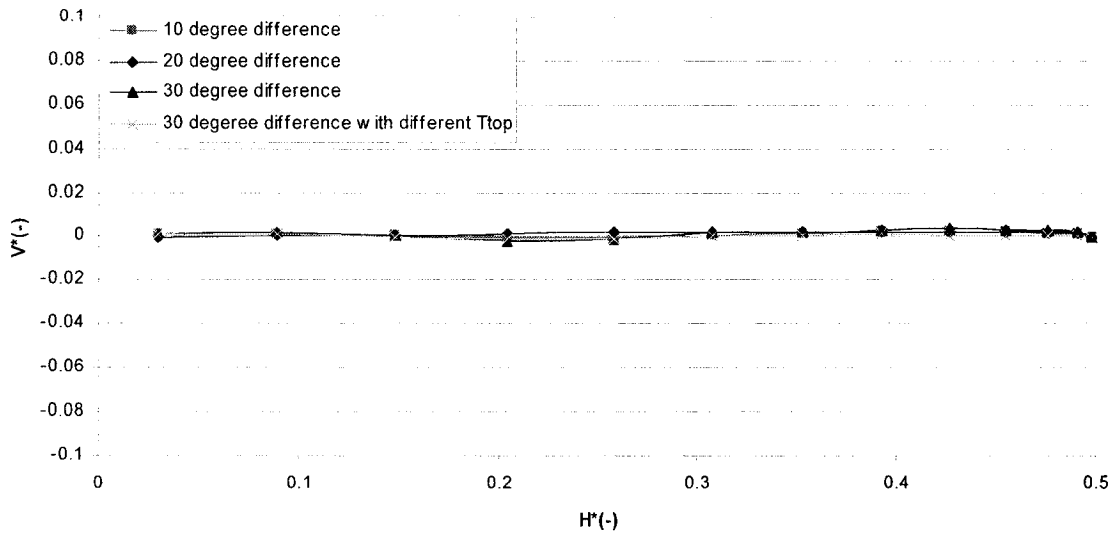
Figure 7-24 Variation of the dimensionless air velocity with the dimensionless height, as predicted by the 3D-TAF model
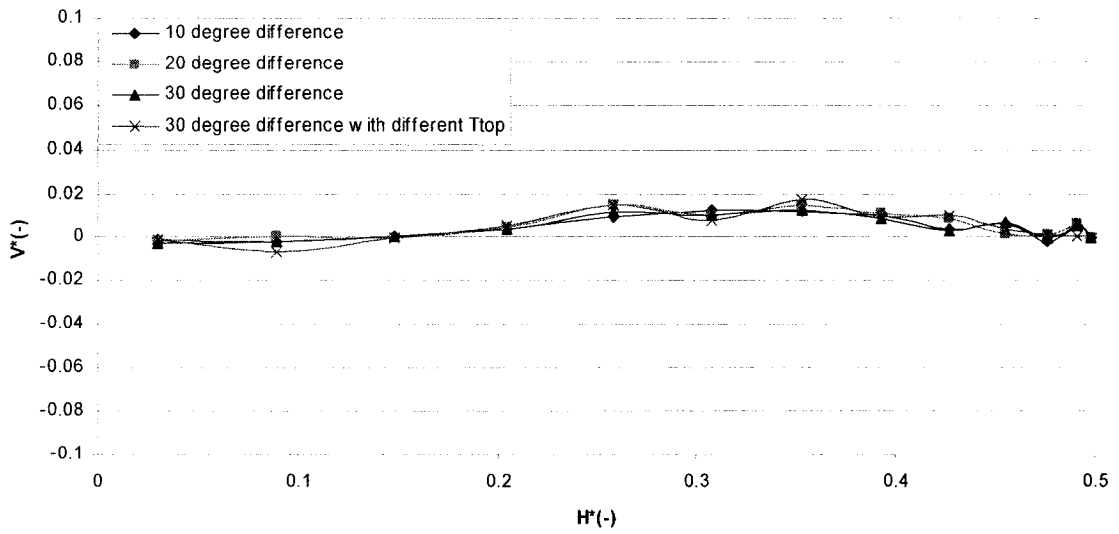
Figure 7-25 Variation of the dimensionless air velocity with the dimensionless height, as predicted by the COMSOL program

7.3 Comparison between the 3D-TAF Model and the Simulation Model of Biosphere II

The simulation results from the 3D-TAF model are compared with the simulation results from Luttmann-Valencia (1990) for Biosphere II, located in Arizona, U.S.. The Biosphere II is simulated as a dome with the radius of 30.9 m, the cover area of 6,000 m^2,

and the ground area of 2,350 m^2. The cover has the normal transmittance of 0.7 and absorptance of 0.2. Luttmann-Valencia (1990) used TRNSYS program for the simulation. Since the TRNSYS does not has a component to simulate a dome, a constant transmittance of the dome-cover was assigned and the dome cover was considered as a planar one that has similar optical property and thermal property, and airflow movement was not simulated. The comparison between the average air temperature inside the dome, as predicted by the 3D-TAF model, and the air temperature predicted by Luttmann-Valencia's model, on June 1st shows the maximum difference of 6.9°C at 12:00 AM (Figure 7-26), which is about 16%. Luttmann-Valencia's model generally predicts lower indoor air temperature when there is no sunshine and higher indoor air temperature when the dome receives solar radiation. The difference can be explained by the fact that the 3D-TAF is a transient heat transfer model; hence the air temperature does not react instantly to the change in solar radiation. Luttmann-Valencia's air model is a quasi-steady state model, and therefore the air temperature changes more rapidly with the change in solar radiation. Moreover, his model does not account for the second transmission through the dome cover.
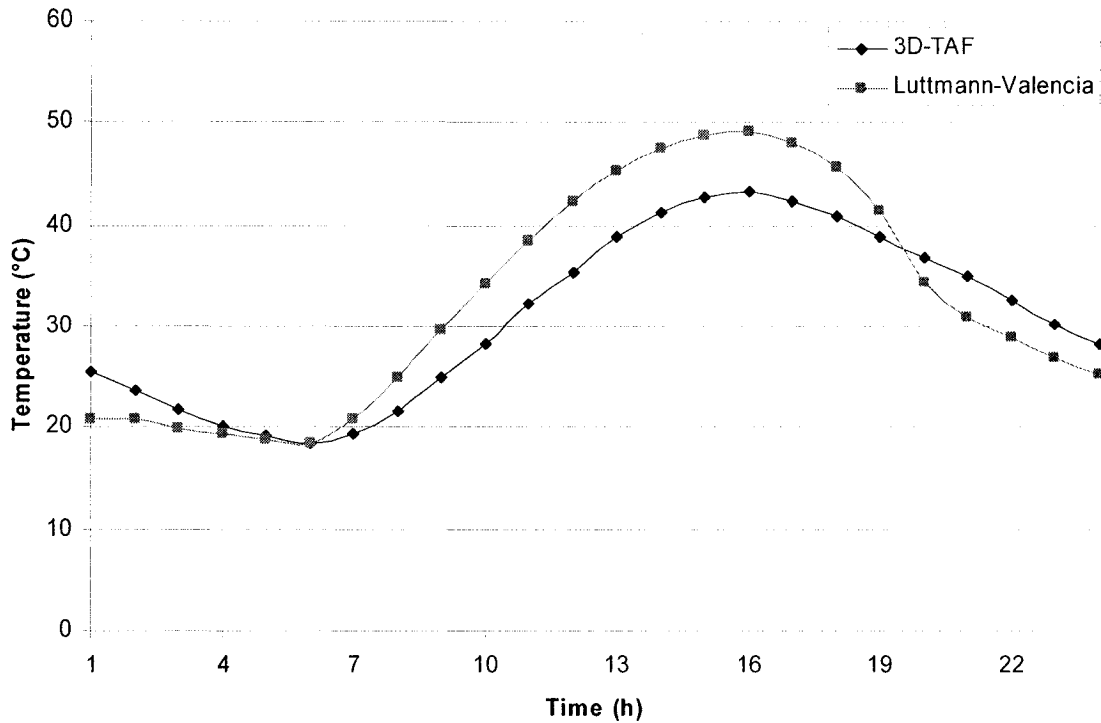
Figure 7-26 Comparison between the dome indoor air temperature as predicted by the 3D-TAF model and the results from the Luttmann-Valencia model on June 1st

7.4 Comparison between the 3D-TAF Model with Simulation Results and Experimental Measurements in a Greenhouse

This section presents the comparison between the average dome indoor air temperature, cover temperature and bare soil temperature predicted by the 3D-TAF model and experimental data and simulation results from Singh et al. (2006), for a greenhouse located in Ludhiana, India. The greenhouse has a semi-cylindrical form with the radius of 6 m, height of 3.5 m and the length of 24 m in the east-west direction. In the 3D-TAF model, the greenhouse was represented by a dome with radius of 6 m and height of 3.5 m. The cover has a normal transmittance of 0.65 and absorptance of 0.2. The reported measured temperature is the average of measurements from several sensors: the inside air temperature was measured at 32 points at four vertical cross-sections at 6 m distance

170

along the length, the cover temperature was measured on three points, and the temperature of bare soil surface and solar radiations normal to earth surface were measured at one point only. Singh et al. (2006) developed a steady state model that considers the energy balance of the greenhouse cover, inside air of greenhouse, and bare soil surface. The temperature of the indoor air, the temperature of the cover and the temperature of the bare soil are represented as single nodes.

The steady state 3D-TAF model and transient 3D-TAF model are used. In the steady state model, the temperature of the glazing and the indoor air temperature are calculated based on the weather data at a specific time. In the transient model, the temperature of the glazing and the indoor air temperature are calculated based on the weather data and the temperature of the previous time step. The soil temperature is calculated in the 3D-TAF model either through equation (4-49) by assigning a constant temperature at the depth of 1.0 m (Figures 7-27 to 7-29) or obtained from the experimental measurements by Singh et al. (2006) (Figures 7-30 and 7-31).

The steady state 3D-TAF model appears to predict best results for the air temperature and cover temperature except at 12:00 AM, in the case when the soil temperature is calculated, and at 11:00 AM, when the measured soil temperature is given as boundary condition. The steady state 3D-TAF model, when excluding these two hours, predicts less than 2.47°C difference of the air temperature and less than 2.29°C difference of the cover temperature, compared with the experimental data. In the case when the soil temperature is assigned as boundary conditions, the steady state 3D-TAF model predicts less than 1.26°C difference of the air temperature and 1.41°C difference of the cover temperature,

compared with the experimental data. The steady state 3D-TAF model predicts closer results with experimental data, compared with Singh et al.'s model. The transient model predicts best results of the soil temperature and predicts similar trends of air and cover temperature, compared with the experimental data. The results are acceptable because (1) the dome in the 3D-TAF model does not have exactly same shape of the greenhouse, (2) the comparison is made with average measured values, and (3) the measured data is available only between 9:00 and 16:00 hours. Since the greenhouse has a semi-cylindrical form, and has the length of 24 m along the east-west cross-section, it has larger glazing area than the hemispherical dome, especially at the east side and the west side, the greenhouse absorbs more solar radiation at 9:00 AM to 10:00 AM in the morning and 15:00 AM to 16:00 AM in the afternoon when the solar altitude is low. Therefore, the air temperature increase in those hours is greater than in the case of a hemispherical glass dome. At noon, the greenhouse has smaller glazing area exposed to the sunshine and therefore the air temperature inside the greenhouse will not increase as rapidly as a dome. All these factors help to explain why the transient 3D-TAF model predicts lower air and cover temperature before 14:00 AM.
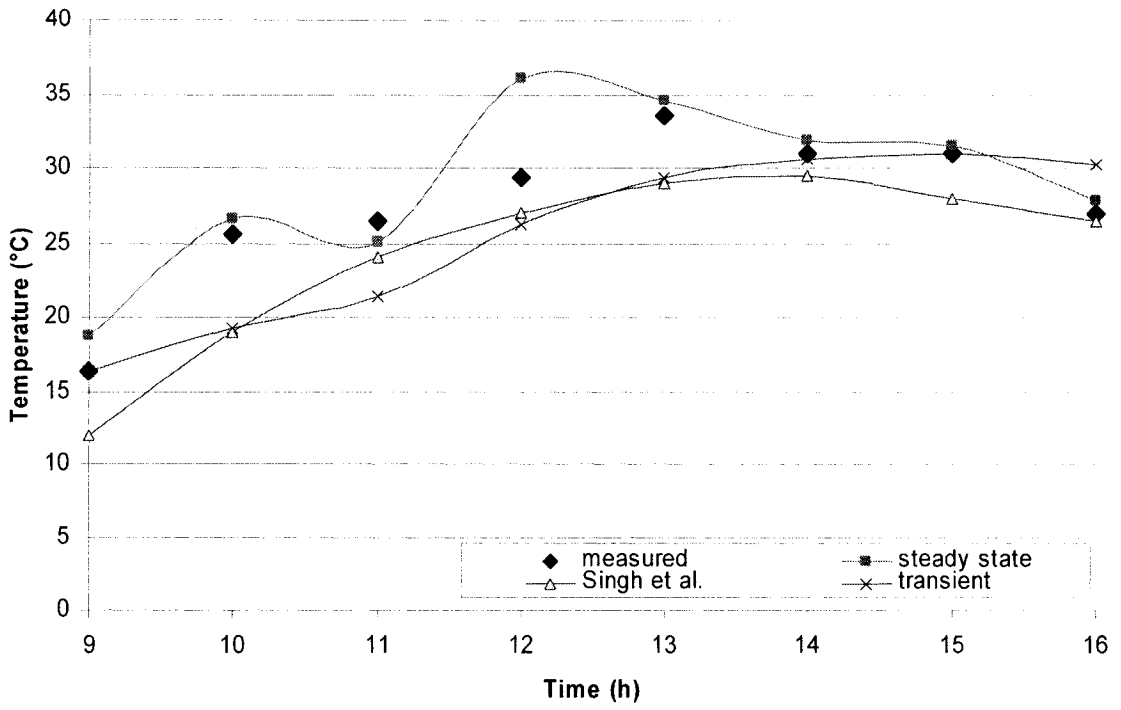
Figure 7-27 Comparison between the indoor air temperature with Singh et al. (2006) on January 26th
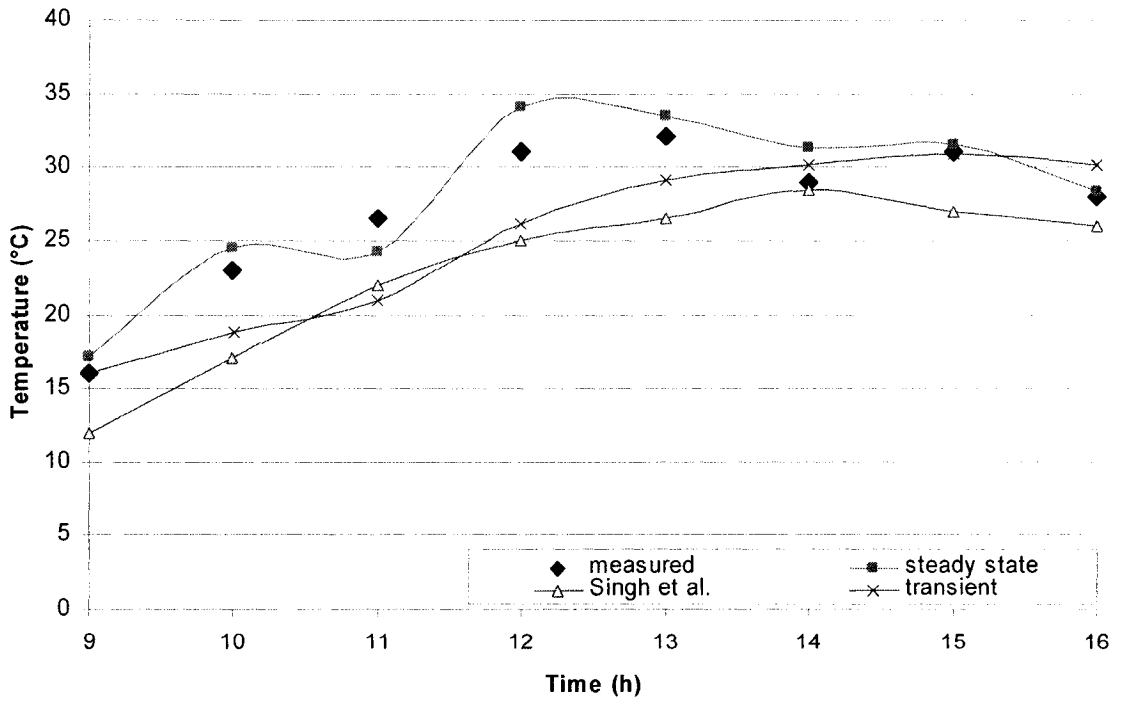
Figure 7-28 Comparison between the cover temperature with Singh et al. (2006) on January 26th
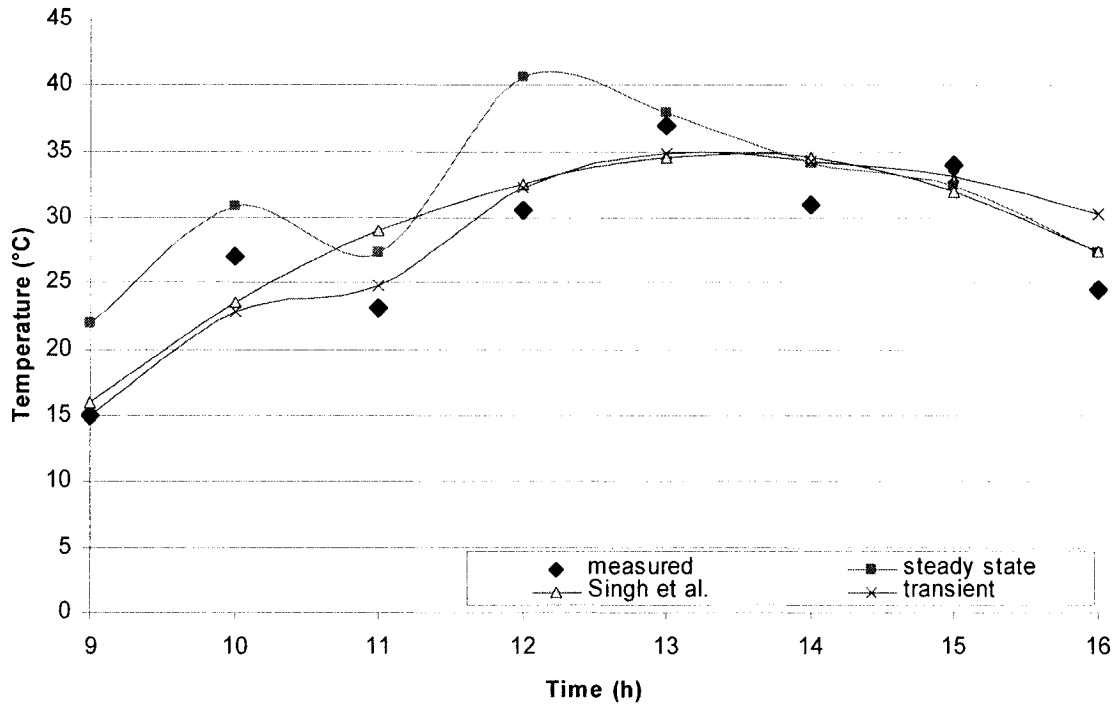
Figure 7-29 Comparison between the bare soil temperature with Singh et al. (2006) on January 26th
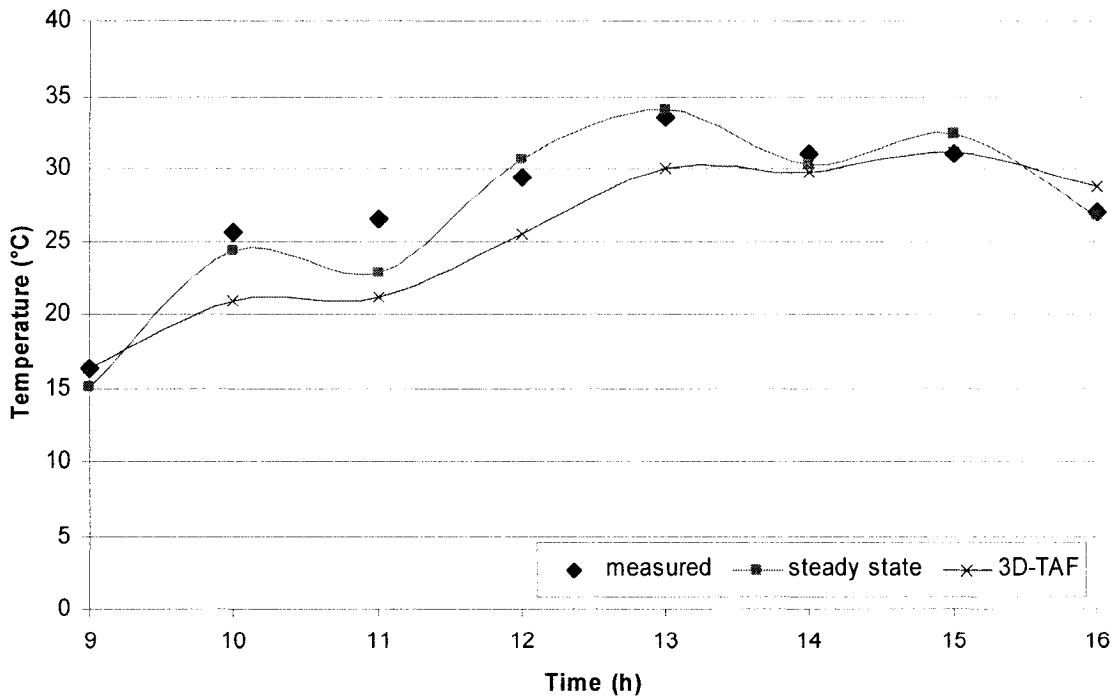
Figure 7-30 Comparison between the indoor air temperature with Singh et al. (2006) on January 26th, with measured soil temperature as boundary condition
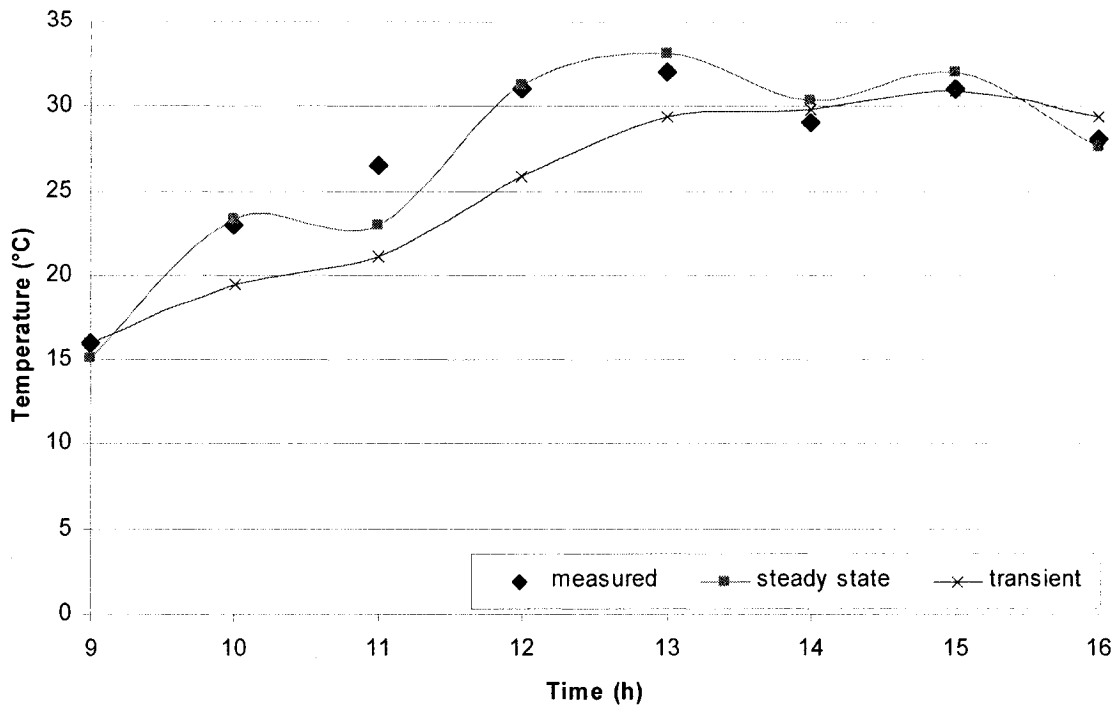
Figure 7-31 Comparison between the cover temperature with Singh et al. (2006) on January 26th, with measured soil temperature as boundary condition

7.5 Conclusion

The comparisons of the computer model with a simplified model under MATLAB environment, from the experimental data, with a CFD model and simulation and experimental results from greenhouses show that the predictions of the model are comparable with those models, simulations and measurements.

Chapter 8 Case Study

This chapter presents a case study of the simulation of the thermal performance of a dome-covered house, located in Montreal. For this purpose, the computer model based on the mathematical model, developed and validated in the previous chapters, is used. This chapter first describes the input and output files. This is followed by the presentation of several results of interest such as the incident solar radiation on cells, the temperature distribution of the air inside the dome, the temperature distribution over the dome surface, and the heating load of the house inside the dome. Finally, sensitivity analysis of the heating load of the house is presented.

8.1 Input File

Input data are arranged in a text file. The following information is required:

a) Global Information

Building azimuth [deg.from north]

Standard longitude [deg. W]

Local longitude [deg. W]

Local latitude [deg. N]

Month [month]

Day of the month [day]

Day of the year [day]

Ground reflectance

Thermal properties of soil: specific heat [J/kg·°C], thermal conductivity [J/m·°C], density [kg/m^3], and ground emissivity.

b) Weather data (hourly values)

Dry bulb temperature [°C]

Wind speed [m/s]

Wind direction [deg. N]

c) Design Parameters

Design room air temperature [°C]

Specific heat of the air [J/kg·°C]

Thermal properties of dome cover: specific heat [J/kg·°C], conductivity [J/m·°C], glazing density [kg/m^3] and glazing emissivity

Optical properties of dome cover: absorptance, reflectance and transmittance

Geometric characteristics: thickness, radius, truncation angle and number of columns (M) and number of rows (N)

House size: length [m], width [m], height [m]

Wall information for each facade: azimuth angle [deg.], tilted angle [deg.], height [m], and width [m], long-wave emissivity of the outside surface, and long-wave emissivity of the inside surface

Roof/floor information: tilted angle [deg.], width [m] and length [m], long-wave emissivity of the outside surface, and long-wave emissivity of the inside surface

Window information for each facade: window-to-wall ratio, width of the window [m], height of the window [m], U-value [W/m^2·°C]

Air infiltration rate of the house [h^{-1}]

Installed lighting density [W/m^2]

Number of occupants

8.2 Output File

The output file presents the hourly data of the following variables: (1) incident solar radiation on each cell of the dome surface, (2) incident solar radiation on the exterior wall/roof surface of the house, (3) temperature of the ouside/inside wall/roof surfaces, (4)

temperature of the floor and ground surface inside the dome, (5) temperature of the outside/inside window surface, (6) temperature of the glazing, (7) the temperature of the air inside the dome, (8) the airflow rates between zones, (9) the infiltration/exfiltration through each cell of the dome surface, (10) the infiltration/exfiltration through the external surface of the house, (11) density and pressure of each zone, and (12) the heating load of the house, (13) convective coefficients for the house external surfaces.

8.3 Case Study

A dome with radius of 20 m, σ_0=20°, built around an L=10 m, W=10 m, H=4 m house (Figure 8-1), located in Montreal is selected for study. The results are compared with a house unprotected by a dome.
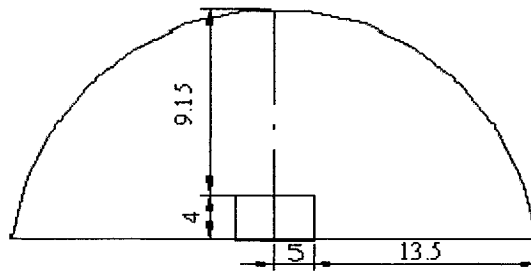
Figure 8-1 Dimension of dome and house

8.3.1 Input Data

The temperature profile, wind speed and wind direction are obtained from Environment Canada (2005). The climatic conditions of the design day per month are presented in Table 8-1. In the first 12 rows of the table, the solar radiation is calculated using the clear sky model (ASHRAE 1992), as it is used in the computer model. For comparison purposes, in the last row, the weather data, including the direct normal solar radiation and diffuse solar radiation over the horizontal surface, are extracted from the EnergyPlus

178

weather file (EnergyPlus, 2006) and applied in the computer program. The U-value of the

window is 1.96 W/m²·°C. Other information is given in Table 8-2.

The natural air infiltration rate for the unprotected house is set equal to 0.15 ACH or

about 3 ACH at 50 Pa pressure difference. This is the average value of blower door tests

on new houses built in Montreal area. In the case of the dome-covered house, the 3D-

TAF model calculates the pressure difference between the outdoor air and the air inside

the dome, and between the air inside the dome and the house. Finally, the natural air

infiltration rates of the dome and house are calculated.

Table 8-1 Climatic conditions of the design day per month

Date	Temperature [°C]			Direct beam solar radiation [W/m²]		Wind speed [m/s]		
	Highest	Average	Lowest	Highest	Average (5 AM~19 AM)	Highest	Average	Lowest
Jan. 21	-18.5	-21.1	-23.3	917	416	13.3	8.8	6.7
Feb. 21	-6.1	-9.8	-13.3	984	529	8.6	5.1	0.0
Mar. 21	3.9	3.2	1.7	996	625	9.7	3.7	0.0
Apr. 21	5	7.3	3.3	960	681	8.9	6.3	2.8
May 21	21.7	15.7	7.2	933	710	8.6	5.4	2.2
June 21	22.1	18.2	12.5	915	711	6.7	3.9	0.8
July 21	26.7	22.1	16.7	907	690	8.6	4.9	2.2
Aug. 21	24.4	19.8	15	914	642	7.2	3.3	0.0
Sep. 21	20.4	15.4	10.9	939	577	3.9	2.3	0.0
Oct. 21	5	2.7	0	939	506	5.8	3.7	1.7
Nov. 21	-5	2.3	-5.6	896	402	5.8	3.4	0.6
Dec. 21	-6.1	-7.7	-12.3	872	356	7.2	5.8	3.6
Jan. 21*	-3.4	-11.7	-16.7	869	360	13.3	8.8	6.7

*with measured solar radiation over the horizontal surface

179

Table 8-2 Input information

Building orientation [deg. from north]	0	Radius (m)	20
Standard longitude [deg.W]	75	Truncation angle [deg.]	20
Local longitude [deg.W]	73.75	Number of columns	42
Local latitude [deg.N]	45.46	Number of rows	13
Ground reflectance	0.2	Length of the house [m]	10
Soil specific heat [J/kg·°C]	730	Width of the house [m]	10
Soil conductivity [W/m·°C]	0.5	Height of the house [m]	4
Soil density [kg/m³]	1500	Brick emissivity	0.93
Ground emissivity	0.8	Gypsum emissivity	0.903
Design room air temperature [°C]	21	Window-to-wall ratio	0.15
Specific heat of the air [J/kg·°C]	1005	Width of the window [m]	3
Glazing specific heat [J/kg·°C]	837	Height of the window [m]	2
Glazing conductivity [J/m·°C]	1.38	U-value of windows[W/m²·°C]	1.96
Glazing density [kg/m³]	2600	Air infiltration rate of the uncovered house [h⁻¹]	0.15
Glazing emissivity	0.84	Installed lighting density [W/m²]	15
Glazing thickness [mm]	24.4	Number of occupants	4

The dome is covered by a single clear glass, with the thickness of 24.4 mm and U-value of 2.44 $W/m^2 \cdot °C$ (LBNL, 2003). The optical glazing properties in terms of the incidence angle are shown in Figure 8-2.
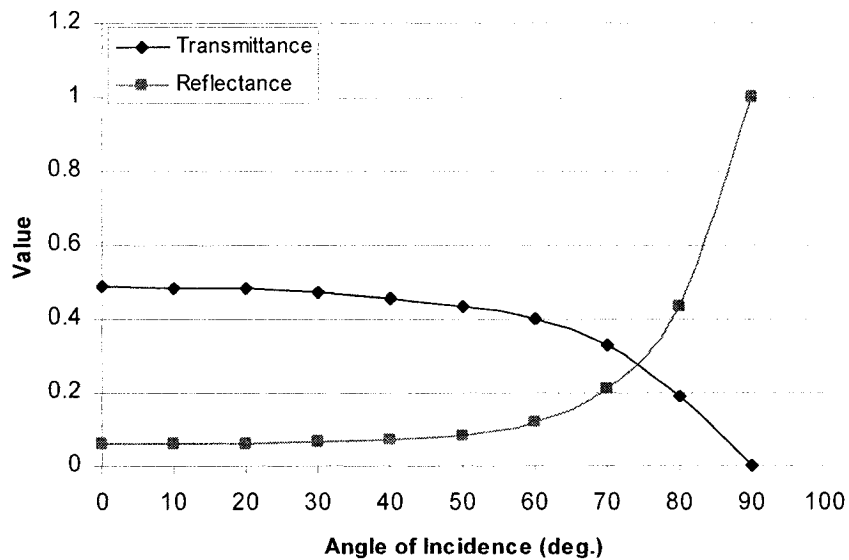
Figure 8-2 Optical properties of the dome cover

The information about layers of the external walls of the house is given in Table 8-3.

Table 8-3 Wall data

Layer name	Specific heat [J/kg·°C]	Conductivity [W/m·°C]	Thickness [mm]	Density [kg/m³]
Face brick	921	1.33	100	2002
Insulation	841	0.043	135	91
Gypsum board	841	0.73	20	1602

The thermal resistance of the external walls, as calculated from Table 8-3, is 3.4 m²·°C/W, equal to the minimum value as requested by the Quebec law.

The information about layers of the roof of the house is given in Table 8-4.

Table 8-4 Roof data

Layer name	Specific heat [J/kg·°C]	Conductivity [W/m·°C]	Thickness [mm]	Density [kg/m³]
Finish*	1088	0.42	130	1249
Insulation	841	0.043	215	91
Gypsum board	841	0.73	20	1602

*Cement plaster, and sand aggregate.

The thermal resistance of the roof, as calculated from Table 8-4, is 5.5 m²·°C/W, while the minimum value as requested by the Quebec law is 5.3 m²·°C/W.

The information about layers of the floor is given in Table 8-5.

Table 8-5 Floor layer information

Layer name	Specific heat [J/kg·°C]	Conductivity [W/m·°C]	Thickness [mm]	Density [kg/m³]
Concrete slab	841	0.81	200	977
Insulation	841	0.043	100	91

8.3.2 Incident Solar Radiation on Selected Cells

In order to see the impact of glazing on the incident solar radiation on each surface, a number of cells are selected for analysis. Table 8-6 shows the positions of the cells of the dome surface.

Table 8-6 Positions of the selected cells

	Low-east	High-east	Low-west	High-west
Azimuth from due north [deg.]	92.1	92.1	268.9	268.9
Tilted angle [deg.]	68.7	18.5	68.7	18.5
Height of the center of the cell from horizontal surface [m]	0.44	10.34	0.44	10.34

The total incident solar radiation on each cell and solar radiation transmitted through each cell are shown in Figures 8-3 and 8-4. It is observed that on January 21st, both the total incident solar radiation and transmitted solar radiation over the low-east cell is higher than that over the high-east cell before 10:00 AM, and after that they becomes lower. For the low-west and high-west, the transition happens at 2:00 PM.
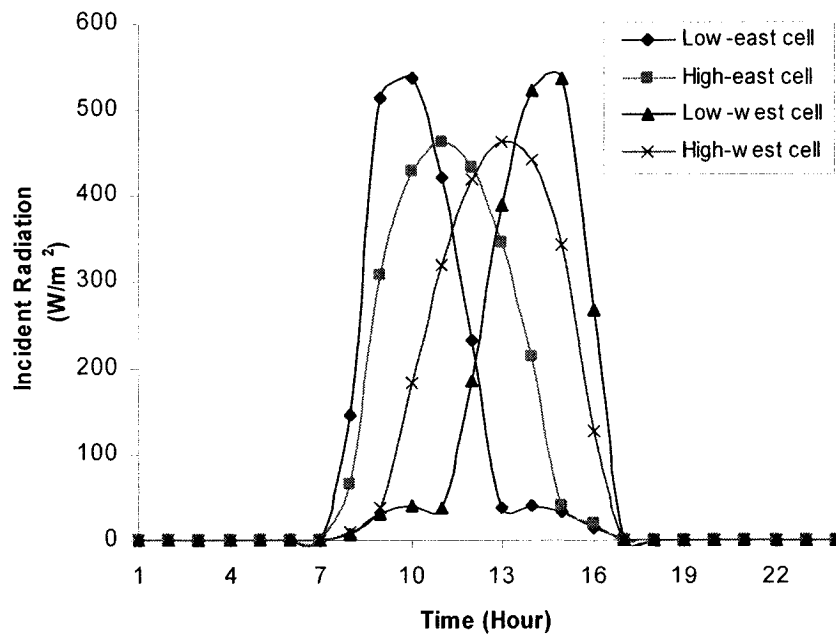
Figure 8-3 Total incident solar radiation on selected cells on January 21st

600

500

400

Transmitted Incident Radiation (W/m²)

300

200

100

0

—♦— Low east
—■— High east
—▲— Low west
—✕— High west

1   4   7   10   13   16   19   22

Time (Hour)
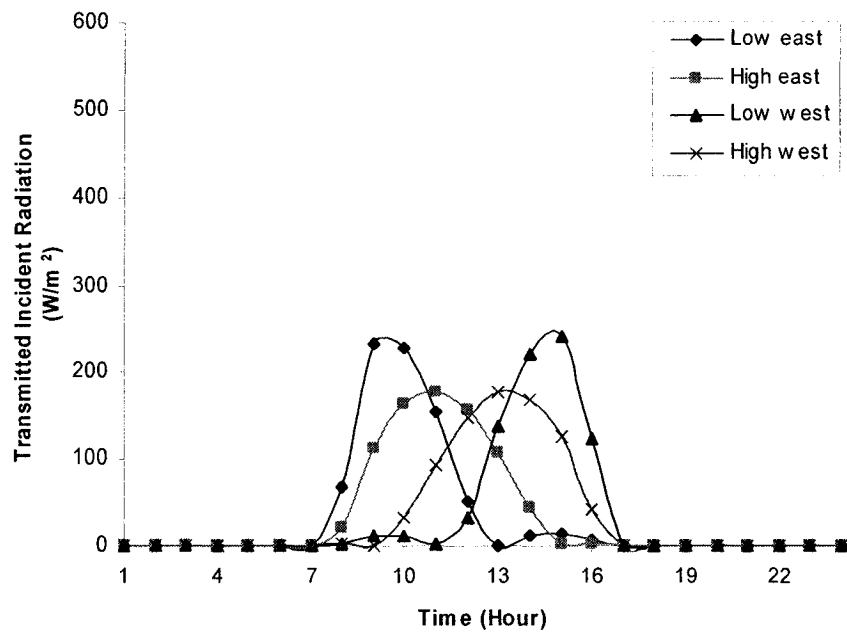
Figure 8-4 Total solar radiation transmitted through selected cells on January 21st

The total incident solar radiation on the outside wall/roof surfaces of the house is shown in Figures 8-5 and 8-6. It is observed that in January, the south wall receives the highest incident solar radiation (Figure 8-5) while in July the roof receives the highest amount of incident solar radiation (Figure 8-6). In summer the roof surface receives twice as much the total incident solar radiation as that in winter.
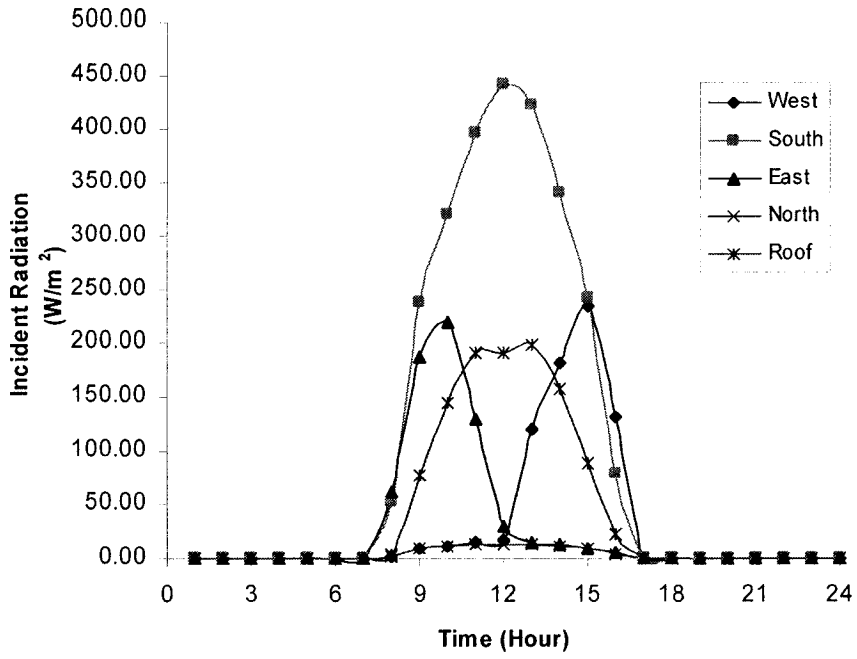
Figure 8-5 Total incident solar radiation over the house on January 21st
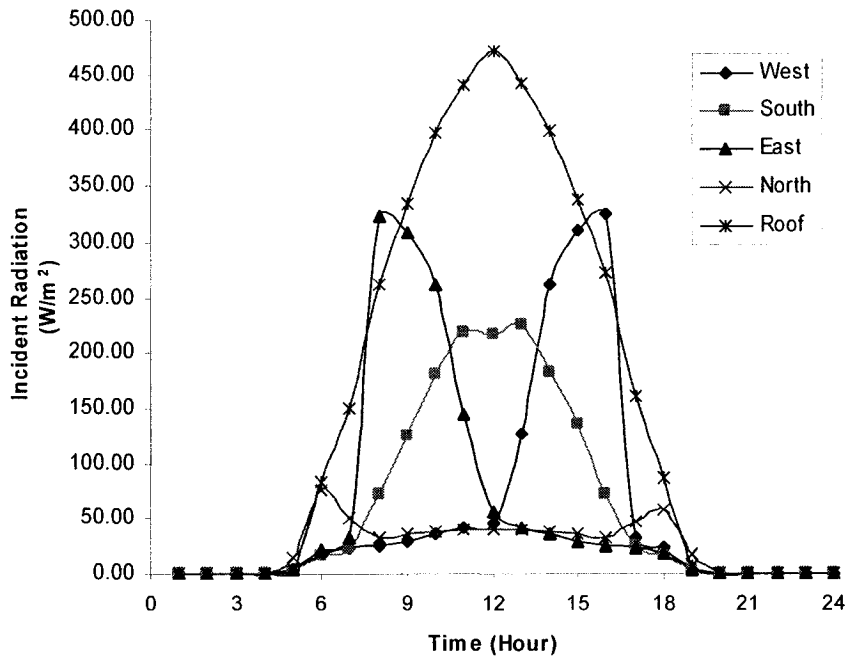
Figure 8-6 Total incident solar radiation over the house on July. 21st

The amount of solar radiation transmitted through the dome glazing and reaches selected cells is shown in Figures 8-7. It is observed that the cells located at the lower part of the dome receive more transmitted solar radiation through dome glazing than the ones located at the upper part. It is observed that less than half of the total incident solar radiation is transmitted through the dome glazing.
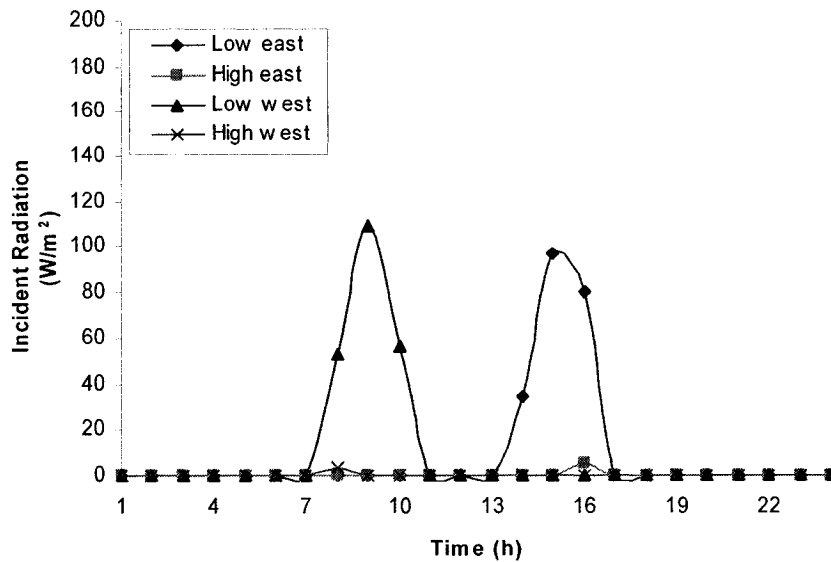
Figure 8-7 Solar radiation transmitted through the dome glazing and reaches selected cells on January 21st

The transmitted solar radiation reaching the ground and roof surfaces on January 21st and July 21st are shown in Figures 8-8 and 8-9, respectively, as well as the solar radiation reaching the cell and reflected to the ground surface. It can be seen that there is larger proportion of reflected solar radiation reaching the ground surface on January 21st than on July 21st, and the amounts of solar radiation reaching the ground surface and the roof surface are almost the same.
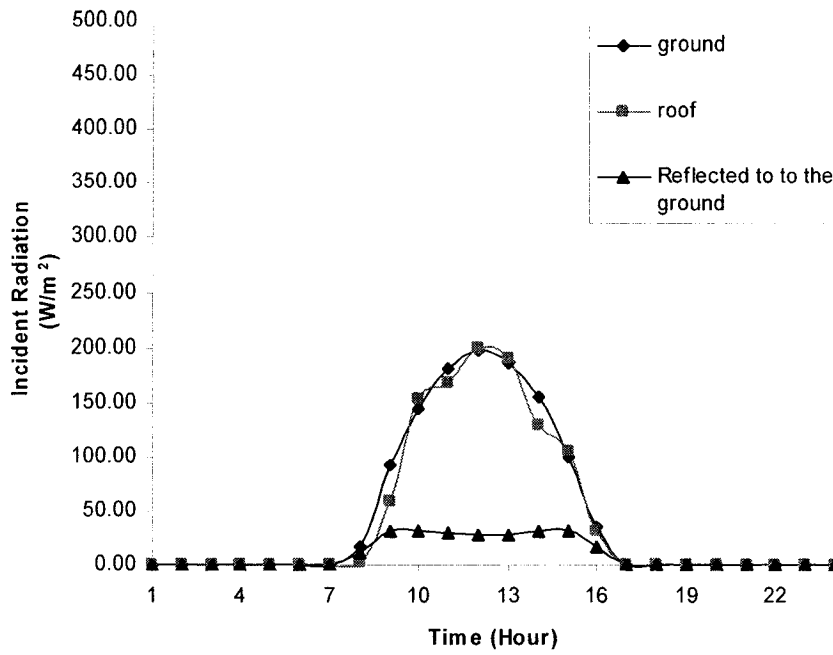
Figure 8-8 Solar radiation over ground and roof on January 21st
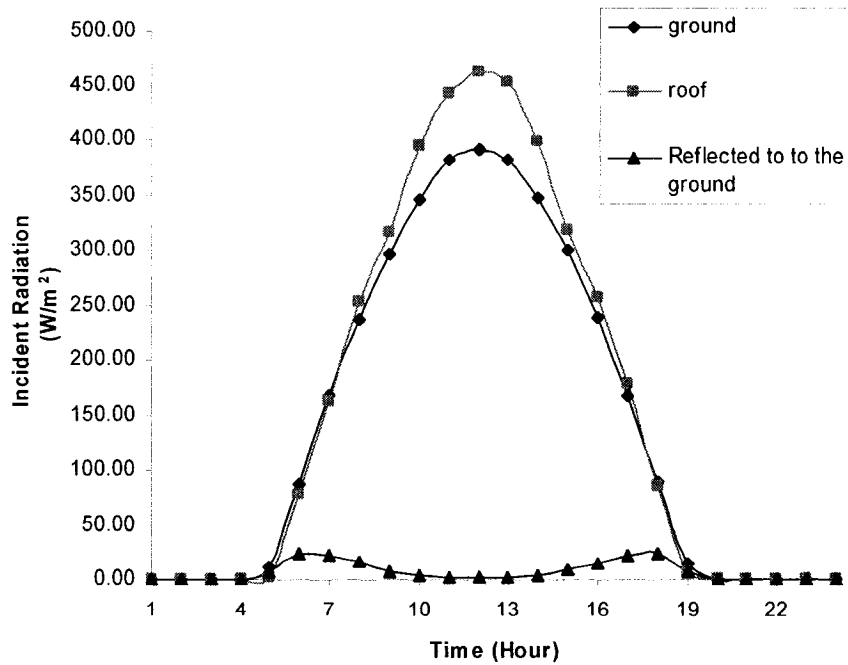
Figure 8-9 Solar radiation over ground and roof on July 21st

8.3.3 Temperature Distribution

The variarion of temperature of the selected surfaces is shown in Figures 8-10. Before 13:00 AM, the temperature of the cells located at the east is higher than the ones located at the west, and from 13:00 AM to 16:00 AM the temperature of the cells located at the west is higher because they receive more solar radiation. Starting from 17:00 AM, the west cell surfaces are cooled by the west wind, and their temperature is near or under the temperature of the east cells. The temperature of the low-west cells is 15.6°C higher than the low-west at 11:00 AM in the morning, and 5.2°C lower at 15:00 AM in the afternoon.
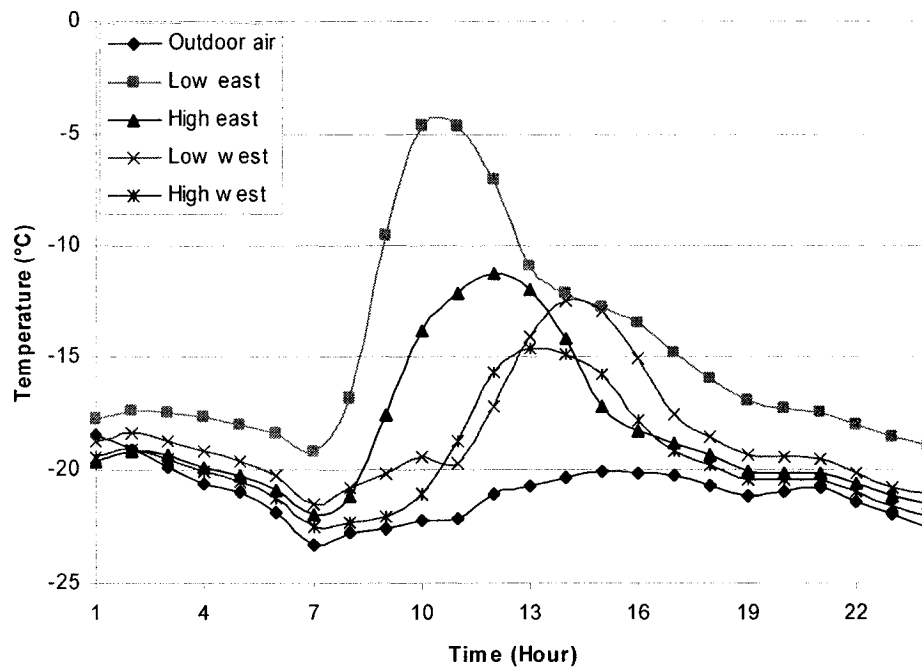
Figure 8-10 Temperature of the selected cells on January 21st

Figure 8-11 presents the temperature distribution over the dome glazing at 10:00 AM. Highest glazing temperature of about 3.1°C is predicted where the cell surface receives

maximum solar radiation (i.e. the cell that is located at the south-east direction and at the bottom of the dome), and the lowest values of about -20.1°C, at the opposite side where the glazing does not receive solar radiation and is exposed to cold wind. The veritical maximum temperature difference between one cell at the bottom and another cell at the top is 16°C.

Surface: Temperature $[°C]$
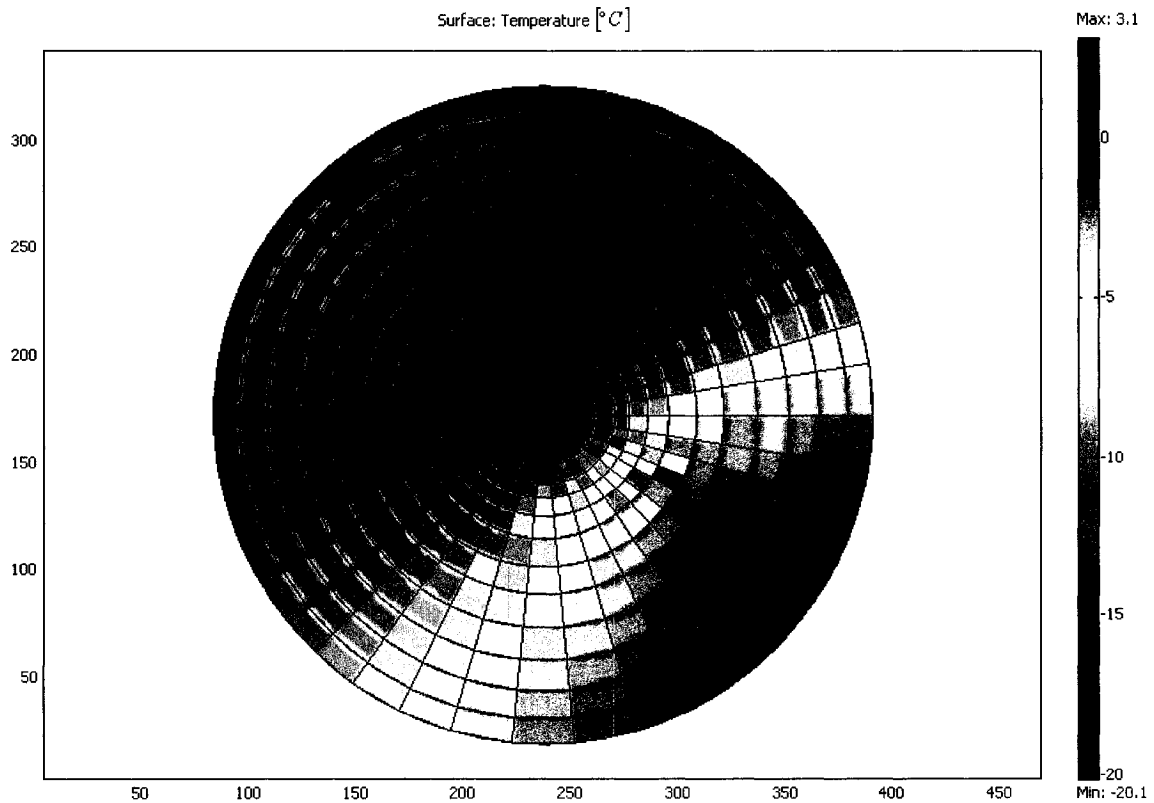
Figure 8-11 Temperature distribution over the dome glazing at 10:00 hours on January 21st

Figure 8-12 presents the air temperature distribution over the east-west cross-section of the dome. The air temperature is higher at the middle of the dome where the house acts as a heater. The air temperature also decreases with the height.

188
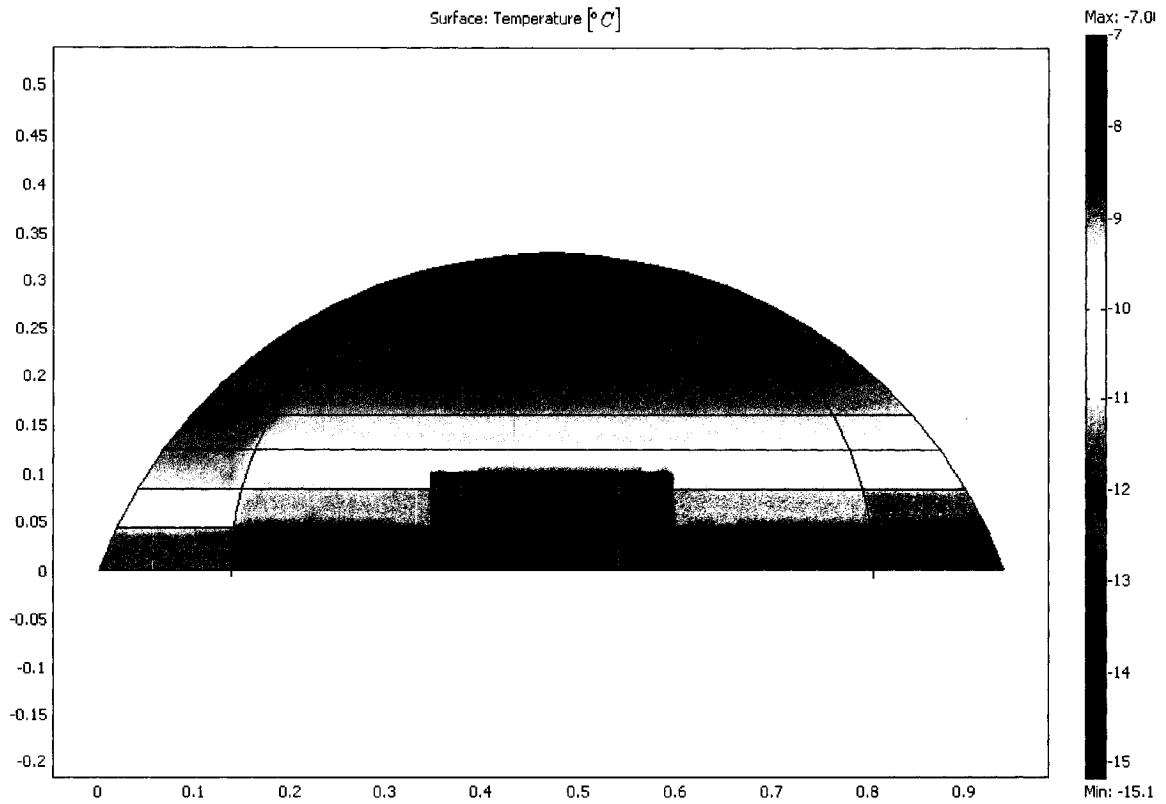
Figure 8-12 Distribution of air temperature at 10:00 AM (E-W cross section) on January 21st

Figure 8-13 presents the variation of the air temperature in the central layer with height at some selected hours. Figure 8-14 presents the variation of the dimensionless air temperature in the central layer with the dimensionless height inside the dome. The associated dimensionless temperature (T*) and the height (H*) inside the dome are defined by:

$$T^* = \frac{T - T_{low}}{T_{high} - T_{low}}$$ (8-1)

$$H^* = \frac{h}{D}$$ (8-2)

189

where:

T=dome air temperature at any given location, °C;

T$_{low}$=lowest temperature, equal to the outdoor air temperature, °C;

T$_{high}$=highest temperature, selected as the maximimum between the roof temperature and the air temperature adjacent to the roof, °C;

h=height inside the dome, m;

D=diameter of the dome, m.

A correlation-based model is developed to predict the dimensionless temperature in terms of the dimensionless height, based on the simulation results (Table 8-7):

$$T^* = aH^* + b \qquad\qquad\qquad (8\text{-}3)$$

where:

a and b=coefficients of the regression model, obtained by the least-squares method (Table 8-7).

The coefficients of the correlation-based model for H*<0.3 is presented in the brackets of Table 8-7. It is observed that the temperature gradient in these hours is around -1.0.
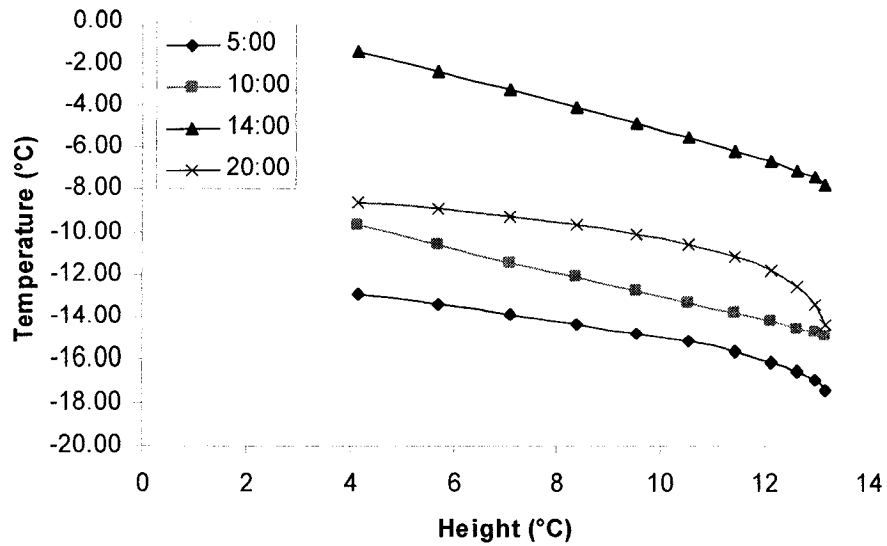
Figure 8-13 Variation of the air temperature with height (central zone) on January 21st
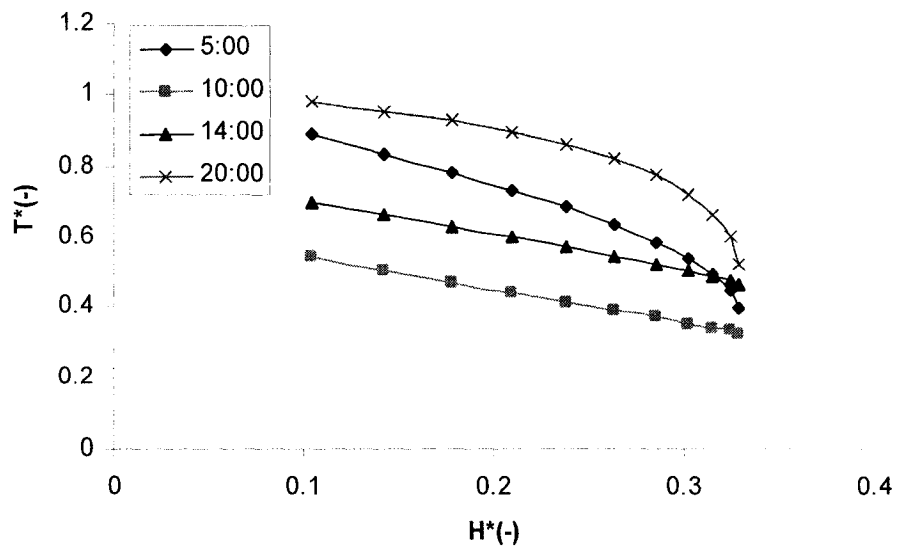
Figure 8-14 Variation of the air temperature with height (central zone, dimensionless plot) on January 21st

Table 8-7 Coefficients of the correlation-based model of the dimensionless temperature with the dimensionless height

	A	b	R^2
5:00 AM	-2.0379	1.1358	0.9579
10:00 AM	-0.9532 (-0.9436)	0.6406 (0.6389)	0.9995 (0.9991)
14:00 AM	-1.0125 (-0.9536)	0.8071 (0.7968)	0.9954 (0.9995)
20:00 AM	-1.7956 (-1.0971)	1.2308 (1.1088)	0.8492 (0.9559)

The variation of average cover temperature and air temperature inside the dome, the temperature of the ground surface inside the dome, and average dome cover temperature, are presented in Figure 8-15. It is observed that the air temperature inside the dome is higher than the outdoor air temperature while lower than the ground temperature. The average difference between the air temperature inside the dome and the outdoor air temperature is 11.4°C. The average dome cover temperature is slightly higher than the outdoor air temperature at night and can be 14.9°C higher at 14:00 AM.
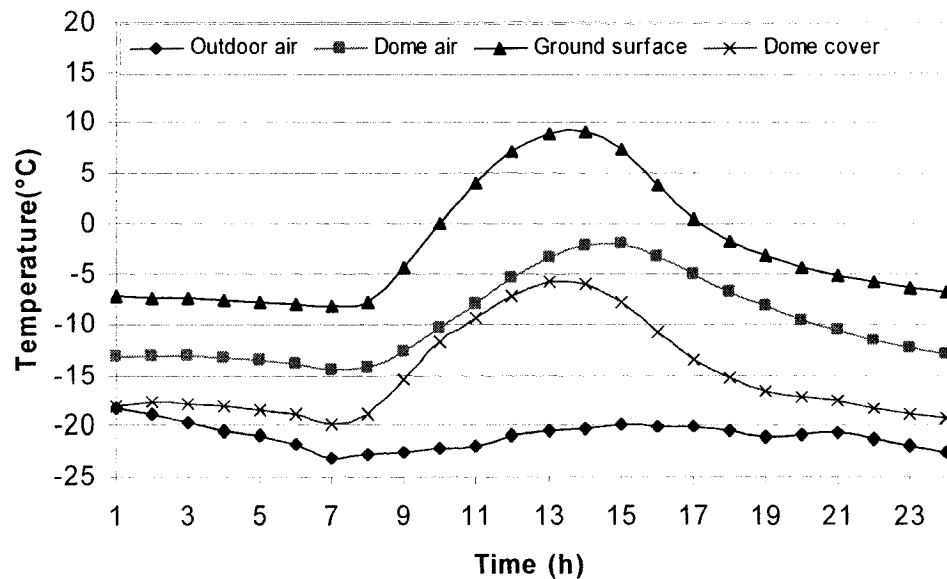
Figure 8-15 Average air temperature inside the dome, ground temperature inside the dome, and average dome cover temperature as predicted by the 3D-TAF model on January 21st

8.3.4 Air Flow Pattern

The mass flow rates of some selected air zones inside the dome are displayed in Table 8-8. The error in calculating the mass flow rate in each air zone is found to be less than $1.6 \cdot 10^{-4}$ kg/s, except for the boundary zone (1,1), where the error is 0.004kg/s or 0.7%. It can be observed that the temperature difference between the lower part of the dome and

the higher part of the dome can reach 7.5°C, and the highest air temperature is near the ground surface.

Table 8-8 Mass flow rate and temperature of selected zones at 10:00AM on January 21st

Location of zones (from bottom to top)		Flow rate in each direction [kg/s]					Mass balance [kg/s]	Temperature [°C]
		right	left	down	up	central		
East	1,1	-0.2107	0.2282	0.0000	0.1682	-0.1888	-0.00385	-7.68
	1,2	-0.1384	0.1724	-0.1682	0.1801	-0.0460	-3.0E-06	-8.91
	1,3	0.0011	-0.0242	-0.1801	0.2103	-0.0072	-6.7E-05	-9.84
	1,4	0.0490	-0.1011	-0.2103	0.2656	-0.0031	2.6E-05	-10.65
	1,5	0.0586	-0.0919	-0.2656	0.2771	0.0216	-1.6E-04	-11.25
	1,6	0.0573	-0.0583	-0.2771	0.2349	0.0434	1.0E-04	-11.80
	1,7	0.0463	-0.0355	-0.2349	0.1723	0.0517	9.0E-06	-12.33
	1,8	0.0323	-0.0210	-0.1723	0.1119	0.0490	-7.5E-05	-12.81
	1,9	0.0198	-0.0104	-0.1119	0.0623	0.0402	7.4E-05	-13.28
	1,10	0.0099	-0.0049	-0.0623	0.0285	0.0288	-6.1E-05	-13.74
	1,11	0.0037	-0.0021	-0.0285	0.0098	0.0172	-4.0E-06	-14.12
	1,12	0.0009	-0.0006	-0.0098	0.0017	0.0077	5.0E-06	-14.41
	1,13	0.0001	0.0000	-0.0017	0.0000	0.0017	-2.0E-06	-14.68
West	22,1	-0.0203	0.0258	0.0000	-0.3236	0.3210	-1.0E-04	-8.84
	22,2	0.0135	0.0060	0.3236	-0.4873	0.1442	1.7E-05	-10.24
	22,3	0.0143	-0.0129	0.4873	-0.4934	0.0047	-3.0E-06	-11.11
	22,4	0.0086	-0.0144	0.4934	-0.4002	-0.0873	1.1E-04	-11.65
	22,5	0.0050	-0.0105	0.4002	-0.2975	-0.0972	-6.9E-05	-12.18
	22,6	0.0023	-0.0053	0.2975	-0.2135	-0.0810	-2.3E-05	-12.73
	22,7	0.0000	-0.0012	0.2135	-0.1482	-0.0640	1.3E-04	-13.31
	22,8	-0.0018	0.0005	0.1482	-0.0956	-0.0514	-1.6E-04	-13.86
	22,9	-0.0024	0.0012	0.0956	-0.0545	-0.0400	-8.3E-05	-14.34
	22,10	-0.0018	0.0012	0.0545	-0.0257	-0.0282	2.0E-05	-14.75
	22,11	-0.0011	0.0009	0.0257	-0.0089	-0.0167	-1.8E-05	-14.99
	22,12	-0.0004	0.0004	0.0089	-0.0015	-0.0074	-3.0E-06	-15.13
	22,13	0.0000	0.0001	0.0015	0.0000	-0.0016	-2.0E-06	-15.15

Table 8-9 presents the average air velocity in the selected zones. It is observed that the air flow rises from the warm east and moves down along the cold west in the dome. The predicted air velocity in each zone is less than 0.16m/s.

Table 8-9 Velocity of selected zones at 10:00AM on January 21st

Location of zones (from bottom to top)		Velocity in each direction [m/s]				
		right	left	down	up*	central
East	1,1	-0.01487	0.016104	0	0.009325	-0.0668
	1,2	-0.01063	0.013242	-0.009282	0.010989	-0.0177
	1,3	9.82E-05	-0.00207	-0.0109508	0.014478	-0.0031
	1,4	0.004791	-0.0099	-0.0144334	0.021208	-0.00151
	1,5	0.006764	-0.01061	-0.02116	0.026524	0.012467
	1,6	0.00806	-0.0082	-0.0264683	0.027987	0.030617
	1,7	0.008302	-0.00636	-0.0279311	0.026817	0.046469
	1,8	0.007785	-0.00505	-0.026767	0.024218	0.059098
	1,9	0.0069	-0.00361	-0.0241742	0.020491	0.07002
	1,10	0.005509	-0.00272	-0.0204547	0.016308	0.080584
	1,11	0.003901	-0.00225	-0.0162838	0.012349	0.092274
	1,12	0.002532	-0.00162	-0.0123352	0.008544	0.111092
	1,13	0.001491	-0.00097	-0.0085354	0	0.167335
West	22,1	-0.00143	0.00182	0	-0.01793	0.113463
	22,1	0.001038	0.00046	0.0178394	-0.0297	0.055441
	22,3	0.001226	-0.0011	0.0296449	-0.03399	0.001999
	22,4	0.000846	-0.00141	0.0338664	-0.03197	-0.04284
	22,5	0.000571	-0.00121	0.0318664	-0.02846	-0.05616
	22,6	0.000324	-0.00074	0.0283782	-0.02541	-0.0571
	22,7	0	-0.00022	0.025352	-0.02302	-0.0574
	22,8	-0.00044	0.000114	0.0229735	-0.02065	-0.06187
	22,9	-0.00084	0.000419	0.0206087	-0.01788	-0.06953
	22,10	-0.00103	0.000686	0.0178463	-0.01464	-0.07886
	22,11	-0.00115	0.000989	0.0146213	-0.01119	-0.08912
	22,12	-0.00112	0.001206	0.0111825	-0.00774	-0.10529
	22,13	-0.00081	0.001072	0.0077372	0	-0.15562

*positive number means flows up while negative number means goes down

Figure 8-16 presents the plan view of the flow directions (up-down) for the perimeter zones at 10:00 AM, on January 21st. It is observed that the air flow arises from the east and south. At such locations the dome cover receives more solar radiation than other parts and is less affected by the cold wind, and thus the air inside the dome is warmer than at other locations where the air moves down. Because the house inside the dome acts as a heater, the air rises up from the center of the dome.

194

Direction of wind

Direction of solar radiation
10:00AM
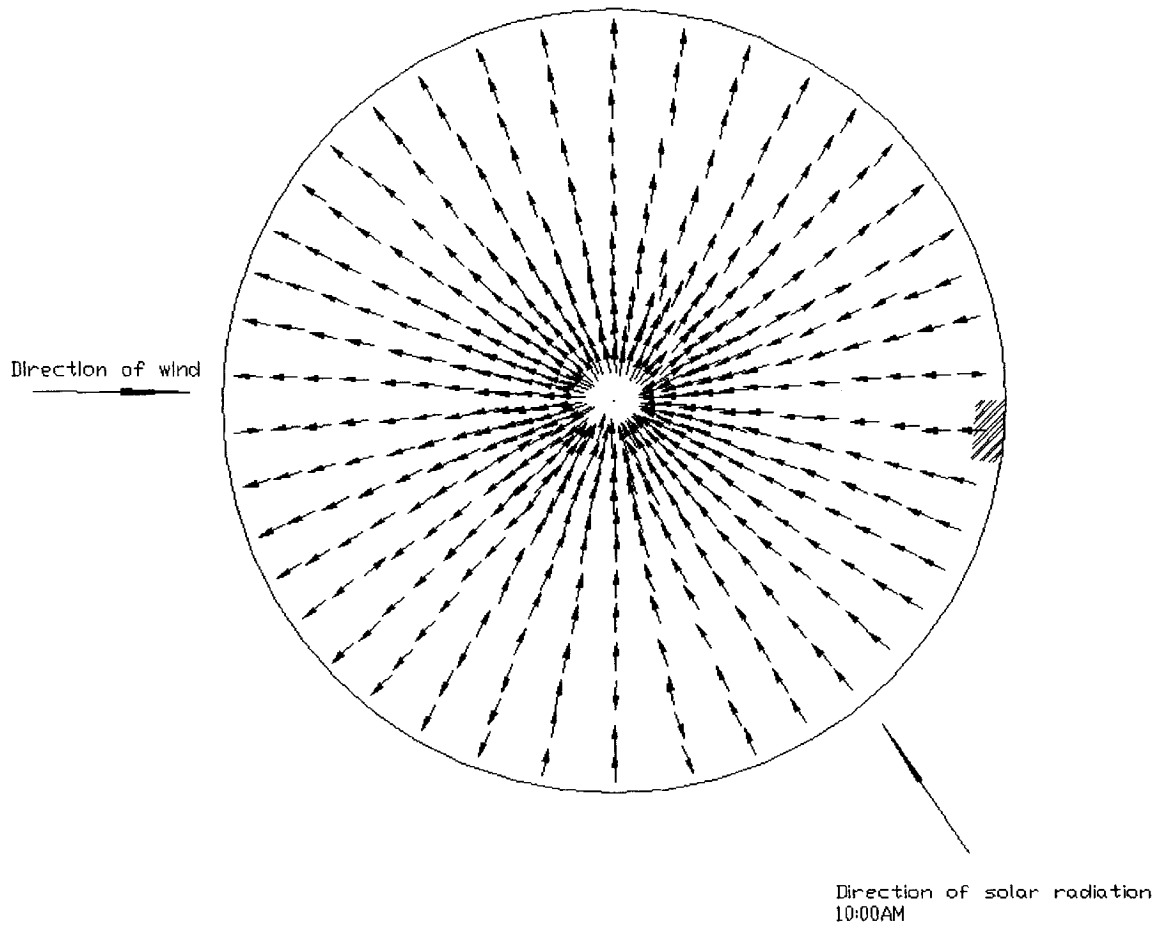
Figure 8-16 Plan view of the flow direction at 10:00 AM on January 21st

Figure 8-17 presents the airflow pattern for the east-west cross-section of the dome and Figure 8-18 shows the plan view at 10:00 AM. It is observed that the airflow rises from the middle of the dome and near the east inside the dome, and then goes down along the west side of cover. The air infiltrates along the wind direction, and also in the lower right-corner cell, where the inside air pressure is lower than the outside pressure. The relative error of the air mass balance due to the infiltration/exfiltration through the dome is equal to 6.8%.

$T_{in} = -14.9°C$

$C_p = -0.55$

$\dot{m} = 2.55 \times 10^{-4}\ kg/s$

Direction of wind

To=-22.2 C
10:00AM

$T_{in} = -8.9°C$

$C_p = 0.243$

$\dot{m} = 2.95 \times 10^{-3}\ kg/s$

$T_{in} = -7.7°C$

$C_p = -0.011$

$\dot{m} = 7.46 \times 10^{-4}\ kg/s$

Solar radiation
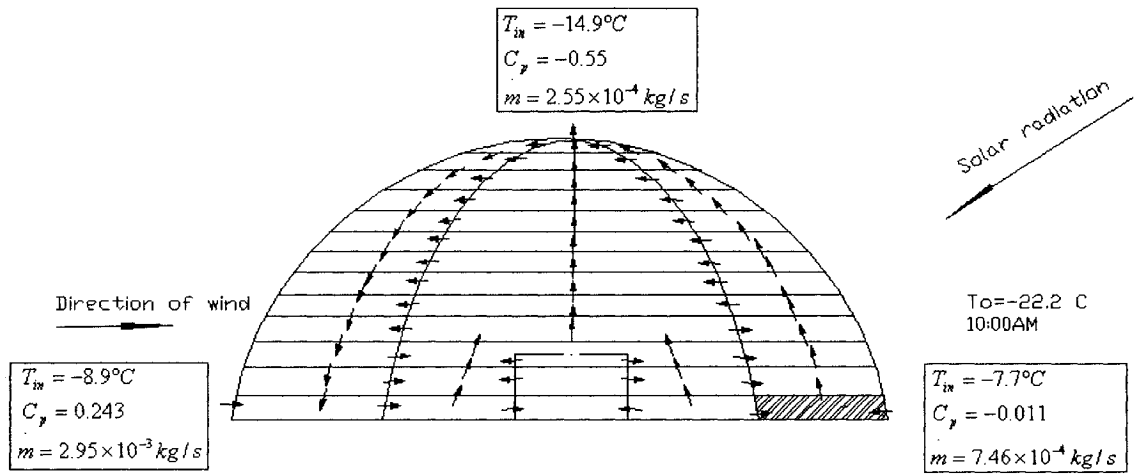
Figure 8-17 Pattern of vertical airflow on the east-west cross-section of the dome as predicted by the 3D-TAF model at 10:00 AM on January 21st

$T_{in} = -8.9°C$

$C_p = -0.085$

$\dot{m} = 8.09 \times 10^{-4}\ kg/s$

$T_{in} = -8.7°C$

$C_p = -0.018$

$\dot{m} = 6.07 \times 10^{-4}\ kg/s$

$T_{in} = -9.0°C$

$C_p = -0.003$

$\dot{m} = 8.14 \times 10^{-4}\ kg/s$

$T_{in} = -8.6°C$

$C_p = -0.096$

$\dot{m} = 9.34 \times 10^{-4}\ kg/s$

Direction of wind

$T_{in} = -8.9°C$

$C_p = 0.243$

$\dot{m} = 2.95 \times 10^{-3}\ kg/s$

$T_{in} = -7.7°C$

$C_p = -0.011$

$\dot{m} = 7.46 \times 10^{-4}\ kg/s$

$T_{in} = -7.8°C$

$C_p = -0.018$

$\dot{m} = 6.22 \times 10^{-4}\ kg/s$

$T_{in} = -7.6°C$

$C_p = -0.085$

$\dot{m} = 7.64 \times 10^{-4}\ kg/s$

$T_{in} = -7.3°C$

$C_p = -0.003$

$\dot{m} = 8.58 \times 10^{-4}\ kg/s$

$T_{in} = -7.3°C$

$C_p = -0.096$

$\dot{m} = 9.16 \times 10^{-4}\ kg/s$

Direction of solar radiation
10:00AM

To=-22.2°C
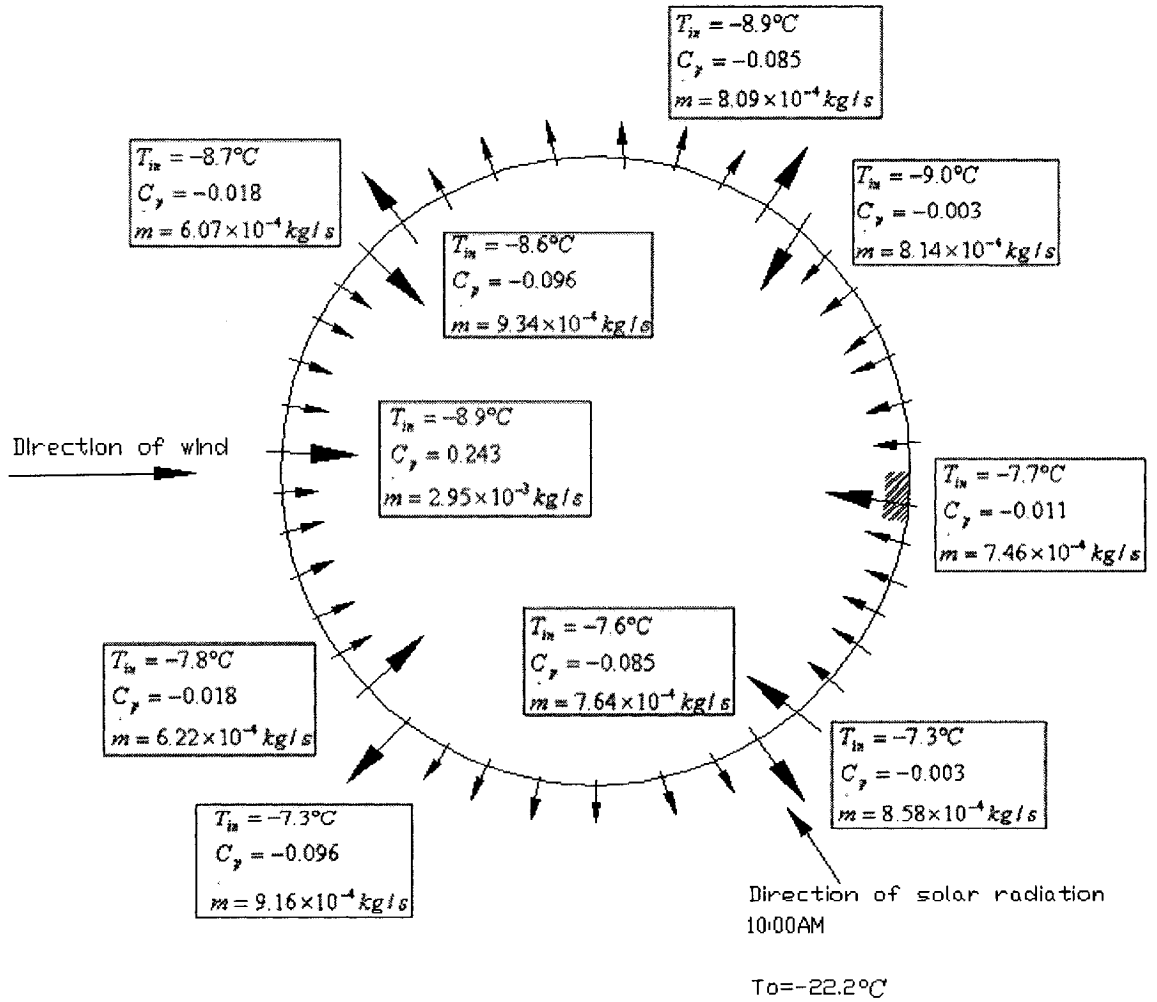
Figure 8-18 Air infiltration/exfiltration through the dome cells of the first layer near the ground as predicted by the 3D-TAF model at 10:00 AM on January 21st

196

8.3.5 Heating Load of the House

The outdoor air temperature of two design days, is given in Figures 8-19 (January 21st)

and 8-21 (December 21st). The heating load of a dome-covered house, compared with a

non-protected house, is given in Figure 8-20 (January 21st) and 8-22 (December 21st).

The dome covere reduces the heating load of 44.6% and 51.4% on January 21st and

December 21st, respectively.
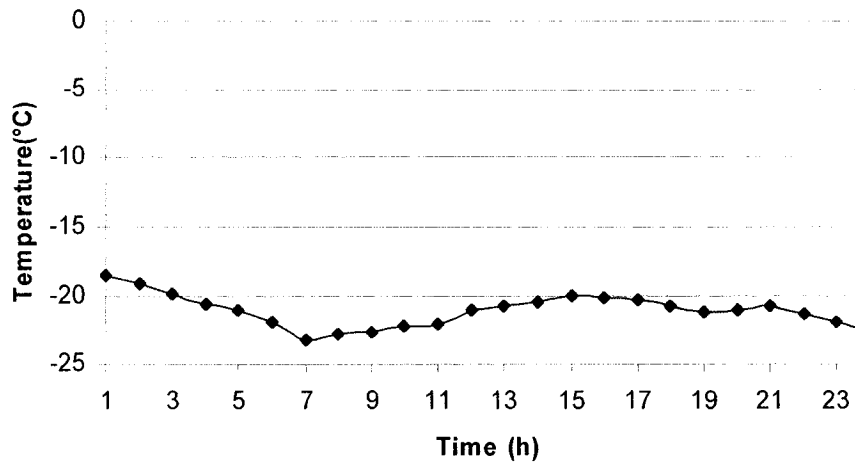
Figure 8-19 Outdoor air temperature on January 21st
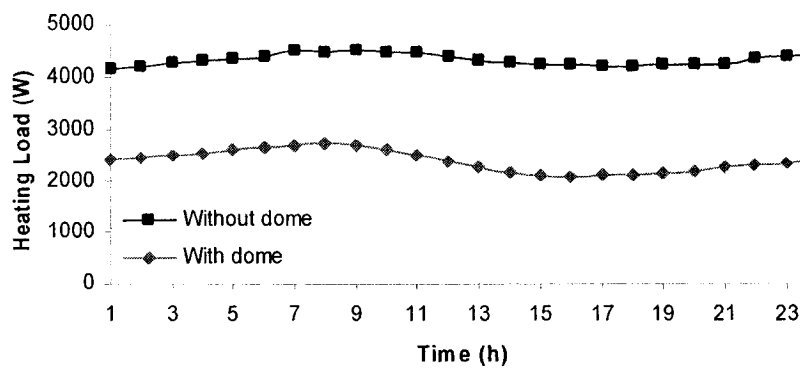
Figure 8-20 Heating load of the dome-covered house vs. the house without dome on January 21st
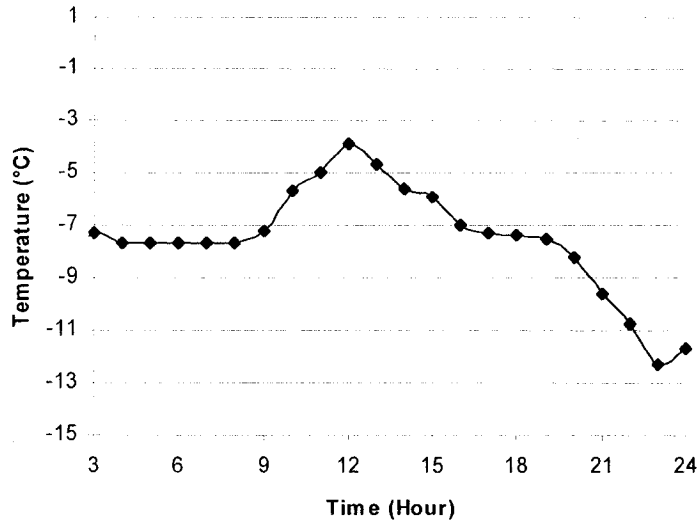
Figure 8-21 Outdoor air temperature on December 21st
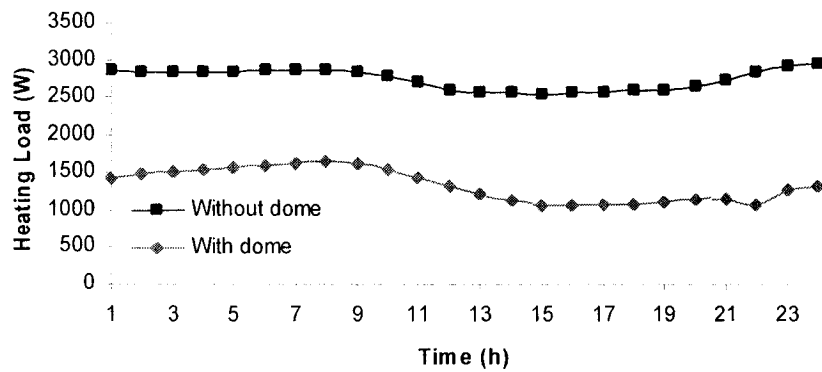
Figure 8-22 Heating load of the dome-covered house vs. the house without dome on December 21st

Table 8-10 compares the daily heating load of the house without and with a dome. A reduction of 62.6% of the annual heating load of the house is expected. The reduction of the heating load is due to: (a) the reduction of infiltration heat loss; the use of the dome reduces the natural infiltration air change rate of the house from 0.15 ACH to 0.06~0.08 ACH; (b) the increase of the air temperature around the house inside the dome; the air temperature inside the dome is, on the average, 11.4°C higher than the outdoor air

temperature on January 21st (Figure 8-15); (c) the reduction of the convective heat transfer coefficient over the external surfaces of the house; it decreases from 14~34 W/m$^2\cdot$°C (without cover) to 2~3 W/m$^2\cdot$°C (with cover) and therefore the convective heat loss is reduced. The reduction of heat losses through walls accounts for 21.5% of the total reduction, for the roof is 12.6%, for the floor is 23.7%, for the windows is 14.9%, and due to infiltration is 23.7%.

The peak heating load of the dome-covered house on January 21st is 2.7kW, compared with 4.5kW for the house without a dome. In the last row of the table, the solar radiation is extracted from weather file (EnergyPlus, 2006), and the peak heating load of the dome-covered house is 1.91kW, compared with 3.52kW for the unprotected house.

Table 8-10 Daily heating load (kWh) during heating season

Day	Without dome	With dome	Reduction [%]
Jan. 21	103.7(4.5kW**)	57.4(2.7kW**)	44.6
Feb. 21	66.8	20.0	70.1
Mar. 21	25.9	0	100
Apr. 21	8.8	0	100
Oct. 21	15.8	0	100
Nov. 21	41.2	13.2	68.0
Dec. 21	65.6	31.9	51.4
Total	327.8	122.5	62.6
Jan. 21*	76.1 (3.52kW**)	37.4 (1.91kW**)	51.4

*weather data from the EnergyPlus weather file
**peak heating load

8.4 Sensitivity Analysis

This section presents the impact of selected changes of the case study on the heating load. The variables used in the sensitivity analysis are: (1) optical properties of the glazing, (2) thermal properties of the ground inside the dome, (3) infiltration airflow rate through the dome, (4) exfiltration airflow rate through the house, (5) truncation angle of the dome, (6) radius of the dome, and (7) C$_p$ values over the dome surface. Those variables are selected

because they affect the amout of transmitted solar radiation, heat loss through the ground, heat loss through the dome/house, and heat transfer rate over the dome surface.

8.4.1 Impact of Optical Properties on the Heating Load of the House

In order to see the impact of the optical properties of the glazing on the heating load of the house, another glass with thickness of 12.7 mm, and U-value of 2.49 $W/m^2.°C$ (LBNL, 2003) is selected for comparison. The optical properties of the glazing are shown in Figure 8-23.
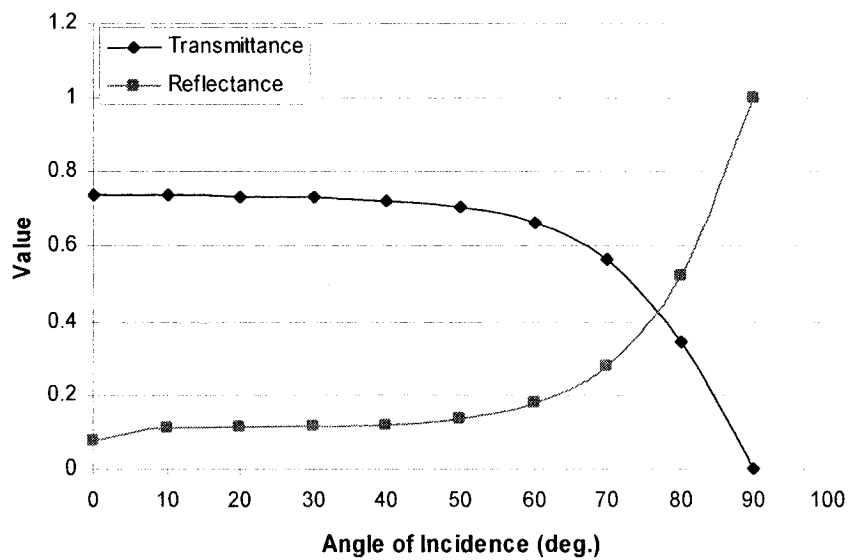
Figure 8-23 Optical properties of the new glazing

Figures 8-24 display the the heating load when the two glazings are used. It can be seen that, since the thinner glazing allows more solar radiation to transmit through the dome, the heating load of the house in winter is reduced by 13.5%.
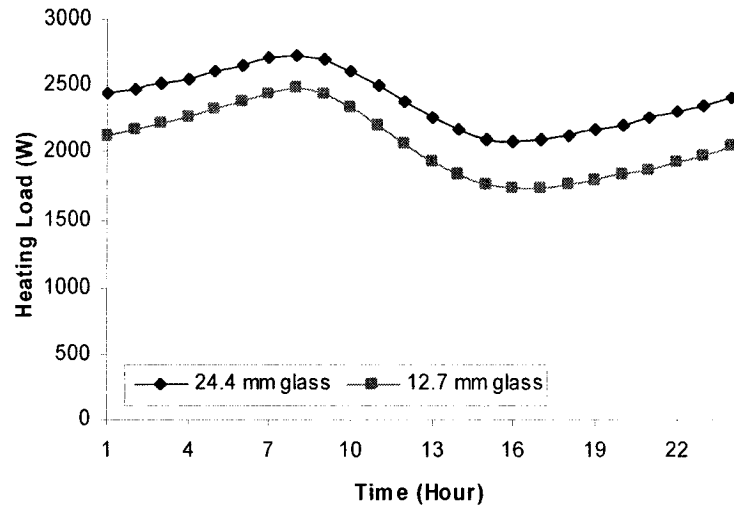
Figure 8-24 Comparison of the heating load using different glazings

The sensitivity coefficient η_τ is defined to see the impact of increase in transmittance of

the glazing on the heating load of the house:

$$\eta_\tau = \frac{\dfrac{HL_2 - HL_1}{HL_1}}{\dfrac{\tau_2 - \tau_1}{\tau_1}} \cdot 100\% \qquad\qquad (8\text{-}4)$$

where:

HL_1=daily heating load of the house with dome glazing thickness of 24.4 mm, kWh;

HL_2=daily heating load of the house with dome glazing thickness of 12.7 mm, kWh;

τ_1=normal transmince of the glazing with thickness of 24.4 mm;

τ_2= normal transmince of the glazing with thickness of 12.7 mm.

The predicted values of η_τ is -26.2%, which means that the increase of the transmittance of the glazing results in the decrease of the heating load of the house.

8.4.2 Impact of Concrete-covered Ground on the Heating Load of the House

A concrete slab of 1.0 m thickness is simulated to cover the ground inside the dome. The thermal properties of the concrete and of the soil are shown in Table 8-11.

Table 8-11 Properties of concrete vs. soil

	Specific heat [J/kg.°C]	Conductivity [W/m·°C]	Density [kg/m^3]
Concrete	841	1.73	2243
Soil	730	0.5	1500

There is a negligible impact of concrete-covered ground on the heating load of the house (Figure 8-25).

The sensitivity coefficient η_m is defined to see the impact of increase in thermal mass of the ground on the heating load of the house:

$$\eta_m = \frac{\dfrac{HL_2 - HL_1}{HL_1}}{\dfrac{(m \cdot c_p)_2 - (m \cdot c_p)_1}{(m \cdot c_p)_1}} \cdot 100\% \qquad (8\text{-}5)$$

where:

HL_1=daily heating load of the house with ground inside the dome composed of soil, kWh;

HL_2=daily heating load of the house with ground of inside the dome composed of concrete, kWh;

202

$(m \cdot c_p)_1$=thermal mass of the ground inside the dome composed of soil, J/°C;

$(m \cdot c_p)_2$= thermal mass of the ground inside the dome composed of concrete, J/°C.

The predicted value of η_m is 42%, which means that the increase of the thermal mass of the ground inside the dome results in the increase of the heating load of the house.
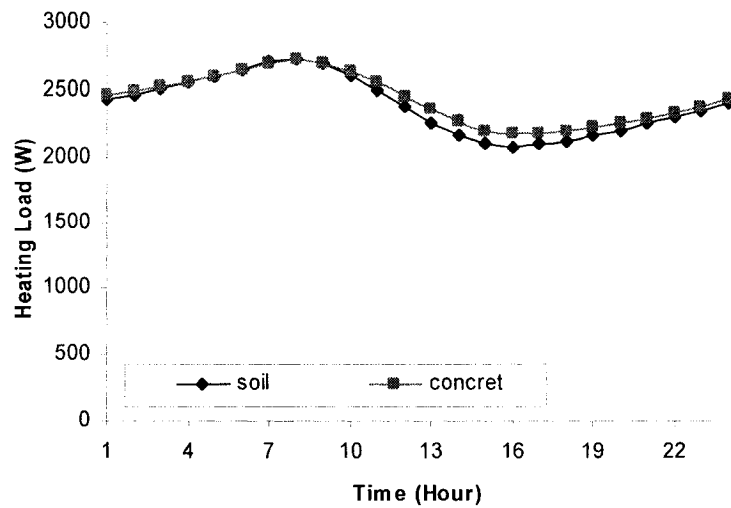
Figure 8-25 Comparison of the heating load using different materials

Figure 8-26 presents the hourly variation of the ground temperature under different schemes. It is observed that during the day, the ground temperature inside the dome is highest using the thinner glazing and lowest using a concrete ground.
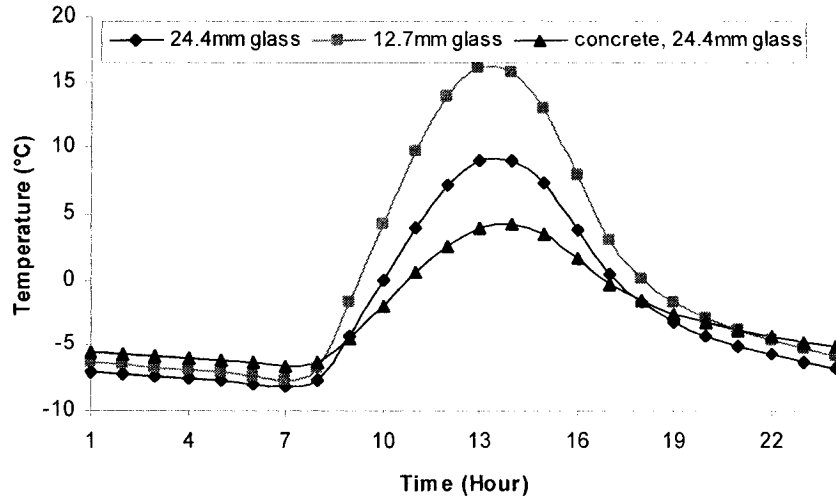
Figure 8-26 Comparison on the ground surface temperature of different schemes on January 21st

8.4.3 Impact of Infiltration Rate on the Heating Load of the House

A typical value of pressure exponent n=0.65 is recommended by ASHRAE (2001a) to calculate the air leakage at pressure difference for 10~75 Pa. Measurements of single cracks (Honma, 1975; Krieth and Eisenstadt, 1957), however, have shown that n can vary if the pressure difference changes over a wide range. Typically, the value n can vary from 0.5 for turbulent flow to 1.0 for laminar flow. Therefore, a sensitivity analysis of the air change rate and heating load due to different values of n (case no.1, n=0.65 and case no.2, n=1.0) is performed. Figure 8-27 presents the comparison between the air infiltration rates (ACH) of the dome/house using the two selected n values. When a higher n value is used (n=1.0 vs. n=0.65), the predicted air leakage is greater. The exfiltration through the house decreases when the air temperature inside the dome increases, and the infiltration increases when the wind speed increases. The average difference of the airleakage of the house due to n between 0.65 and 1.0 is about 0.011ACH, and 0.014ACH for the dome.
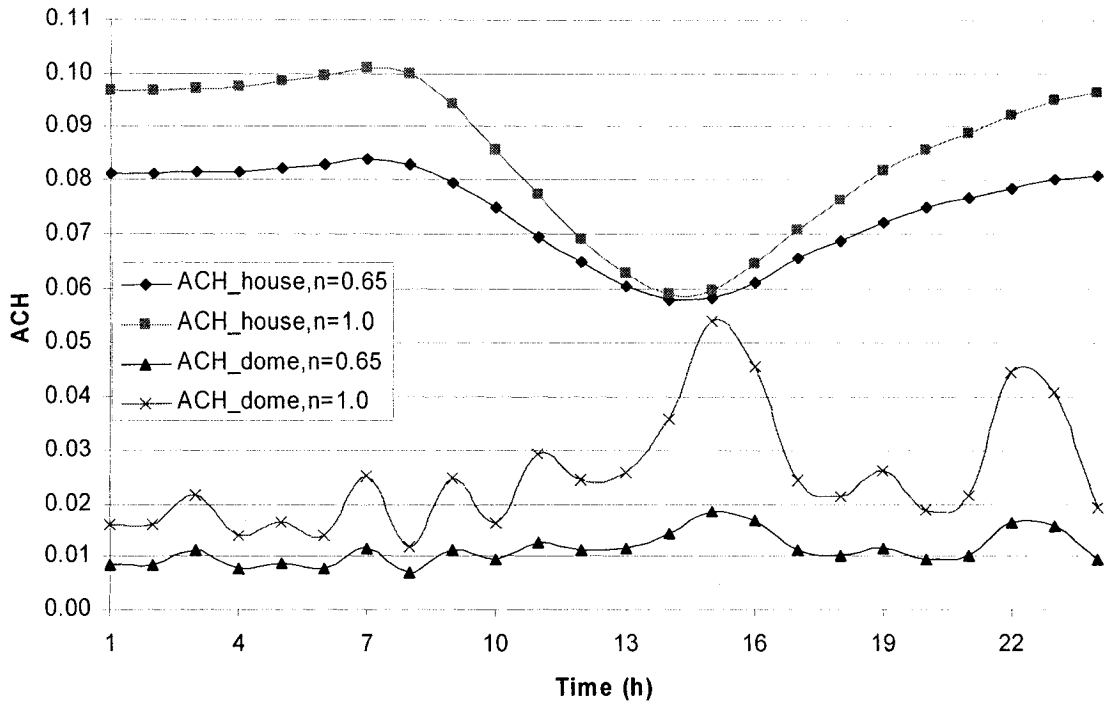
Figure 8-27 Comparison between the air change rates per hour for the dome/house with different n values

Two sensitivity coeffiecients η_d and η_h are defined to analyze the impact of different values of n on the infiltration airflow rate through the dome cover and exfiltration airflow rate through the house:

$$\eta_d = \frac{\dfrac{ACH_{d,2} - ACH_{d,1}}{ACH_{d,1}}}{\dfrac{n_2 - n_1}{n_1}} \cdot 100\% \qquad (8\text{-}6)$$

$$\eta_h = \frac{\dfrac{ACH_{h,2} - ACH_{h,1}}{ACH_{h,1}}}{\dfrac{n_2 - n_1}{n_1}} \cdot 100\% \qquad (8\text{-}7)$$

where:

205

$ACH_{d,1}$=average air infiltration rate through the dome (n=0.65), h^{-1};

$ACH_{d,2}$= average air infiltration rate through the dome (n=1.0), h^{-1};

$ACH_{h,1}$=average air exfiltration rate through the house (n=0.65), h^{-1};

$ACH_{h,2}$= average air exfiltration rate through the house (n=1.0), h^{-1};

n_1=0.65;

n_2=1.0.

The predicted values of η_d and η_h are 232% and 27.9%, respectively. It means that the increase of the value of n results in the increase of the infiltration rate through the dome and exfiltration rate through the house.

Figure 8-28 presents the comparison between the heating load of the house with different n values for both the dome and the house. The use of n=1.0 leads to higher heating load, however, the relative difference is about 3%. However, n=0.65 is recommended for infiltration through the dome because the wind pressure is high and the infiltration air flow is more close to turbulent than laminar state. The use of any value of n leads to about the same heating load of the house.
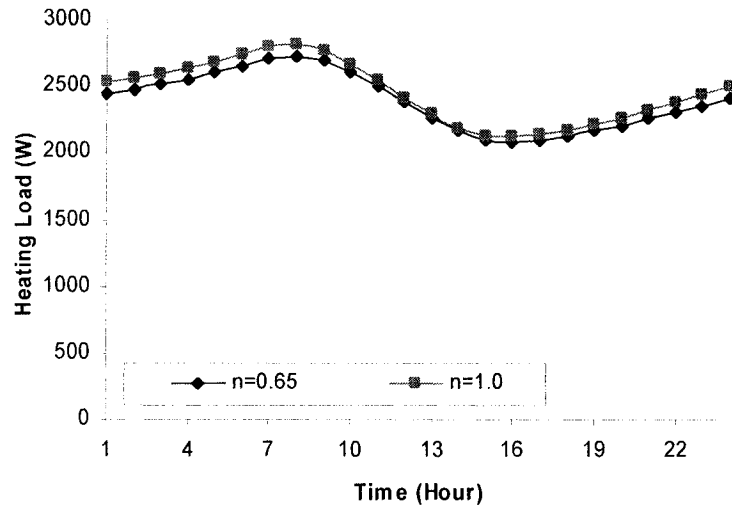
Figure 8-28 Comparison between the heating load of the house with different values of n

The sensitivity coefficient η_n is defined to see the impact of different values of n on the heating load of the house:

$$\eta_\tau = \frac{\dfrac{HL_2 - HL_1}{HL_1}}{\dfrac{n_2 - n_1}{n_1}} \cdot 100\% \tag{8-8}$$

where:

HL_1=daily heating load of the house (n=0.65), kWh;

HL_2=daily heating load of the house (n=1.0), kWh.

The predicted value of η_n is 5.6%, which means that the increase of the values of n results in negligible increase of the heating load of the house.

8.4.4 Impact of Truncation Angle on the Heating Load of the House

The impact on the heating load of changes of the truncation angle from 20° to 0° is shown in Figure 8-29. The Figure shows an increase of 19% of the heating load. The increase of the heating load is due to the modeling approach that assumes the infiltration through the first layer of the dome which is divided into 13 layers. Therefore, the infiltration airflow rate through the hemisphere is much greater that the dome with truncation angle of 20°.
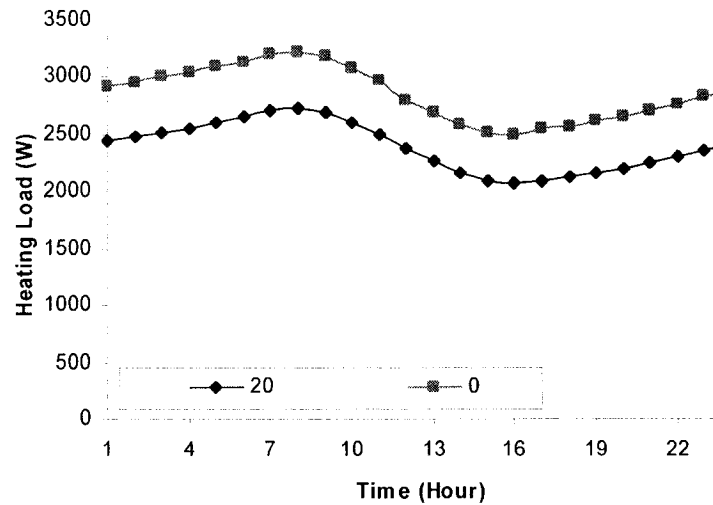
Figure 8-29 Impact of the truncation angle of the dome on the heating load of the house on January 21st

The sensitivity coefficient η_σ is defined to see the impact of different value of σ_0 on the heating load of the house:

$$\eta_\sigma = \frac{\dfrac{HL_2 - HL_1}{HL_1}}{\dfrac{\sigma_{0,2} - \sigma_{0,1}}{\sigma_{0,1}}} \cdot 100\%$$

(8-9)

where:

HL$_1$=daily heating load of the house (σ_0 =20 deg.), kWh;

HL$_2$=daily heating load of the house (σ_0 =0 deg.), kWh;

$\sigma_{0,1}$ =20;

$\sigma_{0,2}$ =0.

The predicted value of η_σ is -19%, which means that the increase of the truncation angle of the dome results in the decrease of the heating load of the house.

8.4.5 Impact of the Radius of the Dome on the Heating Load of the House

The impact on heating load of changes of the radius of the dome from 20 m to 22.5 m is shown in Figure 8-30. The Figure shows an increase over the heating load. It is due to increase of infiltration through the dome, because of greater air leakage area. However, the difference is very small.
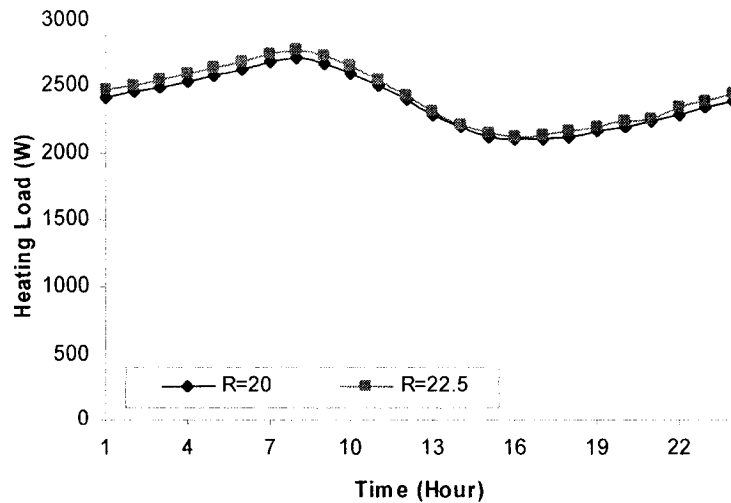
Figure 8-30 Impact of the radius of the dome on the heating load of the house on January 21st

The sensitivity coefficient η_R is defined to see the impact of dome radius (R) on the heating load of the house:

$$\eta_R = \frac{\dfrac{HL_2 - HL_1}{HL_1}}{\dfrac{R_2 - R_1}{R_1}} \cdot 100\% \qquad (8\text{-}10)$$

where:

HL_1=daily heating load of the house (R =20 m), kWh;

HL_2=daily heating load of the house (R=22.5 m), kWh;

R_1 =20 m;

R_2 =22.5 m.

The predicted value of η_R is 14.4%, which means that the increase of the radius of the dome results in the increase of the heating load of the house.

8.4.6 Impact of C_p Value on the Heating Load of the House

To verify if the correlation based model based on measurements by Newman et al. (1984) in a wind tunnel is comparable with other models or measured data, the results of the C_p values obtained from regression model based on the experimental data from Newman et al. (1984) are compared with the experimental results from Taniguchi et al. (1982) with $u_\tau d/v$=442 (u_τ is the shear velocity, in m/s) and mathematical model developed by Montes and Fernandez (2001) based on the finite Fourier series method. The results are shown in

Figures 8-31 and 8-32.

Montes and Fernandez's model is expressed as:

$$c_p = \sum_{n=0}^{12} A_n \cos(n\psi) \qquad (8\text{-}11)$$

where:

A_n =coefficient presented in a Table in Montes and Fernandez (2001);

Ψ=longitudinal angle to the normal direction of the wind, deg..

Figure 8-31 shows that the finite Fourier method predicts highest C_p values at 80° latitude and with Ψ < 50°, but predicts lowest C_p values when Ψ > 110°. At 30° latitude, the Montes and Fernandez's model predicts the lowest C_p values under the above conditions (Figure 8-32). Figure 8-32 indicates that there are some errors in the table of the coefficients presented by Montes and Fernandez (2001), because the C_p values obtained by their method are quite different from others'. The results from Taniguchi et al. (1982)'s experimental data and the regression model are more close to each other. The differences are due to the different air flow conditions (indicated by Reynolds numbers) of the wind tunnel tests. The Reynolds number for a dome with diameter of 40 m and wind speed range of 3~13 m/s, is about $8 \cdot 10^6$~$3.6 \cdot 10^7$, which is closed to Montes and Fernandez (2001)'s. However, the results from Newman et al. (1984) are gathered from experiments for different dome shapes and have been compared with Savory and Toy's (1986), as well as Taylor's (1992) experimental data with Reynolds number up to $1.2 \cdot 10^6$

and found good agreements with each other, and therefore the regression model should be selected.

Figure 8-33 presents a comparison between the heating load of the house on January 21st, when the C_p values are calculated using the regression model developed in this thesis, based on experimental data from Newman et al. (1984) (see section 4.1.2), compared with the heating load when the Cp values are calculated using Montes and Fernandez's model, for a dome-covered house located in Montreal. The dome has a radius of 20 m, and height-to-base diameter ratio of 0.37. The Montes and Fernandez's model predicts higher heating load of the house inside the dome. However, the difference in the total daily heating load due to changes of C_p values is about 4.7%, which is considered to be neglegible.
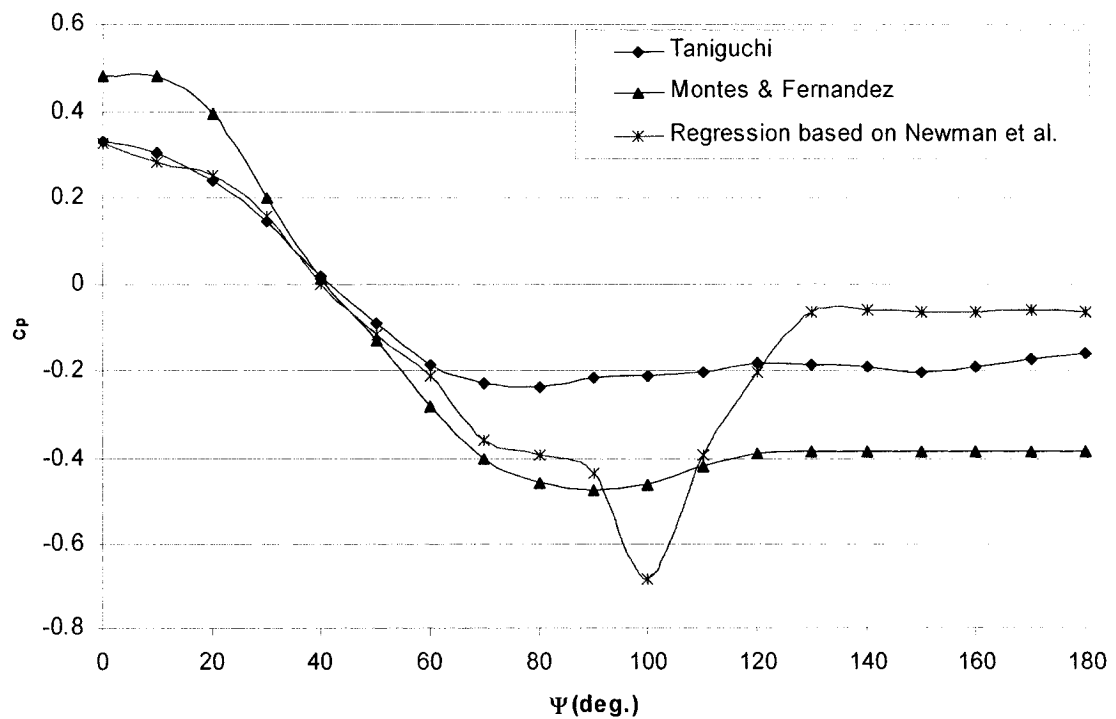
Figure 8-31 C_p value at 80° latitude ($u\tau d/v$=442 for Taniguchi et al. (1982), Re=1.6·10[5] for Newman et al. (1984), Re>4·10[6] for Montes and Fermandez (2001))
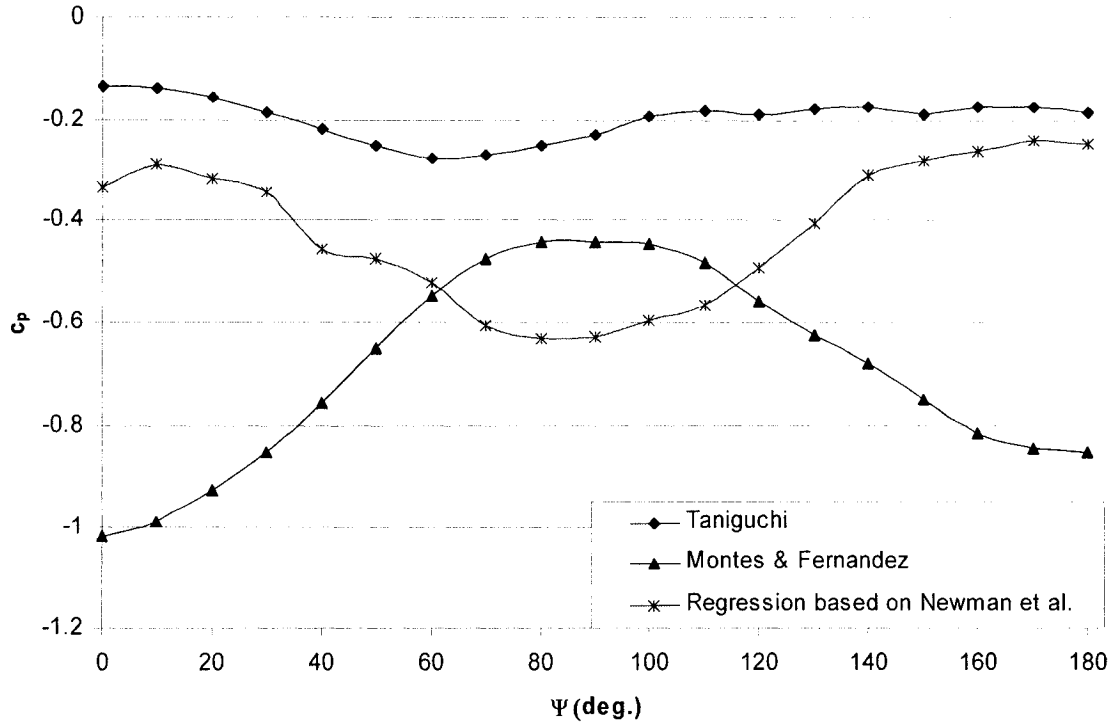
Figure 8-32 C_p value at 30° latitude ($u\tau d/v$=442 for Taniguchi et al. (1982), Re=1.6·10⁵ for Newman et al. (1984), Re>4·10⁶ for Montes and Fermandez (2001))
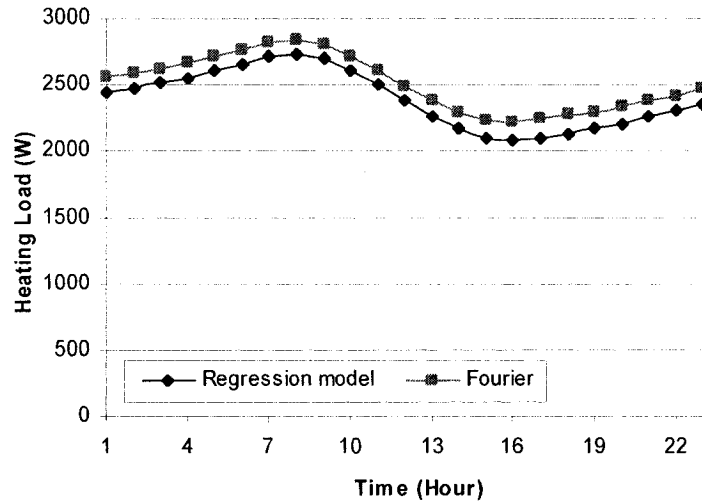
Figure 8-33 Comparison between the heating load of the house on January 21st, predicted by the regression model and Montes and Fernandez (2001)'s model

8.5 Convergence

Figure 8-34 gives an example of the convergence of the iterative process during the

calculation of temperatures for the whole system when the flow stays unchanged at a given hour. The convergence is reached after 20 iterations if the acceptable absolute error is equal to $1.0 \cdot 10^{-6}$°C. Figure 8-35 presents the convergence process at the same time step when the airflow rate is updated during the calculation. It is observed that the absolute error of the air temperature is about 1.0°C after the airflowrate being updated for 10 times. The computation time for one typical day, in this case study is about 10 hours using a desktop computer configured with Intel Pentium 4, 3.06GH$_Z$, 533FSB CPU(512k L2 Cache) and 2· 256 MB SDRAM memory.
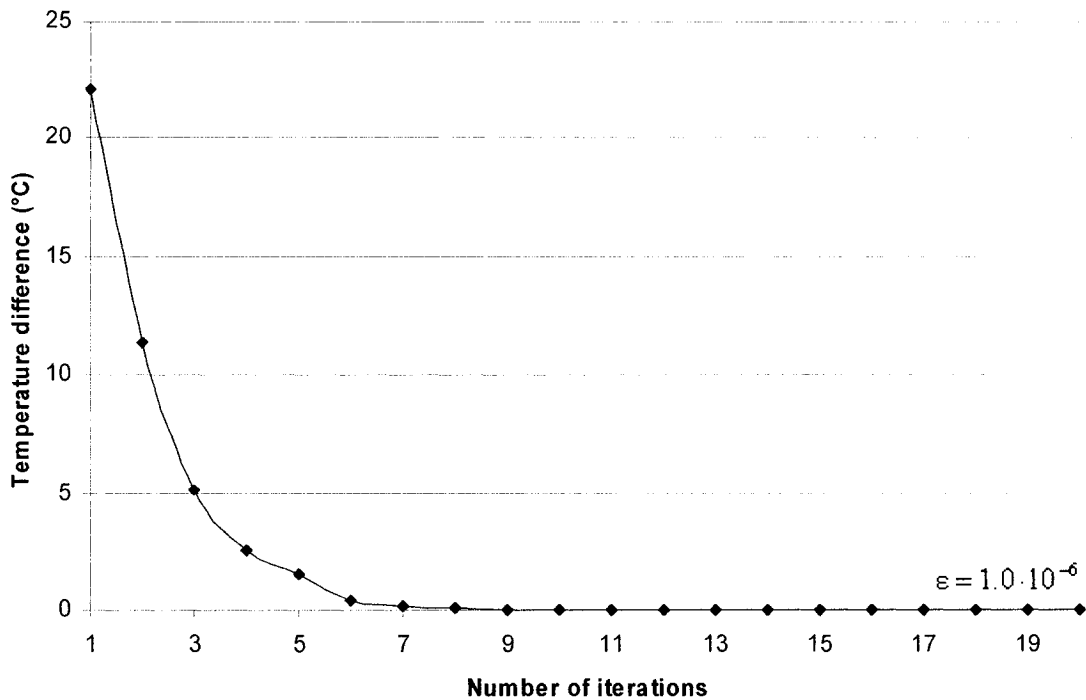
Figure 8-34 Convergence process for the temperature, when the airflow rates stay unchanged, at 10:00 AM, on January 21st
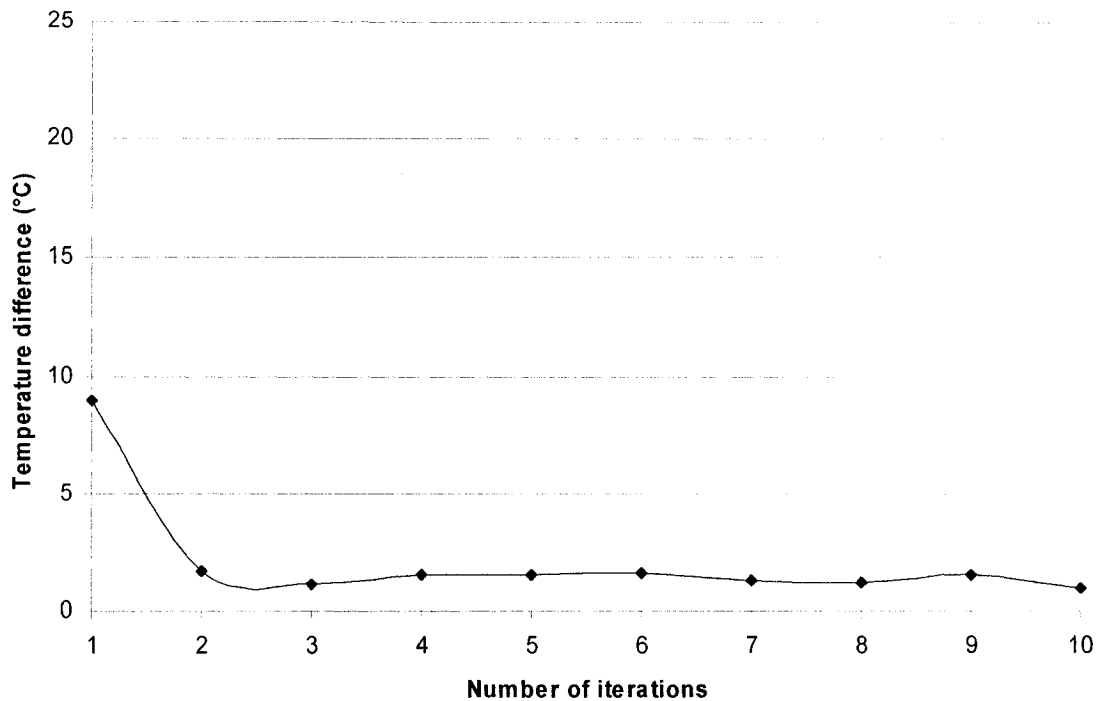
Figure 8-35 Convergence process for the temperature, when the airflow rates are updated, at 10:00 AM, on January 21st

8.6 Conclusion from Case Study

The case study leads to the following conclusions:

- The use of the dome can help to significantly reduce the heating load of a house in cold climate.

- The increase of the transmittance of the glazing, and truncation angle of the dome, result in the decrease of the heating load of the house.

- The increase of the thermal mass of the ground, values of n, and radius of the dome, result in the increase of the heating load of the house.

- The increase of the value of n results in the increase of the infiltration rate through the dome and exfiltration rate through the house.

- The difference in the heating load due to changes of C_p values is negligible.

Chapter 9 Summary, Contributions, and Future Work

9.1 Summary

The following is a brief outline of the achievements of this research:

1) A literature review has been performed on the thermal performance of dome-like structures, and the thermal models and optical models of dome-like structure.

2) Based on the above review, the limitations of the previous studies were identified, and the following areas have been set as requirements for the proposed model: firstly, to take into account the interaction between ground/dome/house surfaces; secondly, to evaluate the temperature distribution over the glazing surface; thirdly, to consider the air flow movement and air temperature distribution inside the dome.

3) The analysis on the physical phenomena and geometric information was carried out. The heat flows involved in the system were identified and the coordinate systems were selected. A comparison between the physical phynomena considered in this study and other mathematical models was made.

4) The thermal model was developed that calculates the temperature of some nodes of interest of the simulation domain, based on heat balance equations that were written for: (a) the dome glazing; (b) the exterior envelope and floor of the house; (c) the air inside the house; (d) the earth surface inside the dome; e) the air inside the dome. In the first section of the math model, the air inside the dome was considered to be well-mixed, and one single node was used to describe the air temperature inside the dome.

Comparison between the simulation results from different versions of the single-node model was made.

5) The air flow model was developed that calculates the airflow rate inside the dome, which is required by the thermal model to estimate the heat convective rate at the interface solid-air (e.g., between the dome cover and the dome air) and the vertical and horizontal temperature gradient of the air inside the dome.

6) The numerical solution of the mathematical model was presented, including the discretization schemes, formation of the system of equations, initial values of the unknowns, solution algorithm and calculation procedure.

7) The computer model was verified with a simplified computer model under MATLAB environment, with results from a 2D CFD model under the COMSOL Multiphysics environment, and with measured data and simulation results from similar structures, published by other researchers.

8) A transparent dome, built above one house located in Montreal was selected for case study. The simulation results predicted a reduction of 62.6% of the annual heating load of a house when a dome is used, compared with the case of an unprotected house. The sensitivity analysis of the impact of some variables used in the model (e.g., the optical properties of the dome glazing, the natural infiltration/exfiltration airflow rate through the dome/house, the shape of the dome, the ground thermal properties, and C_p values) on the heating load of the house was presented.

9.2 Contributions

The contributions of this research can be summarized as follows:

1) The model uses a detailed approach of the transmission of solar radiation through the dome cover and the impact on the temperature of surfaces and air inside the dome. The intersection between the trajectory of the transmitted solar beam and the inside surface is calculated and then the second transmission of solar radiation reaching the inside surface of the dome is calculated. The transmitted diffuse solar radiation is assumed to reach each surface proportionly to the view factor between the source cell and the destination surface.

2) The inside and outside convective coefficients are considered as functions of tilted angle, temperature difference, air velocity and air flow direction. The long-wave radiation is calculated with total interchange view factor.

3) The transient model is developed that takes into account (1) the temperature distribution over the dome glazing surface, (2) the temperature distribution of the air inside the dome, (3) the airflow pattern inside the dome, and (4) the natural infiltration/exfiltration through the dome surface/house surface.

4) The impact of the optical properties of the dome glazing, natural infiltration/exfiltration through the dome/house, ground thermal properties, and C_p values on the heating load of the house are evaluated.

5) Various ways on the verification and validation on the air flow model and thermal

model are presented.

9.3 Recommendations for Future Work

In order to improve the mathematical model and remove the limitation of the model, the future work should include the following areas of interest:

1) The simulation on air flow inside the dome under turbulent conditions, impact on the air temperature distribution inside the dome, and the convective heat flow between the air inside the dome and inside surfaces.

2) The improvement of the zonal model by considering the coexistence of air flow entering and leaving the boundary of two adjacent zones.

3) The modeling of solar radiation passing through the windows of the house.

4) Impact of absorptance and reflectance of the ground surface

5) Variation of number of layers, 2D and 3D heat transfer to the ground

6) Natural ventilation and use of shading in summer.

7) Humidity generation from plants and gardening.

8) The optimization of the dome design dimensions (the truncation angle and radius) for a given house, in terms of annual energy use and life cycle cost.

9) Design and development of a reduced-scale dome-cover house in Montreal, data monitoring and comparison with simulation results.

10) The computer model can be broken into a number of components to be used by other computer programs, such as TRNSYS.

11) The development of a graphical user interface (GUI) to the computer model.

References

Abusada, A.J. (2003). *What does it mean to build sustainably: definition, benefits and approach to multidimensional sustainable building: case study: XX-Project—DELFT.* http://www.iranrivers.com/Electronic_Library/paper/Asce/92.pdf. Last access: October 2003

Adams, J.C., Brainerd, W.S., Martin, J.T., Smith, B.T., and Wagener, J.L. (1992). *Fortran 90 Handbook: Complete ANSI/ISO Reference.* McGraw-Hill Book Company, New York, U.S.

Arai, Y., Togari, S. and Miura, K. (1994). Unsteadystate thermal analysis of a large space with vertical temperature distribution. *ASHRAE Transactions,* 100(2), 396-411

Arslan, S., and Sorguc, A.G. (2004). Similarities between "structures in natures" and "man-made structures": biomimesis in architecture. *Design and Nature II,* Collins M.W. and Brebia C.A. (eds). Southampton:WIT Press, 45-54

Asfia, F.J., and Dhir, V.K. (1996). An experimental study of natural convection in a volumetrically heated spherical pool bounded on top with a rigid wall. *Nuclear Engineering and Design,* 163(3), 333-348

ASHRAE. (1992). *Cooling and heating load calculation manual (2nd ed.).* Atlanta: American Society of Heating, Refrigerating, and Air-Conditioning Engineers, Inc.

ASHRAE. (1993). *ASHRAE handbook-1993 fundamentals, Chapter 3, heat transfer.* Atlanta: American Society of Heating, Refrigerating, and Air-Conditioning Engineers, Inc.

ASHRAE. (2001a). *ASHRAE handbook—2001 fundamentals. Chapter 26, ventilation and infiltration.* Atlanta: American Society of Heating, Refrigerating, and Air-Conditioning Engineers, Inc.

ASHRAE. (2001b). *ASHRAE handbook —2001 fundamentals. Chapter 30, fenestration.* Atlanta: American Society of Heating, Refrigerating, and Air-Conditioning Engineers, Inc.

ASHRAE. (2003). *Promoting sustainable buildings.* http://resourcecenter.ashrae.org/. Last access: Oct 2003

Bartzanas, T., Tchamitchian, M., and Kittas, C. (2005). *Influence of the heating method on greenhouse microclimate and energy consumption.* Biosystems Engineering, 91

(4), 487-499

BFI. (2005). http://www.bfi.org/domes/. Last access: Oct 2005

Boulard, T., Feuilloley, P., and Kittas, C. (1997). Natural ventilation performance of six greenhouse and tunnel types. *Journal of Agricultural Engineering Research*, 67 (4), 249-266

Boulard, T., Kittas, C., Roy, J.C., and Wang, S. (2002). Structures and environment: convective and ventilation transfers in greenhouses, part 2: determination of the distributed greenhouse climate. *Biosystems Engineering*, 83(2), pp 129-147

Boulard, T., Lamrani, M.A., Roy, J.C., Jaffrin, A., Bouirden, L. (1998). Natural ventilation by thermal effect in a one-half scale model mono-span greenhouse. *Transactions of the ASAE*, 41(3), 773-781

Chapra, S.C., and Canale, R.P. (2002). *Numerical method for engineers (4th ed.)*, NJ: McGraw-Hill Book Company

Chow, W.K., Fung, W.Y., and Wong, L.T. (2002). Preliminary studies on a new method for assessing ventilation in large spaces. *Building and Environment*, 37(2), 145-152

COMSOL AB. (2005). *COMSOL multiphysics user's guide.* Burlington, MA.

Croome, D.J., and Moseley, P. (1984a). Temperature prediction methods for lightweight structures. *Conference of "The Design of Air-supported Structures"*, Churchill College, University of Bristol

Croome, D.J., and Moseley, P. (1984b). Energy and thermal performance of airhouses. *Conference of "The Design of Air-supported Structures"*, Churchill College, University of Bristol

Croome, D.J. (1985). Covered northern township. *International Journal of Ambient Energy*, 6(4), 171-186

CRREL. (1999). *Regional climatic constants for equation 6 of the corps of engineers guide spec 02695. (best fit to mean monthly temperature averaged for the period 1895-1996).* U.S. Army Cold Regions Research and Engineering Laboratory, Hanover, NH. http://www.crrel.usace.army.mil/ard/cegs02695.htm. Last access: Nov. 2006

DCLU. (2003). *What does it mean to build sustainably?* http://www.cityofseattle.net/ dclu/sustainability/definition.asp. Last access: October 2003

DOE. (2004). *Buildings energy databook.* Department of Energy, U.S.

EngergyPlus. (2006). http://www.eere.energy.gov/buildings/energyplus/cfm/weather_data3.cfm/region=4_north_and_central_america_wmo_region_4/country=3_canada/c name=CANADA. Last access: Nov. 2006

Environment Canada. (2005). http://www.climate.weatheroffice.ec.gc.ca/climateData/canada_e.html. Last access: Nov. 2005

Frausto, H.U., and Pieters, J. G. (2004). Modeling greenhouse temperature using system identification by means of neural networks. *Neurocomputing,* 56, 423-428

Fisher, D.E., and Pedersen, C.O. (1997). Convective heat transfer in building energy and thermal load calculations. *ASHRAE Transactions,* 103(2), 137-48

Haghighat, F., Lin, Y., and Megri, A.C. (2001). Development and validation of a zonal model –POMA. *Building and Environment,* 36(9), 1039-1047

Hensen, JLM. (1999). A comparison of coupled and de-coupled solutions for temperature and air flow in a building. *ASHRAE Transactions,* 105(2), 962-69

Honma, H. (1975). *Ventilation of dwellings and its disturbances.* Stockholm: FAIBO, Grafiska.

Hottel, H.C., and Sarofim, A.F. (1967). *Radiative transfer.* NJ: McGraw-Hill Book Company

IESNA. (2000). *Lighting handbook, reference and application volume.* New York: Illuminating Engineering Society of North America.

Inard, C., Bouia, H., and Dalicieux, P. (1996). Prediction of air temperature distribution in buildings with a zonal model. *Energy and Buildings,* 24, (2), 125-132

Isaacson, E., and Keller, H.B. (1996). *Analysis of numerical methods.* New York: John Wiley and Sons Inc.

Jain, D. (2007). Modeling the thermal performance of an aquaculture pond heating with greenhouse. *Building and Environment,* 42 (2), 557-565

Jiru, T.E. (2006). *A new generation of zonal models: development, verification and application.* Ph.D. Dissertation, Concordia University, Montreal

John, G., Clements-Croome, D., and Jeronimidis, G. (2005). Sustainable building solutions: a review of lessons from the natural world. *Building and Environment,* 40(3): 319-328

Keeken, E.V. (2001). Environmental impact assessment methods in the Netherlands. in: *Towards Sustainable Building. Maiellaro*, Netherlands: Kluwer Academic Publishers

Knopp, T. (2003). *Finite-element simulation of buoyancy-driven turbulent flows.* Ph.D. Dissertation, Georg-August-Universität Göttingen, Mathematische Fakultät.

Kremers, J., A. (2003). *Defining sustainable architecture.* http://architronic.saed.kent. edu/v4n3/ v4n3.02a.html. Last access: October 2003

Kreith, F., and Eisenstadt, R. (1957). Pressure drop and flow characteristics of short capillary tubes at low Reynolds numbers. *ASME Transactions*, (July) 1070-1078.

Lamrani, M.A., Boulard, T., Roy, J.C., and Jaffrin,A. (2001). Airflows and temperature patterns induced in a confined greenhouse. *Journal of Agricultural Engineering Research*, 78(1), 75-88

Landman, M. (2003) *A definition of "sustainable building".* http://www.me.sc.edu /Research/lss /Papers/GinaCooperThesis.pdf. Last access: October 2003

Laouadi, A., and Atif, M.R. (1998). Transparent domed skylights: optical model for predicting transmittance, absorptance and reflectance, *Lighting Research and Technology*, 30(3), 111-118

Laouadi, A., and Atif, M.R. (1999). Predicting optical and thermal characteristics of transparent single-glazed domed skylights. *ASHRAE Transactions*, 105(2), 325-333

LBNL. (2003). *Window 5.2.* Lawrence Berkeley National Laboratory

Luttmann-Valencia, F. (1990). *A dynamic thermal model of a selfsustaining closed environment life support system.* Ph.D. Dissertation, University of Arizona, Tucson

McQuiston, F.C., Parker, J.D., and Spitler, J.D. (2000) *Heating, ventilating, and air conditioning: analysis and design.* New York: John Wiley & Sons

Monolithic Dome Institute. (2006). http://www.monolithic.com/. Last access: Nov. 2006

Montero, J.I., Hunt, G.R., Kamaruddin, R., Antón, A., and Bailey, B.J. (2001). Effect of ventilator configuration on wind-driven ventilation in a crop protection structure for the tropics. *Journal of Agricultural Engineering Research*, 80 (1), 99-107

Montes, P., and Fernandez, A. (2001). Behaviour of a hemispherical dome subjected to wind loading. *Journal of Wind Engineering and Industrial Aerodynamics*, 89(10), 911-924

Nara, M. (1979). Studies on air distribution in farm buildings (i) —two dimensional

numerical analysis and experiment. *Journal of the Society of Agricultural Structures*, 9(2), 18–25

Natural Resources Canada. (2004). *Energy efficiency trends in Canada 1990-2002.* Ottawa

Newman, B.G., Ganguli, U., and Shrivastava, S.C. (1984). Flow over spherical inflated buildings. *Journal of Wind Engineering and Industrial Aerodynamic*, 18(3), 305-327

Newman, B.G., and Goland, D. (1982). Two-dimensional inflated buildings in a cross wind. *Journal of Fluid Mechanics*, 117,507-530

Norton, J. (2003). *Sustainable architecture: a definition.* http://www.unhabitat.org/HD/ hdv5n2 /forum1.htm. Last access: October 2003

Press, W.H., Teukolsky, S.A., Vetterling, W.T., and Flannery, B.P. (1992). *Numerical Recipes in Fortran: The Art of Scientific Computing* (2nd ed.). Cambridge University Press, Cambridge, UK

Porta-Gándara, M.A., and Gómez-Muñoz, V. (2005). Solar performance of an electrochromic geodesic dome roof. *Energy*, 30(13), 2474-2486

Resource Venture. (2003). *Conventional, green & sustainable building definitions.* http://www.resourceventure.org/sbdefs_body.htm. Last access: October 2003.

Roy, J.C., Boulard, T., Kittas, C., and Wang, S. (2002). Precision agriculture: convective and ventilation transfers in greenhouses, part 1: the greenhouse considered as a perfectly stirred tank. *Biosystems Engineering*, 83(1), 1-20

Royal Netherlands Embassy in Beijing. 2003. *Sustainable building in China, present status and opportunities for Dutch companies*

Savory, E., and Toy, N. (1986). Hemisphere and hemisphere-cylinders in turbulent boundary layers. *Journal of Wind Engineering and Industrial Aerodynamics*, 23, 345-364

Sase, S., Takakura, T., and Nara, M. (1984). Wind tunnel testing on air flow and temperature distribution of a naturally ventilated greenhouse. *Acta Horticulturae*, 148, 329-336

Sharma, P.K., Tiwari, G.N., and Sorayan V.P.S. (1999). Temperature distribution in different zones of the micro-climate of a greenhouse: a dynamic model. *Energy Conversion and Management*, 40 (3), 335-348

Salgado, P., and Cunha, J.B. (2005). Greenhouse climate hierarchical fuzzy modeling.

Control Engineering Practice, 13(5), 613-628

Seginer, I., Boulard, T. & Bailey, B. J. 1994. Neural network models of the greenhouse climate. *Journal of Agricultural Engineering Research*, 59(3), 203-216

Shklyar, A. and Arbel, A. (2004). Numerical model of the three-dimensional isothermal flow patterns and mass fluxes in a pitched-roof greenhouse. *Journal of Wind Engineering and Industrial Aerodynamics*, 92(12), 1039-1059

Singh, G., Singh, P.P., Lubana, P.P.S. and Singh, K.G. (2006). Formulation and validation of a mathematical model of the microclimate of a greenhouse. *Renewable Energy*, 31(10), 1541-1560

Smith, A.M. (1999). *Prediction and measurement of thermal exchanges within pyranometers*. M.A.Sc. Thesis. Virginia Polytechnic Institute, Virginia, U.S.A.

Spencer, J.W. (1971). Fourier series representation of the position of the sun. *Search*, 2 (5), 172

Srach, E. (2004). Form-optimizing processes in biological structures-self-generating structures in nature based pneumatics. *Design and Nature II*, Collins M.W. & Brebia C.A. (eds). Southampton:WIT Press, 3-14

Takenaka Corporation. (2000). http://www.takenaka.co.jp/takenaka_e/engi_e/c01/ c01_1 _2.html. Last access: July 2005

Tang, R., Meir, I.A., and Etzion, Y. (2003). Thermal behavior of buildings with curved roofs as compared with flat roofs. *Solar Energy*, 74(4), 273-286

Taniguchi, S., Kiya, H.S., Arie, M. (1982). Time-averaged aerodynamic forces acting on a hemisphere immersed in a turbulent boundary. *Journal of Wind Engineering and Industrial Aerodynamics*, 9 (3), 982, 257-273

Taylor, T.J. (1992). Wind pressures on a hemispherical dome. *Journal of Wind Engineering and Industrial Aerodynamic*, 40(2), 199-213

Togari, S., Arai, Y., and Miura, K. (1993). A simplified model for predicting vertical temperature distribution in a large space. *ASHRAE Transactions*, 99(1), 84-99

Tsui, E. (1999). *Evolutionary architecture*. New York: John Wiley

UN. (1982). *The United Nations world charter for nature*

Walton, G.N. (1981). *Passive solar extension of the building loads analysis and system thermodynamics (BLAST) program*, Technical Report, United States Army

Construction Engineering Research Laboratory, Champaign, IL.

Walton, G. (1983). *Thermal analysis research program reference manual.* National Bureau of Standards, Gaithersburg, MA

WCED. (1987). World Commission on Environment and Development. *Our common future.* Oxford: Oxford University Press

Wilkinson, M.A. (1992). Natural lighting under translucent domes. *Lighting Research Technology,* 24(3), 117-126

Wittkopf, S., Kuan, S.L., Yuniarti, E., and Grobe, L. (2006). Making the CIE/ISO standard general sky available for CAD-based light simulation software. *Esim2006,* May 3rd–5th, Toronto, Canada

Wurtz, E., Nataf, J-M., Winkelmann, F. (1999). Two- and three-dimensional natural and mixed convection simulation using modular zonal models in buildings. *International Journal of Heat and Mass Transfer,* 42 (5), 923-940

Yashiro, T. (2000). *Sustainable building—a Japanese perspective.* http://web.jia.or.jp/jia/global/uia/ aof2000/person/s-yashiro.htm. Last access: October 2003

Yasser, M.D. (1997). Sustainable architecture in the UAE: past and present, in: *International Conference on Urbanization and Housing,* Goa, India

Yazdanian, M., and Klems, J. (1994). Measurement of the exterior convective film coefficient for windows in low-rise buildings. *ASHRAE Transactions,* 100(1), 1087-1096

Yeung, W.W.H. (2006). Similarity study on mean pressure distributions of cylindrical and spherical bodies. *Journal of Wind Engineering and Industrial Aerodynamics,* In Press, Corrected Proof, Available online 23 August 2006

Zhao, Y., Teitel, M., and Barak, M. (2001). Vertical temperature and humidity gradients in a naturally ventilated greenhouse. *Journal of Agricultural Engineering Research,* 78 (4), 431-436

Appendix A System of Coordinates

The system of coordinates is essential for calculation of the view factors, and of the distribution of transmitted solar radiation to the wall/roof/ground surfaces inside the dome.

The center point for cell (i,j) can be calculated as:

$$x_{i,j} = R\cos\varphi_j \sin\psi_i$$
$$y_{i,j} = R\cos\varphi_j \cos\psi_i \qquad\qquad (A-1)$$
$$z_{i,j} = R\sin\varphi_j$$

where:

R=radius of the dome, m;

φ =tilt of cell (i,j) that is defined as the angle between the outside normal of the cell and the horizontal plane, deg.;

ψ=azimuth angle of each cell (i,j) that is measured from the east, deg..

Each wall of the house is divided into a number of surfaces in order to facilitate the calculation of view factor in the following section. The building azimuth (Ψ_0)is assumed to be equal to zero at the first step, then a transformation formula is applied to get the real coordinates of the surfaces when $\Psi_0 \neq 0$. The dimension of the house is given as length=L, width=W, and height=H.

The west wall surface is divided into a number of $N_1 \cdot P_1$ sub-surfaces (Figure A-1).
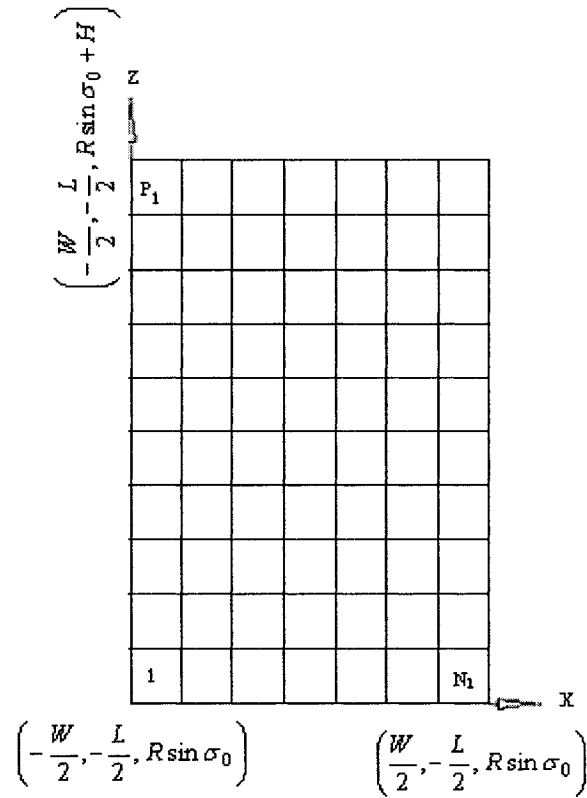
Figure A-1 Coordinates for the west wall surface

The coordinates for each division can be expressed as:

$$x_{i,j} = -\frac{W}{2} + \frac{W}{N_1}(i - 0.5)$$

$$y_{i,j} = -\frac{L}{2} \tag{A-2}$$

$$z_{i,j} = R\sin\sigma_0 + \frac{H}{P_1}(j - 0.5)$$

The equation of the surface is:

$$y = -\frac{L}{2} \tag{A-3}$$

Table A-1 lists the coordinates for each division of other walls/roof, and the equations for those surfaces:

Table A-1 Coordinates of each divisons of the walls/roof and the equations for those surfaces

	Number of divisions	Coordinates for each division	Equation of the surface
South	$M_1 \cdot P_1$	$x_{i,j} = \dfrac{W}{2}$ $y_{i,j} = -\dfrac{L}{2} + \dfrac{L}{M_1}(i - 0.5)$ $z_{i,j} = R\sin\sigma_0 + \dfrac{H}{P_1}(j - 0.5)$	$x = -\dfrac{W}{2}$
East	$N_1 \cdot P_1$	$x_{i,j} = -\dfrac{W}{2} + \dfrac{W}{N_1}(i - 0.5)$ $y_{i,j} = \dfrac{L}{2}$ $z_{i,j} = R\sin\sigma_0 + \dfrac{H}{P_1}(j - 0.5)$	$y = \dfrac{L}{2}$
North	$M_1 \cdot P_1$	$x_{i,j} = -\dfrac{W}{2}$ $y_{i,j} = -\dfrac{L}{2} + \dfrac{L}{M_1}(i - 0.5)$ $z_{i,j} = R\sin\sigma_0 + \dfrac{H}{P_1}(j - 0.5)$	$x = -\dfrac{W}{2}$
Roof	$M_1 \cdot N_1$	$x_{i,j} = -\dfrac{W}{2} + \dfrac{W}{N_1}(i - 0.5)$ $y_{i,j} = -\dfrac{L}{2} + \dfrac{L}{M_1}(j - 0.5)$ $z_{i,j} = R\sin\sigma_0 + H$	$z = R\sin\sigma_0 + H$
Floor	$M_1 \cdot N_1$	$x_{i,j} = -\dfrac{W}{2} + \dfrac{W}{N_1}(i - 0.5)$ $y_{i,j} = -\dfrac{L}{2} + \dfrac{L}{M_1}(j - 0.5)$ $z_{i,j} = R\sin\sigma_0$	$z = R\sin\sigma_0$

In the case when $\Psi_0 \neq 0$, the new coordinates of the walls /roof surfaces is as follows:

$$x_1 = x_0\cos\psi_0 + y_0\sin\psi_0$$
$$y_1 = y_0\cos\psi_0 - x_0\sin\psi_0 \tag{A-4}$$
$$z_1 = z_0$$

where $\left(x_0, y_0, z_0\right)$ represent the old coordinates for $\Psi_0=0$, and $\left(x_1, y_1, z_1\right)$ represent the new coordinates for $\Psi_0 \neq 0$.

Appendix B View Factor

View factors are used for the calculation of the long-wave radiation incident between interior surfaces.

The calculation procedure is as follows:

1) The equation of each surface is obtained in order to calculate the angle between each surface and the line that connect the center of each surface.

2) The equation of a line that passes through any two points (x_1, y_1, z_1) and (x_2, y_2, z_2) is expressed as:

$$\frac{x - x_1}{x_2 - x_1} = \frac{y - y_1}{y_2 - y_1} = \frac{z - z_1}{z_2 - z_1} \tag{B-1}$$

The above equation is rewritten as:

$$L: \qquad \frac{x - x_1}{m} = \frac{y - y_1}{n} = \frac{z - z_1}{p} \tag{B-2}$$

and the equation for a surface is written as:

$$\pi: \qquad A_1 x + B_1 y + C_1 z + D_1 = 0 \tag{B-3}$$

3) The angle between normal of the surface and line can be given by (Figure B-1):
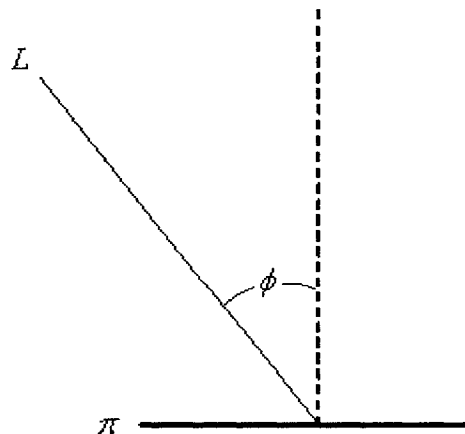
Figure B-1 Angle between line and plane

$$\cos\phi = \frac{\left|A_1 \cdot m + B_1 \cdot n + C_1 \cdot p\right|}{\sqrt{A^2 + B^2 + C^2}\,\sqrt{m^2 + n^2 + p^2}}$$ (B-4)

4) If the distance between the two surfaces is r, the view factor between two surfaces is calculated as follows (Figure B-2):

$$F_{\pi_1 - \pi_2} = A_{\pi_2}\,\frac{\cos\phi_1}{\pi r^2}\,\cos\phi_2$$ (B-5)
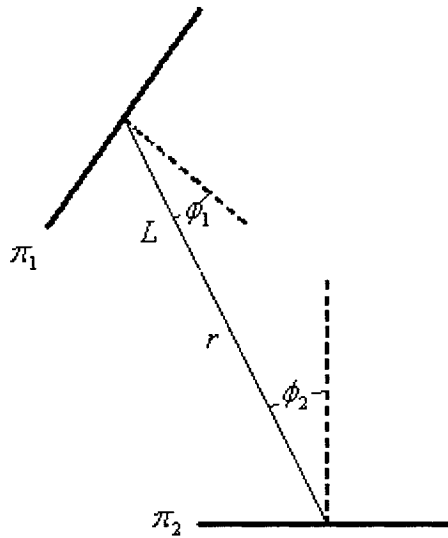
Figure B-2 View factor between two surfaces

If the two surfaces cannot see each other, the view factor between these two surfaces is zero.

The cells of the dome surface that see each wall surface and roof surface are within the area of dome covere within the range of the vertical angle (φ_1 and φ_2)and the horizontal angle (Ψ_1 and Ψ_2). For example, the cells that see the west wall surface are illustrated by the shadow area of Figures B-3 and B-4.
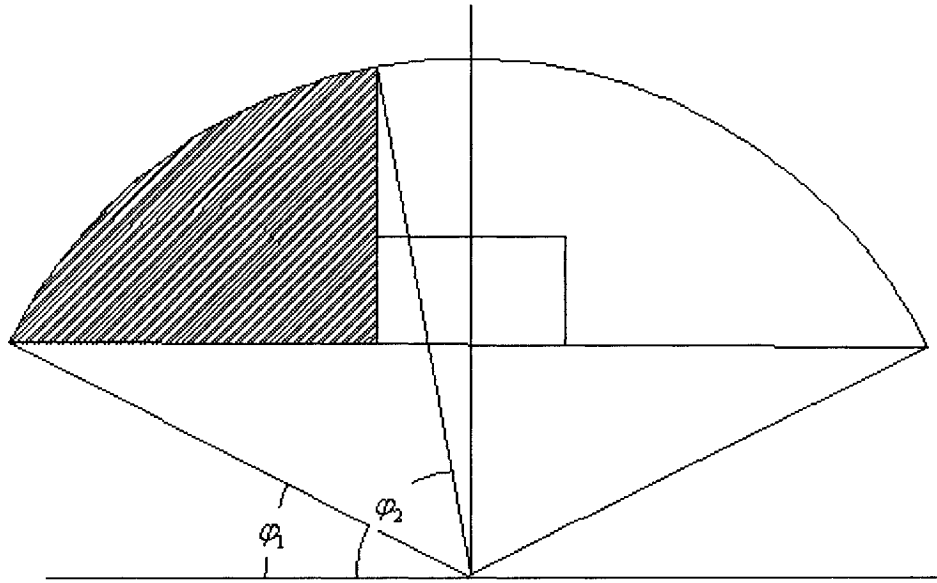
Figure B-3 Part of the dome surface that sees the west wall surface

The shadow area is given as:

$$\varphi_1 \le \varphi \le \varphi_2 \tag{B-6}$$

and

$$\psi_1 \le \psi \le \psi_2 \tag{B-7}$$

The values for each angle are given in Table B-1.
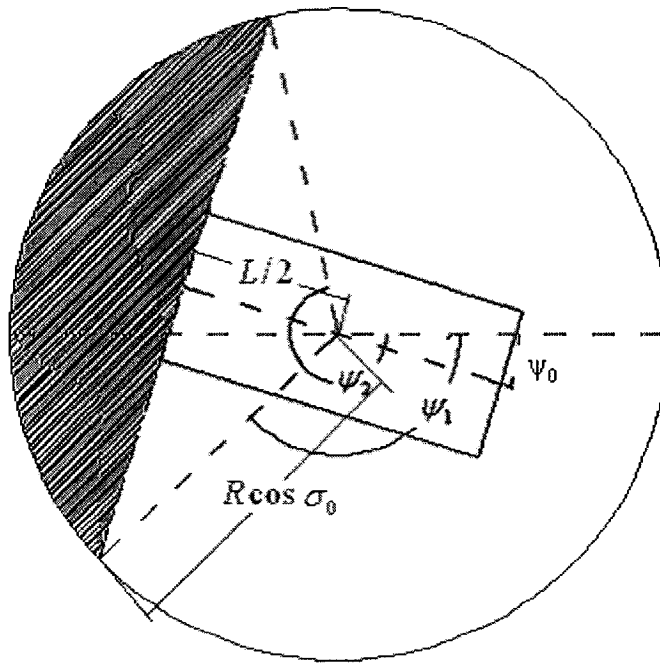
Figure B-4 Plan view of the dome surface that sees the west wall surface

Table B-1 Angles that determine the regions that see each surface

	φ_1	φ_2	ψ_1	ψ_2
E	σ_0	90	$-\cos^{-1}\dfrac{L/2}{R\cos\sigma_0}+\psi_0$	$\cos^{-1}\dfrac{L/2}{R\cos\sigma_0}+\psi_0$
W	σ_0	90	$180-\cos^{-1}\dfrac{L/2}{R\cos\sigma_0}+\psi_0$	$180+\cos^{-1}\dfrac{L/2}{R\cos\sigma_0}+\psi_0$
N	σ_0	90	$270-\cos^{-1}\dfrac{W/2}{R\cos\sigma_0}+\psi_0$	$270+\cos^{-1}\dfrac{W/2}{R\cos\sigma_0}+\psi_0$
S	σ_0	90	$90-\cos^{-1}\dfrac{W/2}{R\cos\sigma_0}+\psi_0$	$90+\cos^{-1}\dfrac{W/2}{R\cos\sigma_0}+\psi_0$
R	$90-\cos^{-1}\dfrac{H+R\sin\sigma_0}{R}$	90	0	360

For example, the range for the part of dome surface that can be seen by the west wall

surface is as follows:

$$\sigma_0 \le \varphi \le 90 \tag{B-8}$$

and

$$180 - \cos^{-1} \frac{L/2}{R\cos\sigma_0} + \psi_0 \le \psi \le 180 + \cos^{-1} \frac{L/2}{R\cos\sigma_0} + \psi_0 \tag{B-9}$$

View factor between the dome cells and the wall surfaces

The coordinates for the center points for each subdivisions of the west wall surface are given by equation (A-2), and the coordinates for the center points of each cell of the dome surface are given in equation (A-1). To avoid identical representation, the coordinates of the west wall surface are rewritten as $(x_{w,ij}, y_{w,ij}, z_{w,ij})$.

Therefore, the equation for line that passes through both the center point of each subdivision of the west wall surface and point (i,j) can be expressed as follows:

$$L_w : \quad \frac{x - x_{ij}}{x_{w,ij} - x_{ij}} = \frac{y - y_{ij}}{y_{w,ij} - y_{ij}} = \frac{z - z_{ij}}{z_{w,ij} - z_{ij}} \tag{B-10}$$

The equation for west wall surface is as follows:

$$S_w : \quad \sin\psi_0 x + \cos\psi_0 y + L/2 = 0 \tag{B-11}$$

The equation for the tangent plane through point (i,j) can be given by:

$$\text{Plane}(i, j): \quad x_{i,j}(x - x_{i,j}) + y_{i,j}(y - y_{i,j}) + z_{i,j}(z - z_{i,j}) = 0 \tag{B-12}$$

Therefore, the view factor between cell (i,j) and the west wall surface is given by:

$$F_{AW} = \sum A_{w,ij} \frac{\cos\phi_1}{\pi r^2} \cos\phi_2 \tag{B-13}$$

where:

$$\cos\phi_1 = \frac{\left|\sin\psi_0\left(x_{w,ij} - x_{ij}\right) + \cos\psi_0\left(y_{w,ij} - y_{ij}\right)\right|}{\sqrt{\sin\psi_0{}^2 + \cos\psi_0{}^2 + 0^2}\sqrt{\left(x_{w,ij} - x_{ij}\right)^2 + \left(y_{w,ij} - y_{ij}\right)^2 + \left(z_{w,ij} - z_{ij}\right)^2}}$$

$$= \frac{\left|\sin\psi_0\left(x_{w,ij} - x_{ij}\right) + \cos\psi_0\left(y_{w,ij} - y_{ij}\right)\right|}{\sqrt{\left(x_{w,ij} - x_{ij}\right)^2 + \left(y_{w,ij} - y_{ij}\right)^2 + \left(z_{w,ij} - z_{ij}\right)^2}}$$

(B-14)

$$\cos\phi_2 = \frac{\left|x_{i,j}\left(x_{w,ij} - x_{ij}\right) + y_{i,j}\left(y_{w,ij} - y_{ij}\right) + z_{i,j}\left(z_{w,ij} - z_{ij}\right)\right|}{\sqrt{x_{ij}{}^2 + y_{ij}{}^2 + z_{ij}{}^2}\sqrt{\left(x_{w,ij} - x_{ij}\right)^2 + \left(y_{w,ij} - y_{ij}\right)^2 + \left(z_{w,ij} - z_{ij}\right)^2}}$$

$$= \frac{\left|x_{i,j}\left(x_{w,ij} - x_{ij}\right) + y_{i,j}\left(y_{w,ij} - y_{ij}\right) + z_{i,j}\left(z_{w,ij} - z_{ij}\right)\right|}{R\sqrt{\left(x_{w,ij} - x_{ij}\right)^2 + \left(y_{w,ij} - y_{ij}\right)^2 + \left(z_{w,ij} - z_{ij}\right)^2}}$$

(B-15)

$$r = \sqrt{\left(x_{w,ij} - x_{ij}\right)^2 + \left(y_{w,ij} - y_{ij}\right)^2 + \left(z_{w,ij} - z_{ij}\right)^2}$$

(B-16)

$$A_{w,ij} = \frac{W\_wall \cdot H\_wall}{N_1 \cdot P_1}$$

(B-17)

From Table B-1, the region of the dome surface that sees the west wall surface can be determined as:

$$\sigma_0 \le \varphi_{ij} \le 90$$

(B-18)

and

$$180 - \cos^{-1}\frac{L/2}{R\cos\sigma_0} + \psi_0 \le \psi_{ij} \le 180 + \cos^{-1}\frac{L/2}{R\cos\sigma_0} + \psi_0$$

(B-19)

The view factors between the dome cells and other wall/roof surfaces are given in Table B-2, where the subscripts S, E, N, and R represent south wall, east wall, north wall and roof, respectively (e.g., the coordinates of the south wall surface are rewritten as $\left(x_{S,ij}, y_{S,ij}, z_{S,ij}\right)$).

Table B-2 View factors between the dome cells and other wall/roof surfaces

	Area	$\cos\phi_1$	$\cos\phi_2$	r
South wall	$\dfrac{L\cdot H}{M_1\cdot P_1}$	$\dfrac{\left|\cos\psi_0\left(x_{S,ij}-x_{ij}\right)-\sin\psi_0\left(y_{S,ij}-y_{ij}\right)\right|}{\sqrt{\left(x_{S,ij}-x_{ij}\right)^2+\left(y_{S,ij}-y_{ij}\right)^2+\left(z_{S,ij}-z_{ij}\right)^2}}$	$\dfrac{x_{i,j}\left(x_{E,ij}-x_{ij}\right)+y_{i,j}\left(y_{E,ij}-y_{ij}\right)+z_{i,j}\left(z_{E,ij}-z_{ij}\right)}{R\sqrt{\left(x_{E,ij}-x_{ij}\right)^2+\left(y_{E,ij}-y_{ij}\right)^2+\left(z_{E,ij}-z_{ij}\right)^2}}$	$\sqrt{\left(x_{S,ij}-x_{ij}\right)^2+\left(y_{S,ij}-y_{ij}\right)^2+\left(z_{S,ij}-z_{ij}\right)^2}$
East wall	$\dfrac{W\cdot H}{N_1\cdot P_1}$	$\dfrac{\left|\sin\psi_0\left(x_{E,ij}-x_{ij}\right)+\cos\psi_0\left(y_{E,ij}-y_{ij}\right)\right|}{\sqrt{\left(x_{E,ij}-x_{ij}\right)^2+\left(y_{E,ij}-y_{ij}\right)^2+\left(z_{E,ij}-z_{ij}\right)^2}}$	$\dfrac{x_{i,j}\left(x_{E,ij}-x_{ij}\right)+y_{i,j}\left(y_{E,ij}-y_{ij}\right)+z_{i,j}\left(z_{E,ij}-z_{ij}\right)}{R\sqrt{\left(x_{E,ij}-x_{ij}\right)^2+\left(y_{E,ij}-y_{ij}\right)^2+\left(z_{E,ij}-z_{ij}\right)^2}}$	$\sqrt{\left(x_{E,ij}-x_{ij}\right)^2+\left(y_{E,ij}-y_{ij}\right)^2+\left(z_{E,ij}-z_{ij}\right)^2}$
North wall	$\dfrac{L\cdot H}{M_1\cdot P_1}$	$\dfrac{\left|-\cos\psi_0\left(x_{N,ij}-x_{ij}\right)+\sin\psi_0\left(y_{N,ij}-y_{ij}\right)\right|}{\sqrt{\left(x_{N,ij}-x_{ij}\right)^2+\left(y_{N,ij}-y_{ij}\right)^2+\left(z_{N,ij}-z_{ij}\right)^2}}$	$\dfrac{x_{i,j}\left(x_{N,ij}-x_{ij}\right)+y_{i,j}\left(y_{N,ij}-y_{ij}\right)+z_{i,j}\left(z_{N,ij}-z_{ij}\right)}{R\sqrt{\left(x_{N,ij}-x_{ij}\right)^2+\left(y_{N,ij}-y_{ij}\right)^2+\left(z_{N,ij}-z_{ij}\right)^2}}$	$\sqrt{\left(x_{N,ij}-x_{ij}\right)^2+\left(y_{N,ij}-y_{ij}\right)^2+\left(z_{N,ij}-z_{ij}\right)^2}$
Roof	$\dfrac{L\cdot W}{M_1\cdot N_1}$	$\dfrac{\left|z_{R,ij}-z_{ij}\right|}{\sqrt{\left(x_{R,ij}-x_{ij}\right)^2+\left(y_{R,ij}-y_{ij}\right)^2+\left(z_{R,ij}-z_{ij}\right)^2}}$	$\dfrac{x_{i,j}\left(x_{R,ij}-x_{ij}\right)+y_{i,j}\left(y_{R,ij}-y_{ij}\right)+z_{i,j}\left(z_{R,ij}-z_{ij}\right)}{R\sqrt{\left(x_{R,ij}-x_{ij}\right)^2+\left(y_{R,ij}-y_{ij}\right)^2+\left(z_{R,ij}-z_{ij}\right)^2}}$	$\sqrt{\left(x_{R,ij}-x_{ij}\right)^2+\left(y_{R,ij}-y_{ij}\right)^2+\left(z_{R,ij}-z_{ij}\right)^2}$

View factor between one cell and another Cell

The coordinates for the center of cell (k, l) can be expressed as:

$$x_{k,l} = R\cos\varphi_k \sin\psi_l$$
$$y_{k,l} = R\cos\varphi_k \cos\psi_l \tag{B-20}$$
$$z_{k,l} = R\sin\varphi_l$$

Therefore, the equation for the line that passes through the center of cell (i,j) and the center of cell (k,l) can be given:

$$L_{i,j-M.N} : \quad \frac{x - x_{i,j}}{x_{k,l} - x_{i,j}} = \frac{y - y_{i,j}}{y_{k,l} - y_{i,j}} = \frac{z - z_{i,j}}{z_{k,l} - z_{i,j}} \tag{B-21}$$

The tangent plane that passes through the center of cell (k, l) can be expressed as:

$$\text{Plane}(k,l): \quad x_{k,l}\left(x - x_{k,l}\right) + y_{k,l}\left(y - y_{k,l}\right) + z_{k,l}\left(z - z_{k,l}\right) = 0 \tag{B-22}$$

Therefore, the view factor between cell (i,j) and cell(k,l) can be expressed as:

$$F_{ij-kl} = A_{k,l} \frac{\cos\phi_1}{\pi r^2}\cos\phi_2 \tag{B-23}$$

where:

$$\cos\phi_1 = \frac{\left|x_{i,j}\left(x_{k,l} - x_{i,j}\right) + y_{i,j}(y_{k,l} - y_{i,j}) + z_{i,j}(z_{k,l} - z_{i,j})\right|}{\sqrt{x_{ij}^2 + y_{ij}^2 + z_{ij}^2}\sqrt{\left(x_{k,l} - x_{i,j}\right)^2 + (y_{k,l} - y_{i,j})^2 + (z_{k,l} - z_{i,j})^2}}$$

$$= \frac{\left|x_{i,j}\left(x_{k,l} - x_{i,j}\right) + y_{i,j}(y_{k,l} - y_{i,j}) + z_{i,j}(z_{k,l} - z_{i,j})\right|}{R\sqrt{\left(x_{k,l} - x_{i,j}\right)^2 + (y_{k,l} - y_{i,j})^2 + (z_{k,l} - z_{i,j})^2}} \tag{B-24}$$

$$\cos\phi_2 = \frac{\left|x_{k,l}\left(x_{k,l} - x_{i,j}\right) + y_{k,l}(y_{k,l} - y_{i,j}) + z_{k,l}(z_{k,l} - z_{i,j})\right|}{R\sqrt{\left(x_{k,l} - x_{i,j}\right)^2 + (y_{k,l} - y_{i,j})^2 + (z_{k,l} - z_{i,j})^2}} \tag{B-25}$$

$$r = \sqrt{(x_{k,l} - x_{i,j})^2 + (y_{k,l} - y_{i,j})^2 + (z_{k,l} - z_{i,j})^2} \qquad \text{(B-26)}$$

and the line should have no intersection point with any wall/roof surface. If the line has intersection point with any wall/roof surface, it means the two cells can not see each other, therefore, the view factor between theses two cells is zero.

The intersection point for this line and any other wall surface can be calculated as below:

Let

$$L_{i,j-M,N} : \quad \frac{x - x_{i,j}}{x_{k,l} - x_{i,j}} = \frac{y - y_{i,j}}{y_{k,l} - y_{i,j}} = \frac{z - z_{i,j}}{z_{k,l} - z_{i,j}} = tmp \qquad \text{(B-27)}$$

So that the each point of the line can be expressed by the parameter tmp and the following group of equations:

$$\begin{aligned} x &= x_{i,j} + tmp(x_{k,l} - x_{i,j}) \\ y &= y_{i,j} + tmp(y_{k,l} - y_{i,j}) \\ z &= z_{i,j} + tmp(z_{k,l} - z_{i,j}) \end{aligned} \qquad \text{(B-28)}$$

The parameter tmp for the intersection point between the line and the wall/roof surfaces can be calculated as follows:

For the west wall surface

$$tmp = \frac{- L/2 - \cos\psi_0 y_{i,j} - \sin\psi_0 x_{i,j}}{x_{k,l} - x_{i,j} + y_{k,l} - y_{i,j}} \qquad \text{(B-29)}$$

For the south wall surface

$$tmp = \frac{W/2 + \sin\psi_0 y_{i,j} - \cos\psi_0 x_{i,j}}{x_{k,l} - x_{i,j} + y_{k,l} - y_{i,j}} \qquad \text{(B-30)}$$

For the east wall surface

$$tmp = \frac{L/2 - \cos\psi_0 y_{i,j} - \sin\psi_0 x_{i,j}}{x_{k,l} - x_{i,j} + y_{k,l} - y_{i,j}} \qquad (B-31)$$

For the north wall surface

$$tmp = \frac{W/2 + \cos\psi_0 x_{i,j} - \sin\psi_0 y_{i,j}}{x_{k,l} - x_{i,j} + y_{k,l} - y_{i,j}} \qquad (B-32)$$

If any intersection point is within certain wall surface, the view factor between these two divided surfaces will become zero. If there is an intersection point between the line and the roof surface, there will be one intersection point for the line and certain wall surface.

View factor between the cell and the ground

For each point of the ground surface with norm of r, the coordinate of the point can be expressed as (Figure B-5):

$$x_r = r\sin\psi$$
$$y_r = r\cos\psi \qquad (B-33)$$
$$z_r = R\sin\sigma_0$$
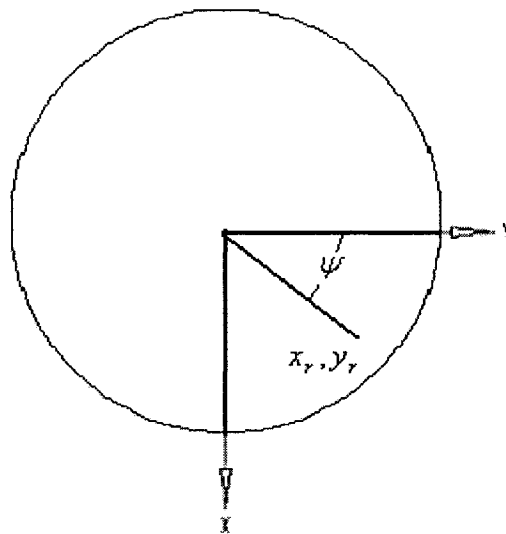
Figure B-5 Coordinates of the ground surface

And the distance between the center of cell (i,j) and the above point can be given:

$$d = \sqrt{\left(x_{i,j} - x_r\right)^2 + \left(y_{i,j} - y_r\right)^2 + \left(z_{i,j} - z_r\right)^2}$$ (B-34)

The line that passes the the center of cell (i,j) and the above point can be expressed as:

$$L_G : \quad \frac{x - x_r}{x_{i,j} - x_r} = \frac{y - y_r}{y_{i,j} - y_r} = \frac{z - z_r}{z_{i,j} - z_r}$$ (B-35)

The equation for the ground is:

$$S_G : \quad z = R\sin\sigma_0$$ (B-36)

Therefore, the view factor between cell (i,j) and the ground surface (assuming the roof and wall do not exist) can be given by:

$$F_{AG} = A_{i,j} \sum \frac{\cos\phi_1}{\pi \cdot d^2} \cdot \cos\phi_2 \cdot dA$$ (B-37)

where:

$$\cos\phi_1 = \frac{\left|z_{i,j} - z_r\right|}{\sqrt{0^2 + 0^2 + 1^2} \sqrt{\left(x_{i,j} - x_r\right)^2 + \left(y_{i,j} - y_r\right)^2 + \left(z_{i,j} - z_r\right)^2}}$$

$$= \frac{\left|z_{i,j} - z_r\right|}{\sqrt{\left(x_{i,j} - x_r\right)^2 + \left(y_{i,j} - y_r\right)^2 + \left(z_{i,j} - z_r\right)^2}}$$ (B-38)

$$\cos\phi_2 = \frac{\left|x_{i,j}\left(x_{i,j} - x_r\right) + y_{i,j}\left(y_{i,j} - y_r\right) + z_{i,j}\left(z_{i,j} - z_r\right)\right|}{\sqrt{x_{i,j}^2 + y_{i,j}^2 + z_{i,j}^2} \sqrt{\left(x_{i,j} - x_r\right)^2 + \left(y_{i,j} - y_r\right)^2 + \left(z_{i,j} - z_r\right)^2}}$$

$$= \frac{\left|x_{i,j}\left(x_{i,j} - x_r\right) + y_{i,j}\left(y_{i,j} - y_r\right) + z_{i,j}\left(z_{i,j} - z_r\right)\right|}{R\sqrt{\left(x_{i,j} - x_r\right)^2 + \left(y_{i,j} - y_r\right)^2 + \left(z_{i,j} - z_r\right)^2}}$$ (B-39)

$$dA = r \cdot dr \cdot d\psi$$ (B-40)

The view factor between cell (i,j) and the ground can further be modified as:

$$F_{AG} = A_{i,j} \cdot \int_{0}^{2\pi} \int_{0}^{R\cos\sigma_0} \frac{\cos\phi_1 \cdot \cos\phi_2}{\pi d^2} r \cdot dr \cdot d\psi \qquad (B-41)$$

This method is complicate and it needs to determine whether the line has an intersection point with any other wall/roof surface.

One alternative way to calculate the view factor between cell (i,j) and the ground can be calculated as follows:

$$F_{AG} = 1 - F_{AW} - F_{AS} - F_{AE} - F_{AN} - F_{AR} - \sum_{\substack{k=1,M \\ l=1,N \\ k\neq i \& l\neq j}} F_{ij-kl} \qquad (B-42)$$

where:

F_{AW}=view factor between cell (i,j) and the west wall surface;

F_{AS}= view factor between cell (i,j) and the south wall surface;

F_{AE}= view factor between cell (i,j) and the east wall surface;

F_{AN}= view factor between cell (i,j) and the north wall surface;

F_{AR}= view factor between cell (i,j) and the roof surface;

F_{ij-kl}= view factor between cell (i,j) and cell (k,l).

Because all the variables on the right hand side have beendetermined before the calculation of the view factor between each cell and the groud inside the dome, this method is employed in the program.

Appendix C Transmitted Solar Radiation

The transmitted solar radiation upon each surface is very important since it is the major factor of the cooling load during the day time in summer and of help to reduce the heating load in winter.

Transmitted solar radiation from one cell to another cell

The beam solar radiation upon the dome can be considered to be divided into two components. One part receives the solar beam directly, and the other part receives transmitted solar beam (Figure C-1).
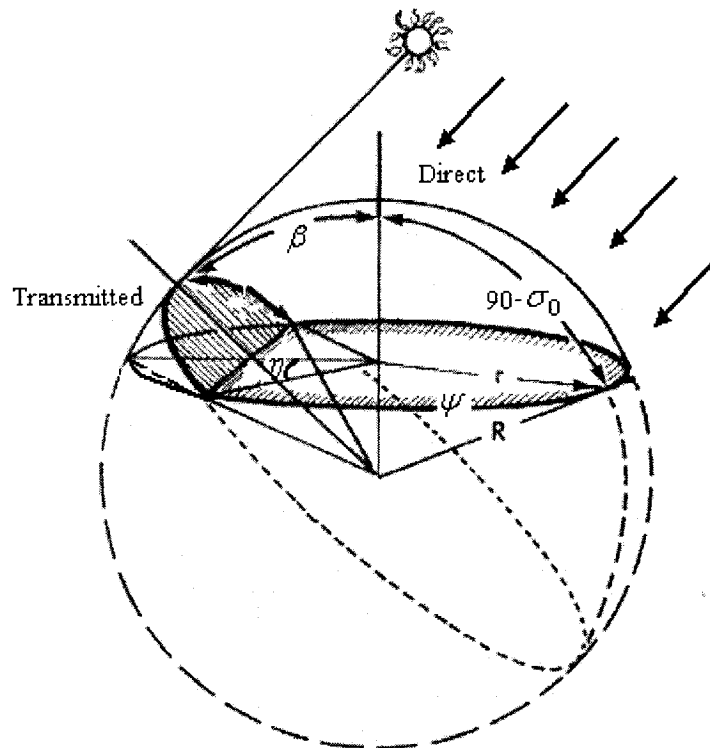
Figure C-1 Solar beam on a dome

Part one that receives transmitted solar radiation is described by:

$$270 + \psi_s - \eta \le \psi \le 270 + \psi_s + \eta \qquad \text{(C-1)}$$

and

$$\sigma_0 \le \varphi \le 90 - \beta \qquad \text{(C-2)}$$

where ψ_s is the solar azimuth (the angle between the shadow of solar beam on the horizontal surface and due south).

η is calculated based on the trigonometrical relationships (Figure C-2 and Figure C-3)

$$\cos\eta = \frac{X}{R\cos\sigma_0} \qquad \text{(C-3)}$$
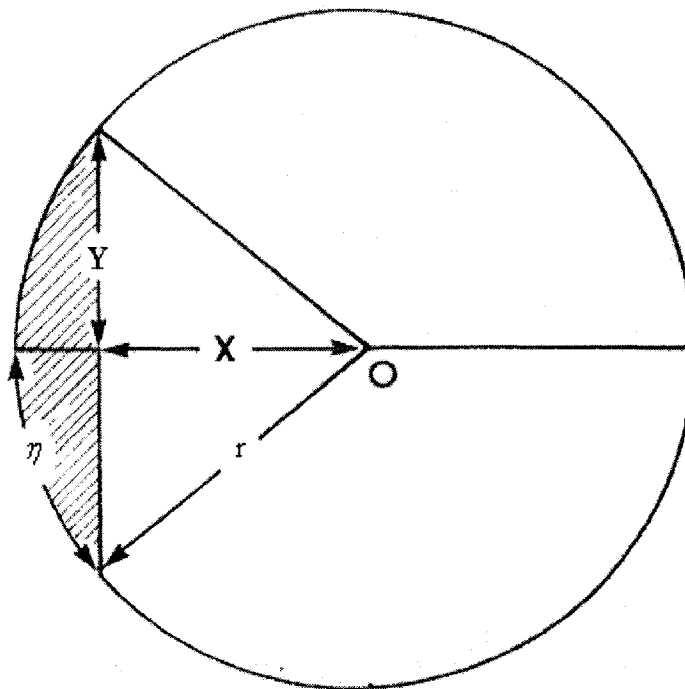
Figure C-2 Area of a segment

However

$$X = R\sin\sigma_0\tan\beta \qquad \text{(C-4)}$$

Therefore

$$\cos\eta = \frac{R\sin\sigma_0\tan\beta}{R\cos\sigma_0}$$

$$= \tan\sigma_0\tan\beta$$

(C-5)

giving

$$\eta = \cos^{-1}(\tan\sigma_0\tan\beta)$$

(C-6)
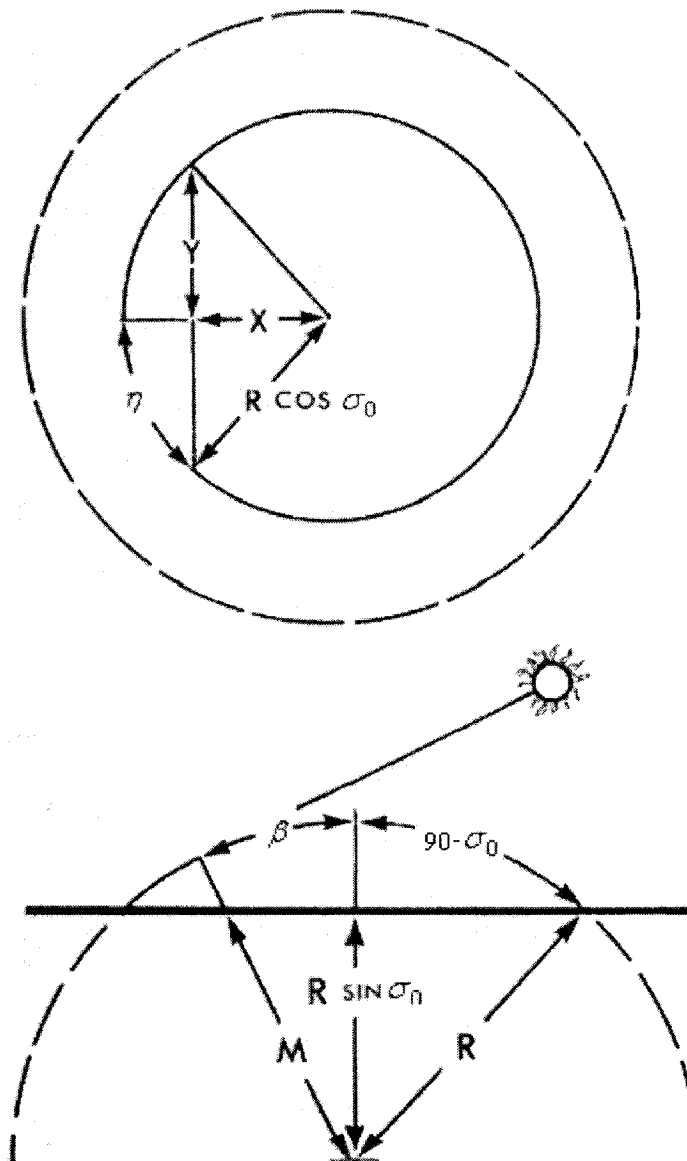
Figure C-3 Plan and section of a dome

Part two is the remaining part of the dome.

Transmitted solar radiation from one cell to cell (i,j)

The solar beam that is transmitted through one cell to the cell (i,j) is expressed using the parameter tmp:

$$x = x_{ij} + tmp \cdot \cos\beta \cdot \cos\psi_s$$
$$y = y_{ij} - tmp \cdot \cos\beta \cdot \sin\psi_s \qquad\qquad (C\text{-}7)$$
$$z = z_{ij} + tmp \cdot \sin\beta$$

The coordinates of the cell should also be fit into the dome surface equation:

$$x^2 + y^2 + z^2 = R^2 \qquad\qquad (C\text{-}8)$$

After solving for the above two equations, the parameter (tmp) is obtained:

$$tmp = -2 \cdot \left(x_{i,j} \cdot \cos\beta \cdot \cos\psi_s - y_{i,j} \cdot \cos\beta \cdot \sin\psi_s + z_{i,j} \cdot \sin\beta \right) \qquad (C\text{-}9)$$

Transmitted solar radiation from one cell to the walls/roof and ground surface

The beam radiation that passes through cell (i,j) and reach any wll/roof surface (Figure C-4) can be given as:

$$I_d' = A_{i,j} \alpha_\theta \cdot \tau \cdot I_{DN} \cos\theta \qquad\qquad (C\text{-}10)$$

where θ is the angle between the solar beam and the out side normal of cell (i,j).
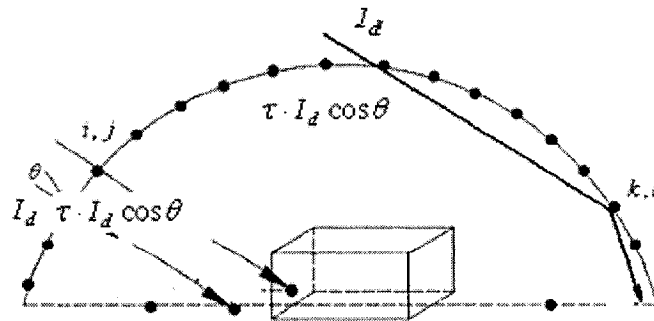
Figure C-4 Beam radiations transmitted through dome surface and reach wall surface

The calculation procedure is as follows:

1. For each line that passes through the center of cell (i,j) and follows the direction of the solar beam, the equations can be given as:

$$x = x_{i,j} - tmp \cdot \cos\beta \cdot \cos\psi_s$$
$$y = y_{i,j} + tmp \cdot \cos\beta \cdot \sin\psi_s \qquad \text{(C-11)}$$
$$z = z_{i,j} - tmp \cdot \sin\beta$$

2. The angle between each line and the west wall surface can be calculated as:

$$\cos\phi_1 = \frac{\left| -\sin\psi_0 \cdot \cos\beta \cdot \cos\psi_s + \cos\psi_0 \cdot \cos\beta \cdot \sin\psi_s \right|}{\sqrt{(-\sin\psi_0)^2 + (\cos\psi_0)^2} \sqrt{(-\cos\beta \cdot \cos\psi_s)^2 + (\cos\beta \cdot \sin\psi_s)^2 + (-\sin\beta)^2}} \qquad \text{(C-12)}$$
$$= \left| -\sin\psi_0 \cdot \cos\beta \cdot \cos\psi_s + \cos\psi_0 \cdot \cos\beta \cdot \sin\psi_s \right|$$

3. After solving for the equations (C-11) and (B-10), the parameter (tmp) for the intersection point for each line and the west wall surface is obtained:

$$tmp = \frac{\sin\psi_0 \cdot x_{i,j} + \cos\psi_0 \cdot y_{i,j} + L/2}{\sin\psi_0 \cdot \cos\beta \cdot \cos\psi_s - \cos\psi_0 \cdot \cos\beta \cdot \sin\psi_s} \qquad \text{(C-13)}$$

where:

$$90 \le \gamma \le 180 \qquad \text{(C-14)}$$

$$\gamma = \psi_s - \psi_0 \qquad \text{(C-15)}$$

The angles between each line and other surfaces, and the parameter (tmp) for the intersection pints are presented in Table C-1:

Table C-1 Angles between each line and other surfaces and the parameter (tmp) for the intersection pints

	$\cos\varphi_i$	tmp	γ
South	$\left|\cos\psi_0 \cdot \cos\beta \cdot \cos\psi_s + \sin\psi_0 \cdot \cos\beta \cdot \sin\psi_s\right|$	$\dfrac{\cos\psi_0 \cdot x_{i,j} - \sin\psi_0 \cdot y_{i,j} - W/2}{\cos\psi_0 \cdot \cos\beta \cdot \cos\psi_s + \sin\psi_0 \cdot \cos\beta \cdot \sin\psi_s}$	$-90 \le \gamma \le 90$
East	$\left|-\sin\psi_0 \cdot \cos\beta \cdot \cos\psi_s + \cos\psi_0 \cdot \cos\beta \cdot \sin\psi_s\right|$	$\dfrac{\sin\psi_0 \cdot x_{i,j} + \cos\psi_0 \cdot y_{i,j} - L/2}{\sin\psi_0 \cdot \cos\beta \cdot \cos\psi_s - \cos\psi_0 \cdot \cos\beta \cdot \sin\psi_s}$	$\gamma \le -90$
North	$\left|\cos\psi_0 \cdot \cos\beta \cdot \cos\psi_s + \sin\psi_0 \cdot \cos\beta \cdot \sin\psi_s\right|$	$\dfrac{-\cos\psi_0 \cdot x_{i,j} + \sin\psi_0 \cdot y_{i,j} - W/2}{-\cos\psi_0 \cdot \cos\beta \cdot \cos\psi_s - \sin\psi_0 \cdot \cos\beta \cdot \sin\psi_s}$	$\gamma \ge 180$
Roof	$|\sin\beta|$	$\dfrac{z_{i,j} - R\sin\sigma_0 - H}{\sin\beta}$	No constraint
Ground	$|\sin\beta|$	$\dfrac{z_{i,j} - R\sin\sigma_0}{\sin\beta}$	No constraint

4. In order to determine whether or not the intersection point is on a certain surface, a transformation of the coordinates for each point is necessary. By making a transformation of counter clockwise Ψ_0, the coordinates for each intersection point become:

$$x_1 = x_0\cos\psi_0 - y_0\sin\psi_0$$
$$y_1 = x_0\sin\psi_0 + y_0\cos\psi_0 \qquad\qquad (C\text{-}16)$$
$$z_1 = z_0$$

where x_0, y_0 and z_0 are the original coordinates of the intersection point and x_1, y_1, z_1 are the new ones. For example, if $x_0=0$, $y_0 = L/2$, the new coordinates becomes (Figure C-5):

$$x_1 = -L/2 \cdot \sin\psi_0 \qquad\qquad (C\text{-}17)$$

and

$$y_1 = L/2 \cdot \cos\psi_0 \qquad\qquad (C\text{-}18)$$

252
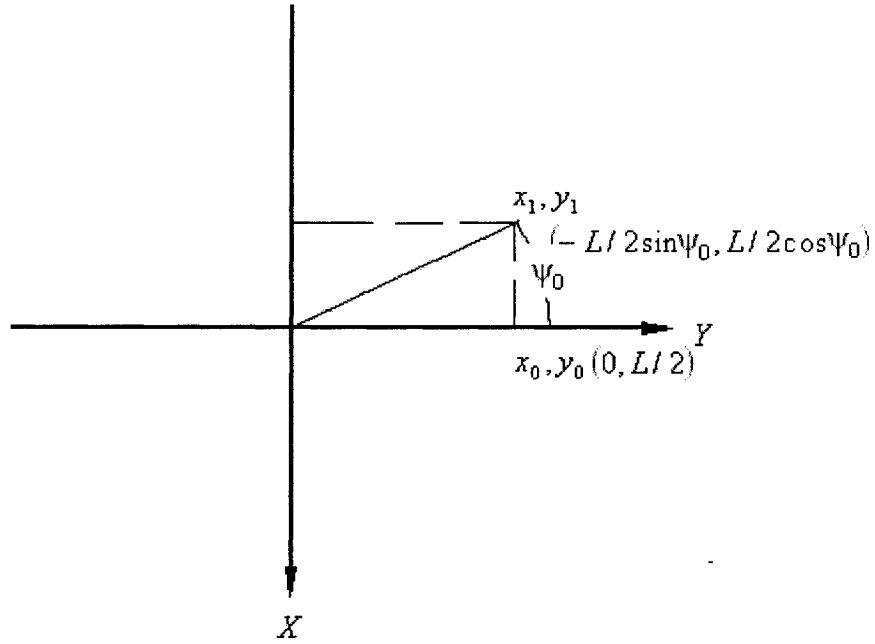
Figure C-5 Coordinate transformation

Table C-2 lists the range of the new coordinates for each surface after the transformation:

Table C-2 Range of the new coordibnates for each surface

	X	y	Z
West	$-\dfrac{W}{2} \leq x \leq \dfrac{W}{2}$	$y = -\dfrac{L}{2}$	$R\sin\sigma_0 \leq z \leq R\sin\sigma_0 + H$
South	$x = \dfrac{W}{2}$	$-\dfrac{L}{2} \leq y \leq \dfrac{L}{2}$	$R\sin\sigma_0 \leq z \leq R\sin\sigma_0 + H$
East	$-\dfrac{W}{2} \leq x \leq \dfrac{W}{2}$	$y = \dfrac{L}{2}$	$R\sin\sigma_0 \leq z \leq R\sin\sigma_0 + H$
North	$x = -\dfrac{W}{2}$	$-\dfrac{L}{2} \leq y \leq \dfrac{L}{2}$	$R\sin\sigma_0 \leq z \leq R\sin\sigma_0 + H$
Roof	$-\dfrac{W}{2} \leq x \leq \dfrac{W}{2}$	$-\dfrac{L}{2} \leq y \leq \dfrac{L}{2}$	$z = R\sin\sigma_0 + H$

5. The beam radiation that passes through the dome surface and then reaches each wall surface is calculated as:

$$Q_{absorbed,rad} = \sum_{\substack{i=1,M \\ j=1,N}} \tau \cdot I_{DN} \cdot A_{i,j} \cdot \cos\theta_{ij} \qquad (C-19)$$

Appendix D Determination on the Windward and Leeward Areas of the Dome Cover/House

Wind direction and velocity are very important because they affect the outside convective coefficient, thus have an impact on the convective heat transfer rate upon the surface, and finally affect the cooling/heating load of the house. This section presents the method used to determine whether the surface of a dome is a windward or leeward. The wind direction is represented by the angle ω_w, which is the angle between the wind direction and the due north.

Windward conditions for a house without a dome cover

The position of the building is assumed be $\psi = \psi_0$. The whole roof surface is in windward state, since the wind is not blocked by other surface. The conditions for whether the surface of a wall is windward are shown in Table D-1.

Table D-1 Windward conditions for a house without a dome cover

Surface	Windward
North	$270 + \psi_0 \leq \omega_w \leq 360$ or $0 \leq \omega_w \leq \psi_0$
East	$\psi_0 \leq \omega_w \leq 180 + \psi_0$
South	$90 + \psi_0 \leq \omega_w \leq 270 + \psi_0$
West	$180 + \psi_0 \leq \omega_w \leq 360$ or $0 \leq \omega_w \leq \psi_0$
Roof	$0 \leq \omega_w \leq 360_0$

Windward condition for the dome

The conditions for whether the surface of cell (i,j) is windward or leeward are shown in Table D-2 and Figure D-1.

Table D-2 Windward conditions for cell (i,j)

Conditions	Direction of the wind	Windward	Leeward
1	$0 \le \omega_w \le 90$	other	$\omega_w \le \psi_{ij} \le 180 + \omega_w$
2	$90 \le \omega_w \le 180$	other	$\omega_w \le \psi_{ij} \le 180 + \omega_w$
3	$180 \le \omega_w \le 270$	$\omega_w - 180 \le \psi_{ij} \le \omega_w$	Other
4	$270 \le \omega_w \le 360$	$\omega_w - 180 \le \psi_{ij} \le \omega_w$	Other
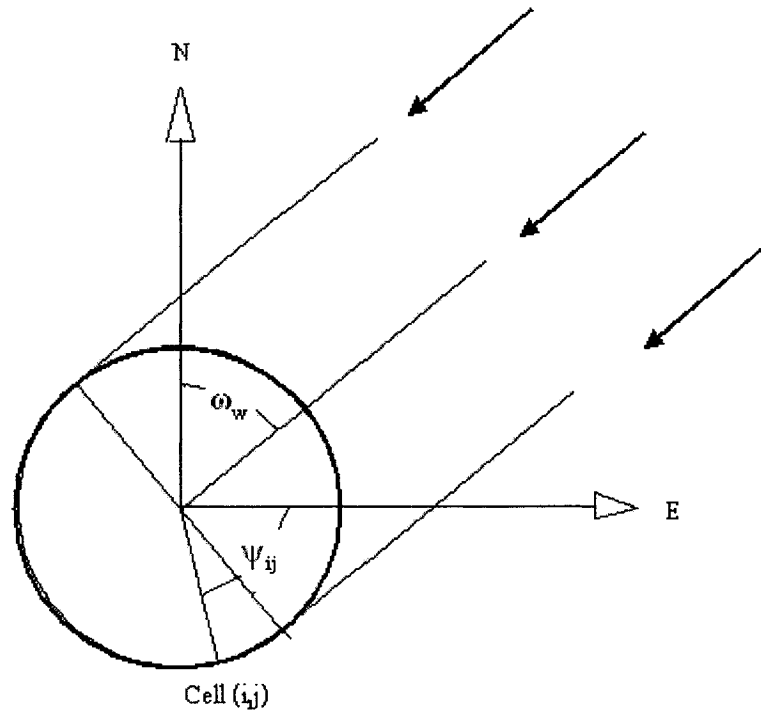
Figure D-1 Wind over the dome surface (condition no.1)

Appendix E Comparison between the 3D-TAF Model and the CFD Model

Figure E-1 Variation of the average dimensionless dome air temperature with the dimensionless height. Comparison between the 3D-TAF model and the COMSOL program (Case 3)

Figure E-2 Variation of the average dome air temperature with height. Comparison between the 3D-TAF model and the COMSOL program (Case 4)

Figure E-3 Variation of the average dimensionless dome air temperature with the dimensionless height. Comparison between the 3D-TAF model and the COMSOL program (Case 4)

Figure E-4 Variation of the average dome air temperature with height. Comparison between the 3D-TAF model and the COMSOL program (Case 5)

259

Figure E-5 Variation of the average dimensionless dome air temperature with the dimensionless height. Comparison between the 3D-TAF model and the COMSOL program (Case 5)

Figure E-6 Variation of the average dimensionless dome air temperature with the dimensionless height. Comparison between the 3D-TAF model and the COMSOL program (Case 6)
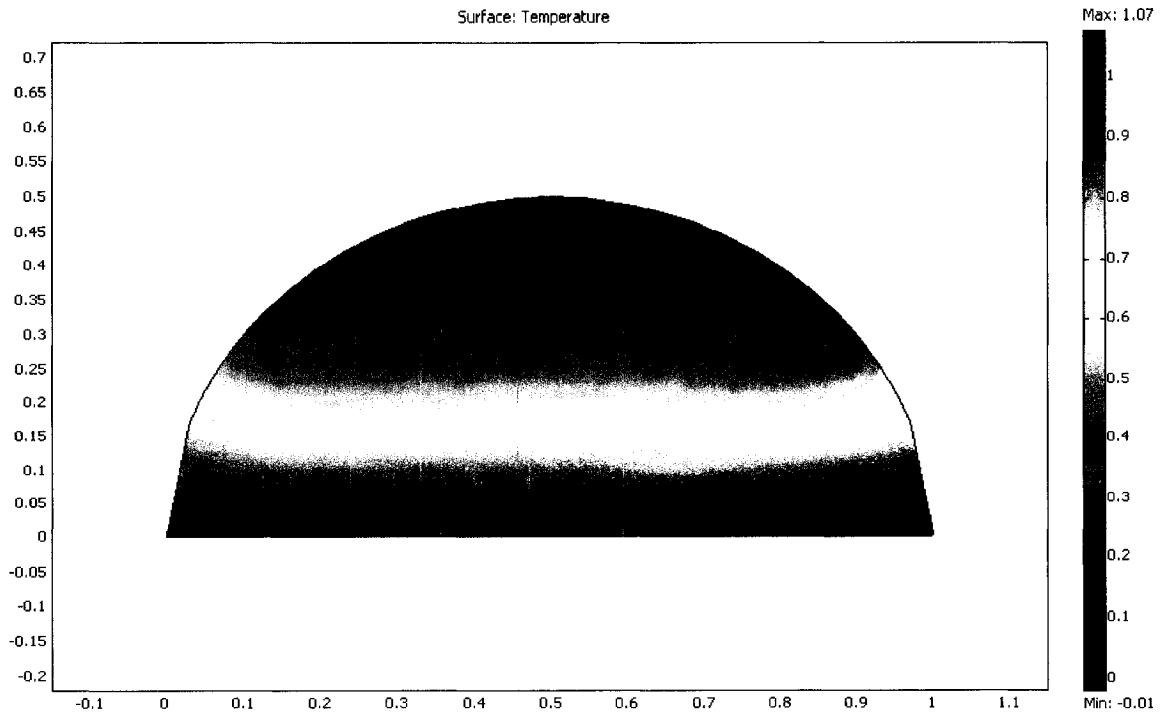
Figure E-7 Temperature distribution predicted by the COMSOL program (Case 3)
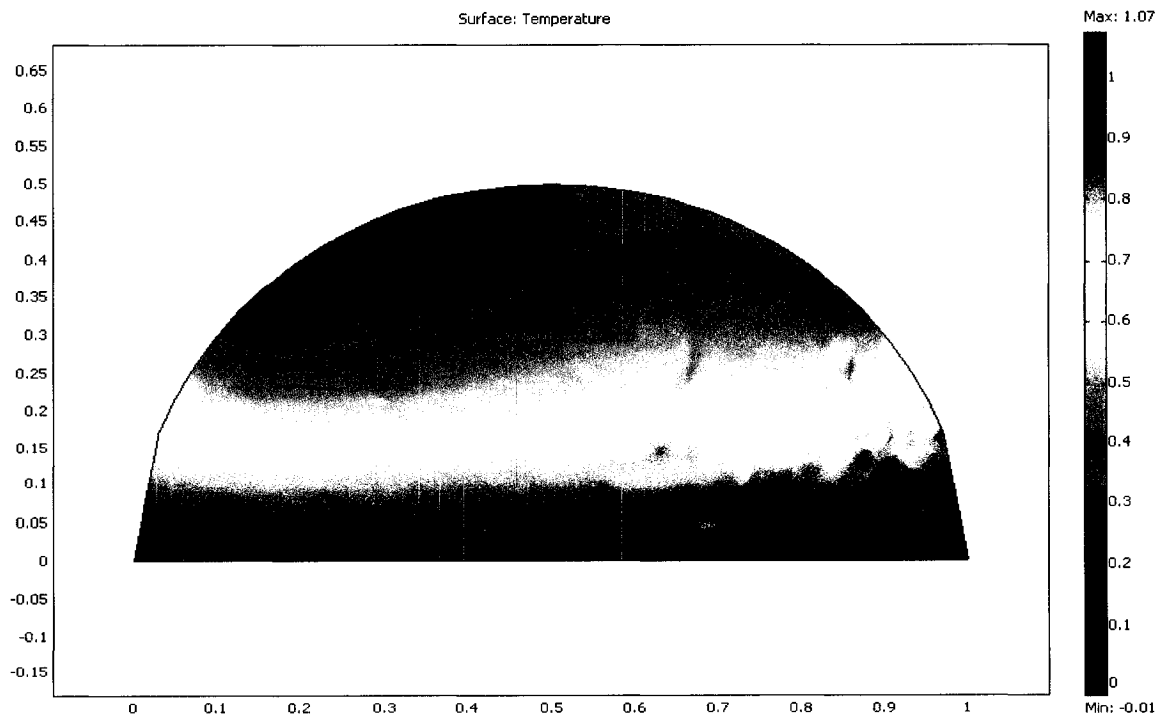
Figure E-8 Temperature distribution predicted by the COMSOL program (Case 4)

261
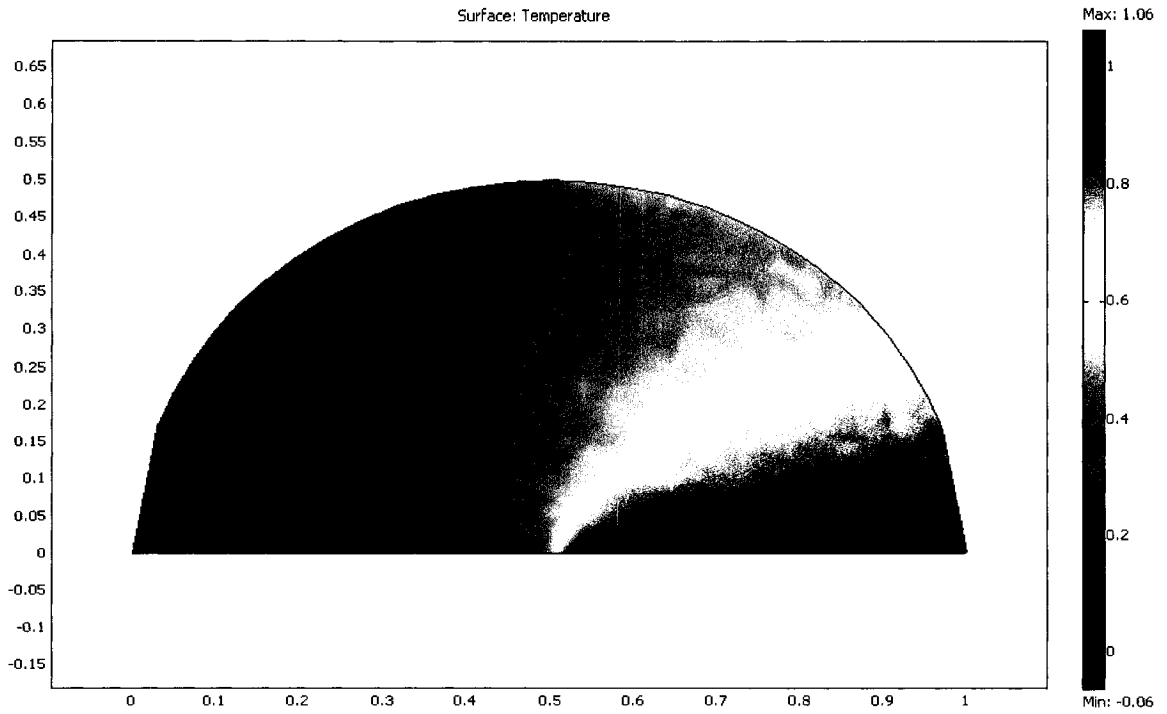
Figure E-9 Temperature distribution predicted by the COMSOL program (Case 5)
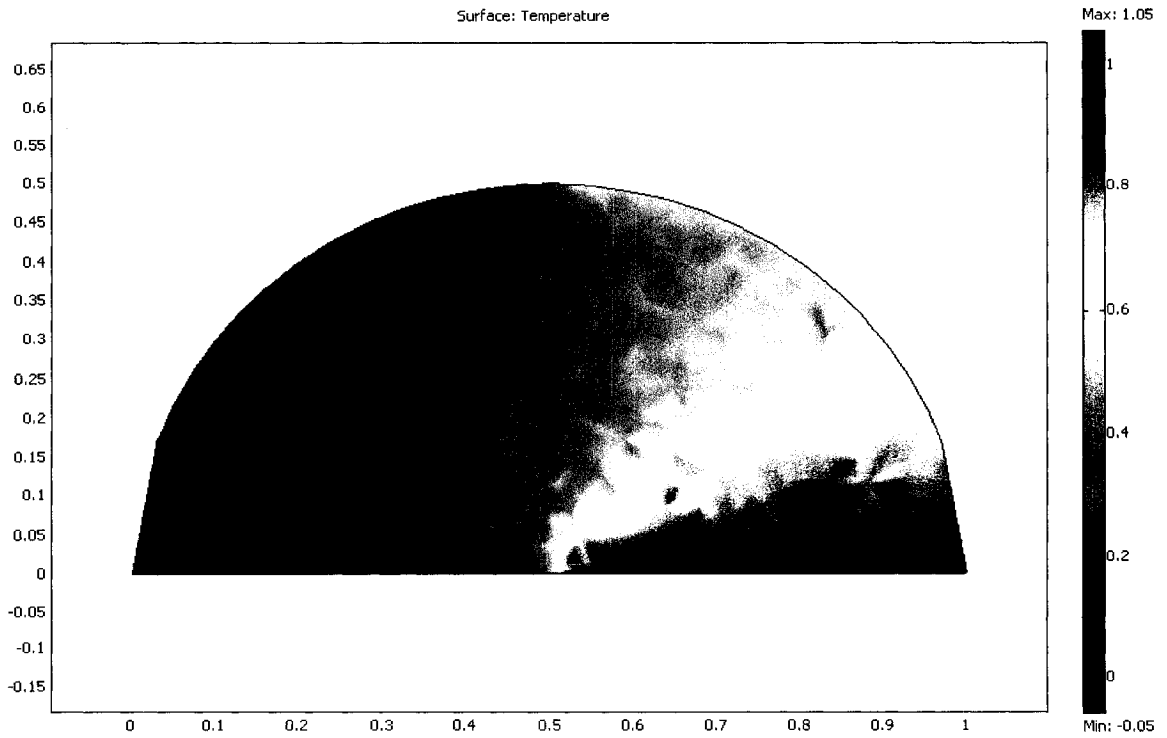
Figure E-10 Temperature distribution predicted by the COMSOL program (Case 6)

262
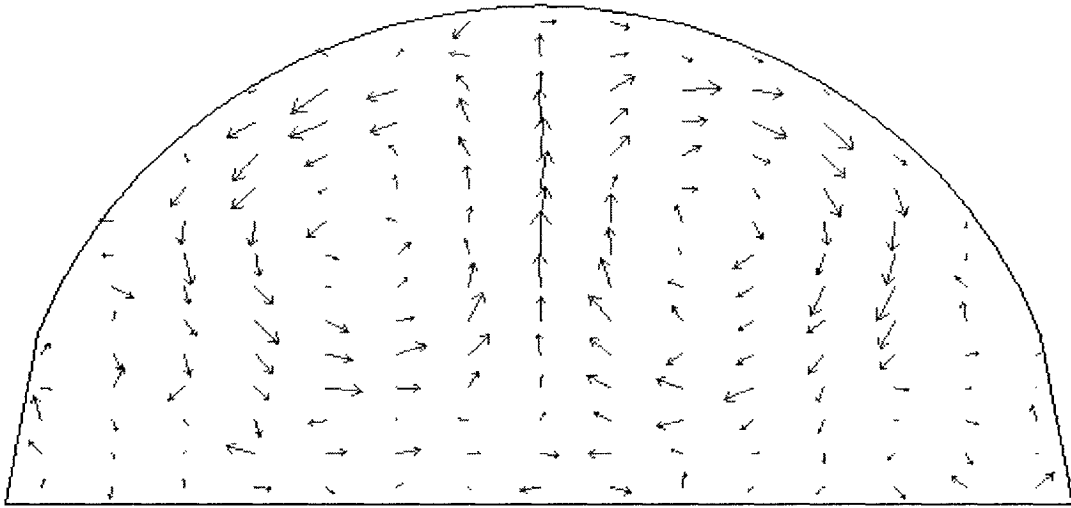
Figure E-11 Velocity field predicted by the COMSOL program (Case 3)
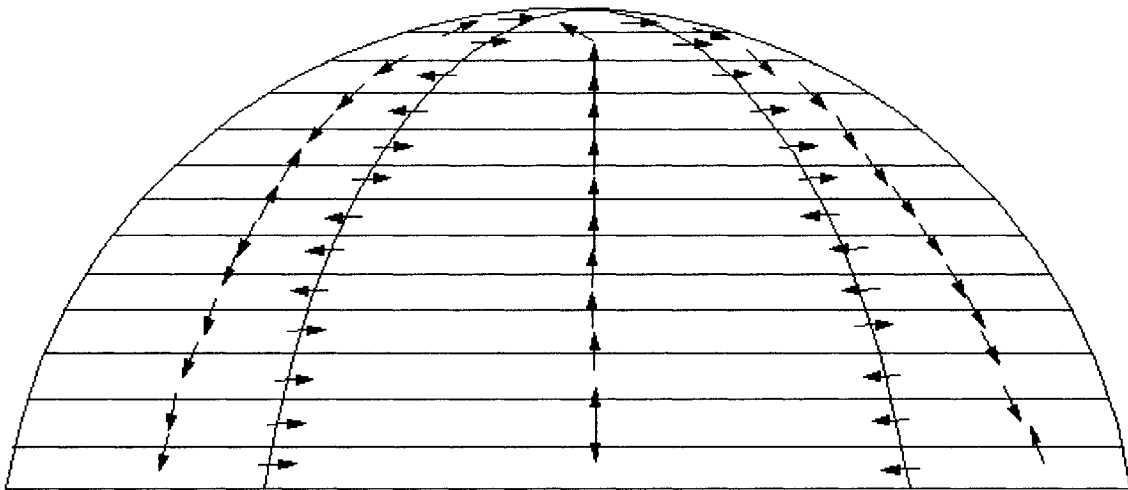
Figure E-12 Velocity field predicted by the 3D-TAF model (Case 3)
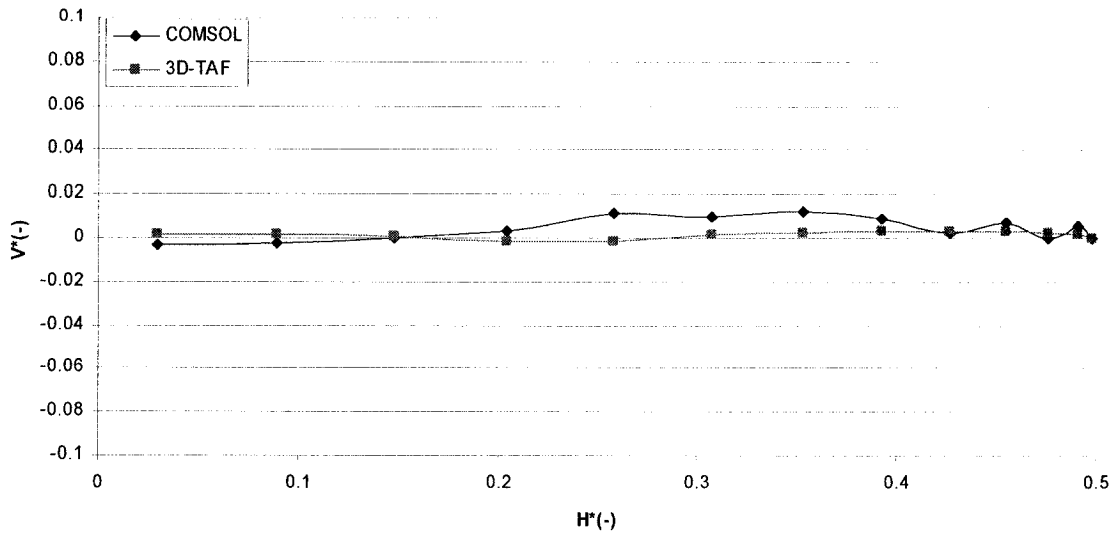
Figure E-13 Variation of the dimensionless air velocity with the dimensionless height. Comparison between the 3D-TAF model and the COMSOL program (Case 3)
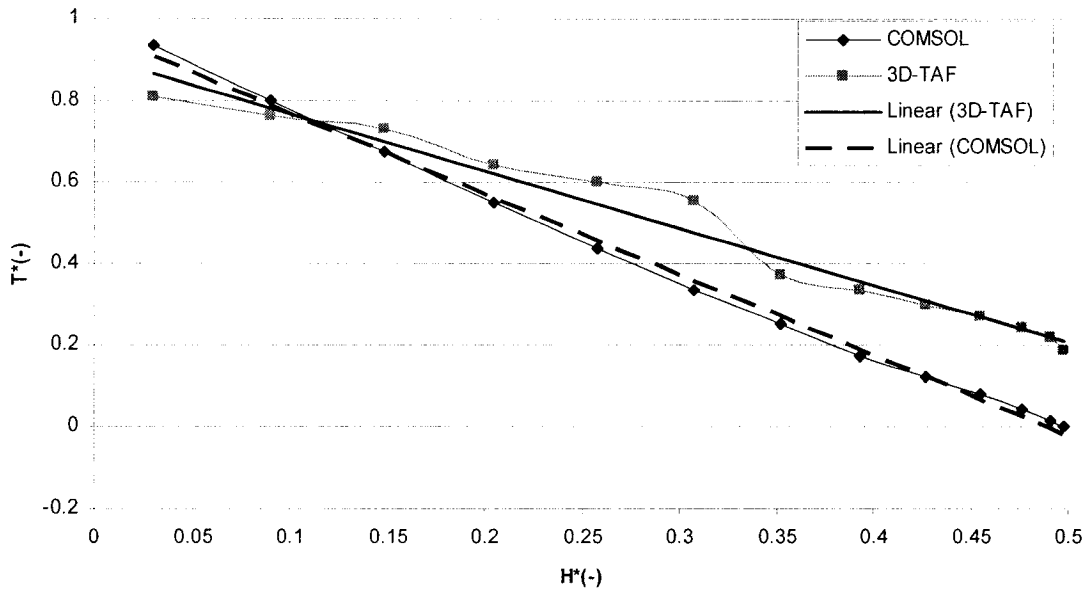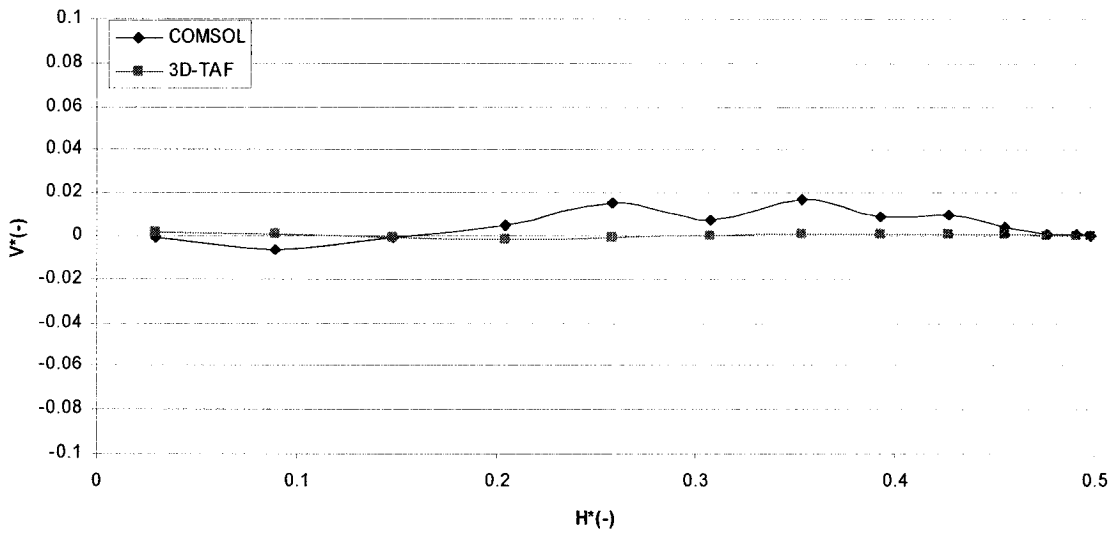

Figure E-14 Variation of the dimensionless air velocity with the dimensionless height. Comparison between the 3D-TAF model and the COMSOL program (Case 4)
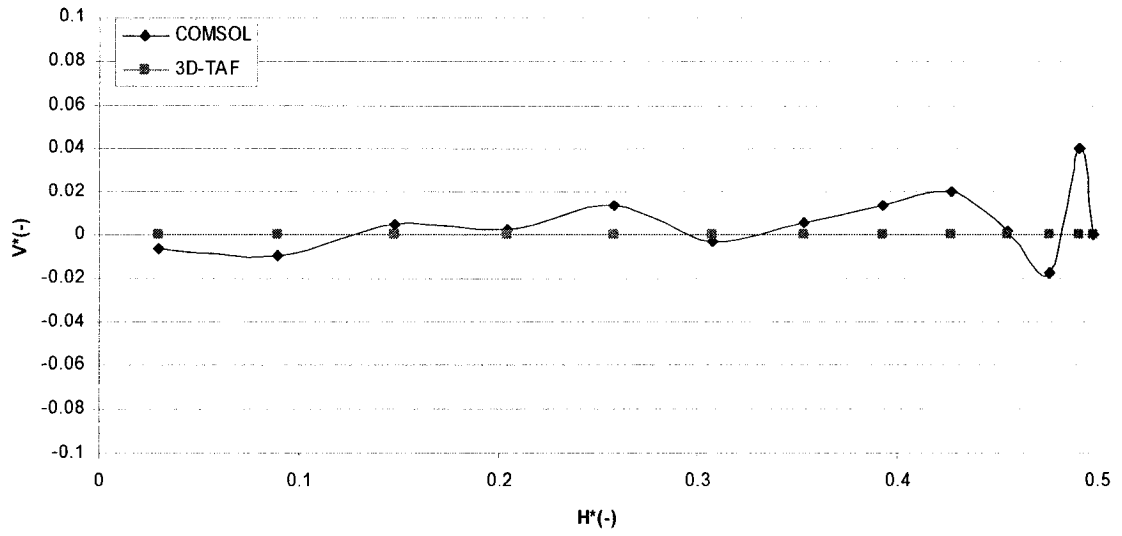
Figure E-15 Variation of the dimensionless air velocity with the dimensionless height. Comparison between the 3D-TAF model and the COMSOL program (Case 5)

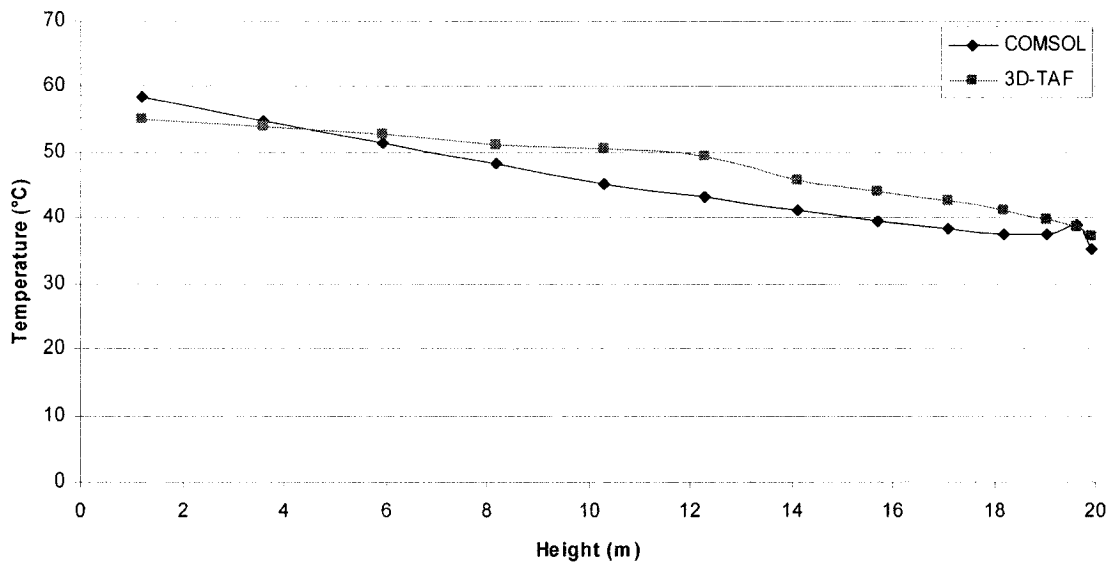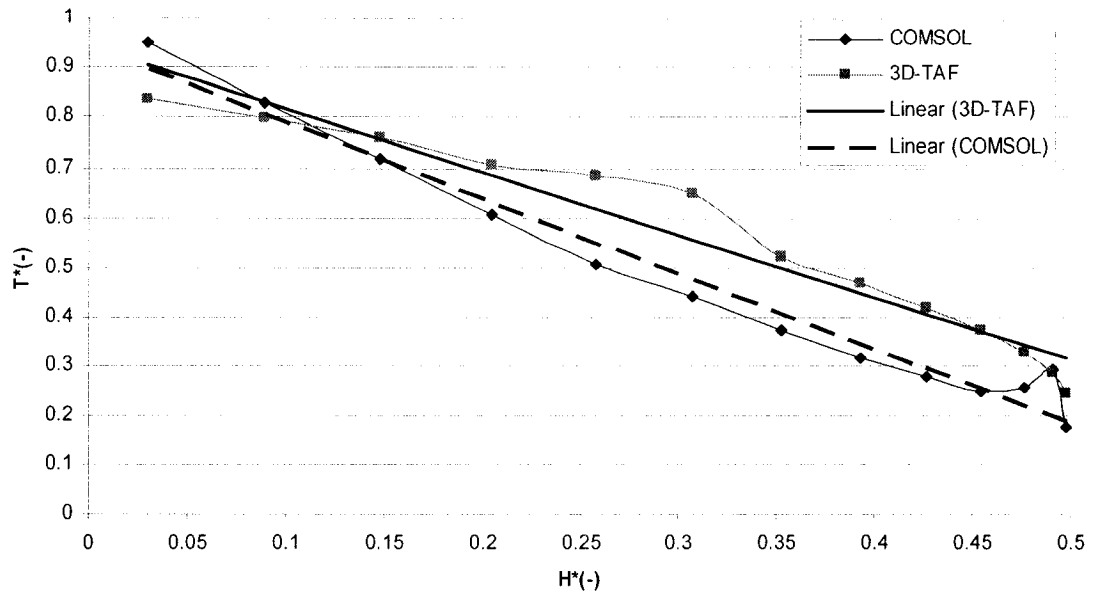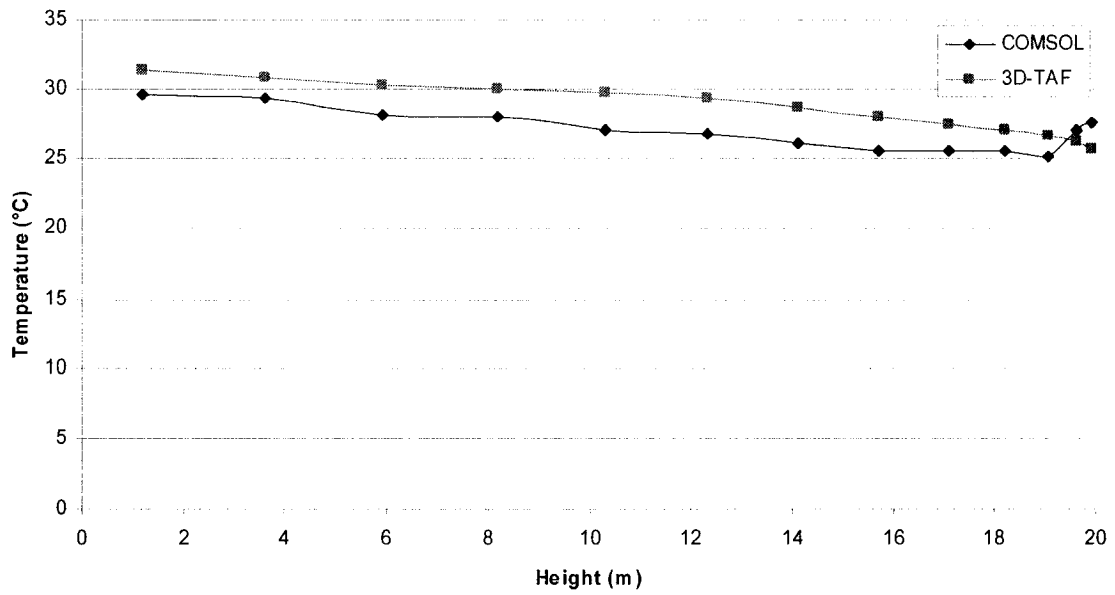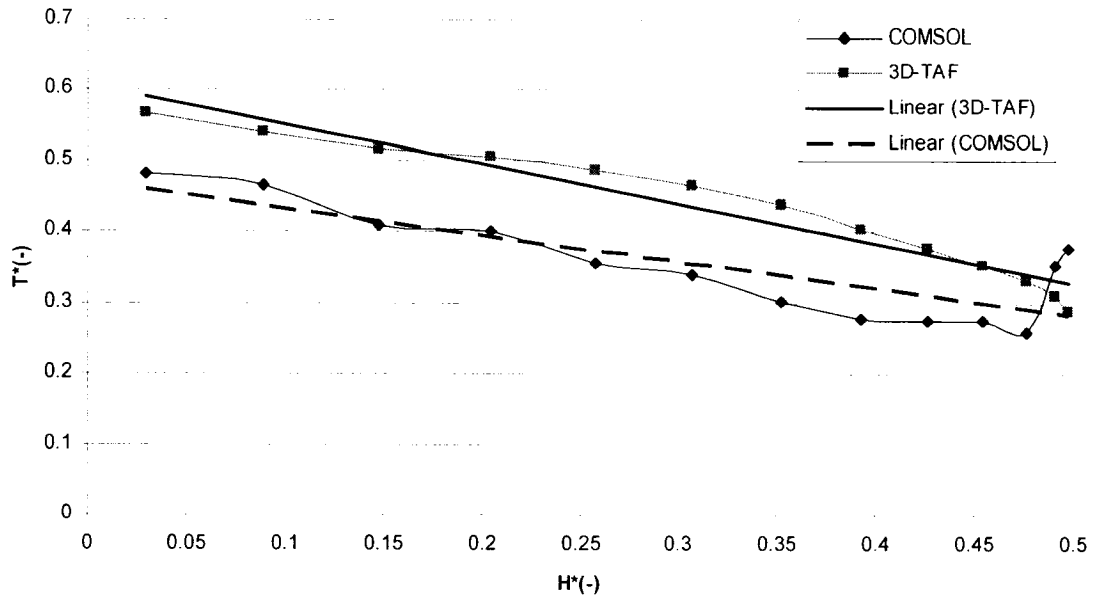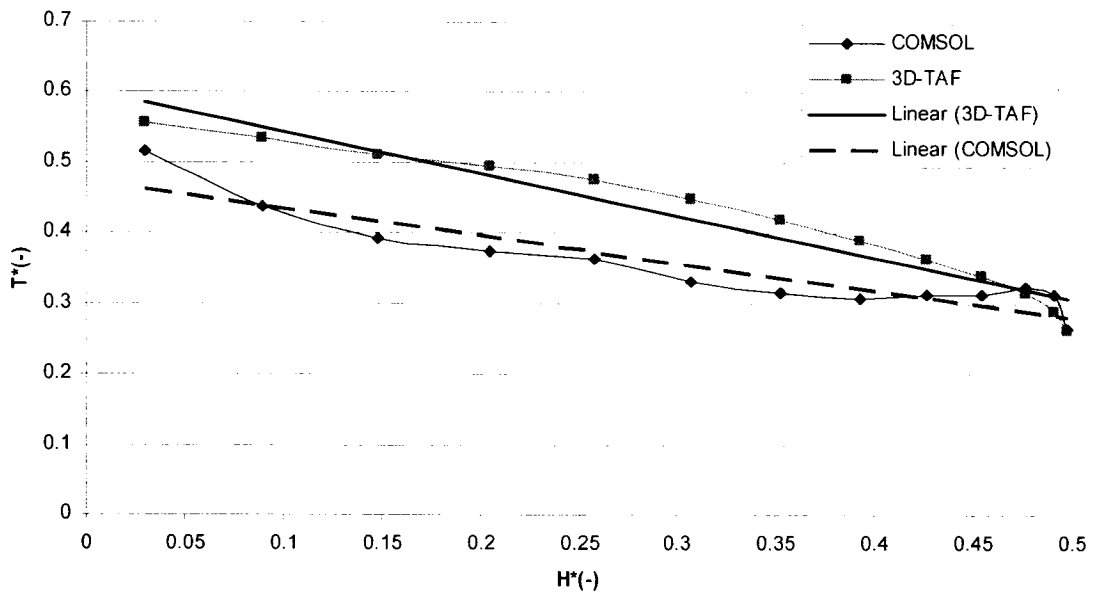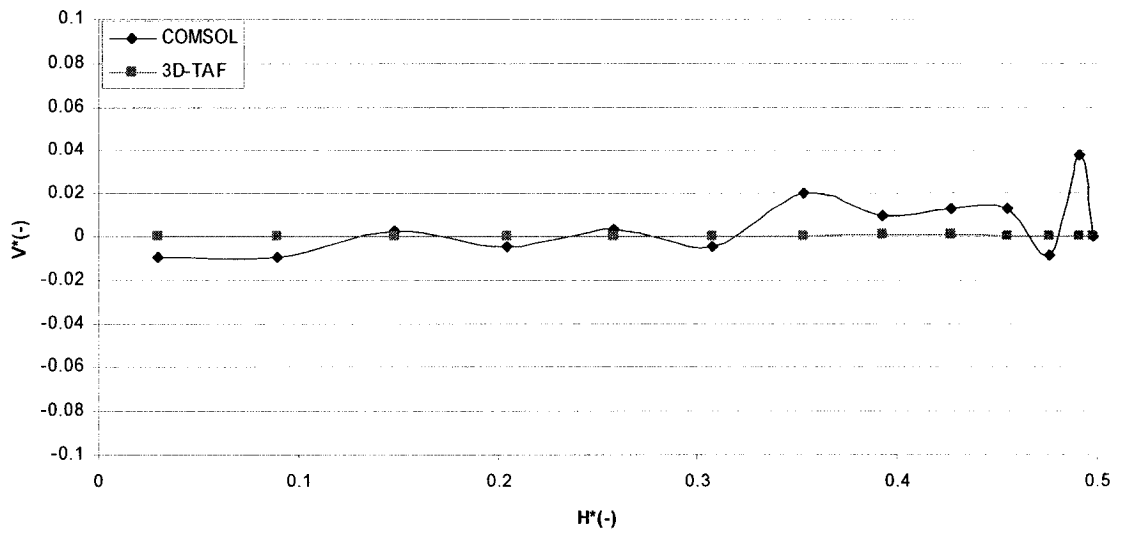Figure E-16 Variation of the dimensionless air velocity with the dimensionless height. Comparison between the 3D-TAF model and the COMSOL program (Case 6)

Appendix F Sample of Input and Output Files

Input Files

File#1:

0 (Building azimuth, deg. from due north)
75 (Local standard longitude, deg. W)
73.75 (Local longitude, deg. W)
45.46(Local latitude, deg. N)
0.2 (Ground reflectance)
730 (Specific heat of soil, J/kg·°C)
0.5 (Conductivity of soil, J/m·°C)
1500 (Density of soil, kg/m^3)
0.80 (Emissivity of ground)
21 (Room air temperature, ·°C)
1005 (Specific heat of air, J/kg·°C)
837 (Specific heat of the dome cover, J/kg·°C)
1.38 (Conductivity of the dome cover, J/m·°C)
2600 (Density of the dome glazing, kg/m^3)
0.84 (Emissivity of glazing)
24.4E-03 (Thickness of the glazing, m)
20 (Radius of the dome, m)
20 (Truncation angle of the dome, deg.)
42 (Number of columns of the dome cover)
13 (Number of rows of the dome cover)
10 (Length of the wall, m)
10 (Width of the wall, m)
4 (Height of the wall, m)
0.93 (Emissivity of brick)
0.903 (Emissivity of gypsum board)
0.15 (Window-to-wall ratio)
3.0 (Width of the window, m)
2.0 (Height of the window, m)
1.96 (U-value of the window, m^2·°C/W)
0.15 (Air infiltration rate of the house, h^{-1})
15 (Installed lighting intensity, W/m^2)
4 (Number of occupants)

File #2:

Extraterrestrial solar irradiance and related data

	ET	DD	A	B	C
Jan	-11.20	-20	1230	0.142	0.058
Feb	-13.90	-10.8	1215	0.144	0.06
Mar	-7.50	0	1186	0.156	0.071
Apr	1.10	11.6	1136	0.18	0.097
May	3.30	20	1104	0.196	0.121
Jun	-1.40	23.45	1088	0.205	0.134
Jul	-6.20	20.6	1085	0.207	0.136
Aug	-2.40	12.3	1107	0.201	0.122
Sep	7.50	0	1151	0.177	0.092
Oct	15.40	-10.5	1192	0.16	0.073
Nov	13.80	-19.8	1221	0.149	0.063
Dec	1.60	-23.45	1233	0.142	0.057

Daily temperature [°C]

Jan	Feb	Mar	Apr	May	Jun	Jul	Aug	Sep	Oct	Nov	Dec
-18.5	-12.2	3.9	3.3	11.7	15.8	18.9	17.2	10.9	4.4	2.2	-9.9
-19.1	-12.2	3.9	2.2	10	14.4	18.3	17.2	11.9	5	2.2	-8.3
-19.9	-12.8	3.9	2.8	9.4	12.5	18.9	17.2	11.9	5	1.7	-7.3
-20.6	-11.1	3.3	1.1	7.2	13.6	17.8	17.2	12.5	5	0.6	-7.7
-21	-11.1	3.3	1.7	7.8	13.5	16.7	15.6	12.3	3.9	0.6	-7.7
-21.9	-11.7	3.3	2.8	8.9	15.2	17.2	15	11.3	3.3	0.6	-7.7
-23.3	-12.2	3.3	3.3	11.1	17	17.2	15.6	11.7	2.8	0	-7.7
-22.8	-13.3	3.3	4.4	12.8	18	19.4	16.7	13.7	3.3	-0.6	-7.7
-22.6	-11.7	2.8	6.7	14.4	18.6	21.7	18.9	15.2	3.3	-1.1	-7.2
-22.2	-10.6	3.3	8.3	16.7	19.7	23.3	20	17.7	3.3	-1.7	-5.7
-22.1	-10	3.3	9.4	17.2	19.8	23.9	21.1	18.8	3.9	-2.2	-5
-21.1	-8.9	3.3	10.6	18.9	20	24.4	21.7	18.9	2.8	-2.8	-3.9
-20.7	-8.3	3.9	11.1	20	19.9	25.6	22.8	20.1	2.8	-2.8	-4.7
-20.4	-7.8	3.9	12.2	20.6	22	26.1	23.9	20.4	2.8	-3.3	-5.6
-20.1	-6.7	3.9	11.7	21.1	22	26.7	24.4	19.5	1.7	-3.9	-5.9
-20.2	-6.1	3.3	12.8	21.1	22.1	26.1	23.9	19.4	1.7	-4.4	-7
-20.3	-6.7	3.3	12.2	21.7	21.4	25.6	23.9	18.8	1.7	-4.4	-7.3
-20.7	-8.9	2.8	11.7	20.6	21.1	25	23.3	17.2	1.7	-5	-7.4
-21.2	-8.9	3.3	11.1	19.4	20.3	23.9	22.2	15.9	1.1	-5	-7.5
-21	-8.9	2.8	10.6	18.3	19.2	23.3	21.1	15.2	1.1	-5	-8.2
-20.8	-9.4	2.8	8.3	18.9	18.2	22.2	18.3	15.5	1.7	-5	-9.6
-21.4	-7.8	2.2	5.6	16.1	16.6	22.8	18.9	14.2	1.7	-5	-10.8
-22	-8.3	2.2	5.6	16.7	16.9	23.3	18.9	13.9	1.7	-5	-12.3
-22.6	-8.3	1.7	5	16.1	18.2	22.2	18.9	12.9	0	-5.6	-11.7

Wind direction [10° from due north] and wind speed [km/h]

Hour	Jan D	Jan S	Feb D	Feb S	Mar D	Mar S	Apr D	Apr S	May D	May S	Jun D	Jun S	Jul D	Jul S	Aug D	Aug S	Sep D	Sep S	Oct D	Oct S	Nov D	Nov S	Dec D	Dec S
1	27	26	25	21	22	22	32	8	23	29	18	14	25	18	21	2	0	0	20	13	28	8	5	19
2	27	26	26	23	21	21	34	3	23	29	14	14	25	13	17	2	15	8	19	14	26	2	4	24
3	27	30	26	18	23	23	34	5	21	32	15	18	24	11	0	0	15	8	19	10	30	0	5	26
4	27	24	26	16	0	0	34	0	22	19	16	14	23	16	0	0	15	3	17	6	30	11	5	21
5	27	26	27	18	18	18	32	2	24	23	16	11	22	16	0	0	18	6	18	10	30	5	5	18
6	27	24	26	11	0	0	32	0	25	18	16	16	24	16	24	2	0	0	17	8	25	5	5	23
7	27	32	24	2	0	0	32	0	26	14	16	16	24	8	14	3	0	0	17	11	29	6	5	18
8	27	22	27	2	3	2	33	0	25	23	14	13	23	13	17	6	17	5	16	8	29	10	5	21
9	27	32	0	0	0	0	32	0	26	26	16	13	21	14	16	11	17	6	21	8	29	14	3	19
10	27	26	22	8	0	0	34	0	25	29	17	18	23	13	21	11	16	3	19	11	30	19	3	26
11	26	35	17	6	11	11	32	11	28	31	14	19	25	19	23	8	17	6	20	13	31	18	3	23
12	26	32	16	14	14	8	33	8	20	29	13	16	26	24	21	16	14	5	21	14	31	16	4	19
13	27	33	12	18	11	14	28	14	19	23	15	21	32	21	21	16	16	6	22	18	33	14	4	19
14	27	39	12	21	12	16	34	16	20	27	15	24	30	23	21	18	14	13	20	16	30	21	3	23
15	26	48	12	24	11	16	31	16	22	29	16	21	27	24	21	14	16	13	21	13	32	18	3	23
16	26	44	12	26	8	18	34	18	29	26	15	14	26	21	22	19	15	13	17	16	30	16	3	26
17	27	32	11	29	7	21	27	21	28	24	22	8	29	31	22	26	14	13	17	18	29	18	3	19
18	26	30	10	24	6	19	29	19	27	21	22	3	30	26	24	18	14	10	18	19	28	11	3	23
19	26	33	5	18	26	23	29	23	28	18	5	6	30	19	24	18	15	13	18	21	31	13	4	19
20	26	28	5	24	6	19	27	19	32	14	10	11	30	18	23	21	16	14	17	19	31	11	4	23
21	28	30	5	26	5	29	28	13	34	11	11	14	30	21	22	23	19	10	19	18	32	11	3	14
22	27	43	4	27	5	35	27	13	30	8	9	10	29	16	22	16	18	13	26	14	32	13	4	19
23	28	41	4	31	5	35	30	11	33	13	11	14	30	14	24	13	19	14	28	10	32	10	4	13
24	27	28	3	29	6	32	32	10	2	14	10	13	31	11	24	18	19	14	17	8	32	10	4	19

Day of the year for calculating ground surface temperature [days]

Jan	Feb	Mar	Apr	May	Jun	Jul	Aug	Sep	Oct	Nov	Dec
21	52	80	111	141	172	203	234	265	295	326	356

Glazing system properties (single clear)

Incident angle	0	10	20	30	40	50	60	70	80	90
Transmittance	0.485	0.483	0.479	0.470	0.456	0.435	0.399	0.330	0.191	0.000
Absorptance	0.455	0.454	0.459	0.467	0.476	0.483	0.484	0.462	0.374	0.000
Rreflectance	0.060	0.062	0.062	0.064	0.068	0.082	0.118	0.209	0.434	1.000

Wall information (thickness [m], conductivity [J/m·°C], density [kg/m³], specific heat [J/kg·°C])

West Wall

0.05	1.333	2002.002	921
0.05	1.333	2002.002	921
0.135	0.043	90.998	841
0.020	0.727	1602.002	841

South Wall

0.05	1.333	2002.002	921
0.05	1.333	2002.002	921
0.135	0.043	90.998	841
0.020	0.727	1602.002	841

East Wall

0.05	1.333	2002.002	921
0.05	1.333	2002.002	921
0.135	0.043	90.998	841
0.020	0.727	1602.002	841

North Wall

0.05	1.333	2002.002	921
0.05	1.333	2002.002	921
0.135	0.043	90.998	841
0.020	0.727	1602.002	841

Roof

0.13	0.415	1248.999	1088
0.215	0.043	90.998	841
0.010	0.727	1602.002	841
0.010	0.727	1602.002	841

Floor

0.100	0.81	977	841
0.05	0.043	90.998	841

Output File

Date: 1, 21   Number of Nodes: 1172

Time (K)   Hour Angle   cosβ (β: Solar Latitude) Ψ_s (Ψ_s: Solar Azimuth) (K=1, 24)

Solar Incidence on Each Cell of the Dome:

Cell location (i,j), Time (K), Direct Beam Solar Radiation [W/m^2], cosβ, Diffuse Solar Radiation from the Sky[W/m^2], Reflected Solar Radiation from the Ground[W/m^2], Total Incident Solar Radiation[W/m^2], Transmittance, Transmitted Solar Radiation[W/m^2] (K=1, 24)

Solar Radiation Reaching the Ground Surface inside the Dome [W/m^2] (K=1, 24)

Solar Radiation Reaching Each Wall Surface:

Solar Radiation Reaching West Wall Surface [W/m^2] (K=1, 24)

Solar Radiation Reaching SouthWall Surface [W/m^2] (K=1, 24)

Solar Radiation Reaching East Wall Surface [W/m^2] (K=1, 24)

Solar Radiation Reaching North Wall Surface [W/m^2] (K=1, 24)

Solar Radiation Reaching Roof Surface [W/m^2] (K=1, 24)

Temperature Variation with Time:

Temperature for the West Wall Surface [°C] (K=1, 24)

Temperature for the SouthWall Surface [°C] (K=1, 24)

Temperature for the East Wall Surface [°C] (K=1, 24)

Temperature for the North Wall Surface [°C] (K=1, 24)

Temperature for the Roof Surface [°C] (K=1, 24)

Temperature for the Floor [°C] (K=1, 24)

Temperature of the Ground Surface inside the Dme [°C] (K=1, 24)

Temperature of the Window [°C] (K=1, 24)

Cell Temperature [°C] (K=1, 24)

Dome Air Temperature [°C] (K=1, 24)

Air Flow Profile:

Air Flow for the Central Zones [kg/s] (K=1, 24)

Air Flow for the Perimeter Zones [kg/s] (K=1, 24)

Infiltration through the Bottom of the Dome Surface [kg/s] (K=1, 24)

Infiltration through the Top of the Dome Surface [kg/s] (K=1, 24)

Exfiltration from the House [kg/s] (K=1, 24)

Air Density: Zone (i,j) Time (k), Density [kg/m^3] (K=1, 24)

Air Pressure: Zone (i,j) Time (k), Pressure [Pa] (K=1, 24)

Heating Load: Time (k), T_o [°C], Q_{HVAC} [W] (K=1, 24)

Heat Loss Components: Time (k), Q_{wall}, Q_{roof}, Q_{floor}, Q_{window}, Q_{inf} [W] (K=1, 24)

Inside Convective Coefficient for the House: West, South, East, North, Roof, Floor [W/m^2·°C] (K=1, 24)

Inside Convective Coefficient for the Window (West, South, East) [W/m^2·°C] (K=1, 24)